University of Birmingham

UNIVERSITY OF
BIRMINGHAM

Siyuan Chen

What we can learn from Pulsar Timing Arrays (Or Not): Constraining astrophysical parametric models with gravitational waves

November 7, 2018

WHAT WE CAN LEARN FROM PULSAR TIMING ARRAYS (OR NOT): CONSTRAINING ASTROPHYSICAL PARAMETRIC MODELS WITH GRAVITATIONAL WAVES

by

SIYUAN CHEN

A thesis submitted to
The University of Birmingham
for the degree of
DOCTOR OF PHILOSOPHY

Institute of Gravitational Wave Astronomy
Astrophysics and Space Research Group
School of Physics and Astronomy
College of Engineering and Physical Sciences
The University of Birmingham
November 7, 2018

Abstract

The detection of gravitational waves (GWs) by the LIGO Virgo Scientific Collaboration in 2015 has been a tremendous achievement and ignited the era of GW astronomy. The first LIGO detection was a black hole binary of about $30 + 30$ solar masses emitting in the audio frequency band. These black holes were remnants of massive stars forming a binary. Driven by the emission of GWs, the black holes spiralled into each other and eventually collided to produce a new heavier black hole. Even though only the last ~ 200 ms of the GW emission have been detected by LIGO, it has been enough to find the masses, rough distance and sky location of the black holes. In addition to these tens of solar mass black holes, we have strong evidence that massive and super massive black holes up to several billion solar masses exist in the centre of galaxies. Since galaxies form hierarchically, super massive black hole binaries (SMBHBs) are expected to form frequently during galaxy mergers along the cosmic history. The more massive a binary is, the longer the orbital period is, i.e. the smaller the orbital frequency is. As GWs are emitted at multiples of the orbital frequency, the GW frequencies emitted by SMBHBs do not fall in the LIGO(Hz) frequency band, but in the mHz to nHz range. In the mHz regime LISA is hoping to find a population of massive black hole binaries that reside in smaller galaxies. The heaviest SMBHBs can be found in the most massive galaxies with masses up the $10^{12}\mathrm{M}_{\odot}$. This is the nHz regime, where Pulsar Timing Arrays (PTAs) are looking for GWs. Together, LIGO, LISA and PTAs will provide an extensive coverage of the GW frequency spectrum, akin to the electromagnetic spectrum.

Focussing on the sources in the PTA nHz regime, we can find super massive black holes in the centre of massive galaxies, which have also been observed to merge. Consequently, the central black holes should also form a binary and merge when their host galaxies collide. The galaxy merger rate can be calculated from astrophysical observables, such as the galaxy stellar mass function, pair fraction and merger time scale. Using galaxy - black hole relations it can be converted into a SMBHB merger rate, i.e. the population of SMBHBs in the Universe.

Additionally, properties of individual SMBHBs, like their eccentricities and the densities of their stellar environment, also have an impact on the emission of GWs. All the GWs emitted by the population of SMBHBs form a gravitational wave background (GWB), which is one of the prime targets for PTAs. Although, PTAs have not been able to detect such a background yet, stringent upper limits on the GWB have been produced.

This thesis aims to investigate what we can learn from these upper limits as well as what could be learned from a detection. To answer this question, astrophysical inference from PTA observations are performed. I introduce an astrophysically motivated parametric model to compute the strength of the GWB. Uncertainties in the galaxy merger rate, galaxy - black hole relations as well as the properties of the individual SMBHBs are all taken into account in the model as parameters. Bayesian sampling analyses are run to see what constraints can be found on these parameters from the current PTA upper limits and simulated detections. As the model is constructed from astrophysical observables, we can directly compare and combine the constraints from PTA with traditional electromagnetic observations to produce a multi-messenger picture of the cosmic formation and evolution of the most massive black holes and galaxies in the Universe.

CONTENTS

LIST OF FIGURES

LIST OF TABLES

Acknowledgement

This thesis is graciously sponsored by my parents. Without your support over the last 7 years, I would not be able to submit this thesis. So, thank you very much. Whether it has been a worthwhile investment or not, I do not know. But, I know that I will make the best out of it. To my little brother, I am sure your university career will be sucessful as well.

Thanks to King's College London for the opportunity to do a undergraduate degree, which started this journey. Thanks to Imperial College London for making me realize that theoretical physics was not for me. And lastly thanks for the University of Birmingham for allowing me to pursue a PhD in astrophysics.

To my PhD predecessors: Sarah Mulroy, Simon Stevenson, Haoyu Wang, Jim Barrett, Hannah Middleton, Serena Vinciguerra, Anna Green, Simon Daley-Yates, Miguel Dovale and Daniel Toyra; thanks for preparing the way. To those who started their PhD with me: Callum Bellhouse, Sam Cooper, Sebastian Gaebel and Alejandro Vigna-Gomez; you still have some time to finish your PhD as well. To my PhD sucessors: Ashley Jarvis, Aaron Jones, Conner Gettings, Janna Goldstein, Coen Neijssel, Joe Bentley, Riccardo Buscicchio, Chiara Di Fronzo and Farrah Zainol; good luck.

Special thanks to Conor et al. for Thursday pub club, although I did not go often, I did enjoy them. To Alejandro, the theorists et al. for Friday staff houses. To Christopher at al. for fun outreach opportunities. To David for tsunami and other IT stuff and Jo for help with various admin stuff.

I want to give my appreciation to my collaborators without whom this work would have been impossible: Walter Del Pozzo, Hannah Middleton, Alberto Sesana, Alberto Vecchio and Christopher J. Conselice. In particular, my supervisors the Albertos. Especially, the Younger, thanks a lot, Alberto, for all of your wisdom, guidance and comments throughout these last 3 years and the thesis write-up.

This work has also been supported by the Large European Array for Pulsars, European and International Pulsar Timing Arrays collaborations, of which I am happy to be a member of.

Many thanks to Sean McGee and Antoine Petiteau for agreeing to be my thesis examiners.

Lastly, thanks to the Institute of Physics, Royal Astronomical Society and University of Birmingham for their financial support for my research.

Statement of Originality

In the first chapter I provide a review of PTAs and give introductory material for later chapters in the thesis. The text is written by myself, the content, however, is entirely the work of others who have been referenced throughout the text.

Chapter 2 reproduces verbatim "S. Chen, A. Sesana, W. Del Pozzo, Efficient computation of the gravitational wave spectrum emitted by eccentric massive black hole binaries in stellar environments, 2017, MNRAS 470, 1738" without the Abstract, Introduction and Discussions sections. I did the calculations for the model, produced the initial code and wrote the first draft of the paper. Alberto Sesana helped with the model calculations and major edits of the paper. Walter Del Pozzo helped with the implementation of the code.

Chapter 3 reproduces verbatim "S. Chen, H. Middleton, A. Sesana, W. Del Pozzo, A. Vecchio, Probing the assembly history and dynamical evolution of massive black hole binaries with pulsar timing arrays, 2017, MNRAS, 468, 404", without the Abstract, Introduction and Conclusions sections, but including the Erratum. I have run most of the analysis, produced most of the figures and contributed to the writing of the paper. Hannah Middleton contributed towards the analysis and edits of the paper. The other authors were all involved in the writing of the paper.

Chapter 4 reproduces verbatim "H. Middleton, S. Chen, W. Del Pozzo, A. Sesana, A. Vecchio, No tension between assembly models of supermassive black hole binaries and pulsar observations, 2018, NatComms, 9, 573", without the Abstract. Supplementary material can be found in appendix A. I have contributed towards the analysis, figures and text for the paper. Hannah Middleton ran most of the analysis, wrote the initial draft of the paper and contributed to the figures and paper edits. All other authors contributed to the writing of the paper.

Chapter 5 is based on a draft for a paper "S. Chen, A. Sesana, C. J. Conselice, Constraining astrophysical observables of Galaxy and Supermassive Black Hole Binary Mergers using Pulsar Timing Arrays, ArXiv e-prints, 1810.04184", without the Abstract, Introduction and Conclu-

sions, that has been submitted for publication to a journal. The main aim is to replace the phenomenological SMBHB merger rate from chapter 2 with a SMBHB merger rate that comes from astrophysical observables. This allows for the direct comparison and combination of the constraints on these observables from traditional electromagnetic observations and observations on gravitational waves with PTAs. I have lead the modelling, coded the model, run the analysis and written the initial paper draft. Alberto Sesana has contributed a lot to the writing of the paper draft. Christopher J. Conselice provided useful insights and comments for the paper draft.

I have written the summary, conclusions and outlook in the last chapter of this thesis.

CHAPTER 1

INTRODUCTION

1.1 Hunting Gravitational Waves with Pulsar Timing Arrays

Supermassive black holes have been found to reside in the centres of massive galaxies and to be closely related to the evolution of their host galaxies (see Kormendy and Ho, 2013, and references therein), which have also been observed to merge (Kauffmann et al., 1993). As two galaxies merge, they trigger the formation of a supermassive black hole binary (Begelman et al., 1980). The black holes in the newly formed SMBHB spiral into each other emitting gravitational waves until they eventually merge (Peters and Mathews, 1963). Since SMBHBs have masses of $10^9 M_\odot$, the emitted GWs are very strong, but their orbital periods are also very long, making them the loudest GW sources at lower (in particular nHz) frequencies. As there are many SMBHBs in the Universe, the superposition of all their emitted GWs forms a stochastic gravitational wave background (e.g. Rajagopal and Romani, 1995; Jaffe and Backer, 2003; Sesana et al., 2008). The detection of GWs in the nHz regime with Pulsar Timing Arrays is a challenging prospect and complements the LIGO detections in the Hz and planned LISA mission in the mHz frequency bands very well, see figure 1.1.

PTAs (Foster and Backer, 1990) use the extremely regularly emitted radio waves from pulsars

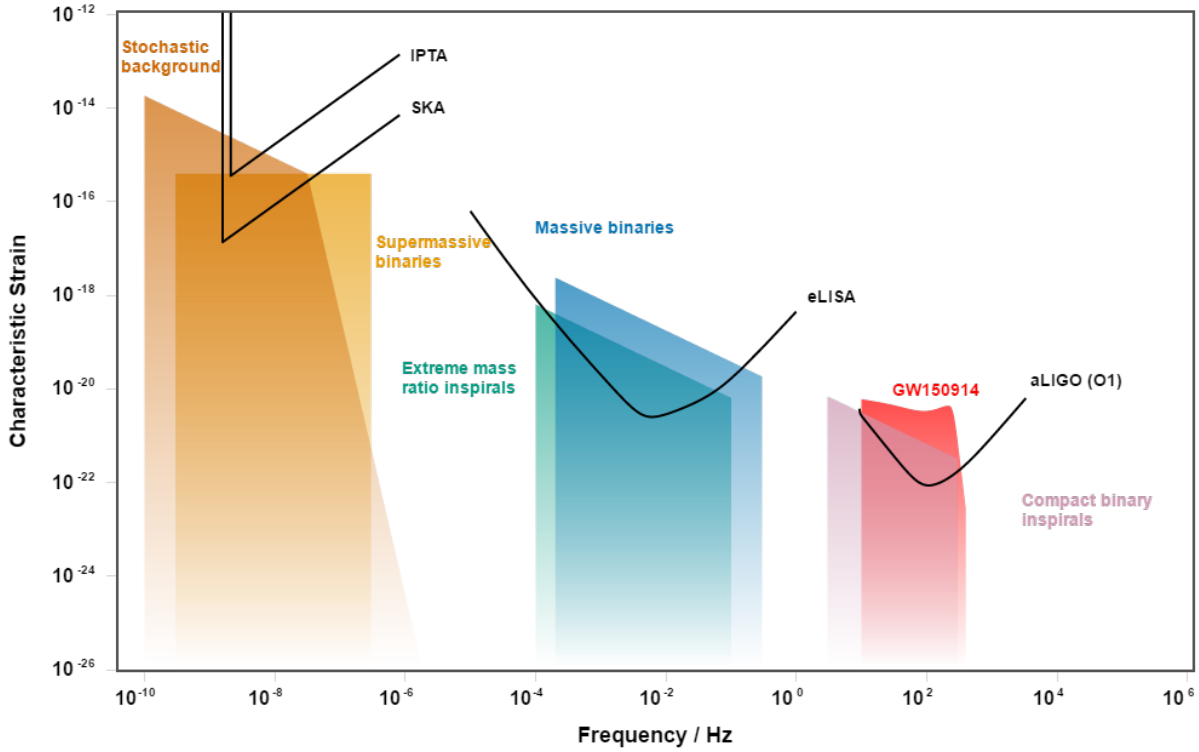

Figure 1.1: Comparison of the sensitivity curves and sources of GWs for the three major running/planned GW Astronomy experiments: PTA, LISA and LIGO, produced using the Gravitational Wave Sensitivity Curve Plotter (Moore et al., 2015a)

to look for GW induced changes in their time of arrival (TOA) series, see figure 1.2. When a radio pulse from a pulsar passes through the GWB its travel time is lengthened and shortened. Thus, the TOA of the pulse at Earth is also influenced accordingly. The TOAs from two different pulsars affected by the GWB are correlated in a characteristic fashion. This correlation, also known as the Hellings-Downs curve (Hellings and Downs, 1983), can be used as a smoking gun for a GW detection. Consequently, it is crucial to precisely time a number of pulsars in an array. To time a pulsar precisely we need a detailed model of the TOA of the pulses, minimizing the uncertainty on their detections (Hobbs et al., 2006; Edwards et al., 2006). Subtracting the measured TOAs from the predicted ones gives us the residuals. These residuals contain information on effects that have not been modelled, are of unknown origin or may just be noise from the instruments. Cross-correlating data from different pulsars across the sky can be used to look for a GWB, even if it is hidden with other sources of noise in the residuals. This is what PTA projects do to achieve their goal of detecting GWs in the nHz regime. A recent review on

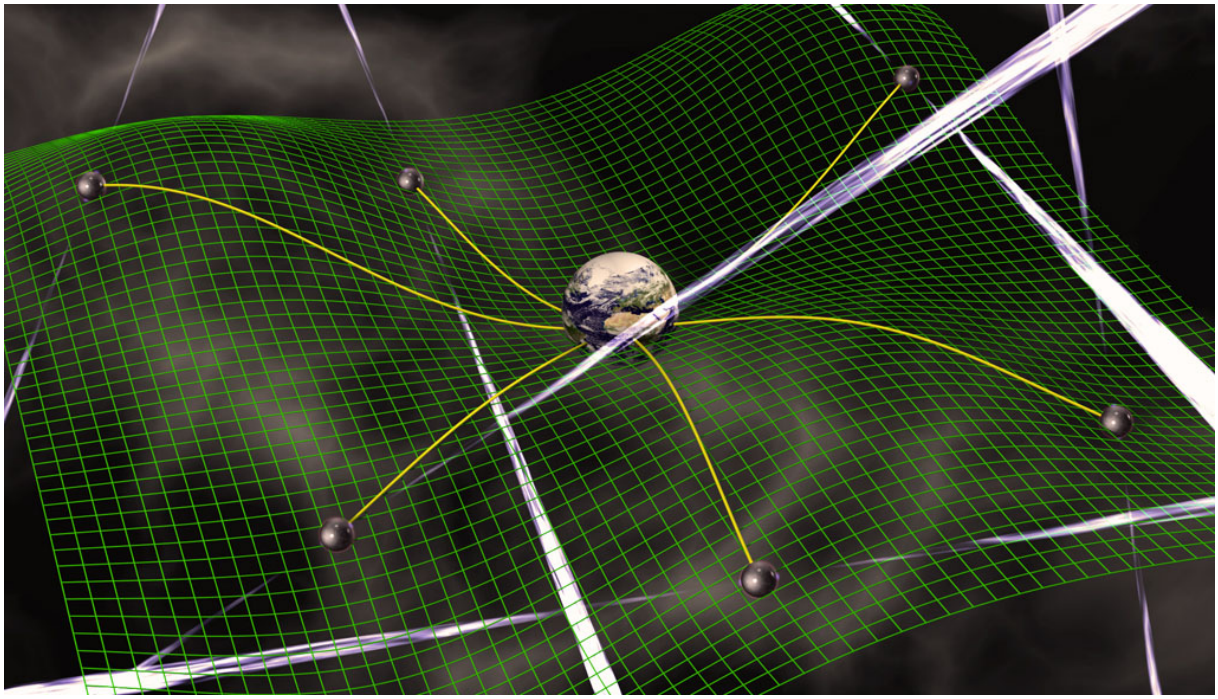

Figure 1.2: Artist's impression of how a Pulsar Timing Array works. Green lines show the perturbed spacetime due to the GWB, pulsars are shown as black spheres emitting radio signals, yellow lines show the null geodesic of the radio pulse towards Earth, credits: David Champion

PTAs can be found in Perrodin and Sesana (2017).

Several collaborations are actively searching for GWs with PTAs: the European Pulsar Timing Array (EPTA) (Ferdman et al., 2010), the North American Nanohertz Observatory for Gravitational waves (NANOGrav) (Jenet et al., 2009) and the Parkes Pulsar Timing Array (PPTA) (Hobbs et al., 2009) have joined forces in the International Pulsar Timing Array (IPTA) (Hobbs et al., 2010). A number of other PTA collaborations, from India with the Giant Metrewave Radio Telescope (GMRT) (Swarup, 1991), China with the Five-hundred-meter Aperture Spherical radio Telescope (FAST) (Nan et al., 2011) and the QiTai radio Telescope (Wang, 2014) and South Africa with MeerKAT (Booth et al., 2009) and the Square Kilometre Arrray (SKA) (Smits et al., 2009), are in the process of joining the IPTA, further driving the prospect of a detection of GWs. PTAs have reached sensitivities at which a detection of a GWB could be possible (e.g. Rosado et al., 2015; Janssen et al., 2015; Taylor et al., 2016b), thus starting to probe the predictions from SMBHB assembly models. Since no detection has been made yet, it is only possible to put an upper limit on the GWB (Lentati et al., 2015; Arzoumanian et al., 2018a;

Shannon et al., 2015; Verbiest et al., 2016). These upper limits can be used to constrain the astrophysical properties of the population of SMBHBs, the properties of their binaries and host galaxies (e.g. Middleton et al., 2016; Simon and Burke-Spolaor, 2016; Taylor et al., 2017b). GW observations on the population of SMBHBs through PTAs allow for a new and independent way to get these constraints compared to using observations in the electromagnetic spectrum.

1.2 Pulsars

Pulsars are spinning neutron stars that constantly emit radio waves along their magnetic axes. If the magnetic axis is offset from the rotation axis and happens to point towards Earth, we will receive regular radio pulses each rotation of the neutron star, similar to the light from a lighthouse, see figure 1.3. Since the first pulsar discovery in 1967, more than 50 years ago (Hewish et al., 1968), they have become both mysterious objects as well as useful tools. Mysterious as we still do not know the exact mechanisms driving the emission of radio waves (see e.g. Harding, 2017; Melrose and Rafat, 2017, and references therein) and useful as they serve as very stable clocks kiloparsecs away from Earth. Especifically, millisecond pulsars (MSPs) (Backer et al., 1982), whose rotation periods are of order of ms, are the most stable natural astronomical clocks. They are therefore a very useful tool for astronomical observations, not only to understand the intrinsic properties of the pulsars, but also to investigate all the effects on the travel time of the radio pulses through interstellar medium to the Earth (see Lorimer and Kramer, 2012, for a review). Some pulsars that are in binaries can also be used to study and test General Relativity in extreme circumstances (Kramer et al., 2006), including the first evidence for GW radiation from the Hulse-Taylor binary (Hulse and Taylor, 1975). This thesis will focus on using pulsars as precise clocks to look for GWs.

The commonly accepted model of pulsar formation and evolution from Lorimer (2008) is schematically shown in figure 1.4. Isolated stars have a chance to become young pulsars after their supernova. Young pulsars slowly spin down over the next tens of Myr until the radio

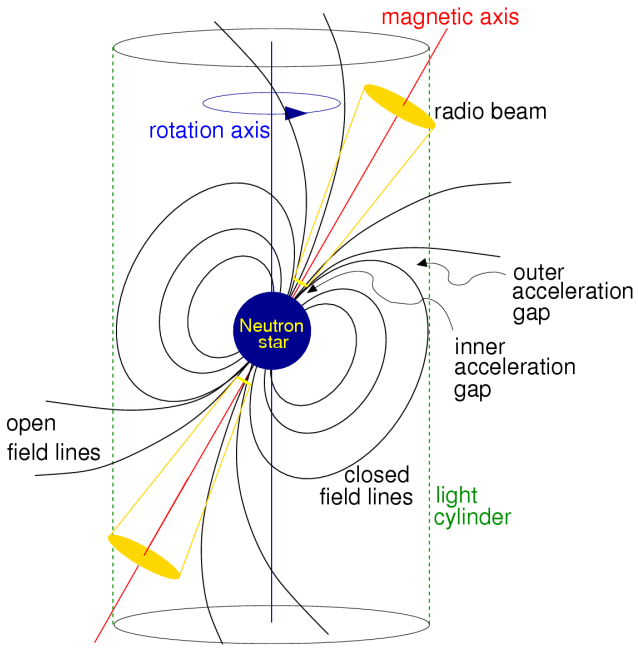

Figure 1.3: Diagram showing the pulsar radio emission, reproduced from Lorimer and Kramer (2012)

emission energy becomes negligible. However, stellar binary systems can also create young pulsars, MSPs and pulsar binary systems. As two stars evolve in a binary, the primary more massive star will first undergo supernova. This supernova can give a strong enough kick to disrupt the binary into one young pulsar and a runaway star. Since many stars in a binary are disrupted from supernovae, there are many young pulsars without companions. If the stellar binary survives the first supernova, the young pulsar still spins down until the secondary star starts to transfer mass and momentum to the neutronstar spinning it up to ms periods again. The resulting pulsar is often referred to as a recycled pulsar. The further evolution of the MSP - star binary depends on the mass of the secondary star. For low masses the second supernova typically leaves the binary intact and a MSP - white dwarf binary system is formed. For high masses the second supernova can disrupt the binary to produce a new young pulsar and a recycled pulsar. In rare cases when the MSP - star binary survives the second supernovae it can become a double neutronstar system. Most MSPs can therefore be found in binary systems with white dwarfs, stars or neutronstars, whilst young pulsars are mostly isolated, see figure 1.5.

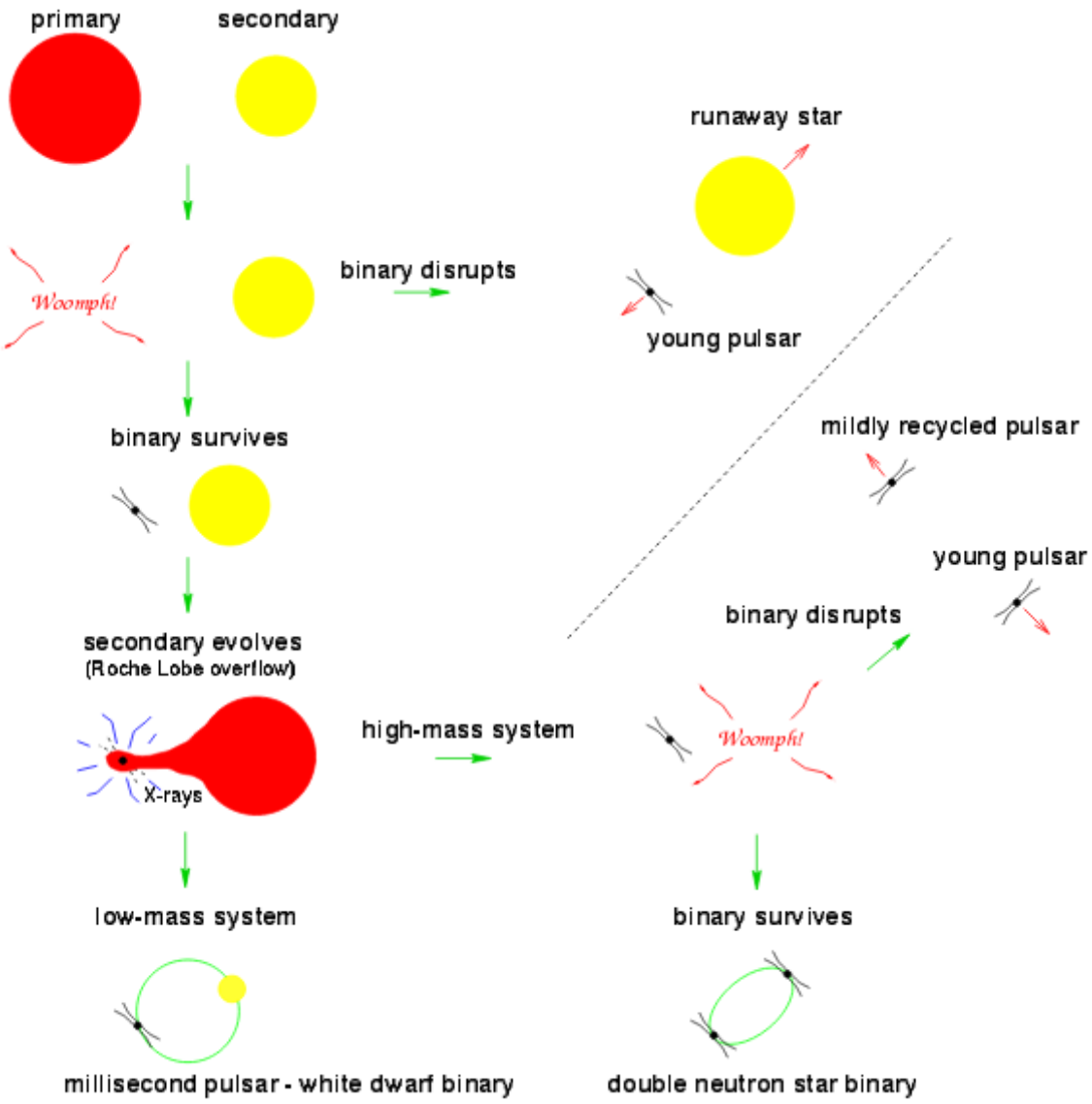

Figure 1.4: Schematic cartoon of the pulsar evolution, reproduced from Lorimer (2008)

Figure 1.5 shows the currently known population of pulsars. There are two distinct population of pulsars: normal young pulsars with rotation periods of seconds and old millisecond pulsars. Normal pulsars have less stable intrinsic physical properties, as they have formed not too long ago and are still evolving. Older MSPs are a lot more stable, i.e. their intrinsic properties do not change much. This makes them more useful as astronomical clocks, which can reach timing precision $\lesssim 100$ ns (Desvignes et al., 2016; Arzoumanian et al., 2018b; Reardon et al., 2016). The induced changes on the timing from GWs from a SMBHB are of the same order (Jenet et al.,

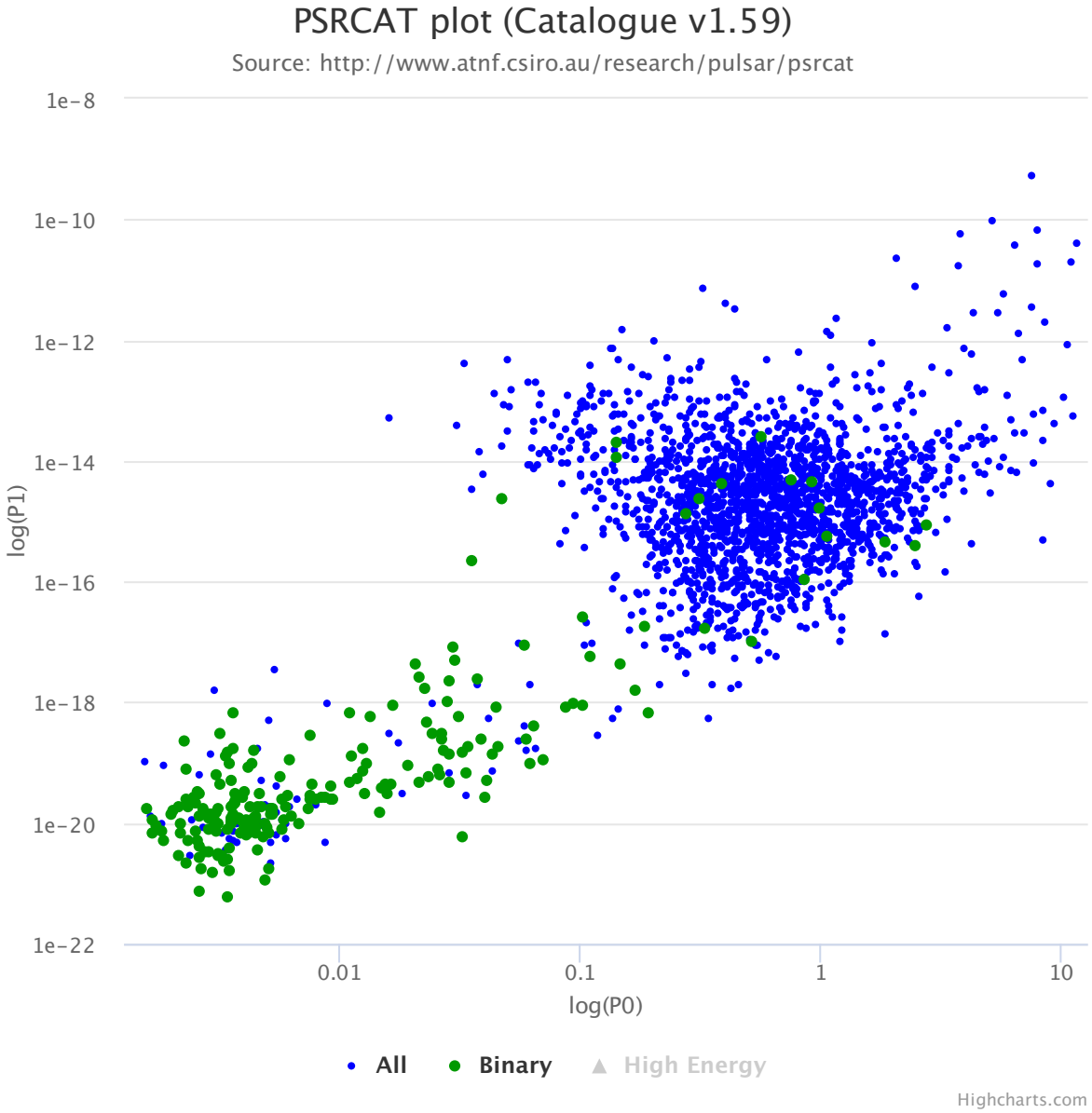

Figure 1.5: The currently known pulsar population plotted in a period $P0$ vs period derivative $P1$ diagram from the ATNF Catalogue (Manchester et al., 2005): blue dots mark isolated pulsars, green dots mark pulsars in binaries

2009)

$$\Delta t \sim 10\text{ns}\left(\frac{1\text{Gpc}}{d_L}\right)\left(\frac{M}{10^9\text{M}_\odot}\right)^{5/3}\left(\frac{10^{-7}\text{Hz}}{f}\right)^{1/3}, \tag{1.1}$$

where d_L is the luminosity distance of the SMBHB, M is its total mass and f the observed GW frequency. A SMBHB with a total mass of $10^9\text{M}_\odot$ at a distance of 1Gpc emitting GWs at 10^{-8}Hz induces a timing noise of $\sim$ 20ns. This fact makes it feasible to look for GWs by timing MSPs with PTAs (Sazhin, 1978; Detweiler, 1979).

1.3 Timing

Having established that pulsars are great astronomical clocks, we now proceed to time the pulses with the following procedure:

1. measure the TOAs of a pulsar from the observation
2. create a timing model for the pulsar from the measured TOAs
3. subtract the modelled from the measured TOAs to get the residuals
4. repeat steps 1 to 3 for each observation to add more TOAs and improve the timing model

A well-fitted timing model should keep the residuals ideally at zero, but in practice there are various sources of noise as well as unknown and undetected interesting physics producing small deviations from zero.

Following Edwards et al. (2006) the timing model can be written as a series of geometric translations between the pulsar and the observatory on Earth:

$$t_e^{psr} = t_a^{obs} - \Delta_\odot - \Delta_{IS} - \Delta_B \tag{1.2}$$

where the time at which the radio pulse is emitted t_e^{psr} is related to the time at which the pulse is received at the radio telescope t_a^{obs} via coordinate transformations/delays: 1. from the observatory a to the solar system barycentre (SSB) $\Delta_\odot$, 2. from the SSB to the barycentre of the pulsar system (BB) Δ_{IS} and 3. from the BB to the pulsar itself Δ_B.

The transformation between the observatory and the SSB contains various delays, that can be split up into

$$\Delta_\odot = \Delta_A + \Delta_{R\odot} + \Delta_p + \Delta_{D\odot} + \Delta_{E\odot} + \Delta_{S\odot}, \tag{1.3}$$

where Δ_A are atmospheric delays due to the scattering of the photons in the ionosphere, Δ_p is the parallax delay, $\Delta_{R\odot}, \Delta_{E\odot}, \Delta_{S\odot}$ are the Roemer, Einstein and Shapiro delay for the solar system coming from transformation to the SSB and $\Delta_{D\odot}$ is the dispersion of photons between the Earth and the Sun due to the electrons in the solar wind.

To avoid timing anomalies from Earth's spin, orbital acceleration or gravitational potential variations TOAs are transformed from the observatory on Earth to the SSB, which can be approximated as an inertial system. The classical light travel time between the observatory (Earth) and the SSB is given by the Roemer delay. The Einstein delay adds the time dilation and gravitational redshift caused by the Planets and Sun from General Relativity. Shapiro delays are due to the slow down of photons when moving through curved spacetime created by massive objects.

The transformation between the SSB and the BB is made of the vacuum travel time of the photons and other delays:

$$\Delta_{IS} = \Delta_{VP} + \Delta_{ISD} + \Delta_{FDD} + \Delta_{ES} \tag{1.4}$$

where Δ_{VP} is the vacuum propagation time of the signal, Δ_{ISD} is the instellar dispersion of the photons, commonly characterized by the dispersion measure (DM), Δ_{FDD} accounts for other frequency dependent propagation delays and Δ_{ES} accounts for the special relativitic time dilation.

Lastly, if the pulsar is isolated, then the transformation between the BB and the pulsar is trivially zero. However, if the pulsar is in a binary like most MSPs, this transformation becomes important and is affected by General Relativistic delays:

$$\Delta_B = \Delta_{RB} + \Delta_{AB} + \Delta_{EB} + \Delta_{SB} \tag{1.5}$$

with $\Delta_{RB}, \Delta_{EB}, \Delta_{SB}$ being the Roemer, Einstein and Shapiro delays in the pulsar binary system and Δ_{AB} a delay due to aberration from the relative transverse velocity between the pulsar and Earth.

Analogous to the transformation from Earth to the SSB, the transformation from the BB to the pulsar itself from pulsar binary systems also contains Roemer, Einstein and Shapiro delays. However, the pulsar binary system is more extreme than the solar system and relativistic effects play a more significant role. In addition to the five classical Keplerian parameters: orbital period P_{b0}, periastron longitude ω_0, eccentricity e, time of periastron passage T_0 and projected semimajor axis x_0 of the binary from the Roemer delay, precision pulsar timing on the most stable and extreme systems can allow for the measurement of up to 5 further post-Keplerian parameters: rate of periastron advance $\dot{\omega}$, relativistic delay term γ and the orbital decay $\dot{P}_b$ from the Einstein delay and the two Shapiro delay range r and shape s terms. These 5 post-Keplerian parameters can all be expressed in terms of the masses of the two objects in the binary, the detailed expressions can be found in equations (80-86) in Edwards et al. (2006). With 2 parameters the two masses can be determined, each additional measured parameter provides one more independent test for General Relativity. The 3 Einstein delay parameters $\dot{\omega}, \gamma, \dot{P}_b$ have first been detected in the Hulse-Taylor pulsar - neutron star binary B1913+16 (Hulse and Taylor, 1975) providing solid evidence for GW emission. Kramer et al. (2006) have used an even better timed double-pulsar system J0737-3039 to measure all 5 post-Keplerian parameters to provide the most stringent tests on General Relativity using pulsar timing to date.

All these delays create a massive model with pulsar specific and many other parameters. The best fit values of all parameters for a given pulsar form the timing model for this pulsar. For a more detailed review on the timing model, see Edwards et al. (2006). This timing model has been implemented into a well used and tested legacy code package: tempo2 (Hobbs et al., 2006) as well as a modern and independent code package: PINT (Luo et al., 2018).

To get the residuals $R_a(t)$ one can subtract the measured TOAs t_a^{obs} from the TOAs predicted by the timing model t_a^{TM}

$$R_a(t) = t_a^{obs} - t_a^{TM}. \tag{1.6}$$

Subscripts a denote the observation at one individual telescope. These residuals can be transformed from time into frequency domain via a Fourier transform to get the spectral density

$S_a(f)$:

$$S_a(f) = \int_{-\infty}^{\infty} R_a(t) e^{-2\pi i t f} dt. \tag{1.7}$$

Ideally the model should predict the observation perfectly, this leaves the residuals to be zero. However, this is not the case in practice. There will be noise from the instruments and other unaccounted effects left in the residuals. The effect of interest for this thesis is GWB induced noise. To distinguish it from other sources of noise we need to time many pulsars in an array.

1.4 Arrays

As there are various sources of noise in the timing residuals, it is impossible to distinguish GWB induced changes in the TOA series from other sources of noise from a single pulsar alone. It is thus necessary to observe many pulsars and look for a correlated source of noise with specific properties between all pulsars. A prime candidate is the GWB from a population of SMBHBs. This background is the stochastic superposition of all the GWs emitted by SMBHBs and affects all pulsars in a common way. Hellings and Downs (1983) have shown that for an isotropic GWB the correlation has a specific shape, see figure 1.6. This correlation is only dependent on the angle ζ between two pulsars i and j:

$$\Gamma_{ij} = \frac{3}{2}\gamma_{ij}\ln\left(\gamma_{ij}\right) - \frac{1}{4}\gamma_{ij} + \frac{1}{2} + \frac{1}{2}\delta_{ij} \tag{1.8}$$

where $\gamma_{ij} = [1-\cos(\zeta)]/2$ and δ_{ij} is the Kronecker delta function for the pulsar pair ij.

This characteristic correlation can act as a smoking gun for the detection of a GWB with PTAs. To fill figure 1.6 with data points, many pairs of pulsars are needed. Ideally, they should be isotropically distributed on the sky to cover the entire ζ axis of figure 1.6. The need to observe and time many pulsars coins the term array. However, each pulsar added to the array increases the computational need. Thus it is important to only include the pulsars with the best timing

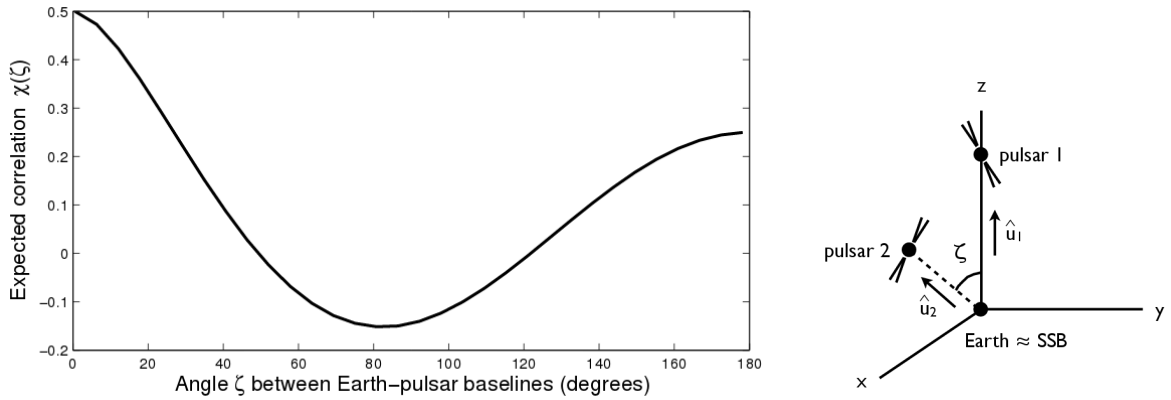

Figure 1.6: Hellings-Downs correlation. The left figure shows the Hellings-Downs correlation between pulsars with angle ζ, the right figure shows the position of the pulsar pair with respect to the Earth(SSB), reproduced from (Jenet and Romano, 2015)

stability, noise properties and sky location to improve the overall sensitivity of the PTA (Siemens et al., 2013). Other sources of noise that might confuse a GWB correlation are shown in the next section.

1.5 Noises

To search for a GWB hidden in the residuals as many sources of noise as possible need to be modelled and taken into account. We can distinguish between correlated and uncorrelated noise. Uncorrelated noise is specific to each pulsar and can be modelled physically, if the source of noise is known and phenomenologically if it is unknown. To model correlated noise between pulsars, understanding the underlying physical cause is necessary. Once all sources of noise and the GWB have been put into a full noise model, the overall analysis can be run on all parameters in the noise model and see whether there is evidence for a GWB. The following describes the sources of noise and how they are modelled in the three different PTA collaborations (Caballero et al., 2016; Arzoumanian et al., 2015; Reardon et al., 2016) and combined in the IPTA (Verbiest et al., 2016).

1.5.1 White noise

White noise is a frequency independent noise affecting all TOAs with the same power and is mostly caused by instrumental uncertainties. White noise is modelled as a Gaussian distribution around the true value of the TOA with a standard deviation of σ_k for the observation k. It can be estimated from the properties of the telescope instruments via the radiometer noise (Cordes and Shannon, 2010)

$$\sigma_k = 0.71\mu\text{s}\Big(\frac{W}{1\text{ms}}\Big)^{3/2}\Big(\frac{P}{1\text{ms}}\Big)^{-1}\Big(\frac{f}{1.4\text{GHz}}\Big)^{-\alpha}\Big(\frac{\Delta f}{1\text{GHz}}\Big)^{-1/2}\Big(\frac{N}{10^6}\Big)^{-1/2}\Big(\frac{S_{sys}}{S_{1400}}\Big), \qquad (1.9)$$

where W is the effective pulse width, P is the spin period of the pulsar, f is the frequency at which the pulsar is observed, α is the spectral index of the flux density powerlaw, Δf is the bandwidth of the receiver, N is the number of pulses used to create one TOA, S_{sys} is the system temperature expressed as a flux density and S_{1400} is the mean flux density from the pulsar at 1400MHz.

However, the true level of noise may be underestimated. There are two common parameters in PTAs that take care of white noise: EFAC E_k and EQUAD Q_k. Both are included in the full noise analysis for each independent pulsar observation. Given the estimate σ_k on the instrumental white noise from equation (1.9), one can add an additional factorial error EFAC E_k and error in quadrature EQUAD Q_k to find the true noise level:

$$\sigma_k \to E_k\sqrt{\sigma_k^2 + Q_k^2}. \qquad (1.10)$$

There is one additional parameter ECORR J_k, which is a NANOGrav specific white noise parameter for simultaneous observations with the same instrument. These simultaneous observations cause the shape of the received pulses to vary slightly between the observations, introducing extra time correlated but frequency independent white noise. The ECORR J_k parameter can take care of this white noise, the detailed mathematics of which can be found in the appendix of

Arzoumanian et al. (2015).

1.5.2 Uncorrelated Red noise

Red noise is frequency dependent, i.e. the power of the noise for different TOAs varies. It can be both of instrumental cause and of astrophysical origin, which makes it very interesting to study. Generic red noise can be both correlated and uncorrelated among pulsars. The power $P_{red}(f)$ of uncorrelated red noise in a specific pulsar is usually modelled phenomenologically with a power law with an amplitude A_{red} and spectral index γ_{red} due to its unknown origin:

$$P_{red}(f) = A_{red}^2 \left(\frac{f}{\mathrm{yr}^{-1}}\right)^{\gamma_{red}}. \tag{1.11}$$

To ensure that this model is an accurate representation for the pulsar specific red noise, other effects that could mimic uncorrelated red noise have to be considered in the noise analysis as well. One major effect are variations of the dispersion measure. The DM can be calculated by integrating the electron column density n_e between Earth and the pulsar at distance d away (You et al., 2007)

$$\mathrm{DM} = \int_0^d n_e dl. \tag{1.12}$$

The dispersion of the radio waves through the interstellar medium impacts the TOAs dependent on the frequency of the emitted photons (Lorimer, 2008)

$$\Delta t = 4.15\mathrm{ms} \times \left[\left(\frac{f_{low}}{\mathrm{GHz}}\right)^{-2} - \left(\frac{f_{high}}{\mathrm{GHz}}\right)^{-2}\right] \times \left(\frac{\mathrm{DM}}{\mathrm{cm}^{-3}\mathrm{pc}}\right). \tag{1.13}$$

The higher the energy and frequency a photon has, the less it will be scattered and thus arrives earlier. The delay between photons with high frequency f_{high} and photons at an observed low frequency f_{low} is directly proportional to the DM. DM variations directly translate into TOA errors and can incorrectly be interpreted as red noise in the residuals. Multi-frequency observations (Lam et al., 2015; Cordes et al., 2016) and the modelling of DM variation (Keith

et al., 2013; Lee et al., 2014) are thus crucial to correctly determine the intrinsic red noise in a pulsar. Each PTA has a slightly different approach to model DM variations, which can be found in Caballero et al. (2016); Arzoumanian et al. (2015); Reardon et al. (2016). DM variations are an interesting means to study the instellar medium, but for the search for GW with PTAs they are a limitation.

1.5.3 Correlated Red noise

In addition to uncorrelated red noise in all pulsars, there are also correlated red noise processes, including GW induced noise, that need to go into the full noise model. To account for the incompleteness of our knowledge on the physical processes causing correlated red noise, we can add a generic and phenomenological correlated red noise of unknown origin for all pulsars, akin to equation (1.11). There are three other types of correlated red noise of interest for PTAs (Tiburzi et al., 2016): clock error, solar system ephemeris error and GWB induced correlated red noises. Clock errors induce a monopole like correlation in the red noise, all TOAs from all pulsars are effectively offset by the clock error. Errors in the solar system ephemeris cause a dipole like correlation with the frequency of the affected planet. Lastly, the GWB has a quadrupole signature in its correlation, the Hellings-Downs correlation. Figure 1.7 shows the effect of the correlated red noise in the residuals. The middle panels show the errors induced by a clock error, all sky positions are correlated with the same strength. Weaker sine-wave like correlations are produced by ephemeris errors in the bottom panels. As the GWB Hellings-Downs correlation in the top panels have similar strength and shape as ephemeris error, these two can easily be confused with each other. All these correlated red noise processes need to be included in the analysis to find GWs with PTAs (Taylor et al., 2017a). Which has recently been done by the NANOGrav collaboration (Arzoumanian et al., 2018a) to produce the most recent and sophisticated upper limit on the GWB.

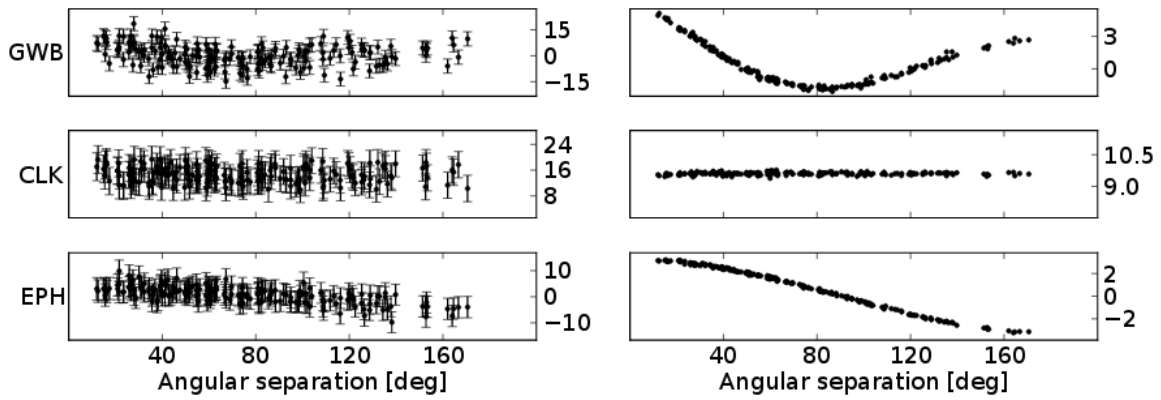

Figure 1.7: Red noise correlations. The left panels show one realization, while the right panels show the average of 1000 realizations, various correlated red noise are shown from the top (GWB), middle (clock CLK) and bottom (ephemeris EPH), reproduced from (Tiburzi et al., 2016)

1.6 Gravitational Wave Background

Galaxies are believed to host super massive black holes in their centres (see Kormendy and Ho, 2013, and references therein). Strong evidence in that claim can be found with spatially resolved dynamics in galaxies (Kormendy and Richstone, 1995). One famous example is our Milky Way, which has many individual stellar orbits traced around a common compact and dark object (Genzel et al., 2010), allowing for an estimate of the central super massive black hole of $M \sim 4.3 \times 10^6 M_\odot$ using Kepler's laws. Other galaxies may not have spatially resolved orbits, however, velocity dispersions can still be measured and used to estimate the mass of the central black holes within a radius $M(r)$ using equation 1 from Kormendy and Ho (2013):

$$M(r) = \frac{V^2 r}{G} + \frac{\sigma_r^2 r}{G}\Big[- \frac{d\ln \nu}{d\ln r} - \frac{d\ln \sigma_r^2}{d\ln r} - \Big(1 - \frac{\sigma_\theta^2}{\sigma_r^2}\Big) - \Big(1 - \frac{\sigma_\phi^2}{\sigma_r^2}\Big)\Big], \tag{1.14}$$

where G is the gravitational constant, V is the rotation velocity, $\sigma_r, \sigma_\theta, \sigma_\phi$ are the radial, polar and azimuthmal components of the velocity dispersion and ν is the density of traced stars used to estimate the black hole mass.

Massive galaxies have been observed to collide, merge and thus initiate the merger of the super massive black holes that reside in their centres (Kauffmann et al., 1993). Dynamical friction is

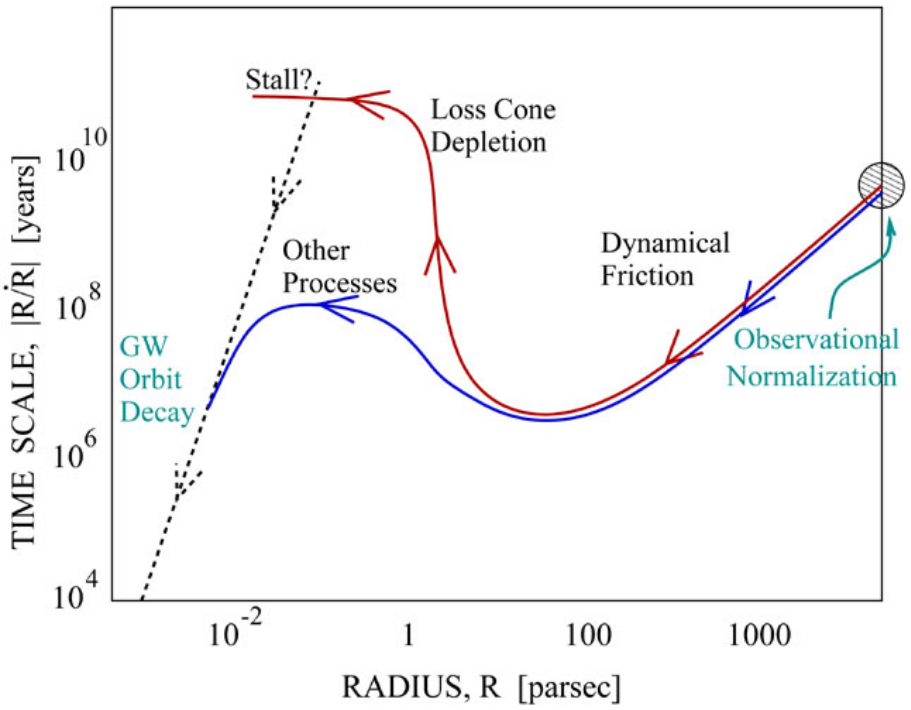

Figure 1.8: Diagram of the SMBHB evolution, reproduced from (Vasiliev et al., 2015)

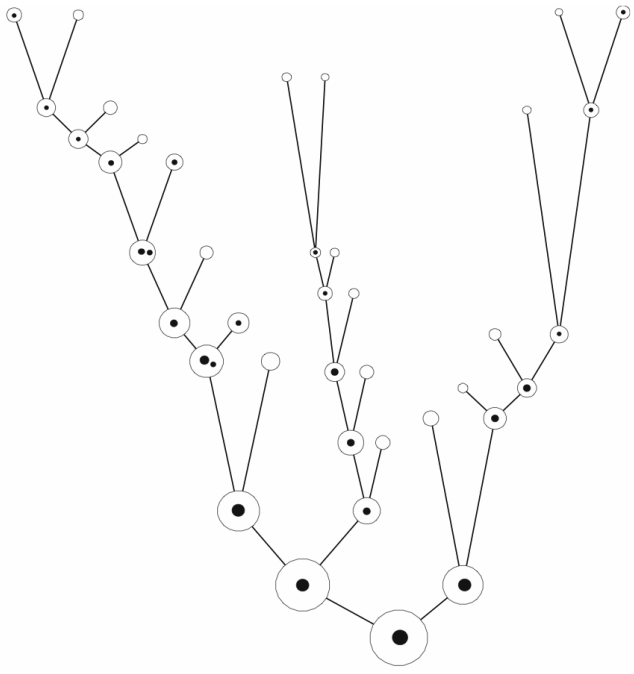

Figure 1.9: Cartoon of the SMBHB merger tree, reproduced from (Volonteri et al., 2003)

the main process driving the merger (Chandrasekhar, 1943). When a massive object moves past a smaller one, the gravitational attraction betweem them causes the small object to be slightly dragged along with the motion of the larger one. To conserve energy and momentum they have to be transferred from the massive to the smaller object. The dynamical friction force $\mathbf{F}_{\rm df}$ acting upon the massive object m from a field of background objects m_* can be described by (Chandrasekhar, 1943; Dosopoulou and Antonini, 2017)

$$\mathbf{F}_{\rm df} = -4\pi G^2 \frac{\mathbf{v}}{v^3}(m+m_*)\ln\Lambda \int_0^v dv_* 4\pi f(v_*) v_*^2, \tag{1.15}$$

with G being the gravitational constant, $\mathbf{v}$ and v being the velocity vector and magnitude of the massive object, $\ln\Lambda$ being the Coulomb logarithm, v_* and $f(v_*)$ being the velocity and velocity distribution of the background objects. Equation (1.15) implies that only objects whose velocity is lower than the massive object will cause dynamical friction.

For super massive black holes, this means that as they move through the stellar background of the merging galaxies, they lose their energy and momentum to them, bringing the black holes to a separation of kpcs to form a pair. From there the supermassive black hole pair further loses energy and momentum via three body scattering to its surrounding stars (Quinlan, 1996). This process is also called hardening in a stellar environment and further reduces the separation to pc scales to create a SMBHB (Begelman et al., 1980). In order to reach sub-pc separation when GW emission can take over the evolution until merger, some mechanism has to further drive the binary to shrink or the binary may stall and not merge. This is often referred to as the "final parsec problem" (Milosavljević and Merritt, 2003), see figure 1.8. Several mechanisms have been proposed:

1. The majority of SMBHBs may still be efficiently driven to sub-pc separation due to hardening in a stellar environment (Vasiliev et al., 2014, 2015; Sesana and Khan, 2015).

2. Some binaries may merge due to gaseous interactions, the SMBHB loses velocity as it moves through the gas disk surrounding it (Ivanov et al., 1999; Cuadra et al., 2009; Tang

et al., 2017).

3. There is also a chance that stalling binaries may be interrupted by a subsequent galaxy merger, i.e. a triplet is temporarily formed. One of the three black holes is ejected with high velocity whilst the remaining two form a binary with smaller separation (Hoffman and Loeb, 2007; Bonetti et al., 2016, 2018).

4. Despite the above suggested mechanisms it is still possible that a significant amount of SMBHBs stalls at the pc scale without producing mergers within a Hubble time of about 13 Gyr. Even in the extreme scenario of all binaries stalling, there should still be a non-negligible GWB (Dvorkin and Barausse, 2017).

A more detailed review of the SMBHB evolution can be found in Dotti et al. (2012). We apply the first mechanism and model the shrinkage of SMBHBs according to Sesana and Khan (2015) in our model to compute the characteristic strain h_c, see chapter 2 for details.

Since there are many galaxies in the Universe merging in a hierachical fashion (White and Rees, 1978), there is also a population of SMBHBs with many low mass black holes and fewer high mass black holes (Volonteri et al., 2003), see figure 1.9. All the GWs emitted by such a population form an incoherently superposed GWB. Individual SMBHBs may produce GWs that can be detected if the binary is massive and close enough (Sesana et al., 2009; Mingarelli et al., 2017). It is more likely that the GWB will be detected first (Rosado et al., 2015; Janssen et al., 2015; Taylor et al., 2016b), which is what we will focus on.

The characteristic strain h_c of the GWB describes the relative strength of the GWs. An amplitude of 10^{-15} means that effectively 1m of spacetime is stretched and squashed by 10^{-15}m. For the GWB it is given by Phinney (2001)

$$h_c^2(f) = \frac{4G}{\pi c^2 f} \int_0^\infty dz \int_0^\infty d\mathscr{M} \frac{d^2n}{dz d\mathscr{M}} \frac{dE}{dt} \frac{dt}{df} \tag{1.16}$$

where G is Newton's constant, c is the speed of light, f is the frequency of the emitted GWs, z

is the redshift and $\mathscr{M} = (M_1 M_2)^{3/5}/(M_1+M_2)^{1/5}$ is the chirp mass of a SMBHB with M_1, M_2 being the masses of the two black holes. The population function $\frac{d^2n}{dzd\mathscr{M}}$ describes the number of SMBHBs per redshift and chirp mass bin and can be written as a phenomenological function or derived from astrophysical observables. The amount of energy emitted in GWs by one individual binary per unit time dE/dt is given by

$$\frac{dE}{dt} = \frac{32}{5}\frac{G^{7/3}}{c^5}\mathscr{M}^{10/3}(2\pi f)^{10/3} g_n(e) \tag{1.17}$$

where $g_n(e)$ is an eccentricity dependent function from the calculations on the GW energy emission by Peters and Mathews (1963). For $e = 0$ the only contributing term is $n = 2$ giving $g_n(e) = 1$.

The frequency evolution of the binary df/dt depends on the mechanism driving it and determines the shape of the spectrum of the characteristic strain h_c. The evolution of the semimajor axis of the binary for GW emission, stellar hardening and gaseous interactions driven binaries from Sesana (2013a) can be rewritten using Kepler's laws as frequency evolution

$$\frac{df}{dt}\Big|_{GW} = \frac{96}{5}(2\pi)^{8/3}\frac{G^{5/3}}{c^5}\mathscr{M}^{5/3} f^{11/3} F(e) \tag{1.18}$$

$$\frac{df}{dt}\Big|_{stars} = \frac{3}{2(2\pi)^{2/3}}\frac{H\rho}{\sigma} G^{4/3} M^{1/3} f^{1/3} \tag{1.19}$$

$$\frac{df}{dt}\Big|_{gas} = \frac{3\dot{M}}{\mu} a_0^{1/2}\left(\frac{4\pi^2}{GM}\right)^{1/6} f^{4/3} \tag{1.20}$$

where for

1. GW: $F(e)$ is another eccentricity dependent function from (Peters and Mathews, 1963). For circular binaries it is 1.

2. stars: $H \sim 16$ is a numerical constant from three body simulations, ρ is the stellar density of the environment and σ is the stellar velocity dispersion.

3. gas: $\dot{M}$ is the binary mass accretion rate, μ is the binary reduced mass and a_0 is the

semimajor axis of the disk which contains the mass of the smaller black hole.

The final frequency dependence of h_c are: 1. GWs from circular orbits $f^{-2/3}$, 2. stellar hardening f and 3. gaseous interactions $f^{1/2}$. As the SMBHB transitions from being driven by stellar and gaseous environments to GW emission the spectrum also changes from a positive to a negative powerlaw, causing a bend in the spectrum at low frequencies. This bend can also be achieved by having eccentric binaries in the population, see chapter 2 of this thesis for the detailed derivation.

Integrating over redshift z and chirp mass $\mathscr{M}$ of a given population of SMBHBs $\frac{d^2n}{dzd\mathscr{M}}$ gives a characteristic amplitude A_{GWB}. Furthermore, assuming purely GW emission driven circular binaries allows to simplify equation (1.16) to

$$h_c(f) = A_{GWB}\left(\frac{f}{\mathrm{yr}^{-1}}\right)^{-2/3} \tag{1.21}$$

The characteristic strain h_c is connected to the induced correlated red noise between two pulsars i and j via the power spectral density (which is the Fourier transform of the common residuals $R_{ij}(t)$ between pulsars i and j)

$$S_{ij}(f) = \Gamma_{ij}\frac{h_c^2}{12\pi^2 f^3} \tag{1.22}$$

where Γ_{ij} is the overlap reduction function and describes the degree of correlation between the noise in the pulsar pair ij, in case of an isotropic GWB it is the Hellings-Downs curve (1.8).

The amplitude A_{GWB} gives insight on the properties of the population, whilst the spectral shape gives information on the properties of the individual binaries. Using current and simulated PTAs observations on the GWB, this thesis aims to see how much we can constrain current models on the population of SMBHBs and galaxy mergers as well as the properties of the SMBHB evolution. The focus will be on doing Bayesian analyses for astrophysical inference on the characteristic strain h_c.

1.7 Methods

To do the astrophysical parameter estimation we follow this general procedure throughout the thesis:

1. Describe an astrophysically motivated and parametric model of the GWB
2. Model the likelihood function of such a GWB: either an upper limit using the current PTA observations or a simulated detection
3. Run a sampling algorithm to determine the constraints that can be put on the parameters

1.7.1 Parametric model

To compare the predicted characteristic strain for the GWB with the observations from PTAs, the model need to be both accurate, i.e. taking as much of the necessary physics into account, and flexible to account for incomplete or inaccurate knowledge of the physics of SMBHBs. Good candidates are parametric models, which can consider astrophysical uncertainties in the values of parameters and have physically motivated functional form at the same time. If the parametric model can efficiently compute the strain for a given set of parameters, PTA observations can be directly used to constrain the uncertainties on the astrophysical parameters. The parametric model used in this thesis is introduced in Chapter 2 and modified in Chapter 5.

1.7.2 Bayes' theorem

We use Bayes theorem

$$p(\theta|d,M) = \frac{p(\theta|M)p(d|\theta,M)}{p(d|M)} \tag{1.23}$$

to find the posterior $p(\theta|d,M)$ for a model with specific parameters θ as the prior $p(\theta|M)$ times the likelihood $p(d|\theta,M)$ divided by the evidence $p(d|M)$. p are probabilities, d is the observed data coming from PTA observations or simulations, M is the selected model for the computation of the GWB strain and θ are the parameters of said model.

The posterior describes the updated knowledge on the parameters of the model, which are the constraints that we are looking for in this thesis.

Prior distributions represent our initial knowledge on the physics, they can either be uninformative or astrophysically motivated, see Chapters 3, 4 and 5.

The likelihood function is the heart of Bayes theorem. It gives the probabilitity to produce the observed data given a specific model with a certain set of parameters. To produce the likelihood function we use PTA observations and simulations. This creates likelihood functions with different analytic shapes for the upper limit and detection cases. For upper limits we use Fermi functions, smoothed step functions, in conjuction with the quoted sensitivity curves of the PTAs as well as the posterior distributions for the GWB strain itself. For detections we use log Gaussians, assuming ideal detection at the injected strain value with a standard deviation according to the strength of the detection. More details on the likelihood functions can be found in Chapters 3 and 4.

The evidence acts as a renormalization for the overall probability of the model to produce the data. Thus a ratio of evidences, i.e. the Bayes factor, can be used for model comparison.

1.7.3 Sampling algorithm

We use cpnest (Del Pozzo and Veitch, 2015), an implementation of the nested sampling algorithm developed by Skilling (2004), to determine the posterior distribution. The algorithm samples the parameter space from the least likely point, moves towards the highest likely point and ends at the maximum likelihood contour. With θ a set of parameters, $p(\theta|M)$ the prior distribution,

$dX = p(\theta|M)d\theta$ the differential prior volume element, $L = p(d|\theta,M)$ the likelihood, w the weight and $Z = \int LdX$ the evidence, the general process can be described as follows

1. Start with N live points each with a sets of parameters θ_N chosen from the prior distribution $p(\theta|M)$, compute the corresponding likelihoods L_N for all live points and initialise the evidence $Z = 0$ and prior volume $X_0 = 1$.

2. Record the live point θ_i with the current lowest likelihood L_i from all live points with weight $w_i = X_{i-1} - X_i$, where $X_i = \exp(-i/N)$, increase the evidence Z by $L_i w_i$ and replace live point i with a new live point $i+1$ from the prior distribution, where $L_{i+1} > L_i$.

3. Do step 2 j times, until adding a new step does not increase the likelihood by more than a user defined small fraction f: $L_{max}X_j < fZ_j$, which corresponds to having reached the contour of maximum likelihood.

This process will give a chain of data points with the parameter set θ_i, corresponding likelihood L_i and weight w_i with increasing likelihood and decreasing weight. The weights w_i in a sense renormalizes the speed at which the parameter space is sampled. The faster it can reach the highest likely point, the steeper the weights drop. The posterior samples can be picked from the data chain by accepting point i weighted by w_i. In addition, nested sampling also returns a number for the total evidence Z, which can be used for model comparison.

1.8 Thesis plan

This thesis is organised as follows:

Chapter 1 provides a general introduction to the motivation, techniques and methods of doing GW science with PTAs. It has been taylored to answer what astrophysics can be learned from PTAs observations on the GWB emitted by a population of SMBHBs for this thesis.

Chapter 2 shows the general model for the computation of the characteristic strain of the GWB from Chen et al. (2017b). It includes a phenomenological description for the SMBHB merger rate, eccentric binaries in a stellar environment and a upper mass limit cutoff when integration the SMBHB population. The advantage of the model is its computational efficiency, whilst being able to accurately recover the correct characteristic strain spectrum.

Initial studies on constraining the model parameters for the GWB have been done in Chen et al. (2017a) and are shown in chapter 3. The results use a current PTA upper limit, simulated detections and mostly wide uniform uniformative priors to determine the constraints on the model parameters with PTA observations alone.

Chapter 4 reproduces the detailed re-analysis of the most stringent published upper limit on the GWB from the Parkes PTA collaboration from Middleton et al. (2018). The focus is to see whether there is tension between different models predicting the number and masses of SMBHBs in the Universe and a GWB upper limit at $A_{yr} = 10^{-15}$.

Chapter 5 is based on the paper draft from Chen et al. (2018) that has been submitted already and aims to introduce a novel way to directly compare and combine constraints on astrophysical observables from traditional electromagnetic observations with PTAs observations on the GWB. We replace the phenomenological SMBHB merger rate from chapter 2 with a merger rate coming from observations of galaxy mergers and galaxy - black hole relations. Using current constraints on the astrophysical observables as priors allows to see how much PTA observations can add to the current constraints.

The summary, conclusions and outlook of this thesis are given in chapter 6.

CHAPTER 2

PARAMETRIC MODEL OF THE CHARACTERISTIC STRAIN OF THE GWB

This chapter reproduces verbatim "S. Chen, A. Sesana, W. Del Pozzo, Efficient computation of the gravitational wave spectrum emitted by eccentric massive black hole binaries in stellar environments, 2017, MNRAS 470, 1738" without the Abstract, Introduction and Discussions sections.

2.1 Analytical modelling of the GW spectrum

The GWB generated by a population of eccentric binaries was first investigated by Enoki and Nagashima (2007) and more recently by Huerta et al. (2015). In this section we follow the same approach and review their main results. Following Phinney (2001), the characteristic strain $h_c(f)$ of the GW spectrum produced by a population of cosmological MBHBs can be written as

$$h_c^2(f) = \frac{4G}{\pi c^2 f} \int_0^\infty dz \int_0^\infty d\mathscr{M} \frac{d^2n}{dz d\mathscr{M}} \frac{dE}{df_r}. \tag{2.1}$$

Here, $d^2n/dzd\mathscr{M}$ defines the comoving differential number density (i.e. number of systems per Mpc^3) of merging MBHBs per unit redshift and unit chirp mass $\mathscr{M} = (M_1 M_2)^{3/5}/(M_1+M_2)^{1/5}$

– where $M_1 > M_2$ are the masses of the binary components – and the *observed* GW frequency at Earth f is related to the *emitted* frequency in the source frame f_r via $f_r = (1+z)f$. The evaluation of equation (2.1) involves a double integral in mass and redshift, generally to be performed numerically, and the computation of the energy spectrum dE/df_r. For an eccentric MBHB, this is given by a summation of harmonics as:

$$\frac{dE}{df_r} = \sum_{n=1}^{\infty} \frac{1}{n} \frac{dE_n}{dt} \frac{dt}{de_n} \frac{de_n}{df_n}, \tag{2.2}$$

where now $f_n = f_r/n$ is the restframe *orbital* frequency of the binary for which the n-th harmonic has an observed frequency equal to f and e_n is the eccentricity of the binary at that orbital frequency. We used the concatenation rule of derivation to highlight the role of the eccentricity. The first differential term in the rhs of equation (2.2) is the luminosity of the n-th GW harmonic given by

$$\frac{dE_n}{dt} = \frac{32}{5} \frac{G^{7/3}}{c^5} \mathscr{M}^{10/3} (2\pi f_n)^{10/3} g_n(e_n) \tag{2.3}$$

where

$$\begin{aligned} g_n(e) = \frac{n^4}{32} \Big[&\Big(J_{n-2}(ne) - 2eJ_{n-1}(ne) + \frac{2}{n} J_n(ne) + 2eJ_{n+1}(ne) - J_{n+2}(ne) \Big)^2 \\ &+ (1-e^2) \Big(J_{n-2}(ne) - 2J_n(ne) + J_{n+2}(ne) \Big)^2 + \frac{4}{3n^2} J_n^2(ne) \Big], \end{aligned} \tag{2.4}$$

and J_n is the n-th Bessel function of the first kind. The other two differential terms describe the evolution of the binary frequency and eccentricity with time, and for an eccentric MBHB driven by GW emission only, are given by

$$\frac{df_n}{dt} = \frac{96}{5} (2\pi)^{8/3} \frac{G^{5/3}}{c^5} \mathscr{M}^{5/3} f_n^{11/3} F(e_n) \tag{2.5}$$

$$\frac{de_n}{dt} = -\frac{1}{15} (2\pi)^{8/3} \frac{G^{5/3}}{c^5} \mathscr{M}^{5/3} f_n^{8/3} G(e_n) \tag{2.6}$$

where

$$F(e) = \frac{1 + (73/24)e^2 + (37/96)e^4}{(1-e^2)^{7/2}} \tag{2.7}$$

$$G(e) = \frac{304e + 121e^3}{(1-e^2)^{5/2}}. \tag{2.8}$$

By plugging (2.3), (2.5) and (2.6) into the expression (2.2), equation (2.1) one obtains (Huerta et al., 2015)

$$h_c^2(f) = \frac{4G}{\pi c^2 f} \int_0^\infty dz \int_0^\infty d\mathscr{M} \frac{d^2n}{dz d\mathscr{M}} \frac{\mathscr{M}^{5/3}(\pi G)^{2/3}}{3(1+z)^{1/3} f^{1/3}} \sum_{n=1}^{\infty} \frac{g_n(e_n)}{F(e_n)(n/2)^{2/3}}. \tag{2.9}$$

We note that Equation (2.9) is strictly valid only if the merger happens at a fixed redshift. However, we will see later that the typical merger timescale, t_c, of MBHBs can be Gyrs (cf Equation (2.22) and figure 2.5), which is comparable to the cosmic expansion time $t_{\rm Hubble}$. Despite this fact, what actually matters is only the last phase of the MBHB inspiral, when the GW power is emitted in PTA band. Let us consider an optimistic PTA able to probe frequencies down to $\approx$ 1nHz (i.e. observing for 30 years). If binaries are circular, then they start to emit in the PTA band only when their orbital frequency is $f_{\rm orb} = 0.5$nHz. For typical MBHBs of $\mathscr{M} > 3 \times 10^8 {\rm M}_\odot$ (which are those dominating the GWB, see e.g. Sesana et al. (2008)), the coalescence time at that point is $\tilde{t}_c < 0.15$ Gyr. The bulk of the PTA signal comes from $z < 1.5$ (Ravi et al., 2015; Simon and Burke-Spolaor, 2016), where the typical cosmic expansion time is already $t_{\rm Hubble}(z) > 1$ Gyr. This is almost an order of magnitude larger than $\tilde{t}_c$, which we also stress becomes much shorter with increasing MBHB masses. On the other hand, if binaries are very eccentric, they start to emit significant GW power in the PTA band when their orbital frequency is much lower than the minimum frequency probed by the array. Figure 2.4 shows that, if $e = 0.9$, considering only the power emitted since $f_{\rm orb} = 0.1$nHz provides a good approximation to the overall spectrum from $f \approx 1$nHz onwards. Although $f_{\rm orb}$ is much lower in this case, eccentric binaries coalesce much faster (see again Equation (2.22)). For typical MBHBs of $\mathscr{M} > 3 \times 10^8 {\rm M}_\odot$ with $e = 0.9$, the coalescence time at that point is $\tilde{t}_c < 10$Myr. Therefore,

$\tilde{t}_c \ll t_{\rm Hubble}$ becomes a better approximation with increasing eccentricity, and Equation (2.9) generally provide a good approximation to the GWB.

In practice, equation (2.9) is evaluated numerically. For each integration element, the sum in the expression has to be computed by solving numerically equations (2.5) and (2.6) to evaluate e_n at each of the orbital frequencies f_n contributing to the spectrum observed at frequency f, and by then computing the appropriate $g_n(e_n)$ function. This procedure is extremely cumbersome and time consuming. Yunes et al. (2009) proposed an analytical approximation for $e(f)$ that helps in speeding up the computation. However, it is accurate only for $e < 0.9$, and even then one is left with the computation of the n harmonics and the evaluation of the Bessel functions. Note that the GW energy spectrum of a binary with eccentricity e peaks at the $n_p \approx (1-e)^{-3/2}$ harmonic, with still significant contributions at $n \sim 10 n_p$ (Berry and Gair, 2010). For a MBHB with $e = 0.9$ this implies the computation of several hundreds of harmonics.

2.1.1 Fitting formula and scaling properties

Our first goal is to compute an efficient and accurate way to numerically calculate $h_c^2(f)$. Although the double integral might be solvable analytically for a suitable form of $d^2n/dzd\mathscr{M}$, a numerical evaluation is generally required. We therefore concentrate on the computation of the single integral element. We thus consider a reference system with a unity number density per Mpc^3 characterized by selected chirp mass and redshift. This corresponds to setting

$$\frac{d^2n}{dzd\mathscr{M}} = \delta(\mathscr{M} - \mathscr{M}_0)\delta(z - z_0)/\mathrm{Mpc}^3. \tag{2.10}$$

Equation (2.9) then becomes

$$h_{c,0}^2(f) = \frac{4G^{5/3}\mathrm{Mpc}^{-3}}{3\pi^{1/3}c^2 f^{4/3}} \frac{\mathscr{M}_0^{5/3}}{(1+z_0)^{1/3}} \sum_{n=1}^{\infty} \frac{g(n,e_n)}{F(e_n)(n/2)^{2/3}}. \tag{2.11}$$

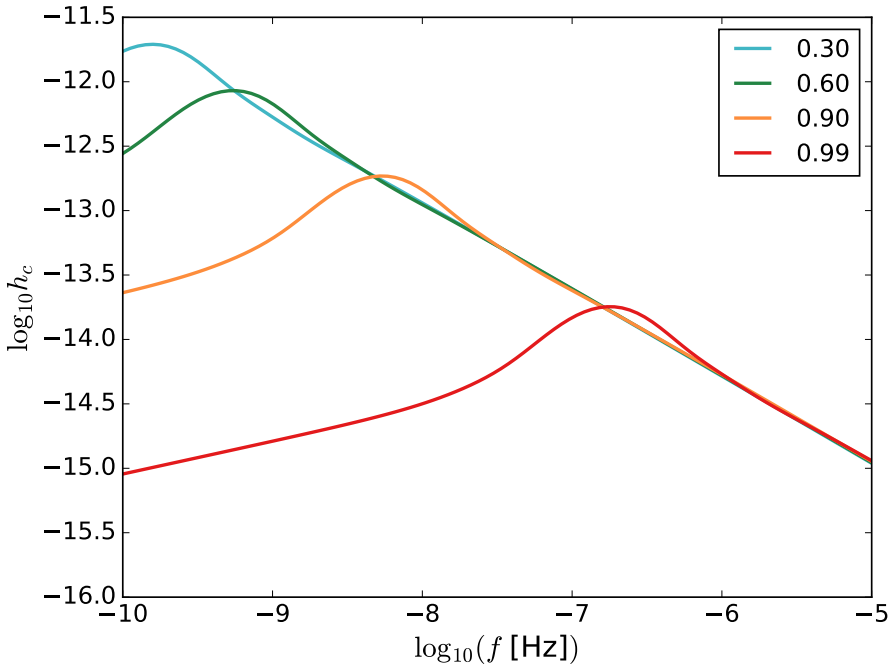

Figure 2.1: characteristic amplitude spectrum for different eccentricities calculated with $n = 12500$ harmonics computed with no lower limit on f_n.

To fully define the system we need to specify an initial MBHB eccentricity e_0 at a reference orbital frequency f_0, so that the eccentricity $e_n = e_n(n, f_0, e_0)$ can to be evaluated for the appropriate $n-$th harmonic at the orbital frequency $f_n = f(1+z_0)/n$ via equations (2.5) and (2.6).

We study the behaviour of equation (2.11) by taking a fiducial binary with $\mathscr{M}_0 = 4.16 \times 10^8 \mathrm{M}_\odot$, $z_0 = 0.02$, $f_0 = 0.1\mathrm{nHz}$ and different eccentricities $e_0 = 0.3, 0.6, 0.9, 0.99$. Results are shown in figure 2.1. Obviously, since the binary circularizes because of GW emission, at high frequency all the spectra eventually sit on the same power law. Moreover, the spectra look self-similar, as also noted by Huerta et al. (2015). This property allows the spectra to be shifted on the $f^{-2/3}$ diagonal, given an analytic fitting expression for one reference spectrum. Self similarity has to be expected because equations (2.5) and (2.6) combine to give (Enoki and Nagashima, 2007)

$$\frac{f}{f_0} = \left(\frac{1-e_0^2}{1-e^2} \left(\frac{e}{e_0} \right)^{12/19} \left(\frac{1+\frac{121}{304}e^2}{1+\frac{121}{304}e_0^2} \right)^{870/2299} \right)^{-3/2} . \tag{2.12}$$

This means that the eccentricity evolution is just a function of the frequency ratio f/f_0 and there

is no intrinsic scale in the problem. Any inspiral will thus pass through any given eccentricity at some frequency during the process. A reference binary with $e_0 = 0.9$ at $f_0 = 10^{-10}$Hz is simply an earlier stage in the evolution of a binary with a smaller e at a higher f, see figure 2.2. Therefore, the spectrum of a binary with a different initial eccentricity e_t specified at a different initial frequency f_t can be simply obtained by shifting the spectrum of the reference binary. What one needs to know is by how much the spectrum has to be shifted along the $f^{-2/3}$ diagonal. To answer this question we identify a reference point of the spectrum. The obvious choice is the peak frequency defined by Huerta et al. (2015). They showed that the deviation of the spectrum of an eccentric binary, defined by fixing the eccentricity e at a given orbital frequency f, with respect to its circular counterpart peaks at a frequency f_p given by[1]

$$\frac{f_p}{f} = \frac{1293}{181}\Big[\frac{e^{12/19}}{1-e^2}\big(1+\frac{121e^2}{304}\big)^{870/2299}\Big]^{3/2}. \tag{2.13}$$

Let us consider two spectra as shown in figure 2.2. The first one is a reference spectrum $h_{c,0}(f)$ defined by $e_0 = 0.9$ at $f_0 = 10^{-10}$Hz, the second one is a generic spectrum $h_c(f)$ characterized by a generic value of e_t at a transition frequency f_t typically different from f_0. By feeding these input into (2.13) we directly get the two peak frequencies $f_{p,0}$ and $f_{p,t}$ respectively, marked in the lower panel of the figure. We want to compute $h(f)$ from $h_{c,0}(f)$. It is clear that the peak frequency at $f_{p,0}$ has to shift to $f_{p,t}$, therefore $h_c(f)$ has to correspond to $h_{c,0}(f')$ where $f' = f(f_{p,0}/f_{p,t})$. However, this transformation just shifts the spectrum horizontally. To get to $h_{c,0}(f)$ we still need to multiply $h_{c,0}(f')$ by a factor $(f_{p,t}/f_{p,0})^{-2/3}$. The total shift has therefore the form

$$h_c(f) = h_{c,0}\Big(f\frac{f_{p,0}}{f_{p,t}}\Big)\left(\frac{f_{p,t}}{f_{p,0}}\right)^{-2/3}. \tag{2.14}$$

In fact, it is easy to verify that by applying equation (2.14) to any of the spectra in figure 2.1 all the other spectra are recovered.

All we need then is a suitable fit for a reference MBHB. For this, we take the reference case

[1]Note that f_p does not coincide with the peak of the characteristic amplitude, as also clear from figure 2.2.

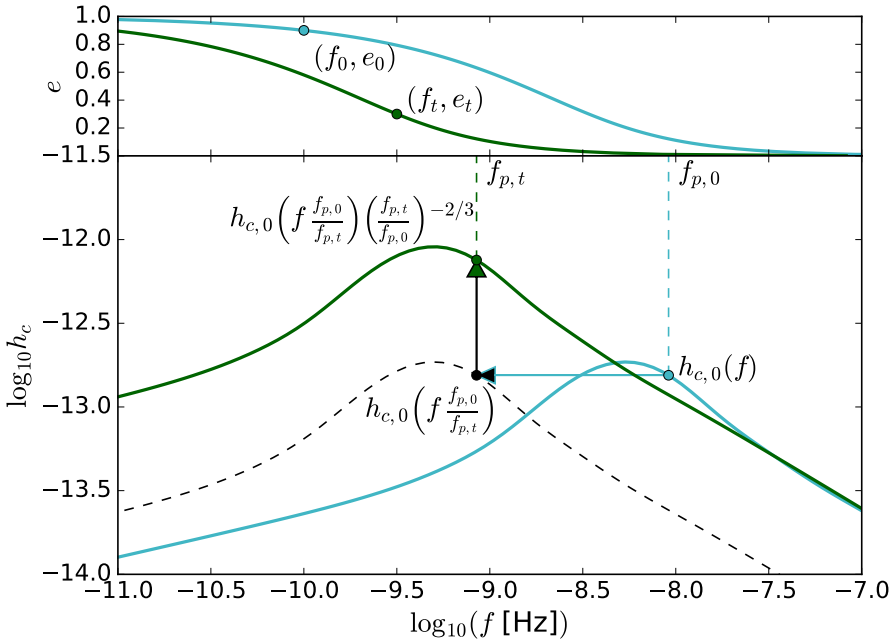

Figure 2.2: Analytical spectral shift. The upper panel shows the eccentricity evolution over frequency for a fiducial spectrum characterized by the initial conditions ($e_0 = 0.9,\ f_0 = 10^{-10}$Hz) (blue) and a generic spectrum characterized by ($e_t,\ f_t$) (green). The lower panel shows the respective GW spectra (again, blue for fiducial and green for generic) and the steps involved in the shifting. The two vertical dashed lines mark the 'peak frequencies' defined in (Huerta et al., 2015), the horizontal arrow shifts the fiducial spectrum by $f_{p,t}/f_{p,0}$ (black dashed spectrum), and the vertical arrow moves it up by a factor $(f_{p,t}/f_{p,0})^{-2/3}$, as described in the main text.

$f_0 = 10^{-10}$Hz and $e_0 = 0.9$ and, based of the visual appearance on the spectrum, we fit a trial analytic function of the form

$$h_{c,\mathrm{fit}}(f) = a_0 \bar{f}^{a_1} e^{-a_2 \bar{f}} + b_0 \bar{f}^{b_1} e^{-b_2 \bar{f}} + c_0 \bar{f}^{-c_1} e^{-c_2/\bar{f}}, \tag{2.15}$$

where a_i, b_i, c_i are constants to be determined by the fit and $\bar{f} = f/(10^{-8}\mathrm{Hz})$. We find that setting

$$a_0 = 7.27 \times 10^{-14} \qquad a_1 = 0.254 \qquad a_2 = 0.807$$
$$b_0 = 1.853 \times 10^{-12} \qquad b_1 = 1.77 \qquad b_2 = 3.7$$
$$c_0 = 1.12 \times 10^{-13} \qquad c_1 = 0.676 \qquad c_2 = 0.6$$

reproduces the spectrum within a maximum error of 1.5% in log-amplitude (i.e. 3.5% in amplitude), as shown in figure 2.3. It also shows the difference between the analytical fit

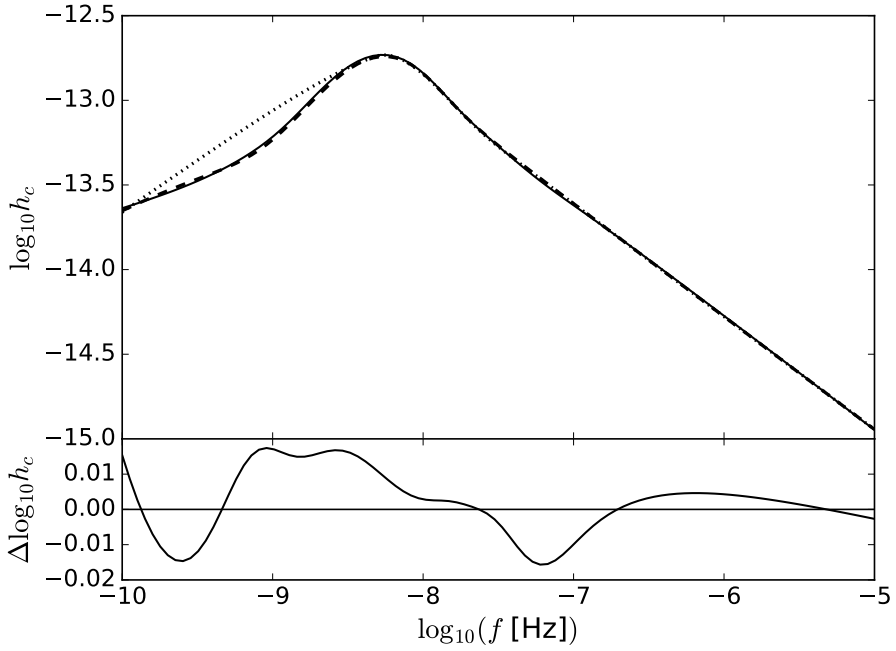

Figure 2.3: Gravitational wave spectrum $h_c(f)$ for the reference binary described in the text, computed by summing $n = 12500$ harmonics (dashed line) compared to the best fit $h_{c,\mathrm{fit}}(f)$ with an analytic function of the form given by equation (2.15) (solid line) and by (Huerta et al., 2015) (dotted line). The lower panel shows the difference $\log_{10} h_{c,\mathrm{fit}} - \log_{10} h_c$ as a function of frequency.

presented in this paper versus (Huerta et al., 2015). The lower frequency shape (left to the peak) is recovered more accurately by equation (2.15).

With this fitting formula in hand, equation (2.14) readily enables the analytical evaluation of the spectrum for any desired pair of reference values f_t, $e_t = e(f_t)$ (note that those can be function of the MBHB parameters, e.g. its chirp mass, or of the environment in which the binary evolve, as we will see in Section 2.2). Moreover, equation (2.11) shows that the spectrum of a binary with different chirp mass and redshift can be simply obtained by multiplying $h_{c,\mathrm{fit}}(f)$ by $(\mathscr{M}/\mathscr{M}_0)^{5/3}$ and $((1+z)/(1+z_0))^{-1/3}$, respectively. Therefore, the overall spectrum of the MBHB population can be generated from $h_{c,\mathrm{fit}}(f)$ as

$$h_c^2(f) = \int_0^\infty dz \int_0^\infty d\mathscr{M} \frac{d^2n}{dz d\mathscr{M}} h_{c,\mathrm{fit}}^2\left(f\frac{f_{p,0}}{f_{p,t}}\right)\left(\frac{f_{p,t}}{f_{p,0}}\right)^{-4/3}\left(\frac{\mathscr{M}}{\mathscr{M}_0}\right)^{5/3}\left(\frac{1+z}{1+z_0}\right)^{-1/3}, \qquad (2.16)$$

where the ratio $f_{p,0}/f_{p,t}$ is calculated by means of equation (2.13).

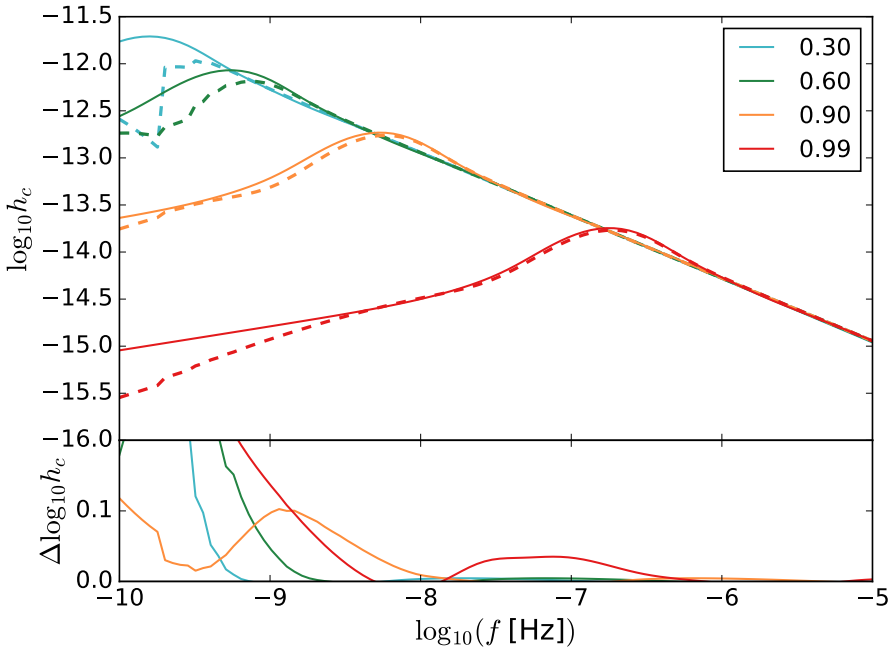

Figure 2.4: characteristic amplitude spectrum for different eccentricities calculated with $n = 12500$ harmonics where only frequencies $f_n \geq 10^{-10}$ contribute (dashed lines) compared to the spectrum computed with no limitations on f_n (solid lines). The lower panel shows the difference $\log_{10} h_{c,\mathrm{fit}} - \log_{10} h_c$ as a function of frequency for the different cases, and it is always < 0.1 for $f > 1\,\mathrm{nHz}$.

2.1.2 Range of applicability

The assumption behind the above derivation is that the dynamics of the MBHB is purely driven by GW emission, i.e., its evolution is defined by equations (2.5) and (2.6) formally back to $\log_{10} f = -\infty$ and $e = 1$. This of course cannot be true in practice, the question is whether the derivation provides a good approximation in the frequency range relevant to PTA detection.

MBHBs are driven by coupling with their environment up to a certain *transition orbital frequency*, f_t. At lower frequencies the evolution is faster than what is predicted by GW emission only and the eccentricity does not indefinitely grow to approach $e = 1$. If the lowest frequency probed by PTA is f_{min} (which is $1/T$, where T is the observation time, as defined in the introduction), then a necessary requirement for the applicability of equation (2.16) is $f_t < f_{\mathrm{min}}$. This is, however, not a sufficient condition because for an eccentric MBHB population, the spectrum at f_{min} is defined by the contribution of binaries emitting at $f_n < f_{\mathrm{min}}$ satisfying the requirement $f_n = f_{\mathrm{min}}(1+z)/n$

for some n. If $f_t = f_{\rm min}$, and therefore the binary evolves faster and is less eccentric at $f_n < f_{\rm min}$, then the contribution of the n-th harmonics of systems emitting at f_n is smaller, affecting the overall spectrum at $f_{\rm min}$ and above. In other words, the spectrum observed at frequency f is composed of higher harmonics of $f_n < f$. These however, only emit GWs if the eccentricity is high enough, which is the case if the binary is purely driven by GW emission, but may not be the case if the binary is driven by its environment at $f_n < f_{\rm min}$. Thus, less energy is emitted at f, giving rise to a drop in the spectrum.

To investigate the impact of this fact on the spectrum we consider the same reference binaries with transition frequency $f_t = f_0 = 0.1$nHz and $e_t = e_0 = 0.3, 0.6, 0.9, 0.99$, but now assuming they *form* at f_t, i.e., discarding the contribution of lower frequencies to the computation of the spectrum. The result is compared to the full spectrum in figure 2.4. As expected, the absence of binaries at $f < f_t$ partially suppresses the signal observed at $f > f_t$. However three things should be noticed: i) the suppression is relevant only up to $f \sim 10 f_t$, ii) the effect is small for highly eccentric binaries – this is because for large e, the gravitational wave strain h_c is dominated by the first, rather than the second harmonic, see figure 4 in Taylor et al. (2016a)–, and iii) this is the most pessimistic case, since for a realistic orbital evolution, binaries do emit also at $f < f_t$, but their contribution to the spectrum at $f > f_t$ is smaller due to the faster evolution and lower eccentricity. Therefore, our approximation should hold in the PTA band as long as the typical transition frequency f_t is few time smaller than $f_{\rm min}$. In the next section we will show that for a typical MBHB population driven by scattering of stars this is indeed generally the case.

2.2 Binaries in stellar environments

Following galaxy mergers, MBHBs sink to the centre because of dynamical friction (Chandrasekhar, 1943) eventually forming a bound pair when the mass in star and gas enclosed in their orbit is of the order of the binary mass. For MBHBs with $M = M_1 + M_2 > 10^8 {\rm M}_\odot$ relevant to PTA, this occurs at an orbital separation of few parsecs, and the corresponding GW emission

is well outside the PTA band. At this point, dynamical friction becomes highly inefficient, and further hardening of the binary proceeds via exchange of energy and angular momentum with the dense gaseous and stellar environment (see Dotti et al. (2012) and references therein).

The bulk of the PTA GW signal is produced by MBHBs hosted in massive galaxy (generally spheroids) at redshift < 1. Sesana (2013b) and Ravi et al. (2015) further showed that the vast majority of the signal comes from 'red' systems, featuring old stellar populations and only a modest amount of cold gas. This fact does not immediately imply that MBHBs cannot be driven by interaction with cold gas in a form of a massive circumbinary disk. After all, because of the observed MBH-host galaxy relations (see, e.g. Kormendy and Ho (2013)), even a mere 1% of the galaxy baryonic mass in cold gas is still much larger than the MBHB mass, and therefore sufficient to form a circumbinary disk with mass comparable to the binary, if concentrated in the very centre of the galaxy. On the other hand, the relative fraction of observed bright quasars declines dramatically at $z < 1$ (e.g. Hopkins et al. (2007)), implying that accretion of large amounts of cold gas, and hence a scenario in which MBHBs evolve in massive circumbinary disks, is probably not the norm. We therefore concentrate here on MBHBs evolving via interaction with stars.

Sesana and Khan (2015) have shown that, following the merger of two stellar bulges, the evolution of the bound MBHBs can be approximately described by the scattering experiment formalism developed by Quinlan (1996). In Quinlan's work, the binary semimajor axis evolution follows the simple equation

$$\frac{da}{dt} = -\frac{HG\rho a^2}{\sigma}, \tag{2.17}$$

where ρ is a fiducial stellar background density and σ the characteristic value of the Maxwellian distribution describing the velocity of the stars. H is a dimensionless constant (empirically determined by the scattering experiments) of order $15-20$, largely independent on the MBHB mass ratio $q = M_2/M_1$ and eccentricity e. Sesana and Khan (2015) found that equation (2.17) is applicable to post merger stellar distributions providing that σ is the typical velocity dispersion of the stellar bulge and ρ is the average stellar density at the MBHB influence radius, $\rho_i =$

$\rho(r_i)$, defined approximately as the radius enclosing a stellar mass twice the total MBHB mass $M = M_1 + M_2$. In the stellar dynamic jargon, this corresponds to a situation where the MBHB 'loss-cone' is full at the binary influence radius. By using different methods, Vasiliev et al. (2015) came to similar conclusions stressing, however, that in the long term the MBHB hardening rate tends to drop compared to equation (2.17), a hint that the loss-cone might not be kept full in the long term. The evolution of the Keplerian orbital frequency f_K of the MBHB can therefore be written as:

$$\frac{df_K}{dt} = \frac{df_K}{dt}\Big|_* + \frac{df_K}{dt}\Big|_{gw} \tag{2.18}$$

where

$$\frac{df_K}{dt}\Big|_* = \frac{3}{2(2\pi)^{2/3}} \frac{H\rho_i}{\sigma} G^{4/3} M^{1/3} f_K^{1/3} \tag{2.19}$$

$$\frac{df_K}{dt}\Big|_{gw} = \frac{96}{5} (\pi)^{8/3} \frac{G^{5/3}}{c^5} \mathscr{M}^{5/3} f_K^{11/3} F(e). \tag{2.20}$$

Equation (2.19) is readily obtained from equation (2.17) by using Kepler's law, and equation (2.20) is the standard GW frequency evolution already seen in the previous section. It is easy to show that at low frequency stellar hardening dominates and GW takes over at a transition frequency that can be calculated by equating the two evolution terms to obtain:

$$\begin{aligned} f_t &= (2\pi)^{-1} \left(\frac{5H\rho_i}{64\sigma F(e)} \right)^{3/10} \frac{c^{3/2}}{G^{1/10}} \frac{(1+q)^{0.12}}{q^{0.06}} \mathscr{M}^{-2/5} \\ &\approx 0.56\pi^{-1} \left(\frac{5H\rho_i}{64\sigma F(e)} \right)^{3/10} \frac{c^{3/2}}{G^{1/10}} \mathscr{M}^{-2/5} \\ &= 0.356\,\mathrm{nHz} \left(\frac{1}{F(e)} \frac{\rho_{i,100}}{\sigma_{200}} \right)^{3/10} \mathscr{M}_9^{-2/5} \end{aligned} \tag{2.21}$$

where $\rho_{i,100} = \rho_i / (100\,\mathrm{M}_\odot \mathrm{pc}^{-3})$, $\sigma_{200} = \sigma / (200\,\mathrm{km\,s}^{-1})$, $\mathscr{M}_9 = \mathscr{M} / (10^9\,\mathrm{M}_\odot)$ and we assume $H = 16$ in the last line. We notice that in the mass ratio $0.1 < q < 1$, that by far dominates the PTA GW signal (see, e.g. figure 1 in Sesana et al. (2012)), the function $(1+q)^{0.12}/q^{0.06}$ falls in the range $[1.08, 1.15]$. Therefore, in the last two lines of equation (2.21) we neglected the mass ratio dependence by substituting $(1+q)^{0.12}/q^{0.06} = 1.12$. A fair estimate of the MBHB coalescence

timescale is provided by the evolution timescale at the transition frequency, $t_c = f_t(dt/df_t)$. By using equations (2.21) and (2.19) one obtains

$$\begin{aligned} t_c &= \frac{5}{96}(2\pi)^{-8/3}\frac{c^5}{G^{5/3}}\mathscr{M}^{-5/3}f_t^{-8/3}F(e)^{-1} \\ &= \frac{2}{3}\frac{c}{G^{7/5}}\Big(\frac{\sigma}{H\rho_i}\Big)^{4/5}\Big(\frac{5}{64F(e)}\Big)^{1/5}\frac{q^{0.16}}{(1+q)^{0.32}}\mathscr{M}^{-3/5} \\ &\approx 0.5\frac{c}{G^{7/5}}\Big(\frac{\sigma}{H\rho_i}\Big)^{4/5}\Big(\frac{5}{64F(e)}\Big)^{1/5}\mathscr{M}^{-3/5} \\ &= 0.136\ \mathrm{Gyr}\ F(e)^{-1/5}\left(\frac{\rho_{i,100}}{\sigma_{200}}\right)^{4/5}\mathscr{M}_9^{-3/5} \end{aligned} \tag{2.22}$$

where, once again, we omitted mild q dependences in the last approximation by substituting $q^{0.16}/(1+q)^{0.32} = 0.75$ ($0.67 < q^{0.16}/(1+q)^{0.32} < 0.8$ for $0.1 < q < 1$).

For an operational definition of f_t and t_c, we need to define ρ_i and σ. The density profile of massive spheroidals is well captured by the Dehnen's density profile family (Dehnen, 1993) which takes the form

$$\rho(r) = \frac{(3-\gamma)M_* a}{4\pi}r^{-\gamma}(r+a)^{\gamma-4}, \tag{2.23}$$

where $0.5 < \gamma < 2$ determines the inner slope of the stellar density distribution, M_* is the total mass of the bulge in star, a is its characteristic radius. The influence radius r_i of the MBHB is then set by the condition

$$2M = \int_0^{r_i} 4\pi r^2 \rho(r) dr \tag{2.24}$$

which gives

$$r_i = \frac{a}{(2M/M_*)^{1/(\gamma-3)} - 1}. \tag{2.25}$$

Inserting r_i back into the Dehnen profile gives

$$\rho_i \approx \frac{(3-\gamma)M_*}{4\pi a^3}\Big(\frac{2M}{M_*}\Big)^{\gamma/(\gamma-3)}, \tag{2.26}$$

where we used the fact that $2M << M_*$. It is possible to reduce the number of effective

parameters $M, M_*, a, \gamma, \sigma$ by employing empirical relations connecting pairs of them, valid for stellar spheroids. In particular we use the $a - M_*$ relation of Dabringhausen et al. (2008), and the $M - \sigma$ and $M - M_*$ of Kormendy and Ho (2013) relations:

$$a = 239\,\mathrm{pc}\,(2^{1/(3-\gamma)} - 1)\Big(\frac{M_*}{10^9 \mathrm{M}_\odot}\Big)^{0.596} \tag{2.27}$$

$$\sigma = 261\,\mathrm{km\ s^{-1}}\,\Big(\frac{M}{10^9 \mathrm{M}_\odot}\Big)^{0.228} \tag{2.28}$$

$$M_* = 1.84 \times 10^{11}\,\mathrm{M}_\odot\,\Big(\frac{M}{10^9 \mathrm{M}_\odot}\Big)^{0.862}. \tag{2.29}$$

This allows to express ρ_i as a function of M and γ only in the form

$$\rho_i = 0.092\,\mathrm{M}_\odot \mathrm{pc}^{-3}\,\mathscr{F}(\gamma)\Big(\frac{M}{10^9 \mathrm{M}_\odot}\Big)^{\mathscr{G}(\gamma)}, \tag{2.30}$$

where

$$\mathscr{F}(\gamma) = \frac{(3-\gamma)92^{\gamma/(3-\gamma)}}{(2^{1/(3-\gamma)} - 1)^3} \tag{2.31}$$

$$\mathscr{G}(\gamma) = -0.68 - 0.138\frac{\gamma}{3-\gamma}. \tag{2.32}$$

Equations (2.28) and (2.30) are expressed as a function of M. However, we notice from equation (2.21) that $f_t \propto M^{-0.3-0.041\gamma/(3-\gamma)}$. Since $\mathscr{M} = Mq^{3/5}/(1+q)^{6/5}$, if $0.1 < q < 1$, then $2.32\mathscr{M} < M < 3.57\mathscr{M}$. It is easy to show that for $0.5 < \gamma < 2$, by substituting $M = 2.9\mathscr{M}$, equation (2.21) returns f_t within 10% of the correct value when $0.1 < q < 1$.

Finally, equation (2.18) defines only the frequency evolution of the MBHB. For a complete description of the system, tracking of the eccentricity evolution is also required. Both scattering experiments and N-body simulations have shown that MBHB-star interactions tend to increase e. The increase is generally mild for equal mass binaries and the eccentricity at the transition frequency largely depends on the initial eccentricity at the moment of binary pairing. Because of this mild evolution at $f_K < f_t$ and in order to keep the problem simple, we approximate the

eccentricity evolution of the MBHB as:

$$\frac{de}{dt} = \begin{cases} 0 \quad \text{if} \quad f_K < f_t \\ -\frac{1}{15}(2\pi)^{8/3}\frac{G^{5/3}}{c^5}\mathscr{M}^{5/3}f_K^{8/3}G(e) \quad \text{if} \quad f_K > f_t \end{cases} \tag{2.33}$$

2.3 Results: Gravitational wave spectra calculation

2.3.1 Dynamics of MBHBs: transition frequency and coalescence time

Before going into the computation of the GW spectrum, we can have a look at how transition frequency f_t and coalescence timescale t_c change as a function of $\mathscr{M}$ and e_t. In the following we consider four selected models representative of a range of physical possibilities having a major impact on the MBHB dynamics. Results are shown in figure 2.5. The top panel shows a model with $\gamma = 1$ and ρ_i given by equation (2.30). We consider this as our default model, because most of the PTA signal is expected to come from MBHBs hosted in massive elliptical galaxies with relatively shallow density profiles. The GW signal is generally dominated by MBHBs with $\mathscr{M} > 3 \times 10^8 \mathrm{M}_\odot$, which are therefore our main focus. At low e_t those systems have $f_t < 0.3$nHz and coalescence timescales in the range $1.5 - 4$ Gyr. For $e_t = 0.9$, f_t is ten times lower, nonetheless t_c is roughly an order of magnitude shorter, in virtue of the $F(e)$ factor appearing in equation (2.22). The effect of a steeper density profile is shown in the second row of plots in figure 2.5, where we now assume $\gamma = 1.5$. The effect of a steeper inner power law, is to make the stellar distribution more centrally concentrated, thus enhancing ρ_i. This makes stellar hardening more efficient and shifts f_t by a factor ≈ 1.3 upwards making t_c a factor of ≈ 2 shorter (using a shallower profile $\gamma = 0.5$ would have an opposite effect of the same magnitude). We recognize that ρ_i given by equation (2.30) relies on a number of scaling relations that are constructed on a limited sample of local, non-merging, galaxies. We therefore also explore the effect of a bias in some of those relations. For example, merging galaxies might be more

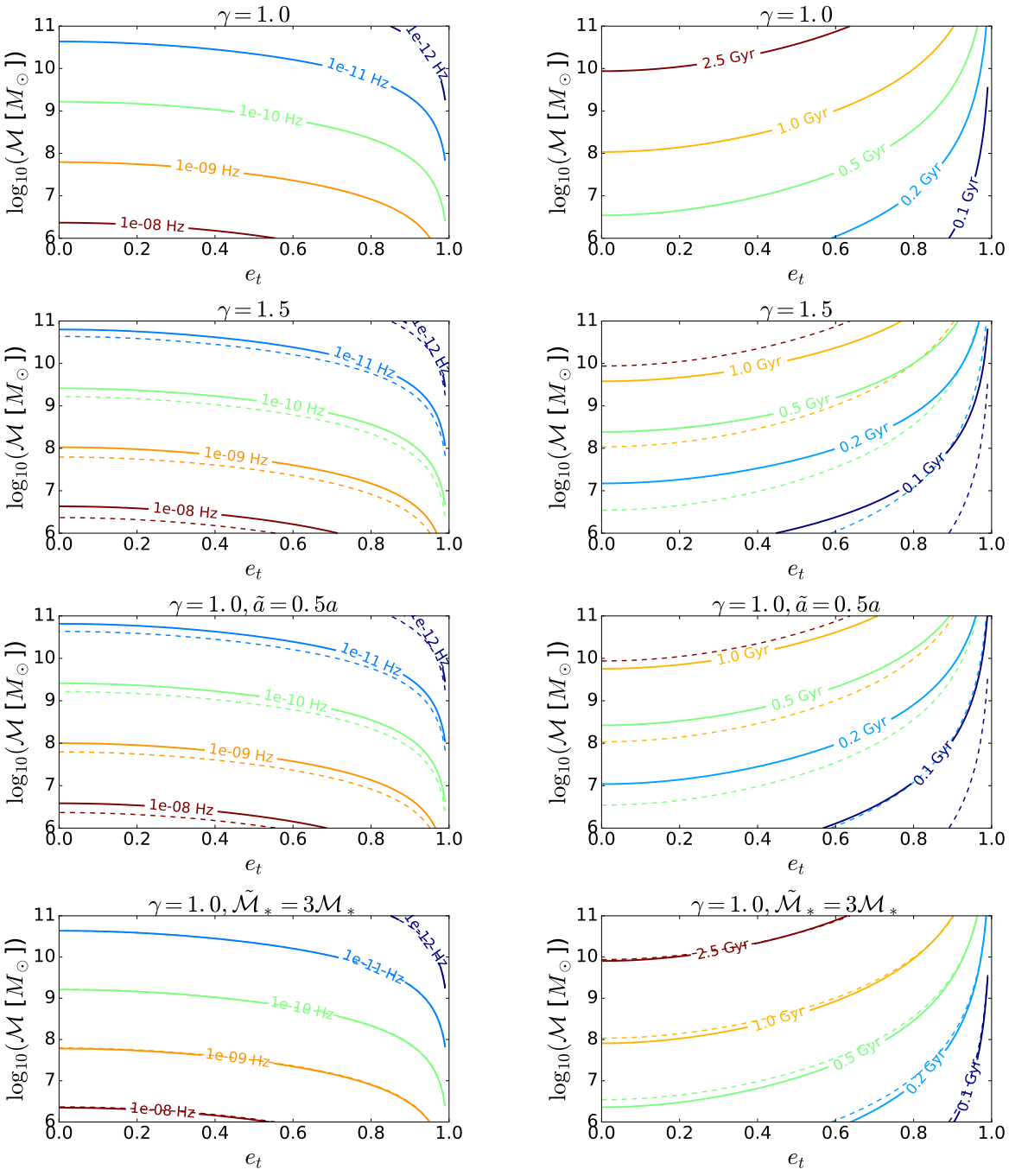

Figure 2.5: Contour plots of transition frequency f_t (left panels) and coalescence timescales t_c (right panels) in the transition eccentricity e_t vs chirp mass $\mathscr{M}$ plane. f_t is computed according to equation (2.21) with ρ_i provided by equation (2.30) calculated assuming the fiducial scaling relations given by equations (2.27,2.28,2.29). Shown are models with $\gamma = 1$ (which is our fiducial model, top row), $\gamma = 1.5$ (second row), $\gamma = 1$ but a decreased by a factor of two in equation (2.27) (third row) $\gamma = 1$ and M_* increased by a factor of three in equation (2.29) (bottom row). The fiducial model is plotted in each of the other panels with dashed lines to highlight changes in f_t and t_c against the other models (plotted as solid lines).

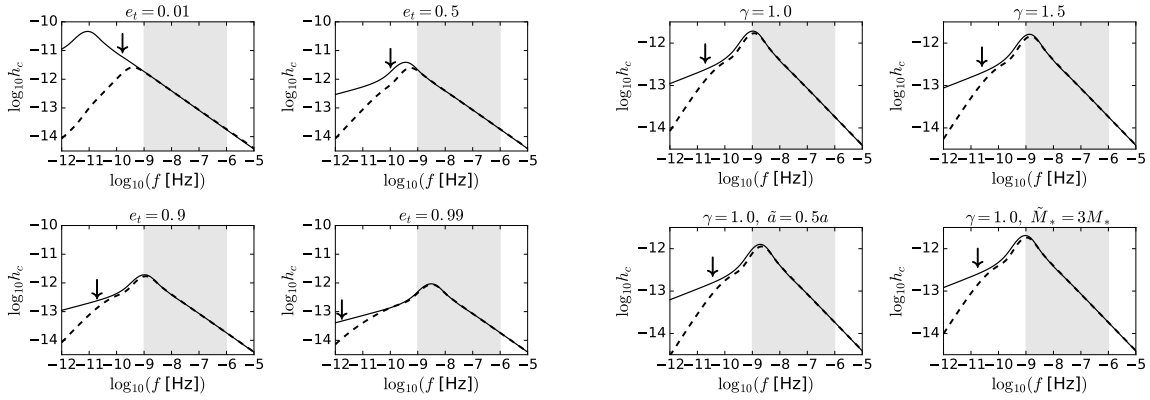

Figure 2.6: Spectra of a single MBHB with $\mathscr{M} = 10^9 \mathrm{M}_\odot$, $z = 0.02$. In each panel the solid line represents the spectrum fitted with equation (2.15), whereas the dashed line considers the full evolution due to interaction with the stellar environment and eccentricity; the arrow indicates the turnover frequency. The left four panels are for our fiducial galaxy model ($\gamma = 1$) and different MBHB eccentricities as indicated in each panel; the right four panels are for $e_t = 0.9$, but assume different prescriptions of the astrophysical relations used to calculate the turnover frequency (i.e. assume different host galaxy models), as specified in each panel. The shaded stripe at $10^{-9}\mathrm{Hz} < f < 10^{-6}\mathrm{Hz}$ indicates the range of frequency relevant to PTA observations.

centrally concentrated and we explore this possibility by arbitrarily reducing the typical scale radius a by a factor of two compared to equation (2.27). The effect is shown in the third row of panels of figure 2.5 assuming $\gamma = 1$, and it is very similar (slightly larger) to the effect of the steeper ($\gamma = 1.5$) density profile shown in the second row. Finally, it has been proposed that the MBH-galaxy relations might be biased high because of selection effects in the targeted galaxy samples. Shankar et al. (2016) propose that the typical MBH mass might be in fact a factor ≈ 3 lower than what is implied by equations (2.28) and (2.29). We therefore explore a model featuring $\gamma = 1$ but with MBH mass decreased by a factor of three for given galaxy properties. Results are shown in the bottom panels of figure 2.5. For a given MBHB mass, this model implies just a minor change in ρ_i and σ, with negligible effects of f_t and t_c, compared to the fiducial model.

2.3.2 GW spectra of fiducial MBHBs

The GW spectrum generated by a MBHB evolving in a fiducial stellar background can now be computed by evaluating dE/df_r in equation (2.2), where the frequency and eccentricity evolution of the pair are now given by equations (2.18) and (2.33), instead of equations (2.5) and (2.6), and the system is defined by the transition frequency f_t as given in equation (2.21) at which e_t must be specified. We consider a fiducial MBHB with $\mathscr{M} = 10^9 \mathrm{M}_\odot$ at $z = 0.02$,and compare the real spectrum including stellar scattering to our approximated formula given by equation (2.15) and appropriately re-scaled as described in section 2.1.1.

Results are shown in figure 2.6 for all the environment models of figure 2.5. In this and the following plots, solid lines are spectra computed via equation (2.15), whereas dashed lines are spectra that includes stellar scattering driving the binary evolution at low frequency. We start by discussing the outcome of our fiducial model with $\gamma = 1$, as a function of e_t, which is shown in the left plot. For circular binaries $f_t \approx 0.2$nHz, well below the minimum PTA frequency $f_{\rm min} = 1$nHz, appropriate for an PTA baseline of 30yrs, achievable within 2030. By increasing e_t, f_t is pushed at lower values, eventually becoming irrelevant. Obviously, the real spectrum diverges from our analytic fit at $f < f_t$. Moreover, for moderately eccentric binaries ($e_t = 0.5$ panel) the two spectra differ significantly up to almost $f = 1$ nHz. This is mostly because the presence of the stellar environment 'freezes' the eccentricity to 0.5 at $f < f_t$; the real spectrum at $f \gtrsim f_t$ is missing the contribution from the very eccentric phase at $f < f_t$ that occurs when the environment is not taken into account and the binary is evolved back in time assuming GW emission only. The problem becomes less severe for larger values of e_t. Even though the presence of the environment freezes the binary eccentricity, e_t is large enough that most of the relevant contribution from the higher harmonics emitted at low frequencies is kept. Most importantly, in all cases, at all $f > f_{\rm min} = 1$nHz, our analytical fit perfectly describes the emitted spectrum. The right plot in figure 2.6 shows the spectrum assuming $e_t = 0.9$ for the four different environment models outlined in the previous subsection. Again, we notice that in all cases the GW spectrum is well described by our fitting formula in the relevant PTA frequency range, and the peak of the

spectrum is only mildly affected (within a factor of two) by the different host models.

2.3.3 Stochastic background from a cosmic MBHB population

Having studied the signal generated by a fiducial system, we turn now to the computation of the overall GW spectrum expected from a cosmological population of MBHBs. To do this, we simply need to specify the distribution $d^2n/dzd\mathscr{M}$. We consider two population models:

- *model-NUM*: the $d^2n/dzd\mathscr{M}$ population is numerically constructed on the basis of a semi-analytic galaxy formation model implemented on the Millennium simulation (Springel et al., 2005), as described in Sesana et al. (2009). In particular, we use a model implementing the $M_{\rm BH} - M_{\rm bulge}$ relation of Marconi and Hunt (2003), with accretion occurring *before* the final MBHB coalescence on both MBHs in the pair.

- *model-AN*: employs a parametrised population function of the form (Middleton et al., 2016)

$$\frac{d^2n}{dzd\log_{10}\mathscr{M}} = \dot{n}_0\Big(\frac{\mathscr{M}}{10^7{\rm M}_\odot}\Big)^{-\alpha} e^{-\mathscr{M}/\mathscr{M}_*}(1+z)^\beta e^{-z/z_*}\frac{dt_r}{dz}, \tag{2.34}$$

  where t_r is time measured in the source reference frame and

$$\frac{dt_r}{dz} = \frac{1}{H_0(1+z)(\Omega_M(1+z)^3+\Omega_k(1+z)^2+\Omega_\Lambda)^{1/2}}. \tag{2.35}$$

  Based on loose cosmological constraints (see Middleton et al. (2016) for details), parameters lie in the range $\dot{n}_0 \in [10^{-20}, 10^3]\,{\rm Mpc}^{-3}{\rm Gyr}^{-1}$, $\alpha \in [-3,3]$, $\mathscr{M}_* \in [10^6, 10^{11}]\,{\rm M}_\odot$, $\beta \in [-2,7]$, $z_* \in [0.2,5]$. $H_0 = 70\,{\rm km\,Mpc}^{-1}{\rm s}^{-1}$ is the Hubble constant and $\Omega_M = 0.3$, $\Omega_k = 0$, $\Omega_\Lambda = 0.7$ are the cosmological energy density ratios. We specialize our calculation to a fiducial mass function with $\log_{10}\dot{n}_0 = -4$, $\alpha = 0$, $\mathscr{M}_* = 10^8{\rm M}_\odot$, $\beta = 2$, $z_* = 2$.

To construct the spectrum we still need to specify a reference eccentricity e_t at a reference binary orbital frequency f_t. Assuming MBHBs evolving in stellar bulges, We take f_t from equation

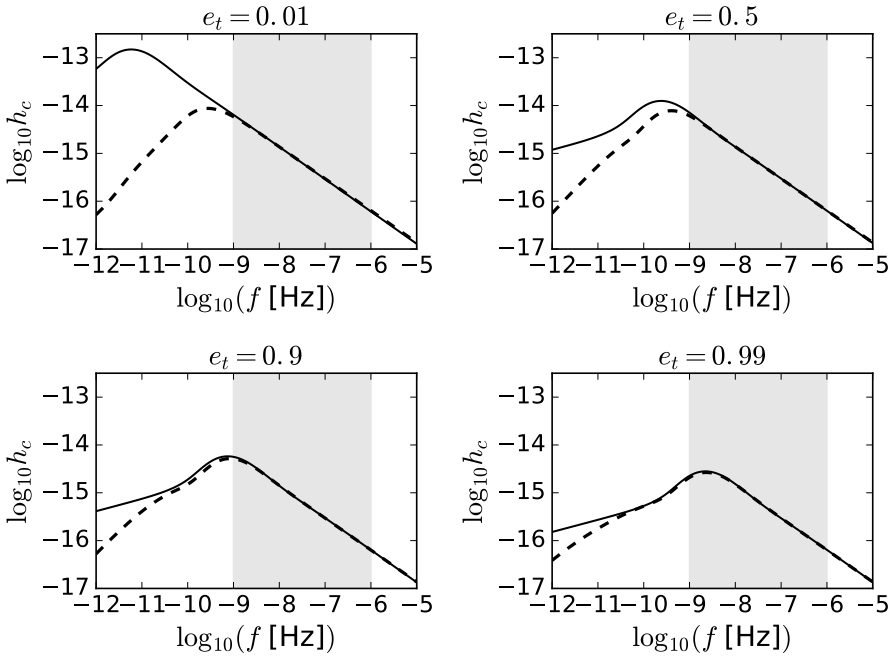

Figure 2.7: Same as the left half of figure 2.6, but the signal has now been integrated over the *model-NUM* MBHB population described in the text.

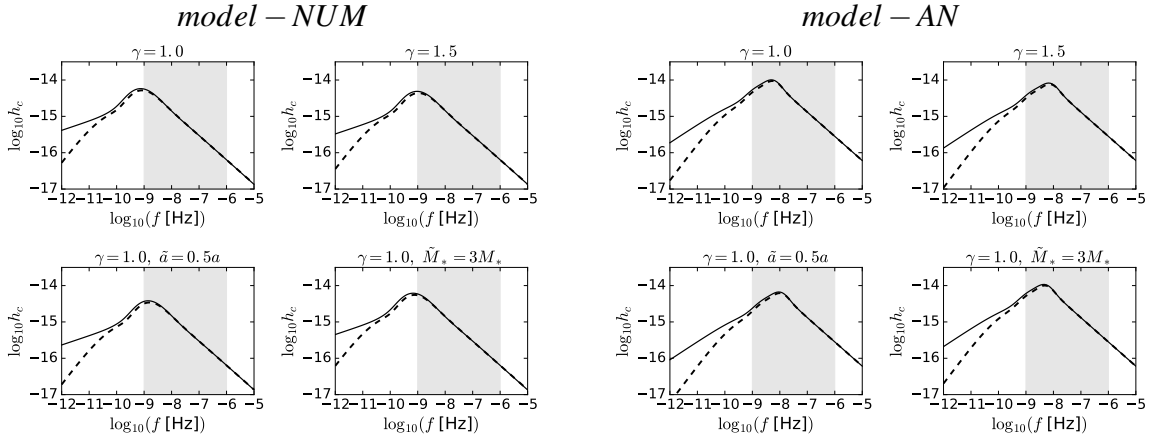

Figure 2.8: Same as the right half of figure 2.6, but the signal has now been integrated over the *model-NUM* (four panels on the left) and *model-AN* (four panels on the right).

(2.21) assuming the four environment models presented in Section 2.3.1. As for e_t we make the simplifying assumption that, regardless of redshift, mass and environment, all MBHBs share the same eccentricity at the transition frequency. We take $e_t = 0.01, 0.5, 0.9, 0.99$.

The simplification that all MBHBs share the same eccentricity at the transition frequency is very drastic. It is more reasonable that there is a distribution of transition eccentricities. To include

that distribution the computation of the GW spectrum changes from equation (2.16) to

$$h_c^2(f) = \int_0^\infty dz \int_0^\infty d\mathscr{M} \int_0^1 de \frac{d^3n}{dz d\mathscr{M} de} h_{c,\rm fit}^2\Big(f\frac{f_{p,0}}{f_{p,t}}\Big)\Big(\frac{f_{p,t}}{f_{p,0}}\Big)^{-4/3}\Big(\frac{\mathscr{M}}{\mathscr{M}_0}\Big)^{5/3}\Big(\frac{1+z}{1+z_0}\Big)^{-1/3}, \tag{2.36}$$

where the 2 dimensional population function $d^2n/dzd\mathscr{M}$ is replaced by a 3 dimensional description $d^3n/dzd\mathscr{M}de$. For the *model-NUM* population each binary needs to be assigned its individual transition eccentricity according to the distribution to produce the numerically simulated eccentric binary population. For the *model-AN* population the eccentricity distribution should also have an analytic expression allowing for the integration of the distribution. To focus on the effects on the GW spectrum of eccentricity, itself, rather than the distribution, we still choose to fix the eccentricty for all binaries in the population.

For each model $h_c(f)$ is computed either via equations (2.1,2.2,2.3,2.18,2.33), i.e., by solving the binary evolution numerically –including the stellar driven phase– and summing-up all the harmonics, or via equation (2.16), i.e., by employing our fitting spectrum for GW driven binaries defined by f_t, e_t.

Results are presented in figures 2.7 and 2.8. Figure 2.7 shows the impact of e_t on the spectrum. We notice that in the true spectrum (the dashed lines), changing the population from almost circular to highly eccentric shifts the peak of the spectrum by more then one order of magnitude. As already described, our model does not represent well the low frequency turnover for small e_t, however in all cases, the GW signal is well described by equation (2.16) in the relevant PTA frequency band ($f > 1\,$nHz), and the factor of ≈ 10 peak shift in the eccentricity range $0.5 < e_t < 0.99$ is fairly well captured. As anticipated, typical turnover frequencies due to three body scattering are at sub-nHz scales, and flattening (and eventually turnover) in the GW spectrum is observable only if MBHBs have relatively high eccentricities at transition frequency. Figure 2.8 shows the impact of changing the physical parameters describing the efficiency of stellar driven MBHB hardening. Those parameters are fixed to a fiducial value in our model, but can in principle have an impact on the spectrum of the signal. When directly compared to 2.7,

the left panel, showing *model-NUM*, clarifies that none of those parameters affect the signal to a level comparable to e_t. The reason is that essentially all of them cause a change in ρ_i, and the f_t dependence on ρ_i is extremely mild ($f_t \propto \rho_i^{3/10}$). For example, shrinking the characteristic galaxy radius a by a factor of two, is equivalent to increasing ρ_i by a factor of eight, which still results in a < 2 shift of f_t. In the right set of panels we see that the same applies to *model-AN*. However, there is a striking difference of almost an order of magnitude in the location of the peak. This is because *model-NUM* and *model-AN* have a very different underlying MBHB mass function. This means that the GWB is dominated by MBHBs with different typical masses, which decouple at different f_t. So even if the underlying MBHB dynamics and eccentricity at transition e_t is the same, the resulting peak frequency can be significantly shifted. It is therefore clear that the location of the GWB spectrum turnover is sensitive to both e_t and to the parameters defining the MBHB cosmological mass function, and much less sensitive to the details of the stellar hardening process. This also means, however, that in absence of additional features in the spectrum, the determination of e_t is highly degenerate with the shape of the MBHB mass function.

2.3.4 Removal of individual sources

Interestingly, as mentioned in the introduction, another feature appearing in the GW spectrum at high frequencies has been pointed out by Sesana et al. (2008), and depends on the shape of the cosmic MBHB mass function. Let us consider circular binaries. In an actual observation, the GW signal generated by a cosmic population of MBHBs at a given observed frequency bin, is given by the sum of all MBHBs emitting at that frequency. This is related to the cosmic density of merging binaries via standard cosmology transformations:

$$\frac{d^2n}{dz d\log_{10}\mathscr{M}} = \frac{d^3N}{dz d\log_{10}\mathscr{M} df}\frac{df}{df_r}\frac{df_r}{dt_r}\frac{dt_r}{dz}\frac{dz}{dV_c} \tag{2.37}$$

where (Hogg, 1999)

$$\frac{dV_c}{dz} = \frac{4\pi c}{H_0} \frac{D_M^2}{(\Omega_M(1+z)^3 + \Omega_k(1+z)^2 + \Omega_\Lambda)^{1/2}}, \tag{2.38}$$

$$D_M = \frac{c}{H_0} \int_0^z \frac{dz'}{(\Omega_M(1+z')^3 + \Omega_k(1+z')^2 + \Omega_\Lambda)^{1/2}}, \tag{2.39}$$

$$\frac{df_r}{dt_r} = \frac{96}{5}(\pi)^{8/3} \frac{G^{5/3}}{c^5} \mathscr{M}^{5/3} f_r^{11/3}, \tag{2.40}$$

$$\frac{df}{df_r} = \frac{1}{1+z}, \tag{2.41}$$

and dt_r/dz is given by equation (2.35). The number of sources emitting in a given observed frequency bin of width $\Delta f = 1/T$ is therefore given by:

$$N_{\Delta f} = \int_{f-\Delta f/2}^{f+\Delta f/2} \int_0^\infty \int_0^\infty \frac{d^3N}{df dz d\log_{10}\mathscr{M}}. \tag{2.42}$$

Each chirp mass and redshift bin contribute to h_c in a measure that is proportional to $\mathscr{M}^{5/6}/(1+z)^{1/6}$ (see, e.g., equation (2.11)). Therefore, it is possible to rank systems in order of decreasing contribution to the GWB. Because of the very small dependence on redshift – $1 < (1+z)^{1/6} < 1.3$ for $0 < z < 5$ considered in our models – we simplify the problem by integrating over z and rank systems based on mass only. It is easy to show that $d^2N/df d\log_{10}\mathscr{M}$ is a strong decreasing function of mass, and is in general $\ll 1$ for the most massive systems when $f > 10$nHz. This means that the contribution to the GWB coming from those massive sources at that frequency, is in fact given by 'less than one source'. Since the actual GW signal is given by a discrete population of sources, having less than a source in a given frequency bin means that in a typical realization of the Universe that source might or might not be there with a given probability. For the practical purpose of the GWB computation, the contribution from those systems at those frequencies is actually not there, at least not in the form of a stochastic GWB (we defer the reader to Sesana et al. (2008) for a rigorous mathematical treatment of this issue).

One can therefore assume that in each bin Δf the most massive sources integrating to 1 in number do not contribute to the GWB. The value $\bar{M}$ corresponding to this condition is implicitly given

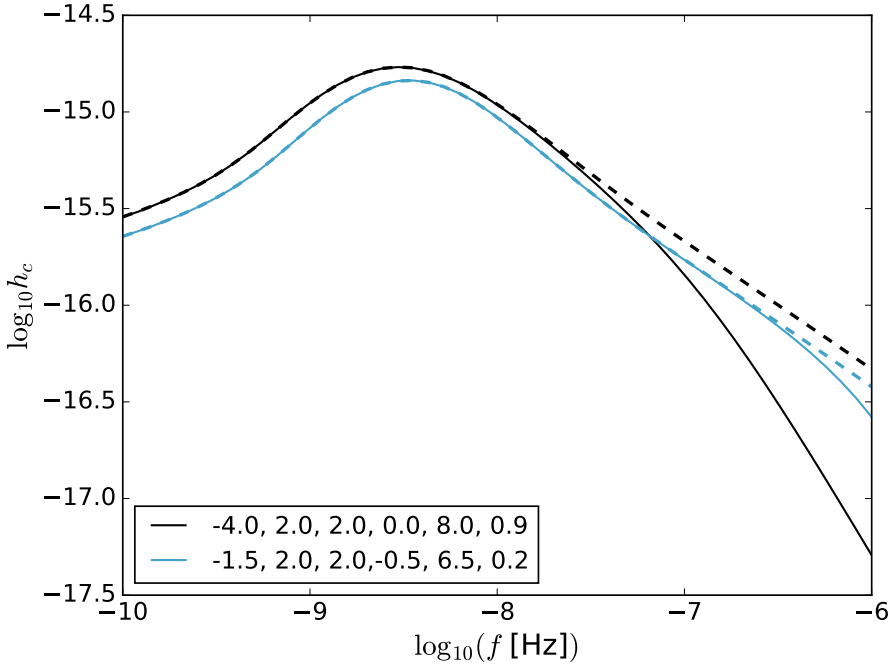

Figure 2.9: Comparison of the spectrum of a population of binaries with different parameters for the *model-AN*. Parameters in the plot are specified in the sequence $\{\log_{10}(\dot{n}_0), \beta, z_*, \alpha, \log_{10}(\mathscr{M}_*), e_t\}$. The solid lines represent the spectrum with the drop in upper mass limit in the high frequency regime, the dashed lines represent the spectrum with no mass limit change.

by imposing

$$
\begin{aligned}
1 = & \int_{\bar{M}}^{\infty} \int_{f-\Delta f/2}^{f+\Delta f/2} \int_0^{z_{\max}} \frac{d^3N}{df\,dz\,d\log_{10}\mathscr{M}} \\
= & \dot{n}_0 \int_{\bar{M}}^{\infty} \left(\frac{\mathscr{M}}{10^7 \mathrm{M}_\odot}\right)^{-\alpha} e^{-\mathscr{M}/\mathscr{M}_*} \mathscr{M}^{-5/3} d\log_{10}\mathscr{M} \\
& \int_0^{\bar{z}} (1+z)^{\beta+1} e^{-z/z_*} \frac{dV_c}{dz} dz \int_{f-\Delta f/2}^{f+\Delta f/2} \frac{dt_r}{df_r} \mathscr{M}^{5/3} df,
\end{aligned}
\tag{2.43}
$$

where in the last equation we substituted the analytical merger rate density given by equation (2.34). Given an observation time T, the frequency spectrum is divided in bins $\Delta f = 1/T$. $h_c(f)$ is therefore calculated at the centroid of each frequency bin by substituting the upper limit $\bar{M}$ defined by equation (2.43) in equation (2.1). Note that in equation (2.43) mass and frequency integrals are analytic, and only the redshift integral has to be evaluated numerically.

Examples of the GW spectrum obtained including the $\bar{M}$ cut-off are shown in figure 2.9 for two different mass functions assuming *model-AN*. Note that the spectrum is significantly reduced only at $f > 10$nHz. This justifies a posteriori our assumption of circular GW driven binaries; at such high frequencies even MBHBs that were very eccentric at f_t had become almost circular because of GW backreaction. The figure illustrates that a detection of both spectral features (low frequency turnover and high frequency steepening) might help breaking degeneracies between e_t and MBHB mass function. The two displayed models have very different e_t (0.2 vs 0.9), but also quite different mass functions, so that the GWB turnover occurs around the same frequency. If the signal can be detected up to $f \approx 10^{-7}$Hz, however, differences in the high frequency slope might help pinning down the MBHB mass function and disentangle it from e_t. In a companion paper (Chen et al., 2017a), we explore the feasibility of this approach and the implication for astrophysical inference.

CHAPTER 3

CONSTRAINING THE POPULATION OF SUPERMASSIVE BLACK HOLE BINARIES

This chapter reproduces verbatim "S. Chen, H. Middleton, A. Sesana, W. Del Pozzo, A. Vecchio, Probing the assembly history and dynamical evolution of massive black hole binaries with pulsar timing arrays, 2017, MNRAS, 468, 404", without the Abstract, Introduction and Conclusions sections, but including the Erratum.

3.1 Astrophysical model

We use the model developed in Chen et al. (2017b) for a population of eccentric MBHBs evolving via three-body scattering against the stellar environment. In Chen et al. (2017b), we expressed the properties of the environment (stellar density, velocity dispersion etc.) as a function of the MBHB total mass only; therefore, the MBHB mass defines the relevant stellar background properties, which we take to be consistent with that typical of elliptical galaxies (where the most massive binaries, dominating the GWB, reside). In a nutshell, the stellar density is modelled with a Dehnen profile (Dehnen, 1993) with total mass set by the intrinsic relation between the MBH and the galaxy bulge masses – usually referred to as $M_{\rm BH} - M_{\rm bulge}$– provided in Kormendy and Ho (2013), scale radius a defined by the empirical $M_{\rm bulge} - a$ relation found by Dabringhausen

et al. (2008)[1], and inner profile slope $\gamma = 1$, appropriate for massive ellipticals. In this model, binaries decouple from the stellar environment at orbital frequencies much lower than the relevant PTA window (which is $f > 1$nHz) and the PTA signal can be constructed taking into account the post-decoupling GW-driven evolution of the eccentric binary only (see Chen et al. (2017b) for a full description of the model). The overall GWB spectrum can therefore be written as:

$$h_c^2(f) = \int dz \int d\mathscr{M} \frac{d^2n}{dz d\mathscr{M}} h_{c,\rm fit}^2 \Big(f \frac{f_{p,0}}{f_{p,t}} \Big) \Big(\frac{f_{p,t}}{f_{p,0}} \Big)^{-4/3} \Big(\frac{\mathscr{M}}{\mathscr{M}_0} \Big)^{5/3} \Big(\frac{1+z}{1+z_0} \Big)^{-1/3} \tag{3.1}$$

where $h_{c,\rm fit}$ is an analytic fit to the spectrum produced by a reference binary at redshift z_0 with chirp mass $\mathscr{M}_0$ and a given eccentricity e_0 at an arbitrary decoupling frequency f_0. These two latter parameters define the peak frequency of the emitted GW spectrum $f_{p,0}$ for this reference binary. Equation (3.1) states that the overall GW spectrum from a given MBHB population can be generated from this reference $h_{c,\rm fit}$ via appropriate power-law scaling of the the chirp mass, redshift, decoupling frequency and eccentricity. Individual contributions must then be integrated over the MBHB mass function $d^2n/dzd\mathscr{M}$; the number of binary mergers per co-moving volume, redshift and (rest-frame) chirp mass interval. The integration limits of equation (3.1) are set to $0 \leq z \leq 5$ and $10^6 \leq \mathscr{M}/\mathrm{M}_\odot \leq 10^{11}$, and following Middleton et al. (2016) we pick

$$\frac{d^2n}{dz d\log_{10}\mathscr{M}} = \dot{n}_0 \left[\left(\frac{\mathscr{M}}{10^7 \mathrm{M}_\odot} \right)^{-\alpha} \exp^{-(\mathscr{M}/\mathscr{M}_*)} \right] \times \left[(1+z)^\beta \exp^{-(z/z_*)} \right] \frac{dt_r}{dz}, \tag{3.2}$$

where t_r is the time in the source rest-frame and dt_r/dz is given by the standard time-redshift cosmological relation (in this work we assume $H_0 = 70 \mathrm{kms}^{-1}\mathrm{Mpc}^{-1}$, $\Omega_M = 0.3$, $\Omega_\Lambda = 0.7$ and $\Omega_k = 0$). The differential merger rate density of equation (3.2) is described by five parameters. $\dot{n}_0$ is the merger rate density normalization. β and z_* describe the redshift evolution of the rate. In particular, β controls the low-redshift power-law slope and z_* the high-redshift cut-off for the distribution; the peak of the merger rate corresponds to a redshift $(z_*\beta - 1)$. α and $\mathscr{M}_*$ are the free parameters of the Schechter function describing the mass distribution. In addition to

[1] We note that this relation connects the scale radius a to the total mass of the system. However, the massive elliptical galaxies that host the dominant PTA GW sources, are bulge dominated so that $M_{\rm bulge}$ can be taken as a fair proxy of the total stellar mass.

those, the computation of the GWB in equation (3.1) requires the specification of the MBHB eccentricity e_t when they decouple from their environment and the evolution is dominated by GW emission[1], giving a total of six model parameters. Decoupling takes place when the condition that stellar scattering and GW emission extract energy from the MBHB at the same rate. This occurs at a frequency f_t, defined by (see Chen et al. (2017b))

$$f_t = 0.356\,\mathrm{nHz}\left(\frac{1}{F(e)}\frac{\rho_{i,100}}{\sigma_{200}}\right)^{3/10}\mathscr{M}_9^{-2/5}, \tag{3.3}$$

where the mass density of the stellar environment is $\rho_{i,100} = \rho_i/(100\,\mathrm{M}_\odot\mathrm{pc}^{-3})$, the velocity dispersion of the stars is the bulge is $\sigma_{200} = \sigma/(200\,\mathrm{km\,s}^{-1})$ and the MBHB total mass is $\mathscr{M}_9 = \mathscr{M}/(10^9\,\mathrm{M}_\odot)$. Expressions for $\rho_{i,100}$ and σ_{200} can be found in Chen et al. (2017b) (equations 28 and 30). Note that ρ_i is a function of the inner slope of the adopted density profile. Here we adopt a Dehnen model with $\gamma = 1$, which results in shallow nuclear stellar density profiles that are typical of massive elliptical galaxies.

The characteristic amplitude described by equation (3.1) is a power-law with a low frequency turnover due to eccentricity and environmental effects. At high frequency, however, because of small number statistics, the actual signal is characterized by sparse resolvable systems outshining the overall GWB. Sesana et al. (2008) showed that the correct estimate of the unresolved GWB level can be recovered by setting an upper limit $\bar{\mathscr{M}}$ to the mass integral given by the condition

$$N_{\Delta f} = \int_{f-\Delta f/2}^{f+\Delta f/2} df \int_{\bar{\mathscr{M}}}^{\infty} d\mathscr{M} \int_0^{\infty} dz \frac{d^3N}{df\,dz\,d\mathscr{M}} = 1, \tag{3.4}$$

where $d^3N/(df\,dz\,d\mathscr{M})$ is the number of individual sources per unit chirp mass, redshift and frequency, which can be directly computed from $d^2n/dz\,d\mathscr{M}$ (see Sesana et al. (2008) for details), and the integral is performed over the frequency bin $\Delta f = 1/T$. The net effect is that the spectrum has a mass function dependent high frequency steepening, that can provide further information

[1] In this pilot study, we make the simplistic assumption that all MBHBs have the same eccentricity at decoupling. In general, MBHBs are expected to have a range of eccentricities when they decouple from their environment. Nonetheless, one can still try to model the population with a single parameter e_t, representing the typical MBHB eccentricity.

about the underlying MBHB population. Note that this is set solely by the MBHB mass function and does not introduce further parameters to the model. Examples of spectra highlighting both the low frequency turnover and the high frequency steepening are shown in Fig. 3.1.

The model was chosen to capture the expected qualitative features of the cosmic MBH merger rate without restricting to any particular merger history; for example, it can reproduce rates extracted from merger tree models (Volonteri et al., 2003; Sesana et al., 2008), and large scale cosmological simulations of structure formation (Springel et al., 2005; Sesana et al., 2009).

3.2 Background detection theory

The S/N ρ imprinted by stochastic GWB in a PTA can be written as (Moore et al., 2015b; Rosado et al., 2015)

$$\rho^2 = 2 \sum_{i=1,N} \sum_{j>i} T_{ij} \int \frac{\Gamma_{ij}^2 S_h^2}{(S_n^2)_{ij}} df. \tag{3.5}$$

We now proceed to define and discuss all the elements appearing in equation (3.5). T_{ij} is the time span over which observations for pulsars i and j overlap. We will make from here on the simplifying assumptions that all pulsars are observed for the same timespan T (typically 10 years or more) and therefore $T_{ij} = T, \forall(i,j)$. However, we should bear in mind that this is generally not the case for real PTAs. The double sum runs over all the possible pairs of pulsars in the array and Γ_{ij} are the Hellings & Downs correlation coefficients (Hellings and Downs, 1983)

$$\Gamma_{ij} = \frac{3}{2}\gamma_{ij}\ln\left(\gamma_{ij}\right) - \frac{1}{4}\gamma_{ij} + \frac{1}{2} + \frac{1}{2}\delta_{ij}, \tag{3.6}$$

where $\gamma_{ij} = [1-\cos(\theta_{ij})]/2$, and θ_{ij} is the relative angle between pulsars i and j. S_h, S_n are the spectral densities of the signal and the noise respectively. The former is connected to the

characteristic amplitude of the signal $h_c(f)$ given in equation (3.1) via:

$$S_h = \frac{h_c^2}{12\pi^2 f^3}, \tag{3.7}$$

where f is the considered frequency. The latter has to be handled with care, especially in the limit of a strong GWB signal. For a pulsar i characterized by random Gaussian irregularities described by a root mean square (rms) value σ_i^2, the power spectral density (PSD) of the noise is given by

$$P_i = 2\sigma_i^2 \Delta t, \tag{3.8}$$

where Δt is the interval between subsequent observations (typically a week to a month, in current PTAs). If red processes were not present in the data, one might then expect a PSD of the noise equal to P_i in the whole sensitivity window down to $1/T$. However, fitting for the spin first and second derivatives when constructing the pulsar timing model subtracts a quadratic function to the timing residual, effectively absorbing power at the lowest frequency bins, should a red signal be present.

To mimic the effect of the timing model we empirically write

$$P_i = 2\sigma_i^2 \Delta t + \frac{\delta}{f^5}, \tag{3.9}$$

where δ is a constant that depends on the parameters of the observations. We find that a good fit to the low frequency behaviour of the published EPTA, NANOGrav and PPTA sensitivity curves is provided by setting

$$\delta = 5 \times 10^{-49} \left(\frac{10\text{yr}}{T}\right)^5 \left(\frac{\sigma_i}{100\text{ns}}\right)^2 \frac{\Delta t}{2\text{weeks}}. \tag{3.10}$$

The scaling in equation (3.9) ensures that the curve maintains the same shape when varying the array parameters, reproducing the power absorption at the two lowest frequency bins (see Fig. 3.1). Moreover the PSD of the noise S_n is not only given by limitations in the pulsar stability,

quadratic spindown fitting, and other sources of noise. The very same signal S_h contributes an equal amount to the noise as to the signal itself, because half of the GWB (the pulsar term) is uncorrelated. However, the smoking-gun of a GWB is provided by its distinctive quadrupole correlation described by the Γ_{ij} coefficients. Therefore only the correlated part of the signal (i.e. the Earth term) contributes to the construction of the detection statistic and to the build-up of the S/N. The pulsar term will just produce an uncorrelated common red noise in all pulsars with PSD S_h. Therefore the power spectral density of the noise has to be written as (Rosado et al., 2015):

$$S_{n,ij}^2 = P_i P_j + S_h[P_i + P_j] + S_h^2(1+\Gamma_{ij}^2). \tag{3.11}$$

Note that equation (3.11) reduces to $S_{n,ij}^2 = P_i P_j$ in the weak signal limit. Note, moreover, that this implies that it does not matter how strong the signal is, the integrand of equation (3.5) is at most of the order $\Gamma_{ij}^2 \ll 1$. This means that *only* with a large number N of pulsars is it possible to produce a confident detection of a GWB with an high ρ. This is easy to see if we make the simplifying assumptions that T, Δt and σ_i are the same for all pulsars. Moreover, we shall assume a sufficiently high number of randomly distributed pulsars in the sky, therefore substituting the individual Γ_{ij} with their average value $\Gamma = 1/(4\sqrt{3})$. Equation (3.5) can then be written as

$$\rho^2 = 2T\Gamma^2 \int \frac{S_h^2}{S_n^2} \sum_{i=1,N} \sum_{j>i} df, \tag{3.12}$$

which reduces to

$$\rho^2 = T\Gamma^2 N(N-1) \int \frac{S_h^2}{S_n^2} df. \tag{3.13}$$

In an actual observation, the GWB is resolved in bins $\Delta f = 1/T$. We can therefore divide the frequency domain in intervals $\Delta f_i = [i/T, (i+1)/T]$ centred at $f_i = (2i+1)/(2T)$ and compute the S/N in each individual frequency bin as

$$\rho_i^2 = T\Gamma^2 N(N-1) \int_{\Delta f_i} \frac{S_h^2}{S_n^2} df \approx \Gamma^2 N(N-1) \frac{S_h^2}{S_n^2}. \tag{3.14}$$

The total S/N of the observation is then simply obtain by summing in quadrature over the

frequency bins

$$\rho = \left(\sum_i \rho_i^2 \right)^{1/2}. \tag{3.15}$$

Note that in the limit of $S_h \gg P$ in a given frequency bin, equation (3.14) reduces to

$$\rho_i^2 = \frac{\Gamma^2}{1+\Gamma^2} N(N-1). \tag{3.16}$$

Therefore, in the presence of a strong signal in M frequency bins, one gets an approximate S/N

$$\rho = \left(\frac{\Gamma^2}{1+\Gamma^2} MN(N-1) \right)^{1/2} \approx \Gamma N M^{1/2}. \tag{3.17}$$

Where we used the fact that $\Gamma \ll 1$ and $N \gg 1$. Equation (3.17) was obtained through a number of drastic simplifications, nonetheless it gives a sense of the maximum S/N one can obtain assuming a strong signal in an ideal array. Since $\Gamma \approx 0.14$, a total S/N≈ 5 in the lowest few frequency bins can only be achieved with approximately $N = 20$ equally good pulsars.

3.3 Simulating observations

Once ρ_i has been computed at each frequency bin, we can then use the general fact that, if h is a signal described by an amplitude A, then $\rho = (h|h)^{1/2}$ and $\sigma_A^{-1} = (\frac{\partial h}{\partial A}|\frac{\partial h}{\partial A})^{1/2} = (\frac{h}{A}|\frac{h}{A})^{1/2}$. Therefore

$$\frac{\sigma_A}{A} = \sigma_{\ln A} = \frac{1}{\rho}. \tag{3.18}$$

To simulate observations, we therefore compute the S/N ρ_i at each frequency bin. If $\rho_i > 1$, we use the strong S/N regime approximation, ie. $S_h \gg P$ and equation (3.16), and have a detection in this frequency bin. We then assume an observed signal with amplitude $A_i = h_c(f_i)$ and error described by a log-normal distribution with width given by equation (3.18). Note that, by doing this we are ignoring any stochastic fluctuation in the measured amplitude of the signal. In reality, the error on the observation will be generally centred at $A_i \neq h_c(f_i)$, with a scatter of the order of

the error on the measurement. We make this choice because our main aim is to investigate to what level the MBHB population model can be constrained *in principle*, independent of statistical variations inherent to the observations. If $\rho_i < 1$, we are in the weak S/N regime, then we assume no signal is detected in the frequency bin, and only an upper limit can be placed. To define what the upper limit is, we notice that, by means of equation (3.7), equation (3.14) can be written as a ratio of the characteristic signal and an equivalent characteristic noise, i.e.,

$$\rho_i = \frac{h_c^2}{h_n^2} \tag{3.19}$$

where,

$$h_n = [N(N-1)]^{-1/4} \left(12\pi^2 f^3 \frac{S_n}{\Gamma} \right)^{1/2}. \tag{3.20}$$

Therefore, when $\rho_i < 1$ we place a 68% (1σ) upper limit at $h_{n,i}$, calculated at the central frequency f_i of the bin.

Examples of signal generation are shown in Fig. 3.1 for spectra with $A = 10^{-15}$ at $f = 1\text{yr}^{-1}$ and an array with $N = 20$, $\sigma = 100$ns, $T = 15$yr, $\Delta t = 1$ week. This setup results in a detection with moderate S/N, $\rho \approx 5$, and with $\rho_i \approx 2$ in the few lowest frequency bins. The equivalent h_n of equation (3.20) is depicted as a black solid line. Note, however that for clarity of representation, we ignored here the contribution of S_h to the noise (when that is taken into account, $h_n = h_c$ whenever $\rho_i > 1$). Note also that, despite the large h_c difference of the two signals, the difference in S/N between them is only about 20%. This is because, as stressed above, in the strong signal limit the S/N of the signal is limited by the GWB uncorrelated self-noise.

3.3.1 Simulation setup

To setup a specific simulation, one has to define both the properties of the GWB (i.e. the six parameters $\dot{n}_0, \beta, z_*, \alpha, \mathscr{M}_*, e_t$ defining the MBHB population) and of the PTA employed for detection (i.e. the four parameters $N, \sigma, T, \Delta t$ defining the sensitivity of the array).

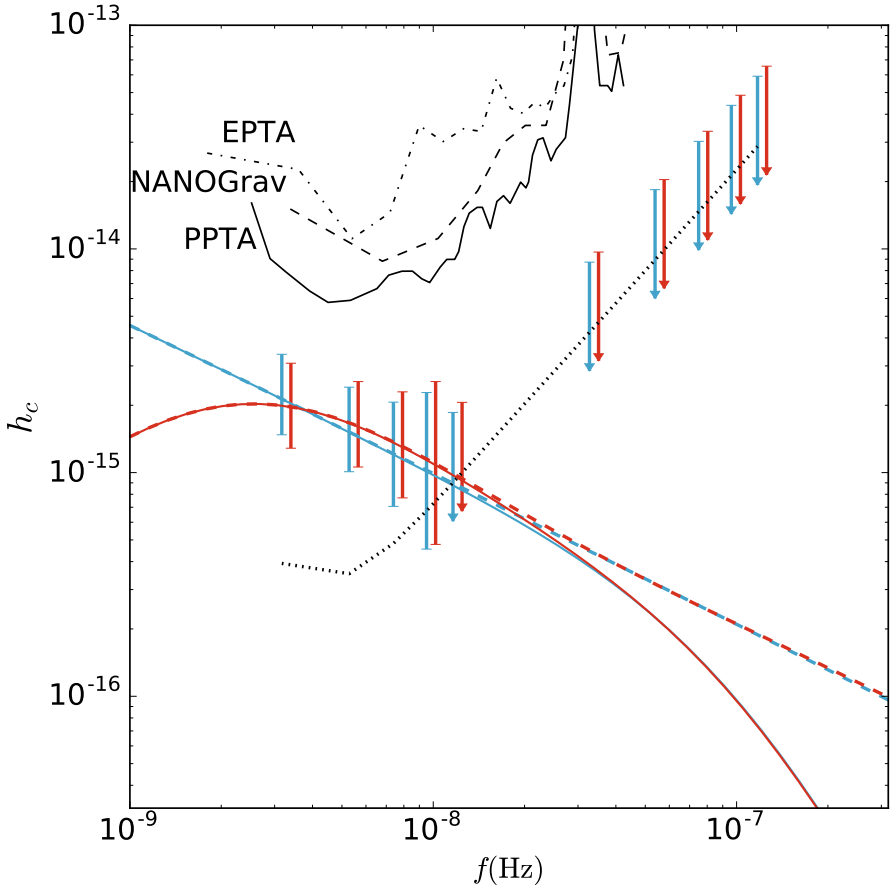

Figure 3.1: Examples of simulated detections for two different spectral shapes. Signal models correspond to the default MBHB population with parameters defined in Section 3.3.1 and high eccentricity ($e_t = 0.9$, red) and almost circular ($e_t = 0.01$), blue). For each model, solid lines are the theoretical spectra including the high frequency steepening due to the mass upper limit defined by equation (3.4), dashed lines depict spectra excluding this feature (therefore with $h_c \propto f^{-2/3}$ at high frequency) for comparison. Error bars centred around the model value are the observed amplitudes with associated uncertainties when $\rho_i > 1$, and downward arrows represent upper limits equal to $2h_n$ (i.e. 2σ) when $\rho_i < 1$ at their base. The black dotted line is the characteristic noise level h_n *excluding* the contribution of the GW signal to the noise budget. Black lines in the upper part of the figure are current EPTA, NANOGrav and PPTA limits. We assume 15 years of observation of 20 pulsars at 100ns rms.

Unless otherwise stated, we use a MBHB mass function defined by $\dot{n}_0 = 10^{-4}\mathrm{Mpc}^{-3}\mathrm{Gyr}^{-1}, \beta = 2, z_* = 2, \alpha = 0, \mathscr{M}_* = 10^8 \mathrm{M}_\odot$. The normalization $\dot{n}_0$ and the redshift dependence β are chosen to be consistent with current estimates of the galaxy merger rate (Lin et al., 2004; de Ravel et al., 2009; Lotz et al., 2011). α and $\mathscr{M}_*$ are chosen to ensure that the shape of the MBHB mass function is consistent with that of nuclear MBHs as inferred from direct measurements and MBH-galaxy scaling relations (e.g. Shankar et al. (2004); Hopkins et al. (2007)). The

adopted parameters result in a GWB with characteristic strain at $f = 1\text{yr}^{-1}$ of $A \approx 5 \times 10^{-16}$, fully consistent with current upper limits. We explore different eccentricities at decoupling and we report results for the illustrative cases of quasi circular and highly eccentric binaries, defined by $e_t = 0.01$ and $e_t = 0.9$ respectively.

We make the simplifying assumption that all pulsars are observed for the same timespan T, with the same cadence Δt and have the same rms σ. Note that our main results are nevertheless general, since these assumptions only affect the computation of the S/N and do not enter in the subsequent analysis of the GWB spectral shape. We consider four different array scenarios:

1. case *PPTA15*: in this case we simply use the curve provided by Shannon et al. (2015), which is representative of current PTA capabilities and results in an upper limit of $A = 10^{-15}$.

2. case *IPTA30*: $N = 20$, $\sigma = 100$ns, $T = 30$yr, $\Delta t = 1$ week. This PTA results in a detection S/N≈ 5 and is based on a future extrapolation of the current IPTA, without the addition of new telescopes.

3. case *SKA20*: $N = 100$, $\sigma = 50$ns, $T = 20$yr, $\Delta t = 1$ week. This PTA results in a high significance detection with S/N$\approx 30-40$, which will be technically possible in the SKA era.

4. case *ideal*: $N = 500$, $\sigma < 1$ns, $T = 30$yr, $\Delta t = 1$ week. This is likely beyond SKA capabilities but provides useful insights of what might be achievable in principle.

As stated above, for each simulations we compute the the S/N ρ_i at each frequency bin. If $\rho_i > 1$, we then assume an observed signal with amplitude $A_i = h_c(f_i)$ and error described by a log-normal distribution with width given by equation (3.18). If $\rho_i < 1$ then we place an upper limit at h_n as defined by equation (3.20).

3.4 Data analysis method

As in Middleton et al. (2016), our aim is to constrain the astrophysical population of merging MBHB given some PTA data. The data consists of an array of measurements and upper limits on the GW spectrum at different frequency bins, as described in the previous section. In Middleton et al. (2016), we assumed circular binaries and an $f^{-2/3}$ power law for the spectrum, meaning that all the information from the background could be summarised with two numbers, an upper limit or detection with some confidence at a given frequency, which we chose to be one over one year. In this paper, we allow for eccentric binaries evolving via scattering of background stars and a finite number of sources at high frequencies, both of which result in a spectrum that is different from the $f^{-2/3}$ power law. Therefore, the shape of the spectrum over the frequency band encodes much more information. In this section, we describe our strategy to infer the astrophysical properties of the merging MBHB population from PTA measurements.

We denote our astrophysical model (section 3.1) as M and our data (section 3.3.1) as d. Our intention is to infer the model parameters θ, given a specific measurement. We start from Bayes theorem,

$$p(\theta|d,M) = \frac{p(\theta|M)p(d|\theta,M)}{p(d|M)}, \tag{3.21}$$

where $p(\theta|d,M)$ is the posterior distribution for the model parameters given the data and the model, $p(\theta|M)$ is the prior, representing any initial knowledge we have on the parameters given the specific model, $p(d|\theta,M)$ is the likelihood for the data given the model and some values of the parameters and finally $p(d|M)$ is the evidence.

As described in section 3.1, our model has six parameters $\theta = \dot{n}_0, \beta, z_*, \alpha, \mathscr{M}_*, e_t$. Unless otherwise stated, for our analysis we choose priors as follows: the parameters β, z_*, α, $\log_{10}\mathscr{M}_*$ and e_t are all uniformly distributed in the ranges $\beta \in [-2,7]$, $z_* \in [0.2,5]$, $\alpha \in [-3,3]$, $\log_{10}\mathscr{M}_*/\mathrm{M}_\odot \in [6,11]$, and $e_t \in [10^{-6}, 0.999]$. The prior for the merger rate parameter, $\dot{n}_0$ is log-uniform for $\dot{n}_0 \in [10^{-20}, 10^3]$ and uniform in $\dot{n}_0$ for $\dot{n}_0 < 0$, thus allowing for the possibility of no mergers. We note that although specific combinations of parameters can mimic MBHB

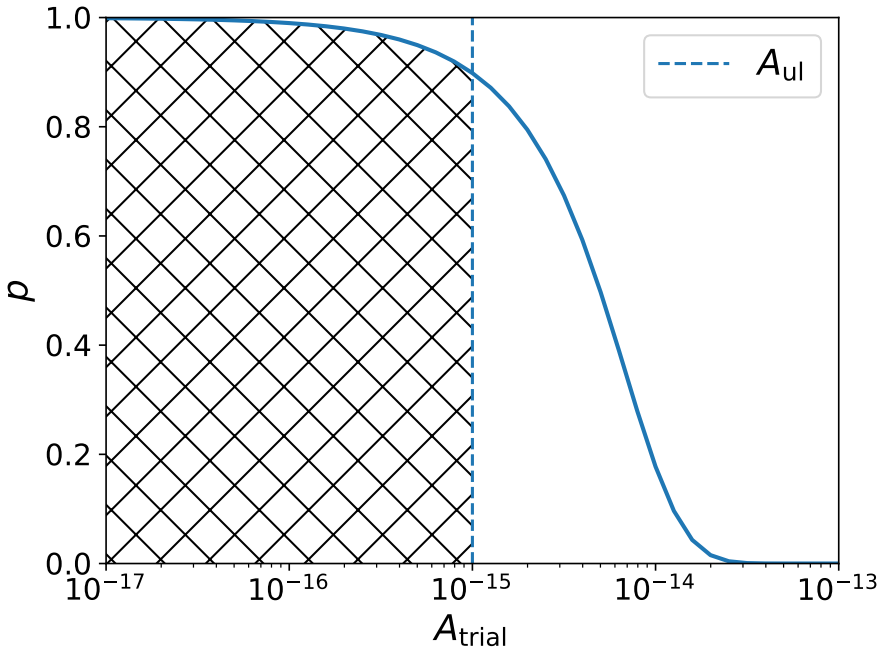

Figure 3.2: Example Fermi-distribution upper limit likelihood function, renormalised such that the 68% PTA upper limit is at $A_{\rm ul} = 1 \times 10^{-15}$. Each value of $A_{\rm trial}$ is accepted with a probability p, such that 68% (hatched area) of the samples are below the upper limit $A_{\rm ul}$.

merger rates extracted from semi-analytic merger tree models (Sesana et al., 2008), cosmological simulations of galaxy formation (Sesana et al., 2009; Kelley et al., 2017a) and observations of galaxy pairs (Sesana, 2013b), the adopted prior range is highly uninformative and allows for exotic MBHBs mass functions that are not necessarily related to galaxy mergers. For example, the upper limit in $\dot{n}_0$ is solely dictated by the constraint that all the dark matter in the Universe is formed by merging MBHs.

The functional form of the likelihood function we adopt depends upon the type of data in each frequency bin. For a given spectrum, there are two possible observational outcomes in a specific frequency bin f; either a GWB detection at $A_{\rm det}(f)$, or a non-detection, resulting in an upper limit based on the PTA sensitivity at that frequency $A_{\rm ul}(f)$. In the case of an upper limit $A_{\rm ul}(f)$ on the GWB, we model the likelihood as a smooth step-like distribution which allows $A_{\rm trial}(f) \ll A_{\rm ul}(f)$ and tails off to 0 for $A_{\rm trial}(f) \gg A_{\rm ul}(f)$. For that we use a Fermi-like distribution,

$$p_{\rm ul}(d|A_{\rm trial}(f)) \propto \left\{ \exp\left[\frac{A_{\rm trial}(f) - A_{\rm ul}(f)}{\sigma_{\rm ul}(f)} \right] + 1 \right\}^{-1}, \tag{3.22}$$

where $A_{\rm trial}(f)$ is the GWB given by our model for a set of parameters drawn from the prior and $\sigma_{ul}(f)$ controls the width and steepness of the distribution as it transits at the step $A_{\rm ul}(f)$ from some constant value for $A_{\rm trial}(f) \ll A_{\rm ul}(f)$ to 0 at $A_{\rm trial}(f) \gg A_{\rm ul}(f)$. $\sigma_{ul}(f)$ can be adjusted so that, for example $p(A_{\rm trial}(f) < A_{\rm ul}(f)) = 68\%$. In our simulations, $A_{\rm ul}(f) = h_n$ as described in section 3.3. We are therefore using the sensitivity of the PTA as a proxy for the 68% (or *1-sigma*) upper limit when the signal is not detected. Figure 3.2 shows an example of the likelihood function renormalized such that the 68% PTA upper limit is at $A_{\rm ul}(f) = 1 \times 10^{-15}$.

In the case of a GWB detection of a central amplitude $A_{\rm det}(f)$ with a Gaussian distribution width of $\sigma_{\rm det}(f)$, we apply a Gaussian in the logarithm for the likelihood,

$$p_{\rm det}\left(d|A_{\rm trial}(f)\right) \propto \exp\left\{-\frac{\left[\log_{10}A_{\rm trial}(f) - \log_{10}A_{\rm det}(f)\right]^2}{2\sigma_{\rm det}(f)^2}\right\}, \tag{3.23}$$

where $\sigma_{\rm det}(f)$ is the error on the detection measurement as described in section 3.3 and $A_{\rm trial}(f)$ is again the value of the GWB given by parameters sampled by the prior. As the dataset d consists of a collection of GWB measurements across the frequency spectrum, we need to combine the likelihood of all the frequency bins in our data. We assume statistical independence among the various frequency bins and thus compute the overall likelihood by multiplication of the likelihoods (either an upper limit or a detection) from each bin. Note that, when we combine bins with detections to bins with upper limits, we consider the lowest frequency upper limit and five further points spaced by ten bins. This is because bins become much denser at high frequency and considering all the upper limits slows done the likelihood computation substantially. We checked that this does not affect our results, since the only constraining upper limit is always the one at the lowest frequency.

We explore the parameter space by means of a Nested Sampling algorithm (Skilling, 2004). We use a tailored version of the parallel implementation of Nested Sampling given in Del Pozzo and Veitch (2015) which is similar in spirit to Veitch and Vecchio (2010) and Veitch et al. (2015). For all the analysis presented in this work we set the number of live points to be $N \sim 2{,}000$ owing an

average number of posterior samples $\sim$ 5,000.

3.5 Results and discussion

In this section we present and discuss in detail the results of our simulations. We will start with the interpretation of upper limits and then move to the case of detections with small and large S/N. We stress that, unless otherwise stated, astrophysical interpretation is constructed uniquely on the basis of PTA observations, i.e. we do not use any additional constraints on the MBHB population (besides the wide, non-informative prior range of the model parameters). PTA inference can prove significantly more constraining if combined with independent information. For example one can assume a narrow prior on the MBHB merger rate and mass function based on simulations or observations of merging galaxies (e.g. Sesana (2013b)). However, we caution that such information is often *indirect* and requires theoretical modelling subject to several assumptions.

3.5.1 Upper limits

We first consider the case of an upper limit and we take as example the most stringent constraint imposed by the PPTA of $A < 10^{-15}$ at $f = 1\text{yr}^{-1}$. Although PTAs often quote limits at $f = 1\text{yr}^{-1}$, those are the result of the integrated array sensitivity across the relevant frequency band. This is shown in the upper-left panel of Fig. 3.3; according to the analysis framework developed in section 3.1, we assume at each frequency bin a 95% upper-limit given by the dashed curve and run our analysis. Consistent with Middleton et al. (2016), the results shown in Fig. 3.3 indicate that current PTA upper limits alone return little astrophysical information, and only loose upper bounds can be placed on the MBHB mass function (upper-right panel) and redshift (lower-left panel) distribution. Those are defined by integrating equation (3.2) in the redshift

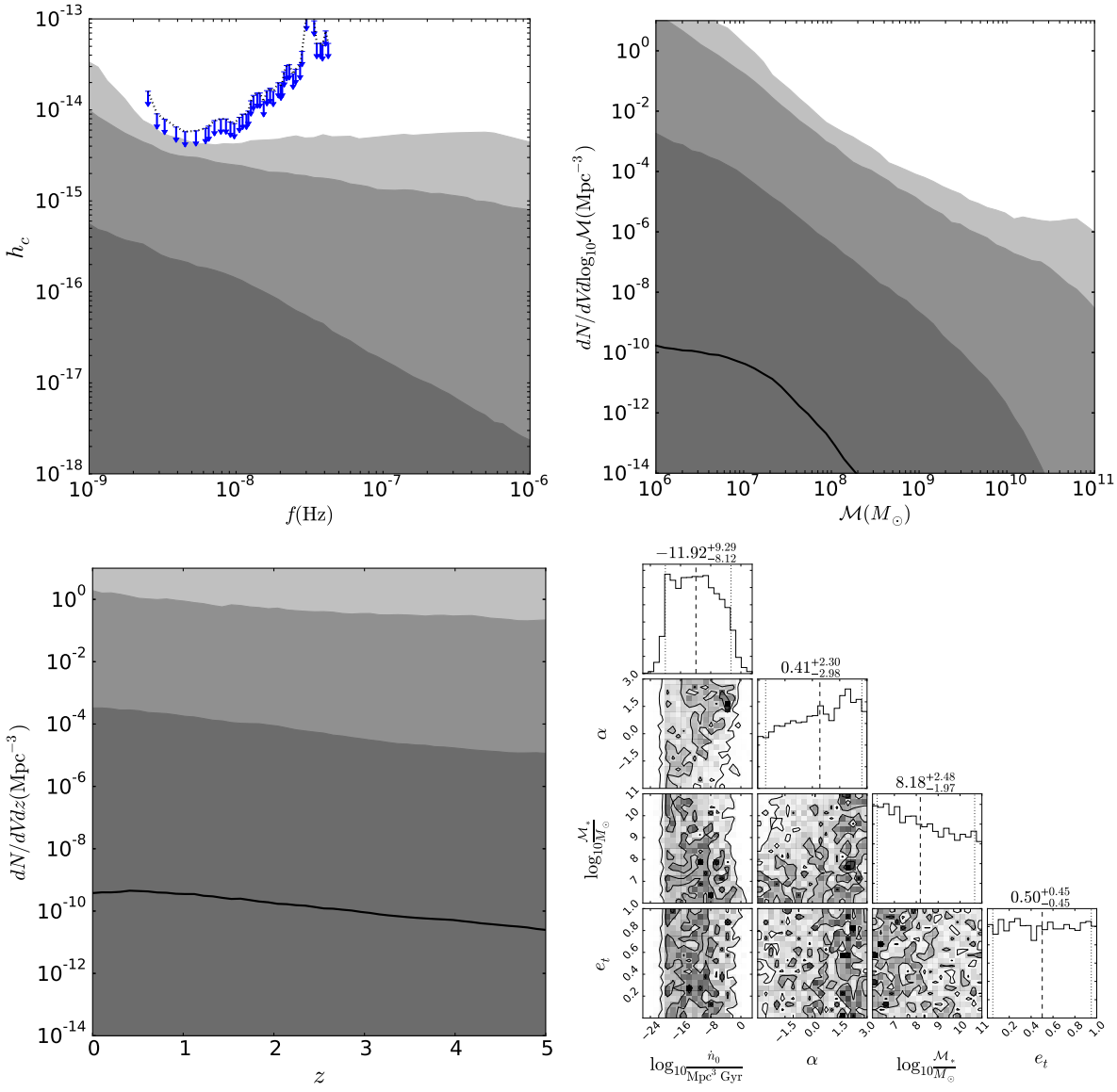

Figure 3.3: Implication of a 95% upper-limit of $A(f = 1\mathrm{yr}^{-1}) = 1 \times 10^{-15}$, which corresponds to the most stringent PTA upper limit to date. The posterior for the spectrum (top left), mass (top right) and redshift functions (bottom left) are shown as shaded areas, with the 68%, 95% and 99.7% confidence regions indicated by progressively lighter shades of grey, and the solid black line marking the median of the posterior. The dotted line with downwards pointing arrows in the top left panel is the 95% upper limit from Shannon et al. (2015). The bottom right triangular plot shows the two-dimensional posteriors for each model parameter pairs, together with their one dimensional marginalised distributions. The lines in each one dimensional distribution mark the median (dashed) and the central 90% (dotted) of the posterior, with the numerical values indicated above each plot.

range [0,5] and in the mass range $[10^6 M_\odot, 10^{11} M_\odot]$, respectively. The triangle plot in the lower-left panel shows that the posterior distributions of the model parameters are essentially flat (β and z_* are not shown, as they are always flat due to strong degeneracy with $\dot{n}_0$), with the exception of $\dot{n}_0$, which is found to be $< 2.5 \times 10^{-3} \mathrm{Mpc}^{-3} \mathrm{Gyr}^{-1}$ at the 95% level. This constraint becomes interesting when compared to independent information on galaxy merger rates. Several observational studies place the merger rate density of massive galaxies at $z < 1$ to be around few$\times 10^{-4} \mathrm{Mpc}^{-3} \mathrm{Gyr}^{-1}$ (Lin et al., 2004; Lotz et al., 2011; Xu et al., 2012). In fact, this is in essence the reason why some tension between PTA upper limits and vanilla MBHB assembly models was highlighted by Shannon et al. (2015). We will return in more depth on this point in a companion paper (Middleton et al. in preparation). A tighter upper limit, constraining $\dot{n}_0$ to be less than $10^{-5} \mathrm{Mpc}^{-3} \mathrm{Gyr}^{-1}$ might rule out a naive one-to-one correspondence between galaxy and MBHB mergers, indicating that delays, stalling or high MBHB eccentricities play a major role in the dynamics.

3.5.2 PTA detection constraints on model parameters

We turn now to the implication of a future PTA detection. We discuss two distinct MBHB populations corresponding to our default mass function model (with parameters given in section 3.3.1) and defined by decoupling eccentricity $e_t = 0.01$ (circular case) and $e_t = 0.9$ (eccentric case).

Circular case

Results for the circular case are shown in Fig. 3.4 to which we refer in the following discussion. In the *IPTA30* scenario (left column), the signal is detected in the lowest eight frequency bins, with total S/N≈ 6. At $f < 10$ nHz the spectrum is well constrained (upper panel), and the reconstructed MBHB mass function and redshift distribution (central panels) are consistent with

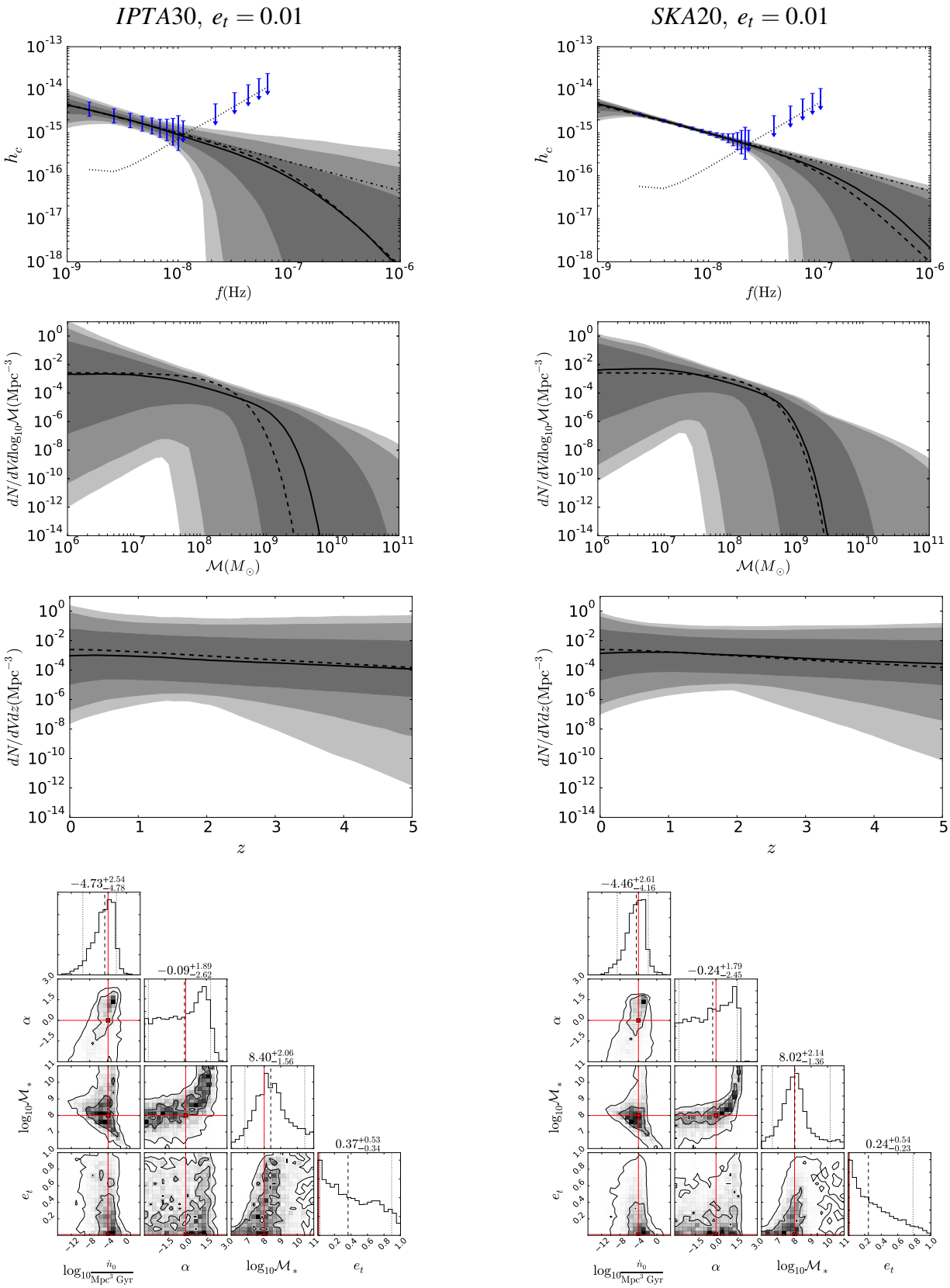
IPTA30, $e_t = 0.01$
SKA20, $e_t = 0.01$
h_c
f(Hz)
$dN/dVd\log_{10}\mathcal{M}(\mathrm{Mpc}^{-3})$
$\mathcal{M}(M_\odot)$
$dN/dVdz(\mathrm{Mpc}^{-3})$
z
$-4.73^{+2.54}_{-4.78}$
$-0.09^{+1.89}_{-2.62}$
$8.40^{+2.06}_{-1.56}$
$0.37^{+0.53}_{-0.34}$
$-4.46^{+2.61}_{-4.16}$
$-0.24^{+1.79}_{-2.45}$
$8.02^{+2.14}_{-1.36}$
$0.24^{+0.54}_{-0.23}$
$\log_{10}\frac{\dot{n}_0}{\mathrm{Mpc}^3\ \mathrm{Gyr}}$
α
$\log_{10}\mathcal{M}_*$
e_t

Figure 3.4

Figure 3.4: Implication of a PTA detection at a moderate (S/N≈5, left column) and high (S/N≈35, right column) significance, assuming a MBHB population with default mass function parameters and almost circular ($e_t = 0.01$) eccentricity at decoupling. As in Fig. 3.3, the posterior for the spectrum, mass and redshift functions (in descending order from the top) are shown as shaded areas, with the 68%, 95% and 99.7% confidence regions indicated by progressively lighter shades of grey, and the solid black line marking the median of the posterior. In each of those panels, the dashed black line indicates the injected model. In the top panels the vertical blue bands indicate the 68% confidence interval of the observed signal amplitude at each frequency bin, and the downward pointing arrows at higher frequency mark the 95% upper limits. The dotted line is the nominal 1σ sensitivity of the considered PTA, as defined by equation 3.20, where the contribution of S_h to the noise has been omitted (see section 3.3 for details). The dot-dash black line shows the simulated spectrum assuming no drop in high mass sources. The lower triangular plots show the two-dimensional posteriors for each model parameter pairs, together with their marginalised distributions. The injected parameter values are marked by red solid lines and the black lines in each one dimensional distribution mark the median (dashed) and the central 90% (dotted) of the posterior, along with the numerical values above each plot.

the injected values. Note, however, that astrophysical constraints are quite poor; even around $\mathscr{M} = 3 \times 10^8 \mathrm{M}_\odot$, where the mass function is best constrained, the 68% confidence interval spans about two order of magnitude, and so does the high mass cut-off. The triangle plot in the lower panel provides more insight into the reconstruction of the model parameters. In general, the posteriors of all the parameters are consistent with the injected values, however the distributions are fairly broad and the contour plots unveil several correlations among model parameters, the most important of which will be investigated later on.

The situation quantitatively improves, but is qualitatively unaltered, in the *SKA20* scenario, shown in the right column. Here the signal is detected in 13 frequency bins, with a total S/N≈ 35. The h_c spectrum is extremely well reconstructed up to 20nHz and the median of the recovered mass and redshift functions match the injected ones almost exactly (central panel); uncertainties are still large though, and the posterior distributions of the model parameters improve only marginally. The characteristic mass scale $\mathscr{M}_*$ is slightly better constrained and, compared to the *IPTA30* case, there is a stronger preference for circular binaries, although higher eccentricity cannot be ruled out.

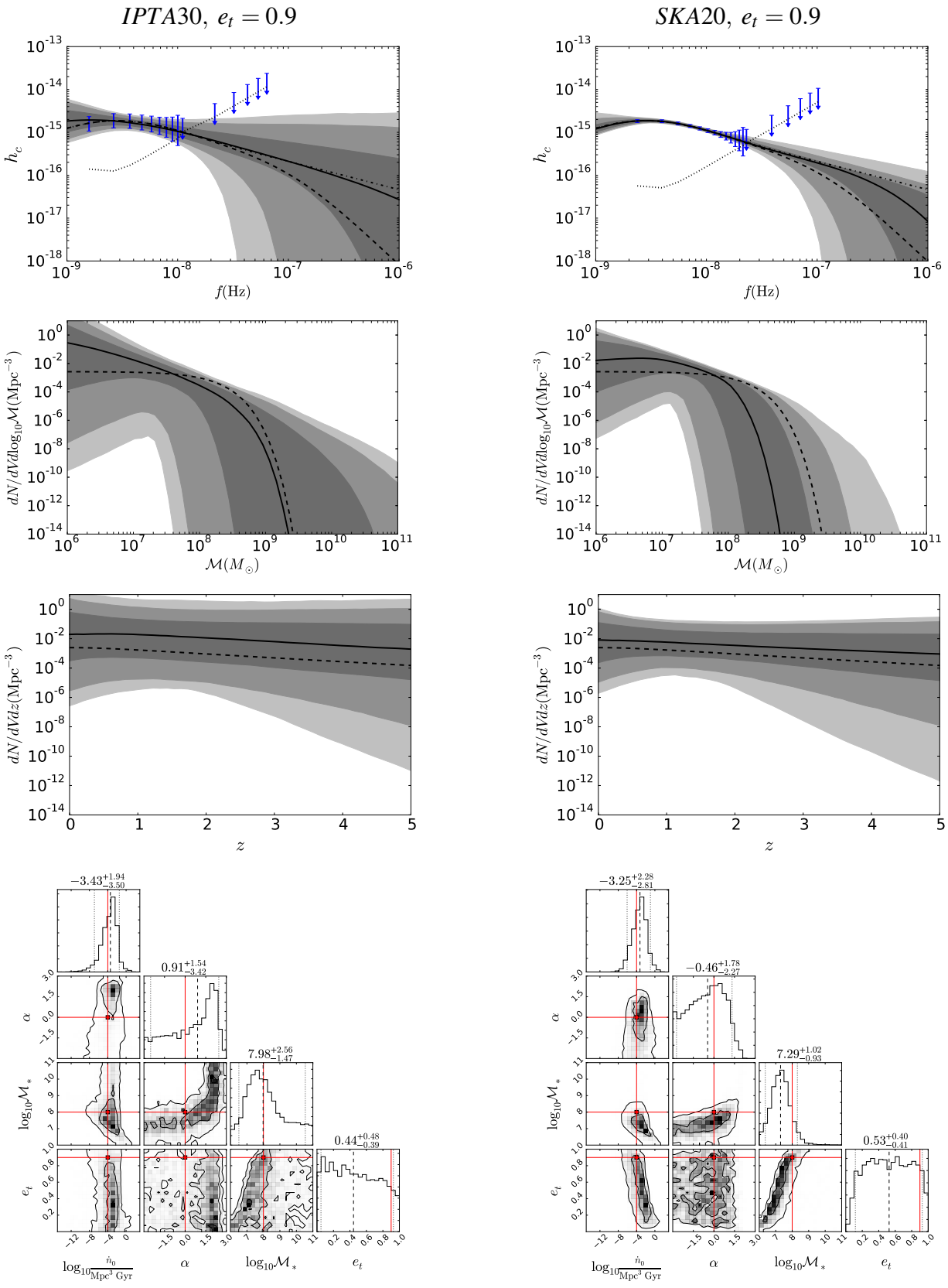

Figure 3.5: Same as figure 3.4 but assuming decoupling eccentricity of $e_t = 0.9$.

Eccentric case: parameter degeneracies

The eccentric case is shown in Fig. 3.5. Again, in the *IPTA30* scenario (left column panels) the signal is detected in the nine lowest frequency bins, with total S/N$\approx$ 5. The recovered GW spectrum is consistent with the injected one, but errors are large and the shape can be hardly determined. The triangle plot in the lower-left panel shows that it is difficult to recover model parameters. Posteriors are consistent with injected values, but the distributions are hardly informative.

Moving to the *SKA20* case (right column panels), we see a clear improvement on the reconstruction of the spectrum (upper panel), but the preferred mass function appears quite offset with respect to the original injection (second panel from the top). Posterior distributions in the triangle plot (lower panel) are now more informative and reveal more defined degeneracies. Particularly interesting is the $\int$-shaped posterior in the $e_t - \mathscr{M}_*$ panel (already visible in the *IPTA30* case). The degeneracy stems from the mass dependence of the decoupling frequency in equation (3.3), i.e. from the fact that more massive MBHBs decouple at lower frequencies than lighter ones. In fact, for a given eccentric MBHB, the peak of the GW spectrum occurs at a frequency $f_p = \mathscr{F}(e_t) f_d$ (see equation 13 in Chen et al. (2017b)), where $\mathscr{F}(e_t)$ is a monotonically increasing function of e_t. This means that, if we observe a turnover in the GWB at a given $\bar{f}$, there is an ambiguity in the determination of the decoupling eccentricity of the MBHB population. The signal can be dominated by lighter MBHB decoupling at higher f_d with lower e_t, or by heavier MBHB decoupling at lower f_d with higher e_t, giving rise to the $\int$-shaped contour in the $e_t - \log_{10}\mathscr{M}_*$ plane. Lighter black holes require a higher $\dot{n}_0$ to produce the observed signal level, however this is still well within the assumed prior. In practice, the detection of a turnover in the GWB, guarantees that MBHBs have some eccentricity at decoupling (which in our models always occur below the observable PTA frequency window), however cannot inform us on the value of their eccentricity, unless independent information on the MBHB mass function becomes available. This causes the peculiar shape of the e_t posterior seen in the lower-right panel of Fig. 3.5, in which the posterior is quite flat down to $e_t \approx 0.1$ and has a sharp decline disfavouring

circular binaries.

3.5.3 Breaking degeneracies: the importance of detection at high frequencies

We saw in the previous section that parameter degeneracies prevent a precise characterization of the properties of the underlying MBHB population. This is because the GWB spectrum does not present sufficient structure to allow proper parameter estimation. In principle, the high frequency steepening of the GWB offers a tantalizing possibility of an independent measurement of the mass function parameters. In practice, unfortunately, the steepening generally occurs at $f > 30$ nHz where PTA sensitivity drops significantly. A measurement might be possible for MBHB population featuring a heavy-biased MBHB mass function, for which the steepening occurs already around $f \approx 10$ nHz. However, even in this case, errorbars on the detected amplitude at the highest frequency bins would be quite large, making a proper measurement of the drop problematic.

Although this is likely out of reach for current and planned PTA efforts, as a proof of principle we show here what information can be recovered with a measurement of the GWB spectrum up to $f = 5 \times 10^{-7}$ Hz, possible with our *ideal* array. Performing a parameter space exploration would be impractical, because for 30 years of observation, the signal would be observed in about 500 frequency bins, making the evaluation of the likelihood function prohibitively time consuming. We therefore interpolate the observations (with relative errorbars) in 20 equally log-spaced bins in the range $10^{-9} - 5 \times 10^{-7}$ Hz. Note that the total S/N of such detection is not much higher than the *SKA20*, however we will see that the high frequency extension makes a critical difference in the recovery of the MBHB population parameters (even if we are not using all the information enclosed in the original 500 frequency bins). This is shown in Fig. 3.6 for our standard MBHB population with $e_t = 0.01$ (left column) and $e_t = 0.9$ (right column). The upper panels show that, contrary to all previous cases, the high frequency steepening is now well

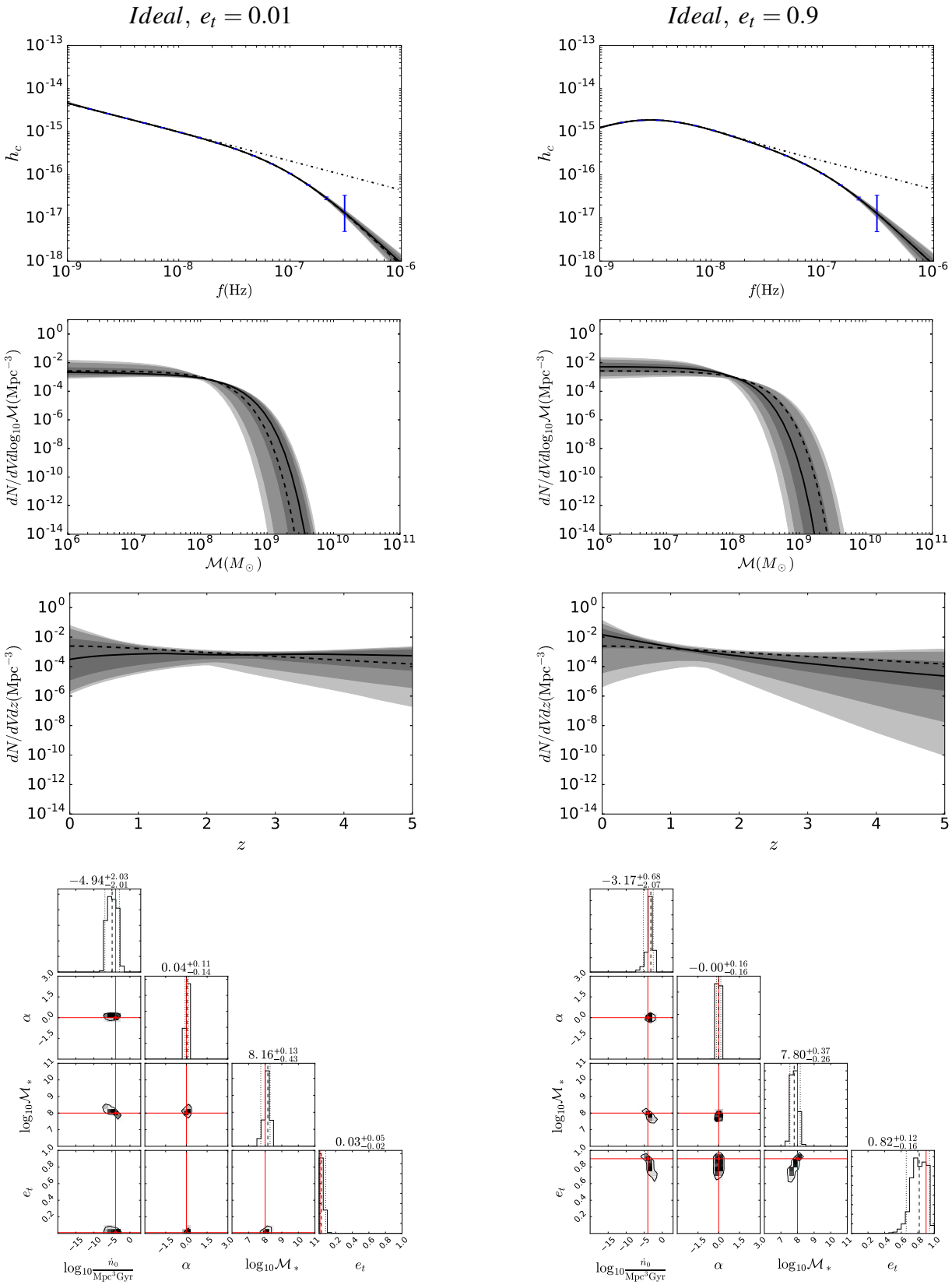

Figure 3.6: Implication of an ideal detection with 500 MSPs timed at sub-ns precision for 30 years. The injected model has default parameters with $e_t = 0.01$ (left column) and $e_t = 0.9$ (right column). Panel sequence and style as in Fig. 3.4.

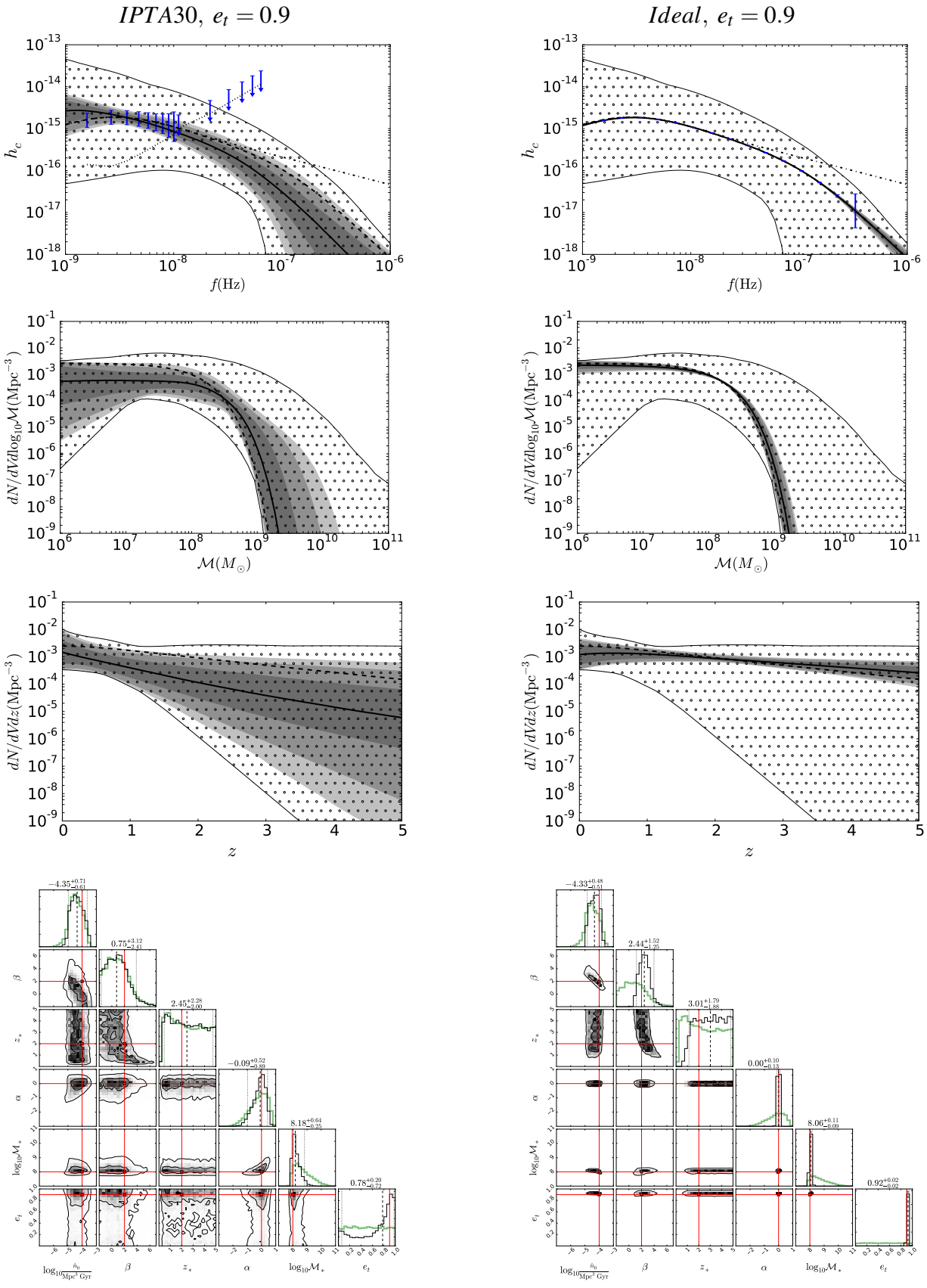
IPTA30, $e_t = 0.9$
Ideal, $e_t = 0.9$
h_c
f(Hz)
$dN/dVd\log_{10}\mathcal{M}(\mathrm{Mpc}^{-3})$
$\mathcal{M}(M_\odot)$
$dN/dVdz(\mathrm{Mpc}^{-3})$
z
$-4.35^{+0.71}_{-0.61}$
$0.75^{+3.12}_{-2.41}$
$2.45^{+2.28}_{-2.00}$
$-0.09^{+0.52}_{-0.89}$
$8.18^{+0.64}_{-0.25}$
$0.78^{+0.20}_{-0.22}$
$-4.33^{+0.48}_{-0.51}$
$2.44^{+1.52}_{-1.25}$
$3.01^{+1.79}_{-1.88}$
$0.00^{+0.10}_{-0.13}$
$8.06^{+0.11}_{-0.09}$
$0.92^{+0.02}_{-0.02}$
$\log_{10}\frac{\bar{n}_0}{\mathrm{Mpc}^3\,\mathrm{Gyr}}$
β
z_*
α
$\log_{10}\mathcal{M}_*$
e_t

Figure 3.7

Figure 3.7: Effects of imposing external constraints on the MBHB mass and redshift distribution on the science return of PTA observations. The injected model has default mass function parameters and $e_t = 0.9$. In the left column we consider a moderate S/N detection with the *IPTA30* array, whereas the right panel is for an ideal detection as reported in Fig. 3.6. Panel sequence and style are as in Fig. 3.4. The additional dotted areas represent the restricted prior based on the astrophysical models of Sesana (2013b). The thick green histograms in the bottom panels show the marginalised prior distribution on the model parameters once the astrophysical constraint is imposed (see main text for full details).

characterized; this is the key element, because its shape depends on the MBHB mass function. Posterior distributions of the population parameters are shown in the lower triangle plots. The parameters defining the MBHB mass function are now well constrained and peak around the injected values; the cut-off mass scale $\mathscr{M}_*$ is determined within a factor of three and the slope α within $\approx$0.2. The recovery of the eccentricity is also much cleaner. Posteriors are still broad, but in the circular case one can confidently say that the typical eccentricity of the MBHBs is < 0.16 (95% confidence) although the posterior peaks at $e_t \approx 0.1$. This is because a non detection of a low frequency turnover is still consistent with mildly eccentric binaries at decoupling, even if the mass function parameters are fairly well determined. Similarly, for the eccentric case, one can state with 95% confidence that the typical eccentricity of the MBHBs is > 0.7 and the posterior is quite flat in the range $0.75 < e_t < 0.95$. One last thing to notice is that, even though the GWB spectrum is pinned down essentially exactly, there remains a remarkable uncertainty in the determination of the overall merger rate density $\dot{n}_0$. This is because of its intrinsic (not shown) degeneracy with the β and z_* parameters defining the redshift distribution of mergers. A low $\dot{n}_0$ normalization with a steep, positive redshift dependence β can result in the same GWB as a much higher $\dot{n}_0$ normalization with a flatter redshift dependence. Unless external information (see below) about the redshift evolution of the merger rate density is available, this degeneracy is unlikely to be disentangled on the basis of GWB measurements alone.

3.5.4 Adding independent constraints

So far, we considered what astrophysical information can be extracted by PTA observation only, deliberately ignoring any constraints on the MBHB population imposed by other observations. The motivation behind this agnostic choice is that those constraints are inevitably indirect, and involve either the rate of merging *galaxies* (e.g. Lin et al. (2004); Lotz et al. (2011); Xu et al. (2012)) or the determination of the mass function of *single MBHs* (see for example Shankar et al. (2004)). The conversion of a galaxy merger rate into a MBHB merger rate implies a number of uncertain assumptions about the relation between galaxy hosts and MBHs (Kormendy and Ho (2013) and references therein) and the effectiveness of the MBHB coalescence following galaxy mergers (e.g. McWilliams et al. (2014); Kelley et al. (2017a)); on the other hand, the mass function of individual MBHs in galaxy centers does not provide direct information on the properties of *merging* MBHBs.

It is nevertheless instructive and interesting to fold those indirect constraints into the analysis to understand to what extent PTA observation can improve the current state of the art of MBHB knowledge. Sesana (2013b) constructed a compilation of observationally-based MBHB merger distributions encompassing a wide uncertainty range in the galaxy merger rate and galaxy host-MBH relations. The outcome of the procedure is a loosely constrained MBHB mass function and redshift distribution resulting in a predicted GWB spanning almost two order of magnitudes in amplitude (at 99.7% confidence). In general, in the best constrained areas (chirp masses in the range $10^7\mathrm{M}_\odot$-$10^{8.5}\mathrm{M}_\odot$ and $z < 1.5$), the uncertainty range spans about two orders of magnitudes. To incorporate this information in our analysis, we draw a large sample of populations from our unrestricted parameter range, and we accept only those for which the mass and redshift functions fall within the range constrained by the Sesana (2013b) models to update our prior. The restricted MBHB mass and redshift functions resulting from this procedure are shown as dotted areas in the central panels of Fig. 3.7. The restricted marginalized priors on the model parameters are shown in the triangular plots in the bottom panels and their median values and 90% confidence intervals are listed in table 3.1. Furthermore, since the merger rates do not constrain the MBHB

parameter	prior	*IPTA30*	*ideal*
$\log_{10}\dot{n}_0$	$-4.47^{+0.73}_{-0.70}$	$-4.35^{+0.71}_{-0.61}$	$-4.43^{+0.48}_{-0.51}$
β	$0.81^{+3.29}_{-2.43}$	$0.75^{+3.12}_{-2.41}$	$2.44^{+1.52}_{-1.25}$
z_*	$2.39^{+2.36}_{-1.95}$	$2.45^{+2.28}_{-2.00}$	$3.01^{+1.79}_{-1.88}$
α	$-0.11^{+0.75}_{-1.25}$	$-0.09^{+0.52}_{-0.89}$	$0.00^{+0.10}_{-0.13}$
$\log_{10}\mathscr{M}_*$	$8.58^{+1.25}_{-0.65}$	$8.18^{+0.64}_{-0.25}$	$8.06^{+0.11}_{-0.09}$
e_t	$0.50^{+0.45}_{-0.45}$	$0.78^{+0.20}_{-0.72}$	$0.92^{+0.02}_{-0.02}$

Table 3.1: List of model parameters credible intervals for our constrained models. Each entry reports the median value together with the errors bracketing the 90% confidence regions. The three columns list the values defined by our restricted prior, and the posterior values as measured by the arrays *IPTA30* and *ideal*.

eccentricity distribution at decoupling, we assume a flat prior on e_t. The resulting prior GWB spectrum is shown in the upper panels of Fig. 3.7. As expected the range of h_c is consistent with what is shown in figure 2 of Sesana (2013b). The difference in shape is due to the inclusion of the high frequency drop, and to the fact that we allow for very eccentric MBHB population, that cause a widening of the allowed h_c range at the low frequency. We assume that the true underlying MBHB population is described by our default models (shown with dashed lines), that falls well within the restricted prior range, and that MBHBs have $e_t = 0.9$ at decoupling.

The results of the analysis for two different PTAs are shown in Fig. 3.7 and measured parameter values are also listed in table 3.1. PTA observations in the foreseeable future (*IPTA30* case, left column) will place significant constraints to the higher end of the mass function, reducing the uncertainty range by more than one order of magnitude at $\mathscr{M} > 10^8\mathrm{M}_\odot$. The redshift function is poorly constrained, because the mass integral of the merger rate is dominated by the abundance of MBHBs with $\mathscr{M} < 10^8\mathrm{M}_\odot$, which remains poorly determined. This is also confirmed by the marginalised posterior distributions in the model parameters shown in the bottom panel. The posteriors on the overall merger rate $\dot{n}_0$ and on the redshift parameters β and z_* are essentially unaltered when compared to the prior, conversely, the prior knowledge of $\mathscr{M}_*$ is significantly updated with a 90% confidence interval shrinking by an order of magnitude. Note that, since $\mathscr{M}_*$ is decently constrained, the detection of the low frequency turnover is now quite informative,

and eccentric binaries are favoured, with a posterior probability distribution correctly peaking around $e_t = 0.9$. In the ideal case, shown in the right column, the mass function is constrained almost exactly, and also our knowledge of the redshift evolution of the merger rate is significantly updated. The posterior distributions of the model parameters show that $\alpha, \mathscr{M}_*$ and e_t are pinned down with high accuracy. Moreover, also the degeneracy between the rate normalization and the redshift evolution is partially broken. The 90% credible interval on $\dot{n}_0$ shrinks by a factor of three compared to the prior, and the slope of redshift dependence β can be fairly well constrained, with a posterior peaking close to the injected value. This latter measurement is particularly interesting, because it would allow a direct comparison to the galaxy merger rate that is often observationally parametrised as being proportional to $(1+z)^{\beta}$.

CHAPTER 4

ANALYZING THE CURRENT PTA UPPER LIMITS WITH OUR FRAMEWORK MODEL

This chapter reproduces verbatim "H. Middleton, S. Chen, W. Del Pozzo, A. Sesana, A. Vecchio, No tension between assembly models of supermassive black hole binaries and pulsar observations, 2018, NatComms, 9, 573", without the Abstract. Supplementary material can be found in appendix A.

4.1 Introduction

Dedicated timing campaigns of ultra-stable radio pulsars lasting over a decade and carried out with the best radio telescopes around the globe have targeted the isotropic gravitational-wave (GW) background in the frequency region $\sim 10^{-9} - 10^{-7}$Hz generated by the cosmic population of merging super massive black hole binaries (SMBHBs). In the hierarchical clustering scenario of galaxy formation, galaxies form through a sequence of mergers (White and Rees, 1978). In this process, the SMBHs hosted at their centers will inevitably form a large number of binaries (Begelman et al., 1980), forming an abundant population of GW sources in the Universe. Detecting and/or placing constraints on their emitted signal will thus provide an insight into the formation and evolution of SMBHs in connection with their galaxy hosts and will help to

better understand the role played by SMBHs in galaxy evolution and the dynamical processes operating during galaxy mergers (for a review see Sesana (2013a)).

No detection at nHz frequencies has been reported so far. The most stringent constraint on an isotropic background radiation has been obtained through an 11 year-long timing of 4 radio-pulsars by the Parkes Pulsar Timing Array (PPTA). It yields an upper limit on the GW characteristic amplitude of $h_{1\mathrm{yr}} = 1.0 \times 10^{-15}$ (at 95% confidence) at a frequency of $1\mathrm{yr}^{-1}$ (Shannon et al., 2015). Consistent results, although a factor ≈ 2 less stringent, have also been reported by the European PTA (EPTA (Lentati et al., 2015)), the North American Nanohertz Observatory for Gravitational Waves (NANOGrav (Arzoumanian et al., 2016)), and the International PTA (IPTA (Verbiest et al., 2016)), an international consortium of the three regional PTA collaborations. Those values are in the range of signal amplitudes predicted by state-of-the-art SMBHB population models, and can therefore be used to constrain such a population. It has been noted, however, that these limits start to be sensitive to uncertainties in the determination of the solar system ephemeris used in the analysis. Recent unpublished work has in fact found that different ephemeris choices can result in a partial degradation of the upper limit (Hobbs and Dai, 2017). This is still an active area of research which may lead to a small upward revision of the upper limit, a circumstance which, if anything, will strengthen the conclusion of our analysis. Here we consider the most stringent upper limit from the PPTA in order to glean what can be learnt at this stage and also determine whether current SMBHB population models are indeed cast into doubt.

Using the PPTA limit, we place bounds on the properties of the sub-parsec population of cosmic SMBHBs (in the mass range $\sim 10^7 - 10^{10}\,\mathrm{M}_\odot$) and explore what constraints, if any, can be put on the salient physical processes that lead to the formation and evolution of these objects. We consider a comprehensive suite of astrophysical models that combine observational constraints on the SMBHB population with state-of-the-art dynamical modelling of binary evolution. The SMBHB merger rate is anchored to observational estimates of the host galaxy merger rate by a set of SMBH-host relations (see Sesana (2013b); Sesana et al. (2016) and section 4.4). Rates

obtained in this way are well captured by a five parameter analytical function of mass and redshift, once model parameters are restricted to the appropriate prior range (see section 4.4). Individual binaries are assumed to hold a constant eccentricity so long as they evolve via three-body scattering and gradually circularize once GW emission takes over. Their dynamical evolution and emission properties are regulated by the density of the stellar environment (assumed to be a Hernquist profile (Hernquist, 1990) with total mass determined by the SMBH mass-galaxy bulge mass relation) and by the eccentricity during the three-body scattering phase, which we take as a free parameter. For each set of model parameters, the characteristic GW strain $h_c(f)$ at the observed frequency f is computed as described in Chen et al. (2017b), and summarized in section 4.4. Our model encapsulates the significant uncertainties in the GW background due to the poorly constrained SMBHB merger rate and has the flexibility to produce a low frequency turnover due to either three-body scattering or high eccentricities. SMBHBs are assumed to merge with no significant delay after galaxies merge. As such, the models do not include the effect of stalling or delayed mergers (Simon and Burke-Spolaor, 2016).

We find that although PTAs have well and truly achieved a sensitivity for which detection is possible based on model predictions, the present lack of a detection provides no reason to question these models. We highlight the impact of the SMBH-galaxy relation by considering a selection of models which cover the entire range of the predicted background amplitude. To be definitive, we consider: (i.) an optimistic model (here labelled KH13, based on Kormendy and Ho (2013)), which provides a prediction of the GW background with median amplitude at $f = 1\mathrm{yr}^{-1}$ of $h_{1\mathrm{yr}} = 1.5 \times 10^{-15}$; (ii.) a conservative model (labelled G09, based on Gültekin et al. (2009)), with median $h_{1\mathrm{yr}} = 7 \times 10^{-16}$; (iii.) an ultra-conservative model (labelled S16, based on Shankar et al. (2016)), with $h_{1\mathrm{yr}} = 4 \times 10^{-16}$; and finally (iv.) a model that spans the whole range of predictions within our assumptions (which we label 'ALL'). Note that the latter contains as subsets KH13, G09 and S16, but it is not limited to them. Moreover, model 'ALL' spans an $h_{1\mathrm{yr}}$ amplitude range that comfortably include GW backgrounds estimated by other authors employing different techniques (e.g. McWilliams et al. (2014); Ravi et al. (2015); Kulier et al. (2015); Kelley et al. (2017a)). Details on the models are provided in section 4.4. We find

all models to be consistent with the current PTA upper limits.

4.2 Results

For each model, we use a Bayesian hierarchical analysis to compute the model evidence (which is the probability of the model given the data and allows for the direct comparison of models) and posterior density functions on the model parameters given the observational results reported by Shannon et al. (2015). We find that the upper limit is now beginning to probe the most optimistic predictions, but all models are so far consistent with the data. Figure 4.1, our main result, compares the predictions under different model assumptions with the observed upper limit. The dotted area shows the prior range of the GW amplitude under the model assumptions, and the orange solid line shows the 95% confidence PPTA upper-limit on h_c. The (central) 68% and 90% posterior probability intervals on h_c are shown by the shaded blue bands. The posterior density functions (PDFs) on the right hand side of each plot gives the prior (black-dashed line) and posterior (blue line) for h_c at a reference frequency of $f \sim 1/5\mathrm{yr}^{-1}$.

The difference between the dotted region and the shaded bands in the main panels in Figure 4.1 indicates the constraining power of the Parkes PTA limit on astrophysical models – the greater the difference between the two regions, the smaller is the consistency of that particular model with the data. We see that although some upper portion of the allowable prior region is removed from the 90% posterior probability interval (less so for S16), none of the models can be ruled out at any significant level. The confidence bands across the frequency range are constructed by taking the relevant credibility region of the posterior distribution of h_c at each frequency, and therefore the boundaries of each band do not follow any particular functional form as a function of frequency. In addition, although eccentricity is allowed by the data, the power-law spectrum of circular binaries driven by radiation reaction alone can clearly be consistently placed within these bands (see also Supplementary Fig. A1 for further details on the individual parameter posteriors including eccentricity). This can be quantified in terms of the model evidences $\mathscr{Z}$,

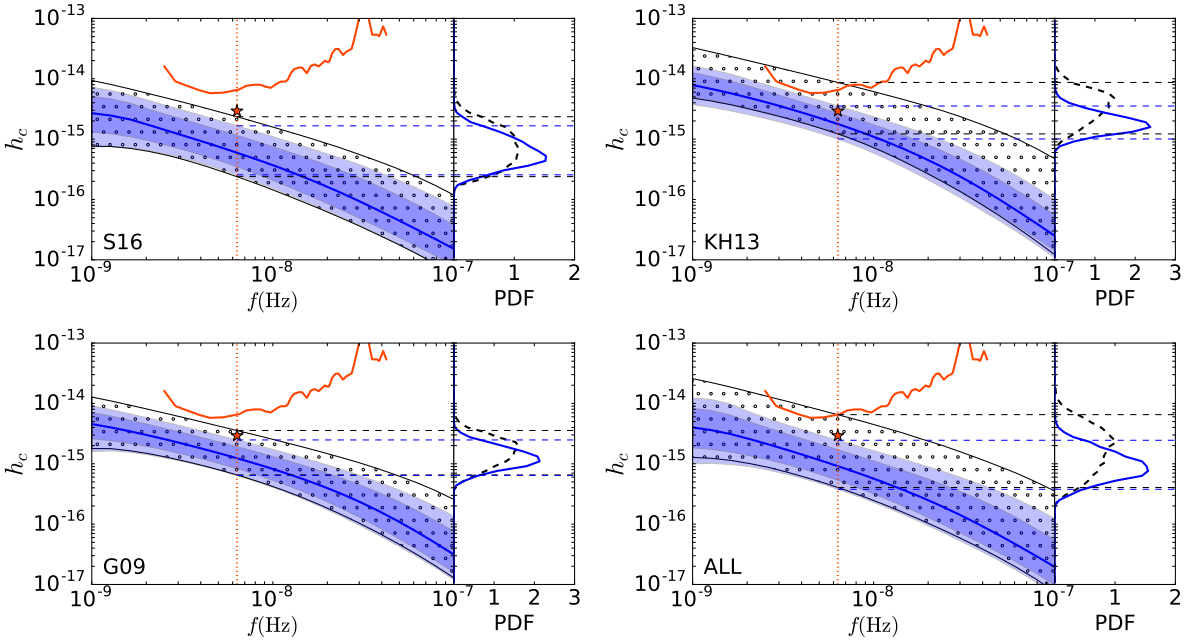

Figure 4.1: Posterior density functions on the gravitational wave characteristic amplitude. The four panels compare the prior and posterior density functions on the GW stochastic background characteristic amplitude in light of the PPTA upper-limit for each of the astrophysical models considered here. The central 90% region of the prior is indicated by the black-dotted band, and the posterior is shown by the progressively lighter blue shading indicating the central 68% and 90% regions, along with the median (solid-blue line). Also shown are the PPTA bin-by-bin limit (orange-solid line) and the corresponding integrated limit assuming $h_c(f) \propto f^{-2/3}$ (orange star and vertical-dotted line). The difference in the prior and posterior indicates how much has been learnt from the PPTA data. The right-hand side one-dimensional distribution shows the prior (black-dashed) and posterior (blue-solid) at a reference frequency of $f \sim 1/5\text{yr}^{-1}$, with the central 90% regions marked (black and blue-dashed lines respectively).

shown in Table 4.1. The normalization is chosen so that a putative model unaffected by the limit yields $\mathscr{Z} = 1$, and therefore the values can be interpreted as Bayes factors against such a model. None of the posterior probabilities of the models with respect to this putative one show any tension. As an example, for models ALL and S16 we find $e^{-1.23} = 0.3$ and $e^{-0.6} = 0.55$ respectively. Similar conclusions can be drawn from the Kullback-Leibler (K-L) divergences between the prior and posterior on the characteristic amplitude for a given model (with which we measure the difference between the prior and posterior). For models ALL and S16, these yield 0.62 and 0.37 respectively. As a comparison, these values correspond to the K-L divergence between two Gaussian distributions with the same variance and means approximately 1.1 (for

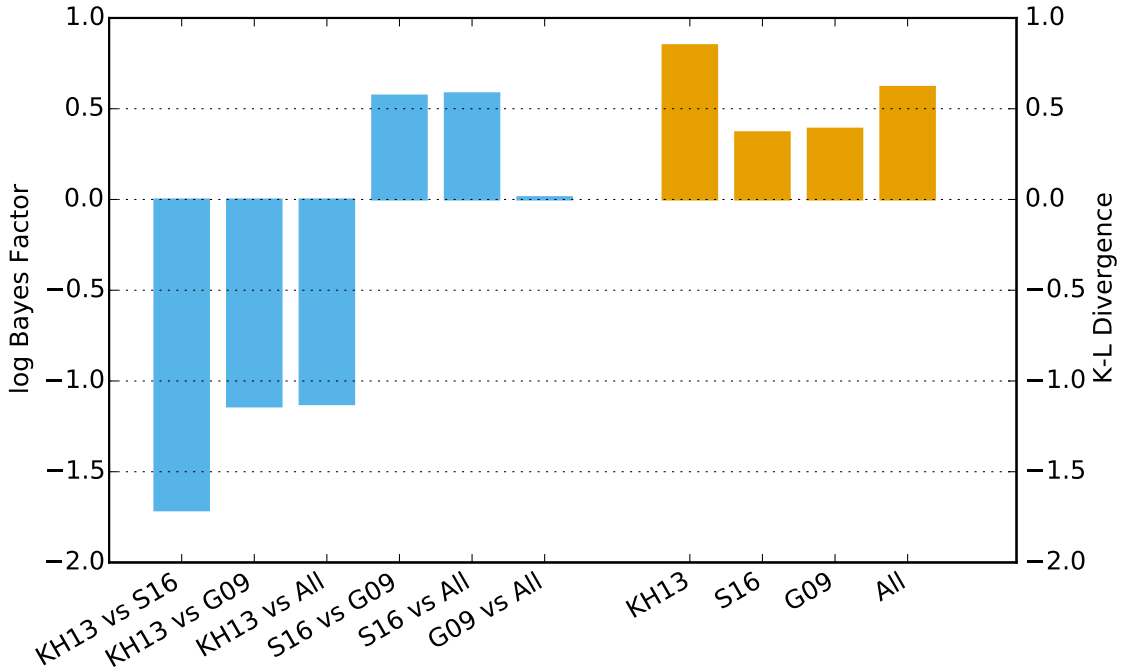

Figure 4.2: Bayes factors and Kullback-Leibler divergences for different models. We compare the Bayes factors between model pairs (left hand, blue bars) and the Kullback-Leibler (K-L) divergences between the prior and posterior of the characteristic amplitude (right hand, orange bars). The small range of Bayes factors indicates that there is little to choose from between these models, although KH13 is weakly disfavoured against the others. The K-L divergences also support this conclusion. Although all values are small, KH13 has the largest K-L divergence (greatest difference between prior and posterior) of the four models.

ALL) and 0.8 (for S16) standard deviation apart [1].

Figure 4.2 summarizes the natural logarithm of the ratio of the model evidences, i.e. the Bayes factors, between all possible combinations of models and also the K-L divergences whose numerical values are listed in Table 4.1. Both metrics clearly indicate that there is little to choose from between the models. The least favoured model in the range of those considered here is KH13, with Bayes factors in favour of the others ranging from ≈ 1.13 to ≈ 1.76. These are

[1] The Kullback-Leibler divergence between two normal distributions $p \sim N(\mu_p, \sigma_p^2)$ and $q \sim N(\mu_q, \sigma_q^2)$ is $D_{KL}(p||q) = \ln(\sigma_q/\sigma_p) - 1/2 + 1/2\left[(\sigma_p/\sigma_q)^2 + (\mu_p - \mu_q)^2/\sigma_q^2\right]$. For $\sigma_p = \sigma_q$ and $\mu_p = \mu_q + \sigma_q$ the KL divergence is 0.5.

Model	$h_{1\mathrm{yr}} = 1 \times 10^{-15}$(PPTA)		$h_{1\mathrm{yr}} = 3 \times 10^{-16}$		$h_{1\mathrm{yr}} = 1 \times 10^{-16}$	
	K-L divergence	$\log \mathscr{Z}$	K-L divergence	$\log \mathscr{Z}$	K-L divergence	$\log \mathscr{Z}$
KH13	0.85	-2.36	2.25	-5.68	5.18	-13.17
G09	0.39	-1.2	1.11	-3.35	2.86	-8.26
S16	0.37	-0.6	0.69	-1.62	1.42	-3.82
ALL	0.62	-1.23	1.33	-2.68	2.50	-5.74

Table 4.1: Kullback-Leibler divergences and evidences for different models. The values in the table show the K-L divergence and natural logarithm of the evidence, $\log \mathscr{Z}$, for each of the four astrophysical models given the PPTA upper limit at $h_{1\mathrm{yr}} = 1 \times 10^{-15}$, and for more stringent putative limits at the levels of 3×10^{-16} and 1×10^{-16}.

however values of order unity, and no decisive inference can be made from the data (Kass and Raftery, 1995). Comparisons between each of the individual model parameters (see section 4.4) posterior and prior distribution functions are described in Supplementary Fig. A1 and Supplementary Table A1 which further support our conclusions. For KH13, the model that produces the strongest GW background, we find a probability of $e^{-2.36} = 0.094$ with respect to a putative model that is unaffected by the limit. KH13 is therefore disfavoured at $\sim 1.6\sigma$. This conclusion is reflected in the value of the K-L divergence of 0.85[1]. We note that Shannon et al. (2015) choose in their analysis only a sub-sample of the Sesana (2013b) models, with properties similar to KH13. Our results for KH13 are therefore consistent with the 91%-to-97% 'exclusion' claimed by Shannon et al. (2015).

4.3 Discussion

It is argued in Shannon et al. (2015) that the Parkes PTA upper-limit excludes at high confidence standard models of SMBH assembly – i.e. those considered in this work – and therefore these models need to be substantially revised to accommodate either accelerated mergers via strong interaction with the environment or inefficient SMBHB formation following galaxy mergers. The work presented here does not support either claim. In particular, the posterior parameter

[1]This is the same K-L between two Gaussian distributions with the same variance and means approximately 1.3 standard deviation apart

distributions (see Supplementary Fig. A1) favour neither high eccentricities nor particularly high stellar densities, indicating that a low frequency spectral turnover induced by SMBHB dynamics is not required to reconcile the PTA upper limit with existing models. Similar to Taylor et al. (2016b), this finding does not support an observing strategy revision in favour of higher cadence observations aimed at improving the high frequency sensitivity, as proposed by Shannon et al. (2015). Likewise, neither stalling nor delays between galaxy and SMBHB mergers, which, by construction, are not included in the models considered here, are needed to explain the lack of a detection of GWs at the present sensitivity level. Compared to previous analyses, our work implies a stronger rejection of the statement that there is tension between PTA data and theoretical SMBHB population models. For example Simon and Burke-Spolaor (2016) invoked time delays to reconcile the PPTA upper limit with selected SMBH-galaxy relations, however they assume a narrow range of possible SMBHB merger histories and do not consider SMBHB dynamics. The analysis of Arzoumanian et al. (2016) tends to favour a spectral turnover due to either high eccentricity or strong environmental coupling, however they use a simplified analysis where each relevant physical parameter is accounted for separately. When allowing all the parameters to vary simultaneously, we find that none of them has a critical impact on the inference, and current SMBHB population models are broadly consistent with the PTA upper limits, without the need to invoke a low frequency spectral turnover.

On the other hand, PTA limits are now starting to provide interesting information about the population of merging SMBHs. The fact that KH13 is disfavoured at $1.4\,\sigma$ with respect to S16 indicates that the population may have fewer high mass binaries, mildly favouring SMBH-host galaxy relations with lower normalizations. This indicates that the gravitational wave background level is likely below the 10^{-15} level, making detection difficult with current telescopes. In this respect, our analysis highlights the importance of upcoming facilities such as MeerKAT (Booth et al., 2009), FAST (Nan et al., 2011) and the Square Kilometer Array (SKA Dewdney et al. (2009)). Their superior timing capabilities, together with their survey potential in finding new stable millisecond pulsars, will provide the necessary ground to improve sensitivity down to $h_{1\mathrm{yr}} \sim 10^{-16}$, which is in line with the lower limit of the expected stochastic gravitational wave

background according to our current understanding of SMBH evolution (Bonetti et al., 2018). Although not yet decisive, our findings highlight the potential of PTAs in informing the current debate on the SMBH-host galaxy relation. Recent discoveries of over-massive black holes in brightest cluster ellipticals (McConnell et al., 2011; Hlavacek-Larrondo et al., 2012) led to an upward revision of those relations (McConnell and Ma, 2013; Kormendy and Ho, 2013). However, several authors attribute the high normalization of the recent SMBH-host galaxy relations to selection biases (Shankar et al., 2016) or to the intrinsic difficulty of resolving the SMBH fingerprint in measurements based on stellar dynamics (see discussion in Rasskazov and Merritt (2017)). Future facilities such as the Extremely Large Telescope (Gilmozzi and Spyromilio, 2007) and the Thirty Meter Telescope (Sanders, 2013) will likely measure many more SMBH masses in elliptical galaxies (Do et al., 2014), providing a better understanding of the SMBH-host galaxy relations. PTA limits may therefore be used to gain more information about the other underlying uncertainties in the model, in particular the massive galaxy merger rate, which is currently poorly constrained observationally (see, e.g. Lotz et al. (2011); Mundy et al. (2017)).

An important question is: what is the sensitivity level required to really put under stress our current understanding of SMBHB assembly? If a null result persists in PTA experiments, this will in turn lead to a legitimate re-thinking of the PTA observing strategy to target possibly more promising frequencies of the GW spectrum. To address this question, we simulate future sensitivity improvements by shifting the Parkes PTA sensitivity curve down to provide 95% upper limits of $h_{1\mathrm{yr}}$ at 3×10^{-16} and 1×10^{-16}. The results are summarized in Table 4.1 and more details are provided in Supplementary Fig. A2, Supplementary Table A2 and Supplementary Note A1). At 3×10^{-16}, possibly within the sensitivity reach of PTAs in the next ≈ 5 years, S16 will be significantly favoured against KH13, with a Bayes factor of $e^{4.06}$, and only marginally favoured over G09, with Bayes factor of $e^{1.76}$. It will still be impossible to reject this model at any reasonable significant level with respect to, say, a model which predicts negligible GW background radiation at $\sim 10^{-9}-10^{-8}$ Hz. However SMBH-host galaxy relations with high normalizations will show a $\approx 2\,\sigma$ tension with more conservative models. At 1×10^{-16}, within

reach in the next decade with the advent of MeerKAT, FAST and SKA, models KH13, G09 and ALL are disfavoured at $3.9\,\sigma$, $2.5\,\sigma$ and $1.2\,\sigma$, respectively, in comparison to S16. K-L divergences in the range $5.18 - 1.42$ show that the data are truly informative. S16 is also disfavoured at 2.3σ with respect to a model unaffected by the data, possibly indicating the need of additional physical processes to be included in the models.

4.4 Methods

4.4.1 Analytical description of the GW background

The GW background from a cosmic population of SMBHBs is determined by the binary merger rate and by the dynamical properties of the systems during their inspiral. The comoving number density of SMBHBs per unit log chirp mass ($\mathscr{M} = (M_1 M_2)^{3/5}/(M_1 + M_2)^{1/5}$) and unit redshift, $d^2n/(d\log_{10}\mathscr{M}\,dz)$, defines the normalization of the GW spectrum. If all binaries evolve under the influence of GW backreaction only in circular orbits, then the spectral index is fixed at $h_c(f) \propto f^{-2/3}$ and the GW background is fully determined (Phinney, 2001). However, to get to the point at which GW emission is efficient, SMBHBs need to exchange energy and angular momentum with their stellar and/or gaseous environment (Sesana, 2013a), a process that can lead to an increase in the binary eccentricity (e.g. Quinlan (1996); Cuadra et al. (2009)). We assume SMBHBs evolve via three-body scattering against the dense stellar background up to a transition frequency f_t at which GW emission takes over. According to recent studies (Sesana and Khan, 2015; Vasiliev et al., 2015), the hardening is dictated by the density of background stars ρ_i at the influence radius of the binary r_i. The bulge stellar density is assumed to follow a Hernquist density profile (Hernquist, 1990) with total mass M_* and scale radius a determined by the SMBHB total mass $M = M_1 + M_2$ via empirical relations from the literature (see full details in Chen et al. (2017b)). Therefore, for each individual system, ρ_i is determined solely by M. In the stellar hardening phase, the binary is assumed to hold constant eccentricity e_t up to f_t, beyond

which it circularizes under the effect of the now dominant GW backreaction. The GW spectrum emitted by an individual binary adiabatically inspiralling under these assumptions behaves as $h_c(f) \propto f$ for $f \ll f_t$ and settles to the standard $h_c(f) \propto f^{-2/3}$ for $f \gg f_t$. The spectrum has a turnover around f_t and its exact location depends on the binary eccentricity e_t. The observed GW spectrum is therefore uniquely determined by the binary chirp mass $\mathscr{M}$, redshift z, transition frequency f_t and eccentricity at transition e_t.

The GW spectrum from the overall population can be computed by integrating the spectrum of each individual system over the co-moving number density of merging SMBHBs

$$h_c^2(f) = \int dz \int d\log_{10}\mathscr{M} \frac{d^2n}{d\log_{10}\mathscr{M}\,dz} h^2_{\rm c,fit}\left(f\frac{f_{\rm p,0}}{f_{\rm p,t}}\right)\left(\frac{f_{\rm p,t}}{f_{\rm p,0}}\right)^{-4/3}\left(\frac{\mathscr{M}}{\mathscr{M}_0}\right)^{5/3}\left(\frac{1+z}{1+z_0}\right)^{-1/3} \tag{4.1}$$

where $h_{\rm c,fit}$ is an analytic fit to the GW spectrum of a reference binary with chirp mass $\mathscr{M}_0$ at redshift z_0 (i.e. assuming $d^2n/(d\log_{10}\mathscr{M}\,dz) = \delta(\mathscr{M}-\mathscr{M}_0)\delta(z-z_0)$), characterized by an eccentricity of e_0 at a reference frequency f_0. For these reference values, the peak frequency of the spectrum $f_{\rm p,0}$ is computed. The contribution of a SMBHB with generic chirp mass, emission redshift, transition frequency f_t and initial eccentricity e_t are then simply computed by calculating the spectrum at a rescaled frequency $f(f_{\rm p,0}/f_{\rm p,t})$ and by shifting it with frequency mass and redshift as indicated in equation 4.1. In Chen et al. (2017b) it was demonstrated that this simple self-similar computation of the GW spectrum is sufficient to describe the expected GW signal from a population of eccentric SMBHBs driven by three-body scattering at $f > 1$nHz, relevant to PTA measurement.

As stated above, the shape of the spectrum depends on ρ_i and e_t. The stellar density ρ_i regulates the location of f_t; the denser the environment, the higher the transition frequency. SMBHBs evolving in extremely dense environments will therefore show a turnover in the GW spectrum at higher frequency. The effect of e_t is twofold. On the one hand, eccentric binaries emit GWs more efficiently at a given orbital frequency, thus decoupling at lower f_t with respect to circular ones. On the other hand, eccentricity redistributes the emitted GW power at higher frequencies,

thus pushing the spectral turnover to high frequencies. In our default model, ρ_i is fixed by the SMBHB total mass M and we make the simplifying assumption that all systems have the same e_t. We also consider an extended model where ρ_i is multiplied by a free parameter η. This corresponds to a simple rescaling of the central stellar density, relaxing the strict $M-\rho_i$ relation imposed by our default model. We stress here that including this parameter in our main analysis yielded quantitatively identical results.

We use a generic simple model for the cosmic merger rate density of SMBHBs based on an overall amplitude and two power law distributions with exponential cut-offs,

$$\frac{d^2n}{d\log_{10}\mathscr{M}\,dz} = \dot{n}_0 \left(\frac{\mathscr{M}}{10^7\mathrm{M}_\odot}\right)^{-\alpha} \exp\left(-\frac{\mathscr{M}}{\mathscr{M}_*}\right)(1+z)^{\beta} \exp\left(-\frac{z}{z_*}\right)\frac{dt_r}{dz} \tag{4.2}$$

where dt_r/dz is the relationship between time and redshift assuming a standard ΛCDM flat Universe with cosmological constant of $H_0 = 70\mathrm{kms}^{-1}\mathrm{Mpc}^{-1}$. The five free parameters are: $\dot{n}_0$ representing the co-moving number of mergers per Mpc^3 per Gyr; α and $\mathscr{M}_*$ control the slope and cut-off of the chirp mass distribution respectively; β and z_* regulate the equivalent properties of the redshift distribution. Equation 4.2 is also used to compute the number of emitting systems per frequency resolution bin at $f > 10$ nHz. The small number statistics of the most massive binaries determines a steepening of the GW spectrum at high frequencies, full details of the computation are found in Sesana et al. (2008) and Chen et al. (2017b). The GW spectrum is therefore uniquely computed by a set of six(seven) parameters $\theta = \dot{n}_0, \beta, z_*, \alpha, \mathscr{M}_*, e_t(, \eta)$.

4.4.2 Anchoring the model prior to astrophysical models

Although no sub-parsec SMBHBs emitting in the PTA frequency range have been unambiguously identified to date, their cosmic merger rate can be connected to the merger rate of their host galaxies. The procedure has been extensively described in Sesana (2013b). The galaxy merger

rate can be estimated directly from observations via

$$\frac{d^3 n_{\rm G}}{dz dM_{\rm G} dq} = \frac{\phi(M_{\rm G},z)}{M_{\rm G}\ln 10}\frac{F(z,M_{\rm G},q)}{\tau(z,M_{\rm G},q)}\frac{dt_r}{dz}. \tag{4.3}$$

Here, $M_{\rm G}$ is the galaxy mass; $\phi(M_{\rm G},z) = (dn/d\log M_{\rm G})_z$ is the galaxy mass function measured at redshift z; $F(M_{\rm G},q,z) = (df_{\rm p}/dq)_{M_{\rm G},z}$, for every $M_{\rm G}$ and z, denotes the fraction of galaxies paired with a companion galaxy with mass ratio between q and $q+\delta q$; $\tau(z,M_{\rm G},q)$ is the merger timescale of the pair as a function of the relevant parameters. We construct a library of galaxy merger rates by combining four measurements of the galaxy mass function $\phi(M_{\rm G},z)$ (Ilbert et al., 2013; Muzzin et al., 2013; Tomczak et al., 2014; Bernardi et al., 2016), four estimates of the close pair fraction $F(M_{\rm G},q,z)$ (Bundy et al., 2009; de Ravel et al., 2009; López-Sanjuan et al., 2012; Xu et al., 2012) and two estimates of the merger timescale $\tau(z,M_{\rm G},q)$ (Kitzbichler and White, 2008; Lotz et al., 2010). For each of the galaxy mass functions and pair fractions we consider three estimates given by the best fit and the two boundaries of the 1σ confidence interval reported by the authors. We therefore have $12\times 12\times 2 = 288$ galaxy merger rates. Each merging galaxy pair is assigned SMBHs with masses drawn from 14 different SMBH-galaxy relations found in the literature, for more details see Supplementary Table A3. SMBHBs are assumed to merge in coincidence with the host galaxies (i.e. no stalling or extra delays), but can acrete either before or after merger according to the three different prescriptions described in Sesana et al. (2009). This gives a total of $14\times 3 = 42$ distinctive SMBH populations for a given galaxy merger model. We combine the 288 galaxy merger rates as per equation 4.3 and the 42 SMBH masses assigned via using Supplementary Table A3 plus accretion prescriptions into a grand total of 12096 SMBHB population models. Given the uncertainties, biases, selection effects, and poor understanding on the underlying physics affecting each of the individual ingredients, we do not attempt a ranking of the models, and give each of them equal weight. The models result in an allowed SMBHB merger rate density as a function of chirp mass and redshift.

We then marginalize over mass and redshift separately to obtain the functions dn/dz and $dn/d\mathscr{M}$. We are particularly interested here in testing different SMBH-host galaxy relations. We therefore

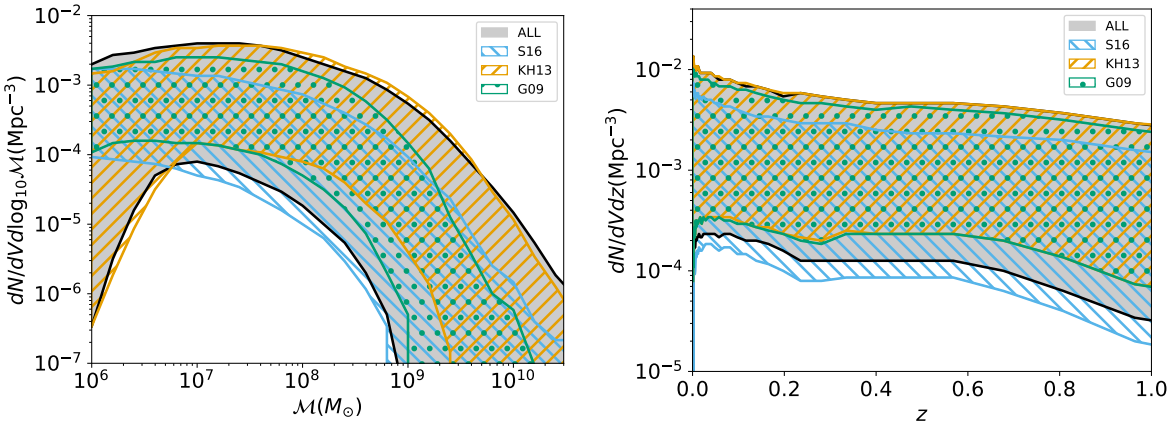

Figure 4.3: Astrophysical prior on the SMBHB chirp mass and redshift distributions. Left panel: mass density distribution $dn/d\mathscr{M}$ of the four astrophysical priors selected in this study (see text for full description). Right panel: redshift evolution of the SMBHB mass density for the same four models. Note that the coloured region represent the 99% interval allowed by each model, this is why individual models can extend beyond the region associated to model ALL (which includes KH13, G09, S16 as subsets).

construct the function dn/dz and $dn/d\mathscr{M}$ under four different assumptions: (i.) Model KH13 is constructed by considering both the $M-\sigma$ and $M-M_*$ relations from Kormendy and Ho (2013); (ii.) Model G09 is based on the $M-\sigma$ relation of Gültekin et al. (2009); (iii.) Model S16 employs both the $M-M_*$ and $M-\sigma$ relation from Shankar et al. (2016); (iv.) Model ALL is the combination of all 14 SMBH mass-host galaxy relations listed in Supplementary Table A3. For each of these four models, the allowed regions of dn/dz and $dn/d\mathscr{M}$ are shown in Figure 4.3. The figure highlights the large uncertainty in the determination of the SMBHB merger rate and unveils the trend of the chosen models; S16 and KH13 represent the lower and upper bound to the rate, whereas G09 sits in the middle and is representative of the median value of model 'ALL'. These prior bands need then to be described analytically using the parameters of equation 4.2. The shape of these priors and how they differ (or not) from model to model are shown by Supplementary Fig. A3.

We then ensured that once the bands of Figure 4.3 are imposed on our model parameters ($\theta = \{\dot{n}_0, \beta, z_*, \alpha, \mathscr{M}_*, e_t(,\eta)\}$), that the resulting distribution of characteristic amplitudes h_c is consistent with that of the original models. We computed the GW background under the assumption of circular GW driven systems (i.e. $h_c \propto f^{-2/3}$) and compared the distributions

of $h_{1\mathrm{yr}}$, i.e. the strain amplitudes at $f = 1\mathrm{yr}^{-1}$. The $h_{1\mathrm{yr}}$ distributions obtained with the two techniques were found to follow each other quite closely with a difference of median values and 90% confidence regions smaller than 0.1dex. We conclude that our analytical models provide an adequate description of the observationally inferred SMBHB merger rate, and can therefore be used to constrain the properties of the cosmic SMBHB population. In particular model KH13 provides an optimistic prediction of the GW background with median amplitude at $f = 1\mathrm{yr}^{-1}$ of $h_{1\mathrm{yr}} \approx 1.5 \times 10^{-15}$; model G09 results in a more conservative prediction $h_{1\mathrm{yr}} \approx 7 \times 10^{-16}$; model S16 result in an ultra conservative estimate with median $h_{1\mathrm{yr}} \approx 4 \times 10^{-16}$; and finally the characteristic amplitude predicted by the compilation of all models (ALL) encompasses almost two orders of magnitudes with median value $h_{1\mathrm{yr}} \approx 8 \times 10^{-16}$.

As for the parameters defining the binary dynamics, we assume that all binaries have the same eccentricity for which we pick a flat prior in the range $10^{-6} < e_t < 0.999$ (see Supplementary Fig. A3). In the extended model, featuring a rescaling of the density ρ_i regulating the binary hardening in the stellar phase, we assume a log flat prior for the multiplicative factor η in the range $0.01 < \eta < 100$. For more detailed results of including this additional density parameter see Supplementary Table A2, Supplementary Note A1 and Supplementary Fig. A4

4.4.3 Likelihood function and hierarchical modelling

By making use of Bayes theorem, the posterior probability distribution $p(\theta|d,M)$ of the model parameters θ inferred by the data d given our model M is

$$p(\theta|d,M) = \frac{p(d|\theta,M)p(\theta|M)}{\mathscr{Z}_M}, \tag{4.4}$$

where $p(\theta|M)$ is the prior knowledge of the model parameters, $p(d|\theta,M)$ is the likelihood of the data d given the parameters θ and $\mathscr{Z}_M$ is the evidence of model M, computed as

$$\mathscr{Z}_M = \int p(d|\theta,M)p(\theta|M)d\theta. \tag{4.5}$$

The evidence is the integral of the likelihood function over the multi-dimensional space defined by the model parameters θ, weighted by the multivariate prior probability distribution of the parameters. When comparing two competitive models A and B, the odds ratio is computed as

$$\mathscr{O}_{\rm A,B} = \frac{\mathscr{Z}_{\rm A}}{\mathscr{Z}_{\rm B}}\frac{P_{\rm A}}{P_{\rm B}} = \mathscr{B}_{\rm A,B}\frac{P_{\rm A}}{P_{\rm B}}, \tag{4.6}$$

where $\mathscr{B}_{\rm A,B} = \mathscr{Z}_{\rm A}/\mathscr{Z}_{\rm B}$ is the Bayes factor and P_M is the prior probability assigned to model M. When comparing the four models KH13, G09, S16 and ALL, we assign equal prior probability to each model. Therefore, in each model pair comparison, the odds ratio reduces to the Bayes factor. Above we have defined the distribution of prior parameters $p(\theta|M)$, to proceed with model comparison and parameter estimation we need to define the likelihood function $p(d|\theta,M)$.

The likelihood function, $p(d|\theta,M)$ is defined following Chen et al. (2017a). We take the posterior samples from the Parkes PTA analysis (courtesy of Shannon and collaborators) used to place the 95% upper limit at $h_{\rm 1yr} = 1\times10^{-15}$, when a single power law background $h_c \propto f^{-2/3}$ is assumed. However, for our analysis we would like to convert this upper limit at $f = 1{\rm yr}^{-1}$ to a frequency dependent upper limit on the spectrum as shown by the orange curve in Figure 4.1. Our likelihood is constructed by multiplying all bins together, therefore the resulting overall limit from these bin-by-bin upper-limits must be consistent with $h_{\rm 1yr} = 1\times10^{-15}$. The $f_{\rm 1yr}$ posterior distribution is well fitted by a Fermi function. To estimate a frequency dependent upper limit, we use Fermi function likelihoods at each frequency bin, which are then shifted and re-normalized in order to provide the correct overall upper limit. In our analysis we consider the contributions by only the first four frequency bins of size $1/11\,{\rm yr}^{-1}$, as the higher frequency portion of the spectrum provides no additional constraint. We have verified that when we include additional

bins the results of the analysis are unchanged. Ideally, we would take the bin-by-bin upper limits directly from the pulsar timing analysis to take account of the true shape of the posterior; however, the method we use here provides a consistent estimate for our analysis.

Having defined the population of merging binaries, the astrophysical prior and the likelihood based on the PPTA upper limit result, we use a nested sampling algorithm (Skilling, 2004; Del Pozzo and Veitch, 2015) to construct posterior distributions for each of the six model parameters. For the results shown here, we use 2000 live points and run each analysis 5 times, giving an average of around 18000 posterior samples.

CHAPTER 5

CONSTRAINING ASTROPHYSICAL OBSERVABLES OF GALAXY AND BLACK HOLE BINARY MERGERS

This chapter is based on a draft for a paper "S. Chen, A. Sesana, C. J. Conselice, Constraining astrophysical observables of Galaxy and Supermassive Black Hole Binary Mergers using Pulsar Timing Arrays, ArXiv e-prints, 1810.04184", without the Abstract, Introduction and Conclusions, that has been submitted for publication to a journal. The main aim is to replace the phenomenological SMBHB merger rate from chapter 2 with a SMBHB merger rate that comes from astrophysical observables. This allows for the direct comparison and combination of the constraints on these observables from traditional electromagnetic observations and observations on gravitational waves with PTAs.

5.1 GWB strain model

Deviations from an unperturbed spacetime arising from an incoherent superposition of GW sources (i.e. a stochastic GWB) are costumarily described in terms of characteristic strain h_c, which represents the amplitude of the perturbation per unit logarithmic frequency interval. We compute h_c following Chen et al. (2017b). The model allows for the quick calculation of h_c

given the chirp mass $\mathscr{M}$, redshift z and eccentricity e at decoupling of any individual binary. The total strain of the GWB can then be computed by integrating over the population $\frac{d^2n}{dzd\mathscr{M}}$, giving the main equation of Chen et al. (2017b):

$$h_c^2(f) = \int dz \int d\mathscr{M} \frac{d^2n}{dzd\mathscr{M}} h_{c,\mathrm{fit}}^2\left(f\frac{f_{p,0}}{f_{p,t}}\right)\left(\frac{f_{p,t}}{f_{p,0}}\right)^{-4/3}\left(\frac{\mathscr{M}}{\mathscr{M}_0}\right)^{5/3}\left(\frac{1+z}{1+z_0}\right)^{-1/3}, \tag{5.1}$$

where $h_{c,\mathrm{fit}}$ is the strain of a reference binary with chirp mass $\mathscr{M}_0$, redshift z_0 and eccentricity e_0 and $f_{p,i}$ is the peak frequency of the spectrum (see equation 13 in Chen et al. (2017b) and relative discussion therein). The main concept of equation (5.1) is to use the self-similarity of the characteristic strain of a purely GW emission driven binary to shift the reference spectrum to match the emission of a binary with arbitrary parameters.

As in Chen et al. (2017b), we assume that the evolution of the binary is driven by hardening in a stellar environment before GW emission takes over at a transition frequency given by (equation 21 in Chen et al. (2017b)):

$$f_t = 0.356\,\mathrm{nHz}\left(\frac{1}{F(e)}\frac{\rho_{i,100}}{\sigma_{200}}\right)^{3/10}\mathscr{M}_9^{-2/5}, \tag{5.2}$$

where

$$F(e) = \frac{1+(73/24)e^2+(37/96)e^4}{(1-e^2)^{7/2}} \tag{5.3}$$

(Peters and Mathews, 1963), $\rho_{i,100} = \rho_i/(100\,M_\odot \mathrm{pc}^{-3})$ is the density of the stellar environment at the influence radius of the SMBHB, $\sigma_{200} = \sigma/(200\,\mathrm{km\,s}^{-1})$ is the velocity dispersion of stars in the galaxy and $\mathscr{M}_9 = \mathscr{M}/(10^9 M_\odot)$ is the rescaled chirp mass. The stellar density is described by a Dehnen profile (Dehnen, 1993) with a fiducial profile parameter $\gamma = 1$. We take the velocity dispersion σ_{200} to be a constant (see Chen et al. (2017b)).

Finally, the spectrum described by equation (5.1) is corrected by including an a high frequency drop related to an upper mass limit calculated, at each frequency, via (equation 39 in Chen et al.

(2017b))

$$N_{\Delta f} = \int_{f-\Delta f/2}^{f+\Delta f/2} df \int_{\bar{\mathscr{M}}}^{\infty} d\mathscr{M} \int_{0}^{\infty} dz \frac{d^3N}{df dz d\mathscr{M}} = 1. \tag{5.4}$$

This upper mass limit $\bar{\mathscr{M}}$ takes into account that, particularly at high frequencies, there is less than 1 binary above $\bar{\mathscr{M}}$ contributing to the signal within a frequency bin $\Delta f = 1/T$. Statistically, this means that in a given realization of the universe, there will be either one or zero loud sources contributing to the signal. In the case the source is present, it can be removed from the GWB computation since it will be likely resolvable as an individual deterministic GW source (see discussion in Sesana et al., 2008).

In Chen et al. (2017b), we used a phenomenological parametric function to describe the SMBHB merger rate $d^2n/(dzd\mathscr{M})$, and introduced an extra parameter e_0 to allow for eccentric binaries at f_t. The quantity $d^2n/(dzd\mathscr{M})$, however, cannot be directly measured from observations. It can be either computed theoretically from galaxy and SMBH formation and evolution models (e.g. Sesana et al., 2008; Ravi et al., 2012; Kelley et al., 2017b) or it can be indirectly inferred from observations of other astrophysical quantities, such as the galaxy mass function, pair fraction, typical merger timescales, and the SMBH – host galaxy relation. Parametrizing the SMBHB merger rate as a function of astrophysical observables would therefore allow to reverse engineer the outcome of current and future PTA observations to obtain useful constrains on those observables. With this goal in mind, in this paper we expand the model from Chen et al. (2017b) in two ways:

1. we multiply the fiducial density profile $\rho_{i,100}$ by an extra parameter ζ_0 to allow for variations in density of the stellar environment;

2. we cast the phenomenological SMBHB merger rate $d^2n/(dzd\mathscr{M})$ in terms of astrophysical observables, such as galaxy mass function and pair fraction, galaxy - black hole relations, etc., as we detail next in Section 5.2.

5.2 Parametric model of the SMBHB merger rate

As detailed in Sesana (2013a); Sesana et al. (2016) the differential galaxy merger rate per unit redshift, mass and mass ratio can be written as

$$\frac{d^3 n_G}{dz' dM dq} = \frac{\Phi(M,z)}{M \ln 10} \frac{\mathscr{F}(M,z,q)}{\tau(M,z,q)} \frac{dt}{dz}, \tag{5.5}$$

where $\Phi(M,z)$ is the redshift dependent galaxy stellar mass function (GSMF), $\mathscr{F}(M,z,q)$ is the differential pair fraction with respect to the mass ratio q (see equation (5.12) below) and $\tau(M,z,q)$ is the merger timescale. M is the mass of the primary galaxy, z is the redshift of the *galaxy pair* and q is the mass ratio between the two galaxies. It is important to note that a pair of galaxies at redshift z will merge at redshift $z' < z$. The timescale $\tau(M,z,q)$ is used to convert the pair fraction of galaxies at z into the galaxy merger rate at $z' < z$ (Mundy et al., 2017). The merger redshift is obtained by solving for z' the implicit equation

$$\int_{z'}^{z} \frac{dt}{d\tilde{z}} d\tilde{z} = \tau(M,z,q), \tag{5.6}$$

where for a flat Lambda CDM model

$$\frac{dt}{d\tilde{z}} = \frac{1}{H_0(1+\tilde{z})\sqrt{\Omega_M(1+\tilde{z})^3 + \Omega_k(1+\tilde{z})^2 + \Omega_\Lambda}}. \tag{5.7}$$

The galaxy stellar mass function $\Phi(M,z)$ can be written as a single Schechter function (Conselice et al., 2016)

$$\Phi(M,z) = \frac{dn_G}{d\log_{10} M} = \ln 10 \; \Phi_0(z) \Big(\frac{M}{M_0(z)}\Big)^{1+\alpha_0(z)} \exp\Big(-\frac{M}{M_0(z)}\Big), \tag{5.8}$$

where $\Phi_0(z)$, $M_0(z)$, $\alpha_0(z)$ are phenomenological functions of redshift of the form (Mortlock

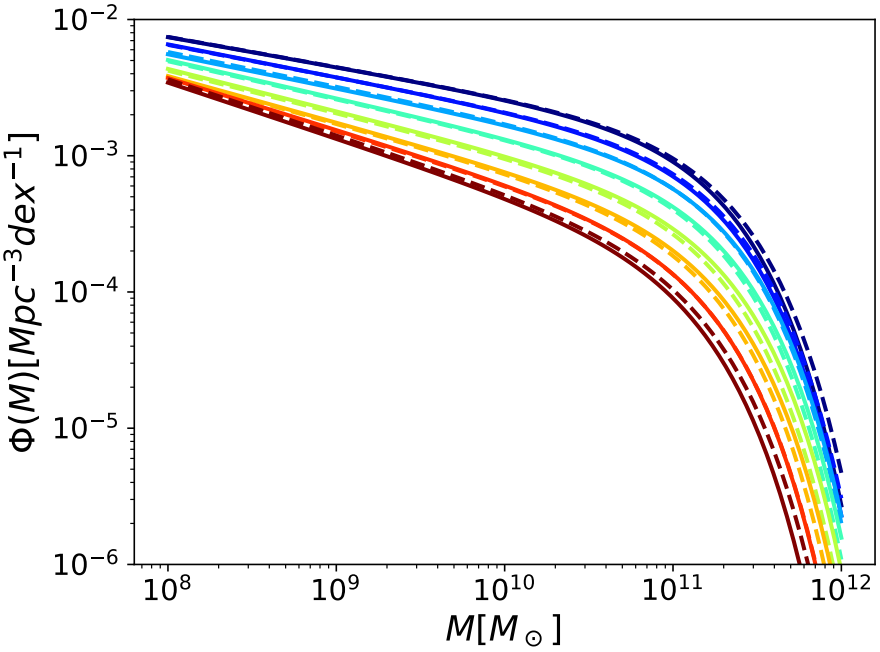

Figure 5.1: Comparison between measured and computed GSMFs for 8 redshift bins in the range $0.4 < z < 3$, where blue represents lower and red higher redshift values. The solid lines represent the original mass functions reported by Conselice et al. (2016) and Mortlock et al. (2015), the dashed lines are best fits obtained using equation (5.8) with the parametric functions $\Phi_0(z), M_0(z), \alpha(z)$ for the central values of the 8 corresponding redshift bins.

et al., 2015):

$$\log_{10}\Phi_0(z) = \Phi_0 + \Phi_I z \tag{5.9}$$

$$M_0(z) = M_0 \tag{5.10}$$

$$\alpha_0(z) = \alpha_0 + \alpha_I z \tag{5.11}$$

The 5 parameters $\Phi_0, \Phi_I, M_0, \alpha_0, \alpha_I$ are sufficient to fit the original Schechter functions at any redshift; an example is shown in figure 5.1. To simplify the notation, in the following Φ_0, M_0, α_0 will implicitly denote their corresponding redshift dependent functions $\Phi_0(z)$, $M_0(z)$, $\alpha_0(z)$.

The differential pair fraction as a function of q is given by

$$\mathscr{F}(M,z,q) = \frac{df_{\text{pair}}}{dq} = f_0'\left(\frac{M}{aM_0}\right)^{\alpha_f}(1+z)^{\beta_f}q^{\gamma_f}, \tag{5.12}$$

where $aM_0 = 10^{11} M_\odot$ is an arbitrary reference mass. Note that, in the literature, pair fractions are usually given as a function of primary galaxy mass and redshift only (e.g. Mundy et al., 2017), such that

$$f_{\rm pair} = f_0 \Big(\frac{M}{aM_0} \Big)^{\alpha_f} (1+z)^{\beta_f}, \tag{5.13}$$

i.e. integrated over the mass ratio of the pairs. The integral of equation (5.12) over q gives

$$f_{\rm pair} = f_0' \Big(\frac{M}{aM_0} \Big)^{\alpha_f} (1+z)^{\beta_f} \int q^{\gamma_f} dq, \tag{5.14}$$

which becomes equivalent to equation (5.13) by setting

$$f_0 = f_0' \int q^{\gamma_f} dq. \tag{5.15}$$

Equation (5.15) allows to map an observational prior of the form of equation (5.13) into the four parameters of our model $f_0', \alpha_f, \beta_f, \gamma_f$.

We use an analogue parametrization for the merger timescale:

$$\tau(M,z,q) = \tau_0 \Big(\frac{M}{bM_0} \Big)^{\alpha_\tau} (1+z)^{\beta_\tau} q^{\gamma_\tau}, \tag{5.16}$$

where $bM_0 = 0.4/h_0 \times 10^{11} M_\odot$, and $\tau_0, \alpha_\tau, \beta_\tau, \gamma_\tau$ are four further model parameters. Equation (5.16) has originally been derived to describe the *galaxy* merger timescale (Snyder et al., 2017). A further delay is, however, expected between the galaxy merger and the SMBHB final coalescence. In fact, after dynamical friction has merged the two galaxies and has brought the two SMBHs in the nuclear region, the newly formed SMBHB has to harden via energy and angular momentum losses mediated by either stars or gas, before GW emission eventually takes over (see Dotti et al., 2012, for a review). Depending on the details of the environment, this process can take up to several Gyrs, and even cause the binary to stall (Sesana and Khan, 2015; Vasiliev et al., 2015; Kelley et al., 2017a). For simplicity, we assume here that this further delay can be re-absorbed in equation (5.16), which we then use to describe the time elapsed between the observed galaxy

pair and the final *SMBHB* coalescence.

Substituting equations (5.8), (5.12) and (5.16) into (5.5) gives

$$\frac{d^3 n_G}{dz' dM dq} = n_{\rm eff}\left(\frac{M}{M_0}\right)^{\alpha_{\rm eff}} e^{-M/M_0}(1+z)^{\beta_{\rm eff}} q^{\gamma_{\rm eff}} \frac{dt}{dz}, \tag{5.17}$$

where the effective parameters are

$$\begin{aligned} n_{\rm eff} &= \frac{\Phi_0 f_0'}{M_0 \tau_0} \frac{b^{\alpha_\tau}}{a^{\alpha_f}} = \frac{\Phi_0 f_0'}{M_0 \tau_0}\left(\frac{0.4}{h_0}\right)^{\alpha_\tau}\left(\frac{10^{11}}{M_0}\right)^{\alpha_\tau - \alpha_f} \\ \alpha_{\rm eff} &= \alpha_0 + \alpha_f - \alpha_\tau \\ \beta_{\rm eff} &= \beta_f - \beta_\tau \\ \gamma_{\rm eff} &= \gamma_f - \gamma_\tau \end{aligned} \tag{5.18}$$

Equation (5.17) is still a function of the merging galaxy stellar masses, which needs to be translated into SMBH masses. The total mass of a galaxy M can be converted into its bulge mass $M_{\rm bulge}$, using assumptions on the ellipticity of the galaxy: more massive galaxies are typically elliptical and have higher bulge to total stellar mass ratio. We use a phenomenological fitting function (Bernardi et al., 2014; Sesana et al., 2016) to compute the bulge mass of a galaxy from its total mass:

$$\frac{M_{\rm bulge}}{M} = \begin{cases} \frac{\sqrt{6.9}}{(\log M - 10)^{1.5}} \exp\left(\frac{-3.45}{\log M - 10}\right) + 0.615 & \text{if } \log M > 10 \\ 0.615 & \text{if } \log M < 10. \end{cases} \tag{5.19}$$

Note that this fit is appropriate for ellipticals and spheroidals, whereas spiral galaxies usually have smaller bulge to total mass ratio. In Sesana (2013a) different scaling relations were used for blue and red galaxy pairs (under the assumption that blue pairs are predominantly spirals and red pairs predominantly elliptical). The result was that the GW signal is completely dominated by red pairs. We have checked on Sesana (2013a) data that approximating all galaxies as spheroidals affects the overall signal by less than 0.05dex. We therefore apply equation (5.19) to all galaxies,

independent on their colour or morphology.

We can then apply a scaling relation between the galaxy bulge mass $M_{\rm bulge}$ and black hole mass $M_{\rm BH}$ of the form (see e.g. Kormendy and Ho, 2013)

$$M_{\rm BH} = \mathcal{N}\left\{M_*\left(\frac{M_{\rm bulge}}{10^{11}M_\odot}\right)^{\alpha_*}, \varepsilon\right\}, \tag{5.20}$$

where $\mathcal{N}\{x,y\}$ is a log normal distribution with mean value x and standard deviation y, to translate galaxy mass M into black hole mass $M_{\rm BH}$. Note that the galaxy mass ratio q is in general different from the black hole mass ratio $q_{\rm BH} = q^{\alpha_*}$. Finally, the galaxy merger rate n_G (5.17) can be converted into the SMBHB merger rate n

$$\frac{d^3n}{dz'dM_{\rm BH}dq_{\rm BH}} = \frac{d^3n_G}{dz'dMdq}\frac{dM}{dM_{\rm BH}}\frac{dq}{dq_{\rm BH}}. \tag{5.21}$$

Equation (5.20) adds three further parameters to the model: $M_*, \alpha_*, \varepsilon$. Lastly, it is convenient to map $M_{\rm BH}, q_{\rm BH}$ into the SMBHB chirp mass $\mathscr{M} = M_{\rm BH}q_{\rm BH}^{3/5}/(1+q_{\rm BH})^{1/5}$, by performing a variable change and integrate over the black hole mass ratio to produce a SMBHB merger rate as a function of chirp mass and redshift only:

$$\frac{d^2n}{dz'd\mathscr{M}} = \int \frac{d^3n_G}{dz'dM_{\rm BH}dq_{\rm BH}}\frac{dM_{\rm BH}}{d\mathscr{M}}dq_{\rm BH}. \tag{5.22}$$

Summarizing, the SMBHB merger rate $d^2n/(dz'd\mathscr{M})$ is described as a function of 16 empirical parameters that are related to astrophysical observable: $(\Phi_0, \Phi_I, M_0, \alpha_0, \alpha_I)$ for the GSMF, $(f_0', \alpha_f, \beta_f, \gamma_f)$ for the pair fraction, $(\tau_0, \alpha_\tau, \beta_\tau, \gamma_\tau)$ for the merger timescale, and $(M_*, \alpha_*, \varepsilon)$ for the galaxy – SMBH scaling relation. Further, the first three sets of parameters can be grouped into the four effective parameters given by equation (5.18). The two extra parameters (e_0, ζ_0) enter the computation of the shape of the GW spectrum via the transition frequency f_t given in equation (5.2). We can therefore express the stochastic GWB in equation (5.1) as a function of 18 phenomenological parameters, see table 5.1.

5.3 GWB simulations and analysis

As in Chen et al. (2017a), we compute the signal-to-noise-ratio S/N $\mathscr{S}$ of a detection of a GWB in the frequency domain as (Moore et al., 2015b; Rosado et al., 2015):

$$\mathscr{S}^2 = 2 \sum_{i=1,N} \sum_{j>i} T_{ij} \int \frac{\Gamma_{ij}^2 S_h^2}{(S_n^2)_{ij}} df. \tag{5.23}$$

where Γ_{ij} are the Hellings-Downs coefficients (Hellings and Downs, 1983):

$$\Gamma_{ij} = \frac{3}{2}\gamma_{ij}\ln\left(\gamma_{ij}\right) - \frac{1}{4}\gamma_{ij} + \frac{1}{2} + \frac{1}{2}\delta_{ij}, \tag{5.24}$$

with $\gamma_{ij} = [1-\cos(\theta_{ij})]/2$ and θ_{ij} being the relative angle between pulsars i and j. S_h and S_n are spectral densities of the signal and noise respectively, and S_n includes the 'self noise' contribution of the pulsar term (see equation 11 in Chen et al. (2017a) for details).

We can simplify equation (5.23) by assuming that all pulsars are identical (except for their position in the sky), i.e. all pulsars have the same properties: rms $\delta_i = \delta$, observation time $T_{ij} = T$ and observation cadence Δt. Furthermore, we also assume that there is a sufficient number of pulsars N, uniformly distributed in the sky, so that each individual coefficient Γ_{ij} can be replaced by the rms computed across the sky $\Gamma = \sqrt{\langle\Gamma_{ij}^2\rangle} = 1/(4\sqrt{3})$, and the double sum over all pairs of pulsars $\sum_{i=1,N}\sum_{j>i}$ becomes $N(N-1)$. For an observation time T the spectrum of the GWB is resolved in Fourier frequency resolution bins of equal width $\Delta f_i = 1/T$, centred at $f_i = (2i+1)/(2T)$. The total S/N in equation (5.23) can thus be split into frequency bin components $\mathscr{S}_i$:

$$\mathscr{S}_i^2 \approx T\Gamma^2 N(N-1)\frac{S_h^2}{S_n^2}\Delta f_i. \tag{5.25}$$

In the strong signal regime ($S_h \gg S_n$) equation (5.25) can further be reduced to the approximate

total S/N of a strong detection in M frequency bins

$$\mathscr{S} = \left(\sum_i \mathscr{S}_i^2\right)^{1/2} = \left(\frac{\Gamma^2}{1+\Gamma^2} MN(N-1)\right)^{1/2} \approx \Gamma N M^{1/2}, \tag{5.26}$$

where we used the fact that $\Gamma \ll 1$ and $N \gg 1$. Equation (5.26) is a drastic simplification, still it provides the relevant scaling between $\mathscr{S}$, number of pulsars in the array, and frequency range in which the signal is resolved. For $\Gamma \approx 0.14$, to achieve a S/N ≈ 5 in the lowest few frequency bins, an array of about 20 equally good pulsars is needed.

PTA data are simulated as in Chen et al. (2017a). For a signal h_c with amplitude $A_{\rm det,i}$ in the i-th frequency bin, the detection S/N $\mathscr{S}_i$ is related to the detection uncertainty $\sigma_{\rm det,i}$ via (see equation 18 in Chen et al. (2017a))

$$\sigma_{\rm det,i} = \frac{1}{\mathscr{S}_i}. \tag{5.27}$$

5.3.1 Simulated datasets

Besides adding a future and an ideal upper limit, we use the same simulation setup as in Chen et al. (2017a), with the simplifying assumptions that all pulsars are observed with the same cadence Δt for the same duration of T and have the same rms of δ. These assumptions only affect the S/N of the detection, thus setting the error bars $\sigma_{\rm det,i}$. This is purely a choice of convenience that does not affect the general validity of our results. We expand upon the 4 cases from Chen et al. (2017a) by adding 2 more upper limit cases to get a total of 6 fiducial cases (3 upper limits and 3 detections):

1. case *PPTA15*: we use the upper limit curve of the most recent PPTA analysis, as given by Shannon et al. (2015), which is representative of current PTA capabilities and results in a GWB upper limit of $A = 10^{-15}$;[1]

[1] A represents the amplitude of the GWB at a reference frequency of $f = 1\text{yr}^{-1}$ under the assumption that its spectrum is described by a single power law with $h_c \propto f^{-2/3}$, appropriate for circular, GW-driven binaries.

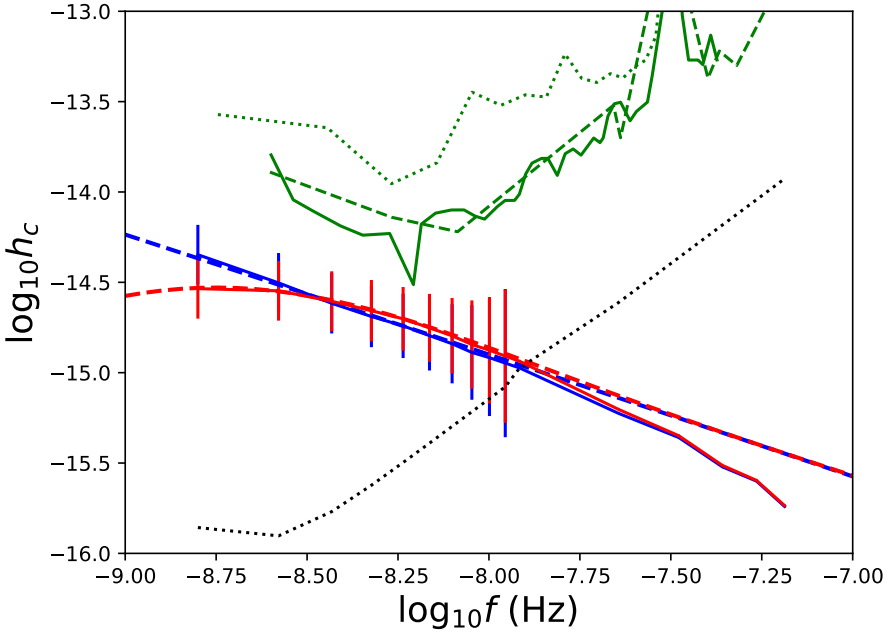

Figure 5.2: Examples of simulated detections for two different spectral shapes. Signal models correspond to the default SMBHB population with parameters defined in Section 5.4 and high eccentricity ($e_t = 0.9$, red) and almost circular ($e_t = 0.01$, blue). For each model, solid lines are the theoretical spectra including the high frequency steepening due to the mass upper limit defined by equation (5.4), dashed lines depict spectra excluding this feature (therefore with $h_c \propto f^{-2/3}$ at high frequency) for comparison. Error bars centred around the model value are the observed amplitudes with associated uncertainties when $\mathscr{S}_i > 1$. The black dotted line represents the nominal 1σ sensitivity curve of the PTA for the *I*PTA30 case. Green lines in the upper part of the figure are current EPTA (dotted), NANOGrav (dashed) and PPTA (solid) upper limits.

2. case *PPTA16*: we shift the *PPTA15* curve down by one order of magnitude, which is representative of an upper limit of $A = 10^{-16}$, reachable in the SKA era;

3. case *PPTA17*: we shift the *PPTA15* curve down by two orders of magnitude, which is representative of an upper limit of $A = 10^{-17}$. Although such sensitivity cannot be achieved in the foreseeable future, we use it to infer what conclusions can be drawn by a non-detection at a level well below currently predicted GWB values;

4. case *IPTA30*: $N = 20$, $\delta = 100$ns, $T = 30$yr, $\Delta t = 1$ week. This PTA results in a detection S/N$\approx 5-10$ and is based on a future extrapolation of the current IPTA, without the addition of new telescopes;

5. case *SKA20*: $N = 100$, $\delta = 50$ns, $T = 20$yr, $\Delta t = 1$ week. This PTA results in a high

significance detection with S/N$\approx 30-40$, which will be technically possible in the SKA era;

6. case *ideal*: $N = 500$, $\delta = 1$ns, $T = 30$yr, $\Delta t = 1$ week. This is beyond SKA capabilities but provides useful insights of what might be achievable in principle.

As stated above, for each simulation we compute the S/N $\mathscr{S}_i$ at each frequency bin. If $\mathscr{S}_i > 1$, we then assume an observed signal with amplitude $A_i = h_c(f_i)$ and error described by a log-normal distribution with width given by equation (5.27). Unlike Chen et al. (2017a), if $\mathscr{S}_i < 1$, we do not place an upper limit at that frequency. This is to save on computational costs, having verified that including the upper limit does not affect the resulting posterior distributions. Examples of signal generation are shown in figure 5.2 for spectra with $A = 5.0 \times 10^{-16}$ at $f = 1/1$yr in the *IPTA30* case. This setup results in an initial detection with low S/N, $\mathscr{S} \approx 7$.

5.3.2 Data analysis method

We apply Bayes' theorem to perform inference on our model M, given some data d and a set of parameters θ:

$$p(\theta|d,M) = \frac{p(\theta|M)p(d|\theta,M)}{p(d|M)}, \tag{5.28}$$

where $p(\theta|d,M)$ is the posterior distribution coming from the analysis of the PTA measurement, $p(\theta|M)$ is the prior distribution and accounts for any beliefs on the constraints of the model parameters (prior to the PTA measurement), $p(d|\theta,M)$ is the likelihood of producing the data for a given model and parameter set, and $p(d|M)$ is the evidence which a measure of how likely the model is to produce the data.

To simulate detections we apply the likelihood from Chen et al. (2017a)

$$p_{\rm det}\left(d|A_{\rm trial}(f)\right) \propto \exp\left\{-\frac{[\log_{10}A_{\rm trial}(f) - \log_{10}A_{\rm det}(f)]^2}{2\sigma_{\rm det}(f)^2}\right\}, \tag{5.29}$$

to each frequency bin for which $\mathscr{S}_i > 1$, and then sum over the frequency bins to obtain the total likelihood. For the upper limit analyses, we use the directly derived likelihood from the PPTA upper limit, as described in Appendix A.3 of Middleton et al. (2018).

Prior distributions are taken from independent theoretical and observational constrains, as described in Section 5.4. The parameter space is sampled using cpnest (Del Pozzo and Veitch, 2015), which is a parallel implementation of the nested sampling algorithm in the spirit of Veitch et al. (2015) and Skilling (2004). Nested sampling algorithms do not only provide posterior distributions, but also the total evidence. This allows us to compute Bayes factors for model comparisons. Each simulation has been run with 1000 livepoints, producing ~ 2500 independent posterior samples.

5.4 Defining the prior ranges of the model parameters

There is a vast literature dedicated to the measurement of the GSMF, galaxy pair fraction, merger timescale and SMBH – host galaxy scaling relations. We now described how independent observational and theoretical work translates into constrained prior distributions of the 18 parameters of our model. A summary of all the prior ranges is given in table 5.1.

5.4.1 Galaxy stellar mass function

At any given redshift, the GSMF is usually described as a Schechter function with three parameters (Φ_0, M_0, α_0). The parameters, however, are independently determined at any redshift. Depending on the number of redshift bins n to be considered in the computation, this can easily lead to a very large number of parameters $3n$. To reduce the dimensionality of the problem from $3n$ to five, we note that the parameters (Φ_0, α_0) show clear linear trends with redshift, whilst M_0 is fairly constant (see Mortlock et al. (2015)). This allows for a re-parametrisation as a function

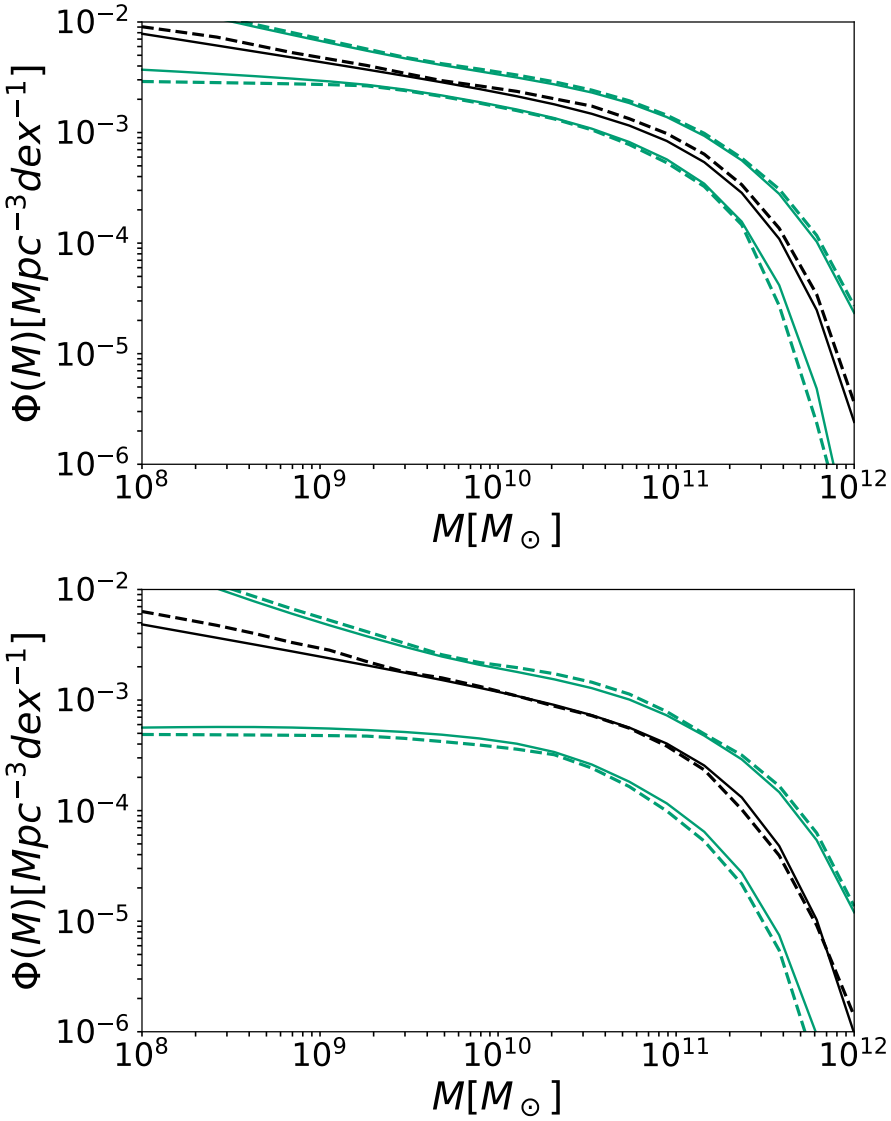

Figure 5.3: Comparison between the allowed region of GSMFs for different redshift bins computed from Conselice et al. (2016) (3 dashed lines) and the region of GSMFs recovered by using the five GSMF parameters $(\Phi_0, \Phi_I, M_0, \alpha_0, \alpha_I)$ (3 solid lines). Black lines represent the median, whilst green lines represent the upper and lower bounds of the 99% confidence region. The top and bottom panel show the GSMF in the $0 < z < 1$ and $1 < z < 3$ redshift bins respectively.

of the 5 parameters $(\Phi_0, \Phi_I, M_0, \alpha_0, \alpha_I)$ performed in Section 5.2.

A comprehensive list of published values for the parameters (Φ_0, M_0, α_0) for various redshift bins can be found in Conselice et al. (2016), which forms the basis of our prior distribution. We compute $\Phi(M, z)$ between $10^9 M_\odot$ and $10^{12} M_\odot$ for all sets of (Φ_0, M_0, α_0), dividing the sample in two redshift bins: $0 < z < 1$ and $1 < z < 3$. This gives a range of values for $\Phi(M, z)$, shown

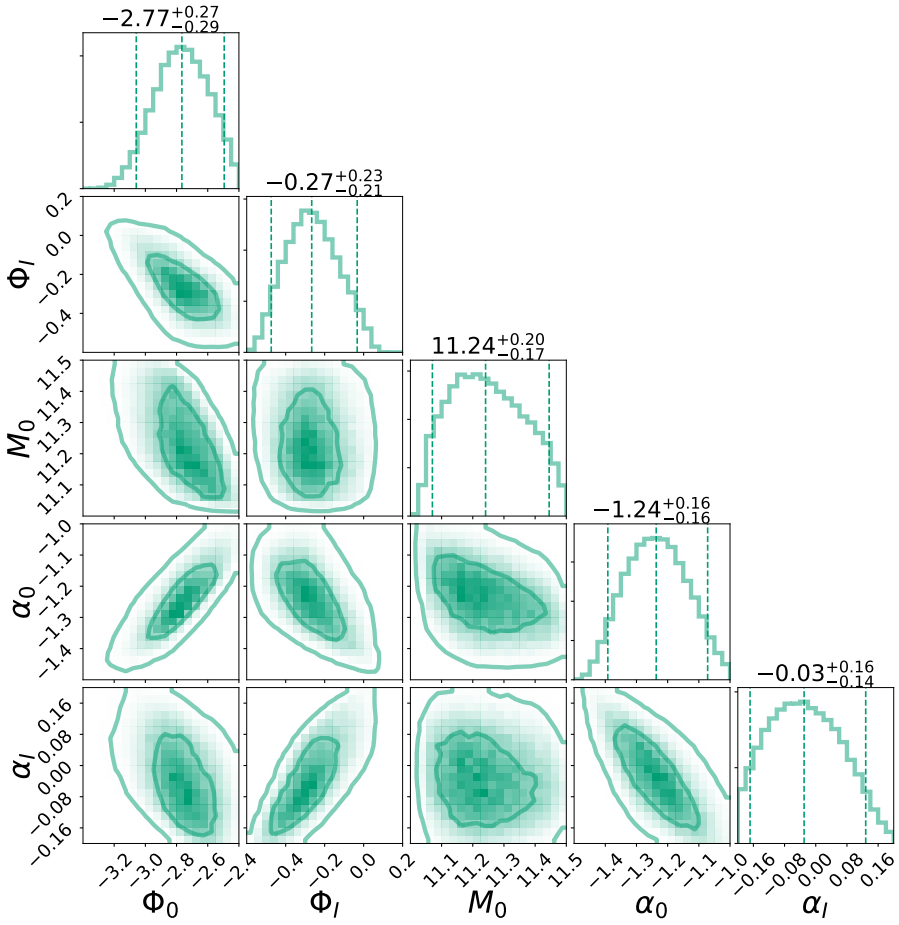

Figure 5.4: Corner plot showing the prior distributions of the five GSMF parameters $(\Phi_0, \Phi_I, M_0, \alpha_0, \alpha_I)$ used in this work.

in figure 5.3. We then take uniform distributions of $(\Phi_0 \in [-3.4, -2.4], \Phi_I \in [-0.6, 0.2], M_0 \in [11, 11.5], \alpha_0 \in [-1.5, -1.], \alpha_I \in [-0.2, 0.2])$, compute the $\Phi(M, z)$ for each sample and redshift bins and compare them against the allowed range. If the value is within the range, the sample is accepted, otherwise it is rejected. The resulting prior distributions are shown in figure 5.4.

5.4.2 Pair fraction

Constraints on the pair fraction have been derived by counting the numbers of paired and merged galaxies in various surveys with a number of different photometric and spectroscopic techniques (see, e.g., Conselice et al., 2003; Xu et al., 2012; Robotham et al., 2014; Keenan et al., 2014). Recently, Mundy et al. (2017) have combined data from several surveys to produce an overall

up-to-date constraint. We base our prior range on the results reported in table 3 of their paper, for the All+GAMA+D17 survey combination and galaxy separation of $5-30$ kpc:

$$f_{\rm pair} = \begin{cases} 0.028 \pm 0.002 \times (1+z)^{0.80\pm0.09} & \text{for } \log M > 10 \\ 0.024 \pm 0.004 \times (1+z)^{0.78\pm0.20} & \text{for } \log M > 11 \end{cases} \tag{5.30}$$

This is one of the flatter redshift dependences within the Mundy et al. (2017) compilation. It is, however, likely the more accurate measurement, coming from a combination of deep surveys. Moreover, while stronger redshift dependences are common for Milky Way-size galaxies, most $f_{\rm pair}$ measurements of galaxies with $M > 10^{11} M_{\odot}$ have a relatively flat redshift dependence. Most of the GWB will come from SMBHBs hosted in those massive galaxies, this justifies our choice. Noting that both sets of parameters and uncertainties in equation (5.19) are similar, we use flat priors for $f_0 \in [0.02, 0.03]$ and $\beta_f \in [0.6, 1]$ for all galaxy masses. Steeper redshift dependences are allowed in our set of 'extended prior', introduced in section 5.4.5 below. Mundy et al. (2017) also find no significant dependency on galaxy mass, thus we pick $\alpha_f, \gamma_f \approx 0$, adding the possibility of a mild deviation by imposing a flat prior $\alpha_f, \gamma_f \in [-0.2, 0.2]$.

5.4.3 Merger timescale

In this paper, we define the merger timescale, as the time elapsed between the observation of a galaxy pair at a given projected separation (usually 20 or 30 kpc) and the final coalescence of the SMBHB. Galaxy merger timescales have been computed both for simulations of isolated galaxy mergers (Lotz et al., 2011) and from ensemble of halos and galaxies extracted from large cosmological simulations (Kitzbichler and White, 2008; Snyder et al., 2017), resulting in a large dynamical range. We therefore choose the parametrisation given by equation (5.16), which is sufficiently generic to cover the whole range of possible effects influencing the total merger time. To include further delays of the SMBHB due to the hardening phase, we choose wide uniform prior ranges $\tau_0 \in [0.1, 2]$ Gyr and $\beta_\tau \in [-2, 1]$. The mass dependencies are generally found to be

milder, playing a minor role. We therefore choose flat prior ranges $\alpha_\tau, \gamma_\tau \in [-0.2, 0.2]$.

5.4.4 $M_{\rm bulge} - M_{\rm BH}$ relation

Since SMBHs are thought to have an important impact on the formation and evolution of their host galaxy and vice versa, the relation between their mass and several properties of the host galaxy has been studied and constrained by a number of authors (see Kormendy and Ho, 2013, for a comprehensive review). Here we use the tight relation between the SMBH mass and the stellar mass of the spheroidal component (i.e. the bulge) of the host galaxy, which has been described as a power-law of the form of equation (5.20) with some intrinsic scattering. Although non-linear functions have been proposed in the literature (see, e.g., Graham and Scott, 2013; Shankar et al., 2016), the non-linearity is mostly introduced to describe the (observationally very uncertain) low mass end of the relation. Since the vast majority of the GWB is produced by SMBH with masses above $10^8 M_\odot$ (Sesana et al., 2008), we do not consider here those alternative parametrizations.

To construct the prior distributions, we apply the same method as in Section 5.4.1. We define the allowed region of the $M_{\rm BH} - M_{\rm bulge}$ relation as the one enclosed within a compilation of relations collected from the literature in Middleton et al. (2018). We then draw relations from a uniform distribution of $\log_{10} M_* \in [7.75, 8.75]$ and $\alpha_* \in [0.9, 1.1]$ and accept them if they fall within the region allowed by observations. Additionally, we assume a flat distribution for the scattering $\varepsilon \in [0.3, 0.5]$. Figure 5.5 shows the obtained prior distributions for $(M_*, \alpha_*, \varepsilon)$.

5.4.5 Eccentricity and stellar density

The last two parameters deal with the properties of the individual binary. As the eccentricity at decoupling is not well constrained (see, e.g. Sesana and Khan, 2015; Mirza et al., 2017), we choose an uninformative flat prior $e_0 \in [0.01, 0.99]$. The other additional parameter describes

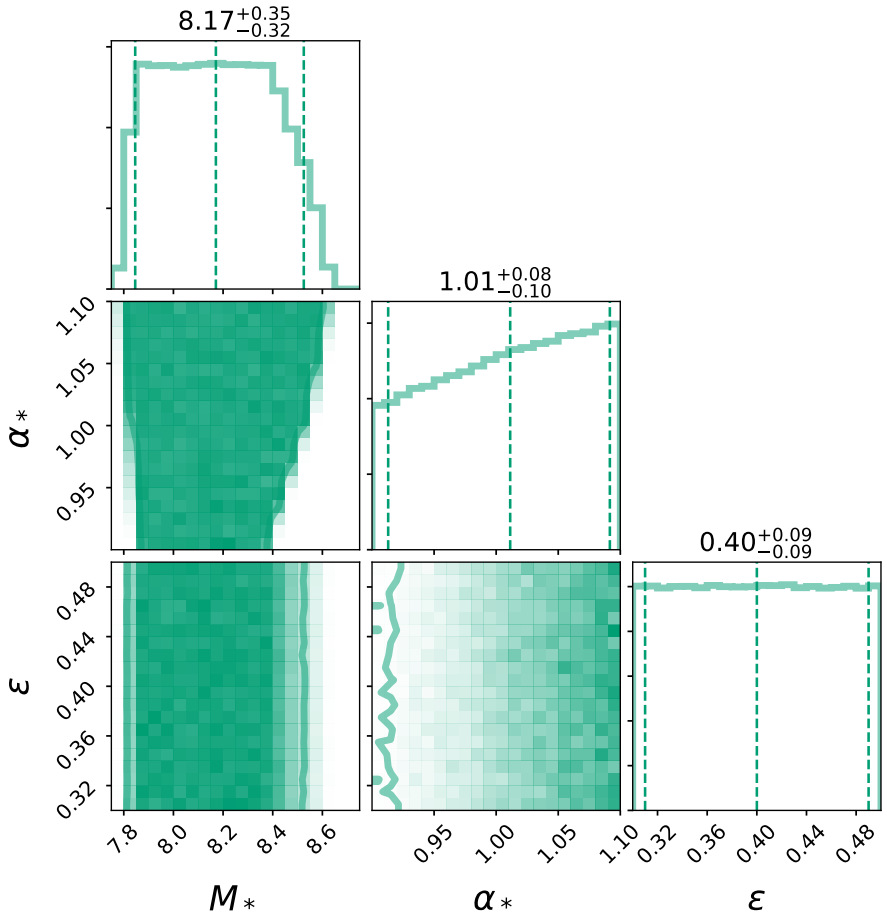

Figure 5.5: Corner plots showing the prior distributions of the $M_{\rm bulge} - M_{\rm BH}$ relation (M_*, α_*) and scatter ε parameters used in this work.

the stellar density around the SMBHB (see section 5.1). ζ_0 is a multiplicative factor added to the density at the SMBHB influence radius, $\rho_{i,100}$, calculated by using the fiducial Dehnen profile defined in Chen et al. (2017b). This has an impact on the frequency of decoupling, as a higher density of stars in the galactic centre means more efficient scattering. The SMBHB thus experiences a faster evolution, reaching a higher f_t before transitioning to the efficient GW emission stage. We choose to include densities that are between 0.01 and 100 times the fiducial value, which is consistent with the large variation of stellar densities observed in cusped vs cored galaxies (Kormendy et al., 2009). This translates into a flat prior $\log_{10}\zeta_0 \in [-2, 2]$.

parameter	description	standard	extended
Φ_0	GSMF norm	-2.8 ± 0.3	-2.8 ± 0.3
Φ_I	GSMF norm redshift evolution	-0.25 ± 0.22	-0.25 ± 0.22
$\log_{10} M_0$	GSMF scaling mass	11.25 ± 0.2	11.25 ± 0.2
α_0	GSMF mass slope	-1.25 ± 0.17	-1.25 ± 0.17
α_I	GSMF mass slope redshift evolution	0 ± 0.15	0 ± 0.15
f_0	pair fraction norm	[0.02,0.03]	[0.01,0.05]
α_f	pair fraction mass slope	[-0.2,0.2]	[-0.5,0.5]
β_f	pair fraction redshift slope	[0.6,1]	[0,2]
γ_f	pair fraction mass ratio slope	[-0.2,0.2]	[-0.2,0.2]
τ_0	merger time norm	[0.1,2]	[0.1,10]
α_τ	merger time mass slope	[-0.2,0.2]	[-0.5,0.5]
β_τ	merger time redshift slope	[-2,1]	[-3,1]
γ_τ	merger time mass ratio slope	[-0.2,0.2]	[-0.2,0.2]
$\log_{10} M_*$	$M_{\rm bulge} - M_{\rm BH}$ relation norm	8.17 ± 0.33	8.17 ± 0.33
α_*	$M_{\rm bulge} - M_{\rm BH}$ relation slope	1 ± 0.1	1 ± 0.1
ε	$M_{\rm bulge} - M_{\rm BH}$ relation scatter	[0.3,0.5]	[0.2,0.5]
e_0	binary eccentricity	[0.01,0.99]	[0.01,0.99]
$\log_{10} \zeta_0$	stellar density factor	[-2,2]	[-2,2]

Table 5.1: List of the 18 parameters in the model, including their description, standard and extended prior distribution ranges. Squared brackets indicate flat distributions, while $\pm$ signs indicate rough boundaries for the distributions found in section 5.4.

5.4.6 Extended prior ranges

Unless otherwise stated, the prior ranges just described are used in our analysis. However, we also consider 'extended' prior ranges for some of the parameters. Although observational determination of the galaxy mass function is fairly solid, identifying and counting galaxy pairs in large galaxy surveys is a delicate endeavour, especially beyond the local universe. We therefore also consider extended prior ranges $f_0 \in [0.01, 0.05]$, $\alpha_f \in [-0.5, 0.5]$ and $\beta_f \in [0, 2]$, allowing for more flexibility in the overall normalization, redshift and mass evolution of the galaxy pair

fraction. Likewise, SMBHB merger timescales are poorly constrained. The prior range adopted in Section 5.4.3 is rather wide, but notably does not allow for stalling of low redshift binaries (the maximum allowed merger timescale being 2 Gyrs). Also in this case we consider extended prior ranges $\tau_0 \in [0.1, 10]$ Gyr, $\alpha_\tau \in [-0.5, 0.5]$ and $\beta_\tau \in [-3, 1]$, allowing the possibility of SMBHB stalling at any redshift. Finally we also consider a wider prior on the scatter of the $M_{\rm BH} - M_{\rm bulge}$ relation $\varepsilon \in [0.2, 0.5]$, mostly because several authors find $\varepsilon \approx 0.3$, which is at the edge of our standard prior. All standard and extended priors are listed in table 5.1.

5.5 Results and discussion

Having defined the mathematical form of the signal, the prior ranges of all the model parameters, the simulated data and the form of the likelihood function, we performed our analysis on the six limits and detections described in Section 5.3.1. In this section, we present the results of our simulations and discuss their astrophysical consequences in detail. We first present the implications of current and future upper limits and then move onto discussing the different cases of detection. Note that, although all 18 parameters are left free to vary within their respective priors, we will present posteriors only for the subset of parameters that can be significantly constrained via PTA observations. Those are the overall normalization of the merger rate $n_{\rm eff}$, the parameters defining the merger timescale $\tau_0, \alpha_\tau, \beta_\tau$, the parameters defining the $M_{\rm BH} - M_{\rm bulge}$ relation M_*, ε, the eccentricity at the transition frequency e_0, and the normalization of the stellar density ζ_0. Because the large number of parameters and the limited information enclosed in the GWB shape and normalization, other parameters are generally unconstrained. Corner plots including all 18 parameters for all the simulated upper limits and detections are presented in Appendix B. All runs are performed using the standard prior distributions derived in Section 5.4, unless stated otherwise.

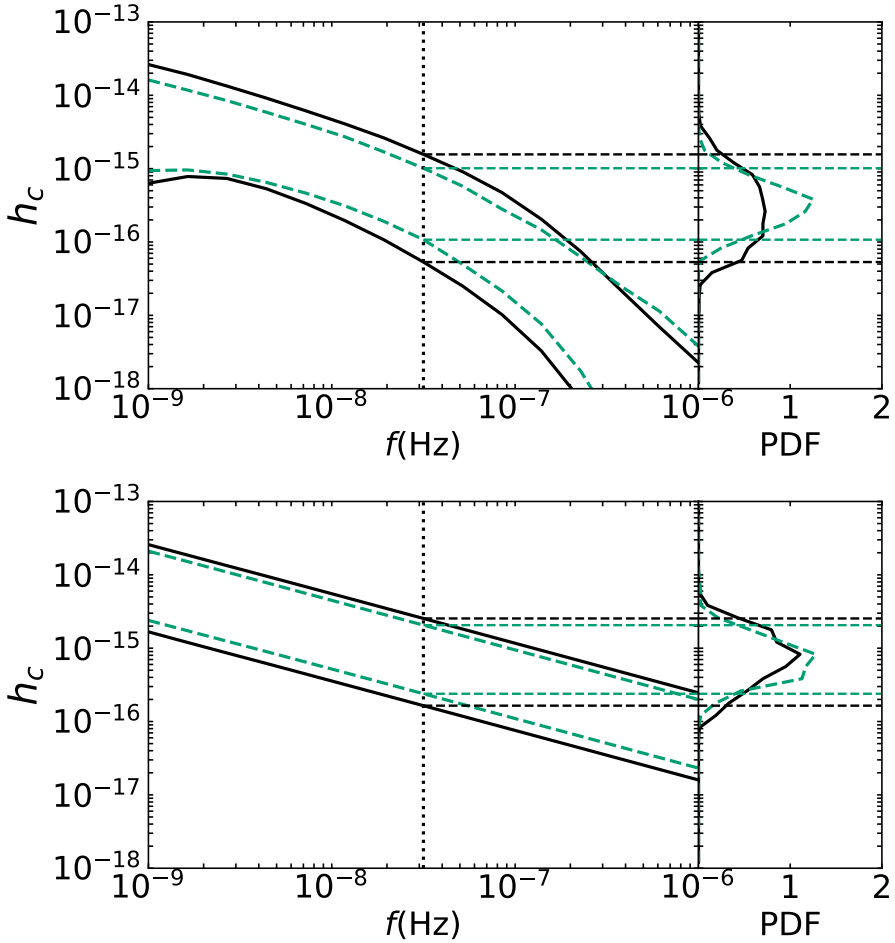

Figure 5.6: Comparison of the predicted strain h_c of the GWB from this model (green dashed lines) and the *ALL* model from Middleton et al. (2018) (solid black lines), the top panel shows the predicted strain h_c from the full model, the bottom panel restricts the model to circular eccentricity without the drop at high frequencies. The left panels show the frequency - strain plot, while the right panels show the posterior density function (PDF) at $f = 1/1\text{yr}$.

5.5.1 Predicted GWB Strain

A direct product of combining the GWB model described in Section 5.1 to the astrophysical priors presented in Section 5.4 is a robust update to the expected shape and normalization of the signal. Thus, before proceeding with the analysis of our PTA simulations, we present this updated prediction. In figure 5.6 the predicted strain of the GWB using our standard prior is compared to the *ALL* model from Middleton et al. (2018). The shapes and normalization of the two predictions are fairly consistent. At $f = 1\text{yr}^{-1}$ our model predicts $10^{-16} < h_c < 10^{-15}$ at 90% confidence, which is slightly more restrictive than the *ALL* model. This has to be expected

since model *ALL* from Middleton et al. (2018) is constructed following the method of Sesana (2013a). The latter, in fact, gave equal credit to all measurements of the galaxy mass function, pair fractions and SMBH – galaxy scaling relations, without considering any possible correlations between their underlying parameters. Our detailed selection of the prior range takes correlations between different parameters into account (see e.g. figure 5.4) and is likely more restrictive in terms of galaxy pair fraction.

The bottom panel of figure 5.6 shows the predicted h_c range assuming circular, GW driven binaries and no high frequency drop, hence producing the standard $f^{-2/3}$ spectral shape. In this simplified case $h_c(f = 1\mathrm{yr}^{-1})$ is a factor of ≈ 2 higher, spanning from 2×10^{-16} to 2×10^{-15}. Still, most of the predicted range lies below current PTA upper limits, as well as being consistent with other recent theoretical calculations (Dvorkin and Barausse, 2017; Kelley et al., 2017b; Bonetti et al., 2018).

5.5.2 Upper limits

Current Upper limit at $A(f = \mathrm{yr}^{-1}) = 1 \times 10^{-15}$

Firstly, we discuss the implication of current PTA upper limits. Here, we use the PPTA upper limit, nominally quoted as $A(f = 1\mathrm{yr}^{-1}) = 1.0 \times 10^{-15}$, which represents the integrated constraining power over the entire frequency range assuming a $f^{-2/3}$ power-law. As it has been recently pointed out by Arzoumanian et al. (2018b), that the sensitivity of PTAs have become comparable to the uncertainty in the determination of the solar system ephemeris SSE – the knowledge of which is required to refer pulse time of arrivals collected at the telescopes to the solar system baricenter. Thus, it has become necessary to include an extra parametrized model of the SSE into the GWB search analysis pipelines. This leads to a more robust albeit higher upper limit, as part of the constraining power is absorbed into the uncertainty of the SSE. A robust upper limit including this effect has recently been placed by the NANOGrav Collaboration at

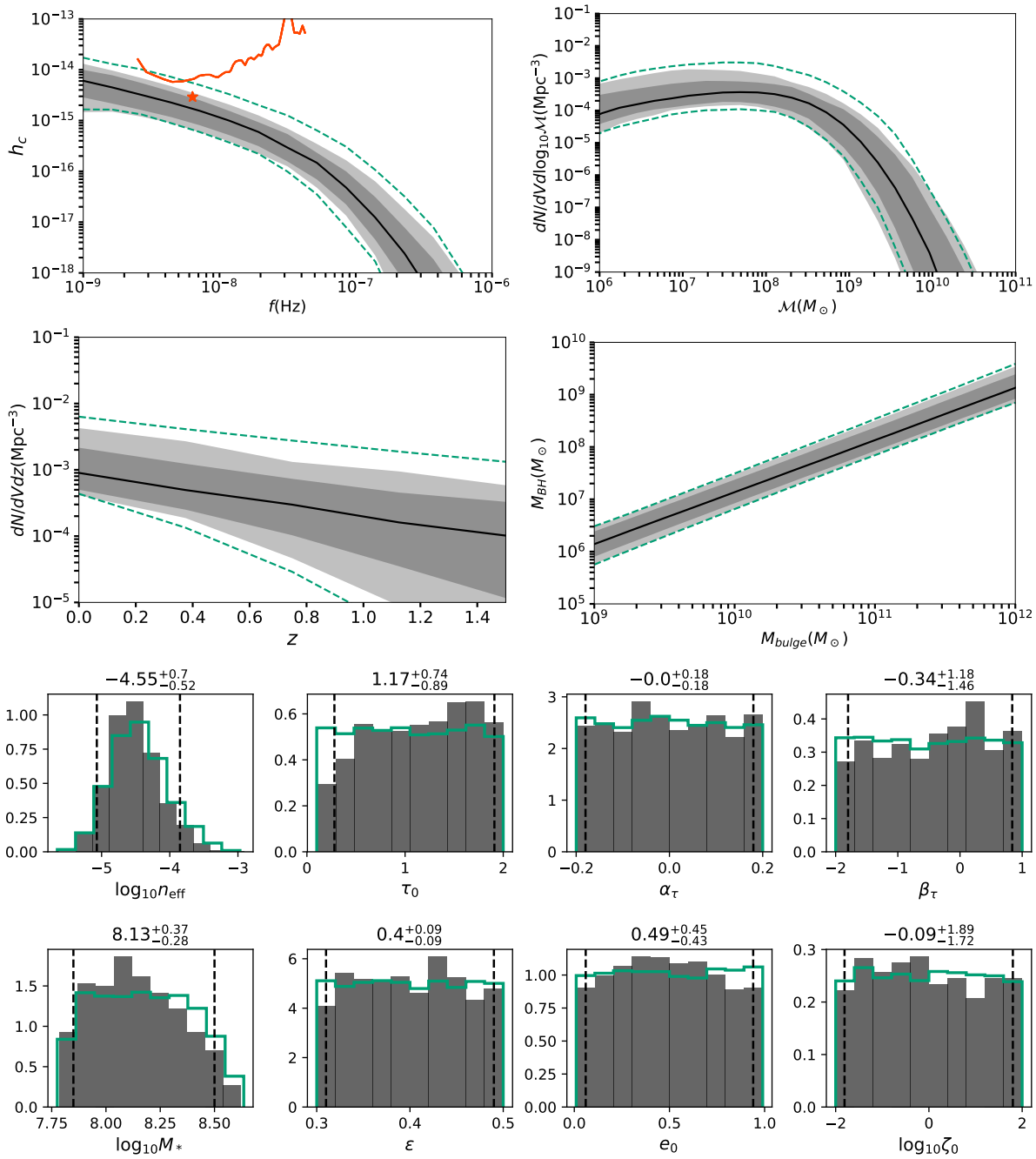

Figure 5.7: Implication of a 95% upper-limit of $A(f = \mathrm{yr}^{-1}) = 1 \times 10^{-15}$, corresponding to the most stringent PTA upper limit to date. The posterior for the spectrum (top left), mass (top right), redshift functions (centre left) and $M_{\rm bulge} - M_{\rm BH}$ relations (centre right) are shown as shaded areas, with the central 68% and 90% confidence regions indicated by progressively lighter shades of grey, and the solid black line marking the median of the posterior. The solid orange line and star in the top left panel indicate the frequency dependent and nominal frequency integrated 95% upper limit from Shannon et al. (2015) respectively. The bottom row shaded histograms show the marginalized posteriors for selected model parameters with the prior distributions indicated in green, see Section 5.4 and table 5.1.

$A(f = 1\text{yr}^{-1}) = 1.45 \times 10^{-15}$, which is higher but of the same order as the PPTA upper limit. We therefore consider the PPTA upper limit in this analysis, with the understanding that the recent NANOGrav upper limit would lead to very similar implications.

Figure 5.7 shows that upper limits add very little knowledge to our understanding of the SMBHB population as constrained by the priors on our model parameters. This is in agreement with there being no tension between the current PTA non-detection of the GWB and other astrophysical observations, as extensively discussed in Middleton et al. (2018). The range of characteristic strain of the GWB predicted by the prior ranges of our model $10^{-16} < h_c < 10^{-15}$, shown in the upper left plot of figure 5.7, is only mildly reduced by current PTA observations. Therefore, PTAs are starting to probe the interesting, astrophysical region of the parameter space, without yet being able to rule out significant areas, as can be seen in the posterior distribution of the model parameters shown at the bottom of figure 5.7. This results into a logarithmic Bayesian evidence $\log_e \mathscr{Z}(10^{-15}) = -0.55$. The evidence is normalized so that an ideal reference model that is unaffected by the measurement has $\log_e = 0$. The log evidence can therefore be directly interpreted as the Bayes factor against such a model. In this specific case, we find $e^{-0.55} = 0.58$, indicating that current upper limits do not significantly disfavour the prior range of our astrophysical model. This can also be seen in the bottom row posteriors of figure 5.7 where the posterior and prior distributions are almost identical, e.g. the effective merger rate (top left histogram) has an upper limit of $n_{\text{eff}} \sim 1.4(2.1) \times 10^{-4}\text{Mpc}^{-3}\text{Gyr}^{-1}$ for the posterior(prior) respectively.

Future Upper limit at $A(f = \text{yr}^{-1}) = 1 \times 10^{-16}$

To investigate what useful information on astrophysical observables can be extracted by future improvements of the PTA sensitivity, we have shifted the upper limit down by an order of magnitude to $A(f = 1\text{yr}^{-1}) = 1.0 \times 10^{-16}$, indicative of the possible capabilities in the SKA era (Janssen et al., 2015).

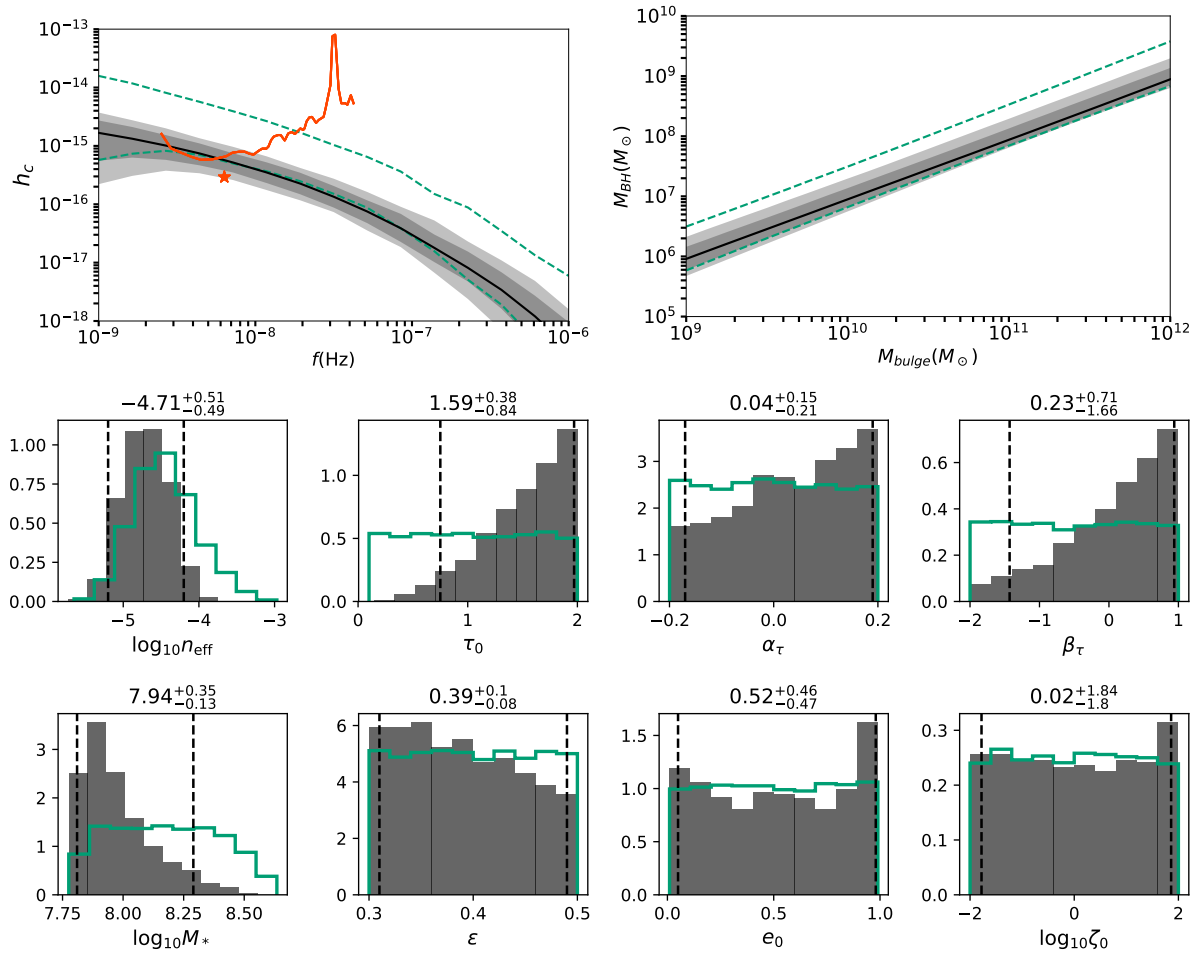

Figure 5.8: Same as figure 5.7 without the posterior distributions for the mass and redshift functions, but for an upper limit of $A(f = \mathrm{yr}^{-1}) = 1 \times 10^{-16}$

Results are shown in figure 5.8. Unlike the current situation, a future upper limit can put significant constraints on the allowed parameter space, also reflected in value of the Bayesian evidence $\log_e \mathscr{Z}(10^{-16}) = -4.32$. The odds ratio compared to a reference model untouched by the limit is now $e^{-4.32} = 0.013$, indicating that our astrophysical prior would be disfavoured a 2.5σ level. The Bayes factor $\mathscr{B} = \exp \mathscr{Z}(10^{-15})/\exp \mathscr{Z}(10^{-16}) \approx 43$ provides evidence that there is tension between current constraints on astrophysical observables (defining our prior) and a PTA upper limit of 10^{-16} on the GWB level. The top left panel of 5.8 shows that h_c is relegated at the bottom of the allowed prior range, and the top right panel indicates that a low normalization to the $M_{\rm BH} - M_{\rm bulge}$ relation is preferred. The bottom row posteriors in figure 5.8 show significant updates with respect to their prior distributions. A more restrictive upper limit on the effective merger rate (top left histogram) at $n_{\rm eff} \sim 6.3 \times 10^{-5} \mathrm{Mpc}^{-3}\mathrm{Gyr}^{-1}$ can be placed

and the distribution of all parameters defining the merger timescale are skewed towards high values, meaning that longer merger timescales, i.e. fewer mergers within the Hubble time, are preferred. Besides favouring lower merger rates, light SMBH are also required, as shown by the posterior of the M_* parameter. Lastly, there is tentative evidence that SMBHBs have to be very eccentric and in dense stellar environments, although the whole prior range of these parameters is still possible.

Ideal Upper limit at $A(f = \mathrm{yr}^{-1}) = 1 \times 10^{-17}$

Pushing the exercise to the extreme, we shift the future upper limit down by another order of magnitude to $A(f = 1\mathrm{yr}^{-1}) = 1.0 \times 10^{-17}$, which might be reached in the post-SKA era of PTA observations (Janssen et al., 2015). Nonetheless, this unveils what would be the consequences of a severe non detection, well below the level predicted by current SMBHB population models. Figure 5.9 compares inference on model parameters for the *P*PTA17 run, assuming either standard or extended prior distributions.

If we assume standard priors, constraints derived in the *P*PTA16 case are pushed to the extreme. The Bayesian evidence is now $\log_e \mathscr{Z}(10^{-17}) = -13.69$. The odds ratio compared to a reference model untouched by the limit becomes $e^{-13.69} \approx 10^{-6}$, indicating that our astrophysical prior would be severely disfavoured at a 5σ level. This would rule out the vast majority of our current constraints on the GSMF, pair fraction, merger timescale and $M_{\mathrm{bulge}} - M_{\mathrm{BH}}$ relation. Although the effective merger rate is only limited to be smaller than $n_{\mathrm{eff}} \sim 5.6 \times 10^{-5}\mathrm{Mpc}^{-3}\mathrm{Gyr}^{-1}$, all other parameters in the bottom row corner plots in figure 5.9 show rather extreme posterior distributions. Since our standard prior does not allow stalling of low redshift SMBHBs (the maximum normalization of the local merger timescale being 2 Gyrs), skewing the merger timescale to extreme values is not sufficient to explain the non detection. Further, the normalization to the $M_{\mathrm{BH}} - M_{\mathrm{bulge}}$ is severely pushed to the low end, at $M_* < 10^8 M_\odot$, thus completely ruling out several currently popular relations (e.g., Kormendy and Ho, 2013; McConnell and Ma, 2013).

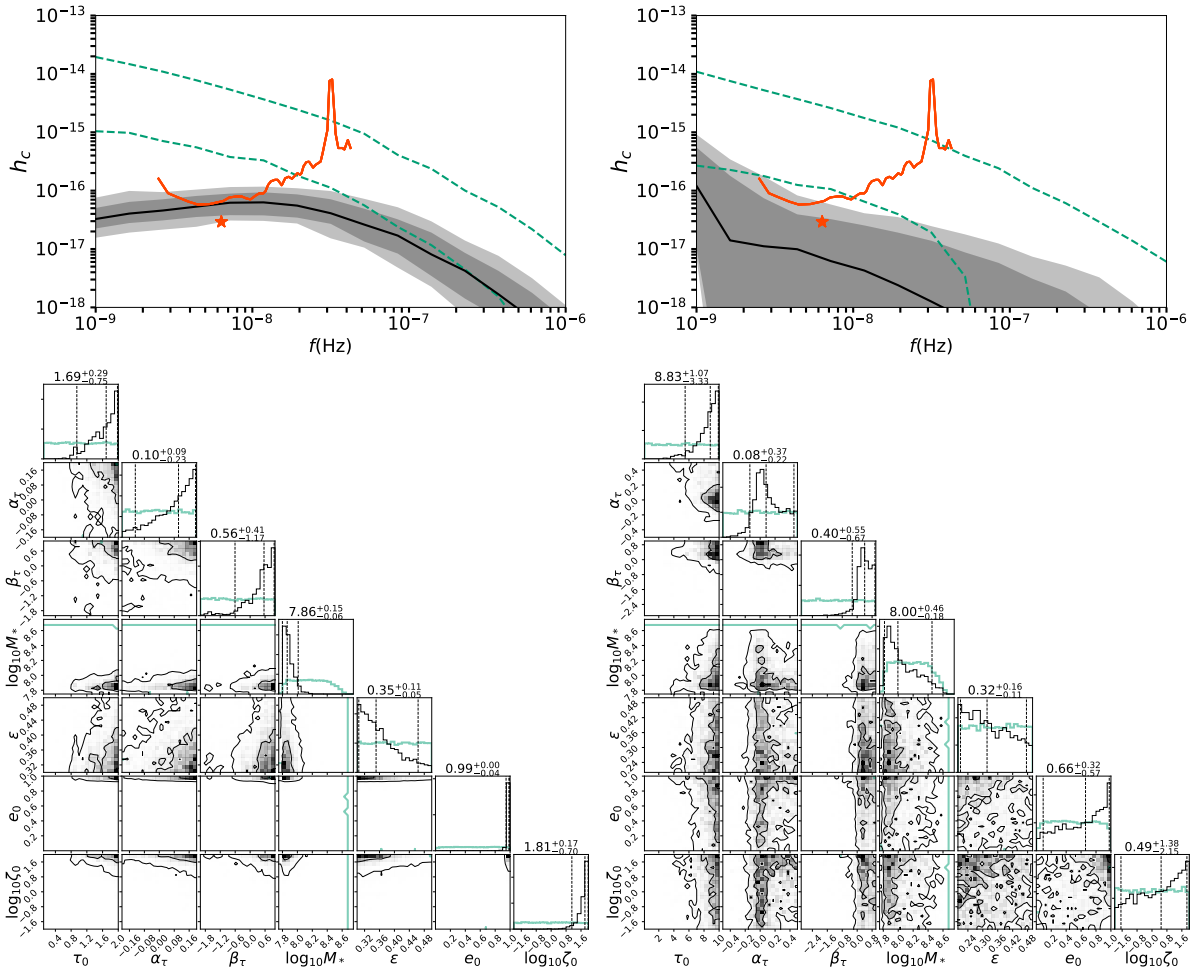

Figure 5.9: Implications of a 95% upper-limit of $A(f = \mathrm{yr}^{-1}) = 1 \times 10^{-17}$ with standard (left column) and extended (right column) prior distributions. In each column, the top panel shows the posterior of the recovered GWB spectrum with the central 68% and 90% confidence regions indicated by progressively lighter shades of grey. The bottom corner plots show the (one)two-dimensional posteriors for each model parameter pairs as shaded area, the different levels of shading indicate the 5%, 50% and 95% confidence regions. In each sub-panel, the green lines show the 100% confidence levels for the prior.

Even with the smallest possible $M_{\rm BH} - M_{\rm bulge}$, a non detection at $A(f = 1\mathrm{yr}^{-1}) = 1.0 \times 10^{-17}$ requires a very high frequency turnover of the GWB (see upper left panel of figure 5.9), which can be realized only if all binaries have eccentricity $e_0 > 0.95$ and reside in extremely dense environments (at least a factor of 10 larger than our fiducial Dehnen profile).

As mentioned above, our standard prior on the total merger timescale (see Section 5.4.3), implies that stalling hardly occurs in nature. Although this is backed up by recent progresses in N-body simulations and the theory of SMBHB hardening in stellar environments (see, e.g., Sesana and

Khan, 2015; Vasiliev et al., 2015), we want to keep an open mind and check what happens when arbitrary long merger timescales, and thus stalling, are allowed. We note, however, that such a model is intrinsically inconsistent, because when very long merger timescales are allowed, one should also consider the probable formation of SMBH triplets, due to subsequent galaxy mergers. Triple interactions are not included in our models but they have been shown (Bonetti et al., 2018; Ryu et al., 2018) to drive about 1/3 to the stalled SMBHBs to coalescence in less than 1 Gyr. Therefore, we caution that actual constrains on model parameters would likely be more stringent than what described in the following. The extended prior distributions relaxes the strong evidence of -13.69 to $\log_e \mathscr{Z}(10^{-17}) = -4.56$ and the Bayes factor becomes comparable to the *P*PTA16, this is mainly due to allowing binaries to stall as the merger timescale increases to $\tau_0 > 5.5$ Gyr. The extreme constraints on the other parameters are consequently loosened, although posterior distributions of M_*, e_0, ζ_0 indicate that light SMBHBs are favoured, along with large eccentricities and dense environments. Thus allowing the effective merger rate to drop to below $n_{\rm eff} \sim 1.1 \times 10^{-5}\mathrm{Mpc}^{-3}\mathrm{Gyr}^{-1}$.

Table 5.2 summarizes the increasing constraining power as the upper limits are lowered. As they become more restrictive, fewer mergers are allowed. The effective merger rate is therefore pushed to be as low as possible with long merger timescales, low SMBHB masses, large eccentricities and dense environments. Bayes factors comparing the current observational constraints, i.e. the prior ranges, with posterior constraints can be calculated from the evidences. These, however, show that the tension increases from 0.6σ with the current upper limit of $A(f = \mathrm{yr}^{-1}) = 1 \times 10^{-15}$ to 5σ with an ideal upper limit at $A(f = \mathrm{yr}^{-1}) = 1 \times 10^{-17}$. Relaxing the upper bound on the merger time norm and other constraints (see Section 5.4.5) can alleviate the tension between current observations and such a upper limit to 2.6σ (although this does not take into account for triple-induced mergers, as mentioned above).

parameter	$\log_{10} n_{\rm eff}$	τ_0	$\log_e \mathscr{Z}$
standard prior: no upper limit	< -3.68	> 0.2	0
standard prior: $A = 1 \times 10^{-15}$	< -3.85	> 0.28	-0.55
standard prior: $A = 1 \times 10^{-16}$	< -4.2	> 0.75	-4.32
standard prior: $A = 1 \times 10^{-17}$	< -4.25	> 0.94	-13.69
extended prior: $A = 1 \times 10^{-17}$	< -4.96	> 5.5	-4.56

Table 5.2: List of bounds for selected parameters and evidences for the upper limit cases. The 95% upper bounds for the effective merger rate, the 95% lower bounds for the merger time norm and the evidences are reported in the columns. The five rows list the values for the standard prior, current, future and ideal upper limit posteriors from top to bottom.

5.5.3 Simulated detections

Although it is useful to explore the implication of PTA upper limits, it is more interesting to consider the case of a future detection, which is expected within the next decade (Rosado et al., 2015; Taylor et al., 2016b; Kelley et al., 2017b). We therefore turn our attention at simulated detections and their potential to put further constraints on the astrophysics of galaxy evolution and SMBHB mergers. The amplitude of the simulated GWB is defined by the 16 parameters describing the SMBHB merger rate. We fix those as follows: $(\Phi_0, \Phi_I, M_0, \alpha_0, \alpha_I, f_0, \alpha_f, \beta_f, \gamma_f, \tau_0, \alpha_\tau, \beta_\tau, \gamma_\tau, M_*, \alpha_*, \varepsilon)$ = (-2.6, -0.45, $10^{11.25}$, -1.15, -0.1, 0.025, 0.1, 0.8, 0.1, 0.8, -0.1, -2, -0.1, 10^8, 1, 0.3). The low frequency turnover is defined by the two extra parameters (e_0, ζ_0). We fix $\zeta_0 = 1$ and we produce two GWB spectra distinguished solely by the assumed value of the eccentricity: $e_i = 0.01$ (circular case) and $e_i = 0.9$ (eccentric case). This set of parameters is chosen such that it results in a GWB strain of $h_c = 5.0 \times 10^{-16}$ at 1/1yr (i.e. well within current upper limits), whilst being consistent with the current constraints of all the relevant astrophysical observables:

- GSMF: the values for $(\Phi_0, \Phi_I, M_0, \alpha_0, \alpha_I)$ are chosen, such that they accurately reproduce the currently best measured GSMF, i.e., they are close to the best fit values of the re-parametrisation described in Section 5.4.1;

- merger timescale: $\tau_0 = 0.8$ Gyr is chosen to match the predicted merger timescales found in simulations by Lotz et al. (2010), while $\beta_\tau = -2$ is chosen to match the expected redshift evolution of the merger timescale from Snyder et al. (2017);

- $M_{\rm bulge} - M_{\rm BH}$ relation: $(M_*, \alpha_*, \varepsilon)$ have been chosen to produce the injected characteristic strain amplitude, consistent with the allowed prior shown in figure 5.5.

The other parameters are chosen to be close to the centre of their prior ranges, except for the eccentricity, as mentioned above.

Circular case

Figure 5.10 shows a comparison of the results of the *IPTA30* (left column) and *SKA20* (right column) setups for the circular case ($e_0 = 0.01$). In the *IPTA30*(*SKA20*) case the GWB has been detected in 10(14) frequency bins up to frequencies of $\sim 1(2) \times 10^{-8}$ Hz, for a total detection S/N $\mathscr{S} \approx 7(35)$. Qualitatively, both detections provide some extra constraints on selected prior parameters. The injected spectrum, mass and redshift function are recovered increasingly better as the S/N increases. Still, a broad portion of the initial parameter space is allowed, especially for the redshift evolution of the SMBHB merger rate. It should be noted that PTAs have the most constraining power around the bend of the mass function, at the SMBHB chirp mass $\mathscr{M} \approx 3 \times 10^8 M_\odot$. The posterior panels at the bottom of figure 5.10 show that there is not much additional information gained compared to the prior knowledge for most of the parameters (full corner plots shown in Appendix B), with three notable exceptions:

1. merger timescale. τ_0 is marginally constrained around the injected value (0.8 Gyrs) in the *IPTA30* case, the constraint becomes better in the *SKA20* case. β_τ is also skewed towards low values (consistent with the $\beta_\tau = -2$ injection). A clean PTA detection thus potentially allow to constrain the timescale of SMBHB coalescence, which can help in understanding the processes driving the merger;

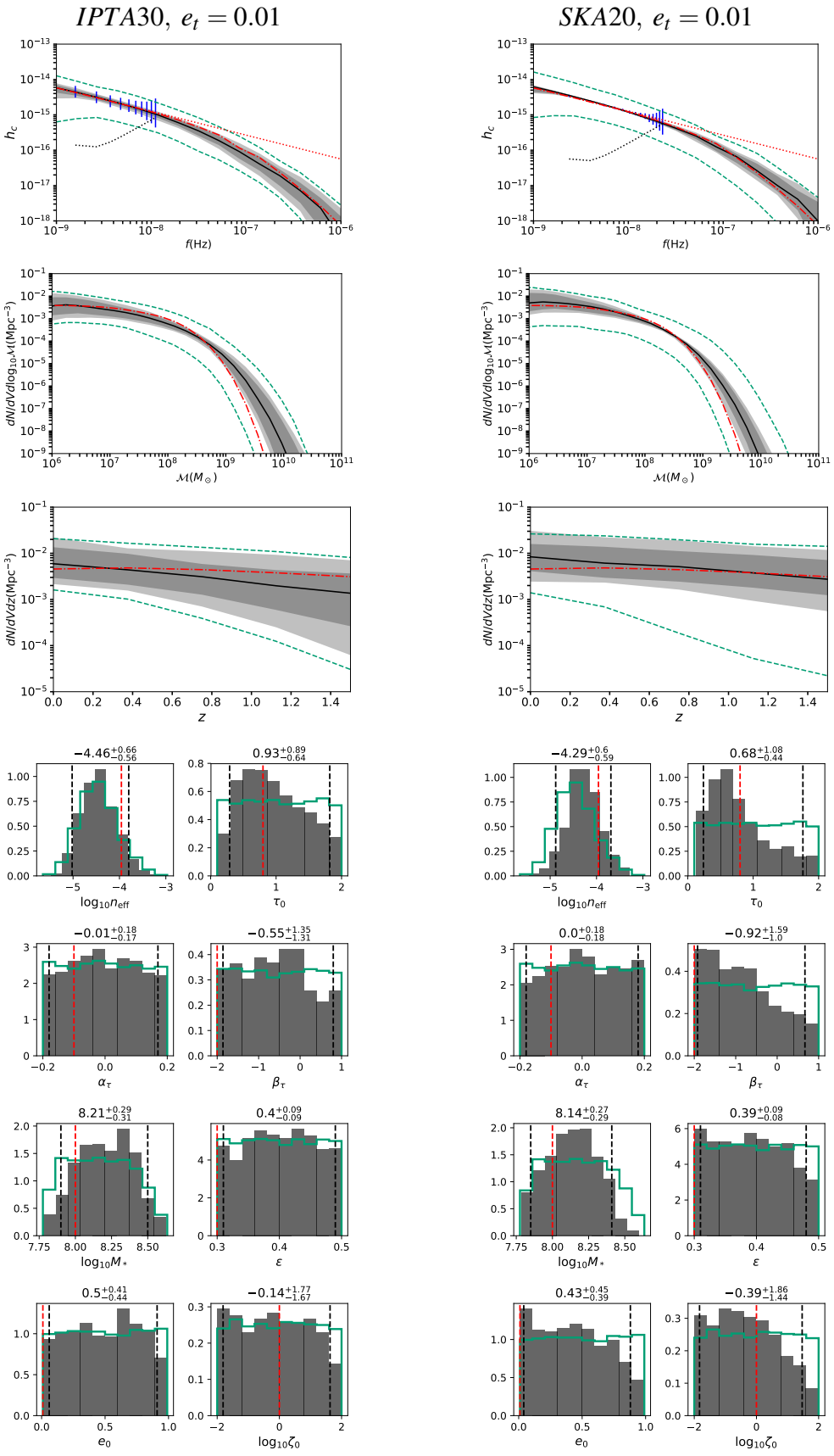
IPTA30, $e_t = 0.01$
SKA20, $e_t = 0.01$
h_c
f(Hz)
$dN/dVd\log_{10}\mathcal{M}$(Mpc^{-3})
$\mathcal{M}(M_\odot)$
$dN/dVdz$(Mpc^{-3})
z
$-4.46^{+0.66}_{-0.56}$
$\log_{10} n_{\rm eff}$
$0.93^{+0.89}_{-0.64}$
τ_0
$-0.01^{+0.18}_{-0.17}$
α_τ
$-0.55^{+1.35}_{-1.31}$
β_τ
$8.21^{+0.29}_{-0.31}$
$\log_{10} M_*$
$0.4^{+0.09}_{-0.09}$
ε
$0.5^{+0.41}_{-0.44}$
e_0
$-0.14^{+1.77}_{-1.67}$
$\log_{10}\zeta_0$
$-4.29^{+0.6}_{-0.59}$
$0.68^{+1.08}_{-0.44}$
$0.0^{+0.18}_{-0.18}$
$-0.92^{+1.59}_{-1.0}$
$8.14^{+0.27}_{-0.29}$
$0.39^{+0.09}_{-0.08}$
$0.43^{+0.45}_{-0.39}$
$-0.39^{+1.86}_{-1.44}$

Figure 5.10

Figure 5.10: Implications of a PTA detection at a low (S/N≈7, left column) and moderate (S/N≈35, right column) significance, assuming a SMBHB population with default parameters and almost circular ($e_t = 0.01$) at decoupling. As in figure 5.7, the posterior for the spectrum, mass and redshift functions (in descending order from the top) are shown as shaded areas. In each of those panels, the dash–dotted red line indicates the injected model. In the top panels the vertical blue bands indicate the 68% confidence interval of the observed signal amplitude at each frequency bin. The dotted line is the nominal 1σ sensitivity of the considered PTA. The dotted red line shows the simulated spectrum assuming no drop due to missing sources at high frequencies. The bottom row histograms in shades of grey show the marginalized posteriors for selected model parameters with the prior distributions indicated in green. The injected parameter values are marked by red dashed lines.

2. $M_{\rm bulge} - M_{\rm BH}$ relation. The M_* panels show a tightening of the M_* distribution with increasing S/N. A detection would thus also allow to constrain the $M_{\rm bulge} - M_{\rm BH}$ relation;

3. eccentricity and stellar density. The posterior distributions for e_0 and $\log_{10}\zeta_0$ show some marginal update. In particular in the *SKA20* case, extreme eccentricities, above $e_0 > 0.9$ can be safely ruled out. Note that the absence of a low frequency turnover also favours small value of ζ_0, fully consistent with the injected value $\zeta_0 = 1$.

Eccentric case

The results for the *IPTA30* and *SKA20* eccentric cases are shown in figure 5.11, with full corner plots reported in Appendix B. In general results are comparable to the circular case shown above, as the only difference is in the injected eccentricity parameter. The left column (*IPTA30* case) of figure 5.11 shows nearly identical posterior distributions to its circular counterpart reported in figure 5.10, this also translates into similar recovered spectrum, mass and redshift functions.

However, in the *SKA20* case, the detection S/N is high enough to allow a clear detection of the spectrum turnover in the lowest frequency bins. Which is not the case for the *IPTA30* case, as can be seen in the top row spectra plots of figure 5.11. This has important consequences for astrophysical inference since an observable turnover is only possible if binaries are significantly eccentric and/or evolve in very dense environments. This is shown in the e_0 and ζ_0 posterior

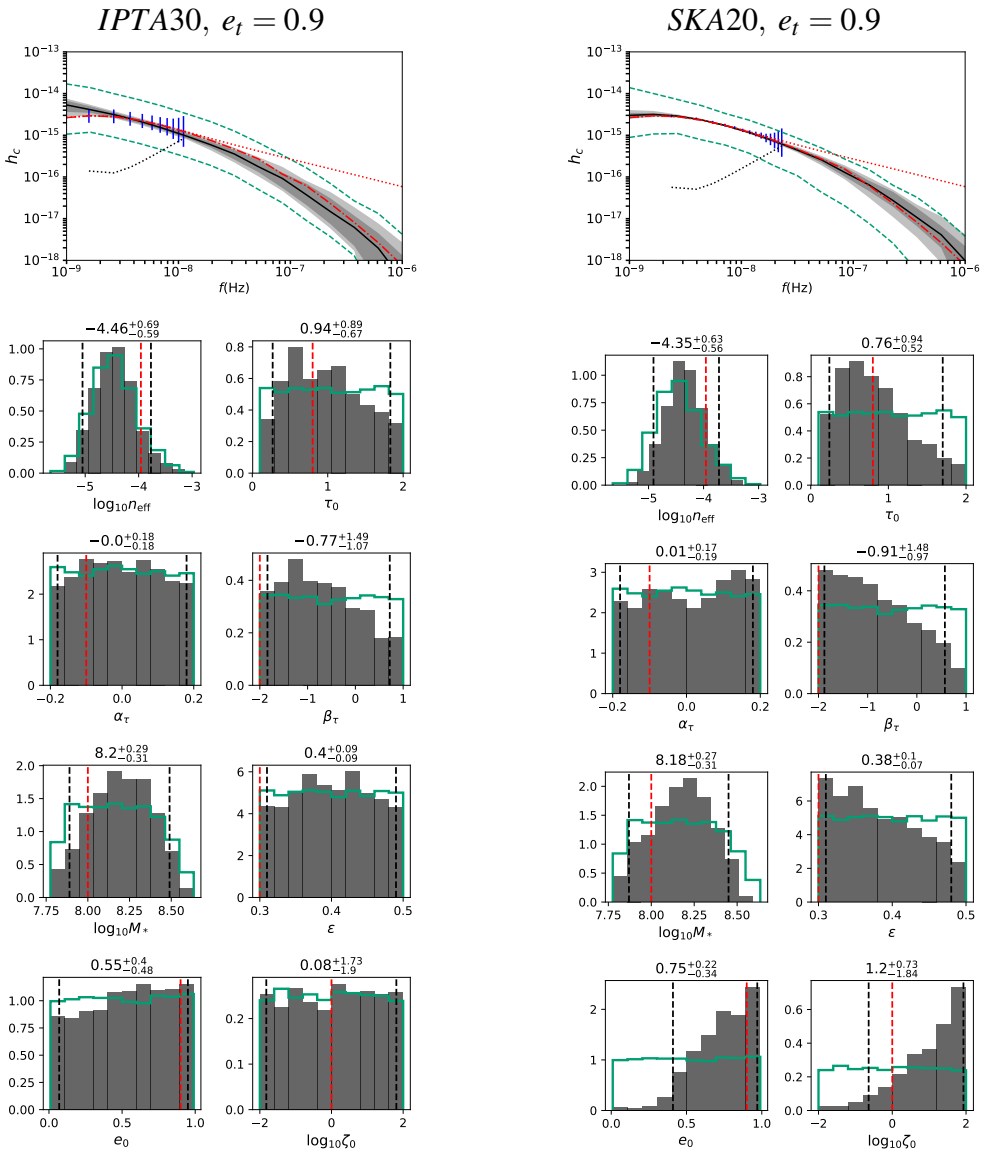

Figure 5.11: Same as figure 5.10 but assuming decoupling eccentricity of $e_t = 0.9$. The posterior panels of the mass and redshift functions are analogue to those in the circular case and thus not shown here.

distributions at the bottom right of figure 5.11: eccentricities $e_0 < 0.4$ are excluded and densities higher than what predicted by the fiducial Dehnen model are strongly favoured. The full corner plot B10 reported in Appendix B also highlights the $e_0 - \zeta_0$ degeneracy, as a low frequency turnover can be caused by either parameters; a very eccentric binary in a low density stellar environment has the turnover at the same frequency as a lower eccentric binary in a denser stellar environment. Additionally, a large region in the $e_0 - \zeta_0$ plane has been ruled out($e_0 > 0.41$ and $\log_{10} \zeta_0 > -0.63$). This also prompts some extra constrain in the $M_{\rm BH} - M_{\rm bulge}$ relation, as can

be seen in the trends in the α_* and ε distributions.

Summarizing, little extra astrophysical information (besides the non-trivial confirmation that SMBHBs actually do merge) can be extracted in the *IPTA30*, whereas many more interesting constrains emerge as more details of the GWB spectrum are unveiled in the *SKA20* case. Although posteriors on most of the parameters remain broad, the typical SMBHB coalescence timescale can be constrained around the injected value; the posterior distributions of $n_{\rm eff}$ and M_* are tightened, providing some extra information on the SMBHB merger rate and on the $M_{\rm BH} - M_{\rm bulge}$ scaling relation; significant constrains onto the SMBHB eccentricity and immediate environment can be placed if a low frequency turnover is detected.

Ideal case

We show ideal detections for both the circular and eccentric cases in figure 5.12. Although, such detection may not be achievable by PTAs in the foreseeable future, these results show what might be constrained in principle by combining astrophysical prior knowledge to precise measurements of the amplitude and shape of the nano-Hz stochastic GWB.

The spectra, mass and redshift functions (not shown in the figure) are recovered extremely well in both cases. Both corner plots also show interesting constrains on some key parameters. The typical merger timescale τ_0 is correctly measured and constrained within less than 1 Gyr uncertainty, and clear trends in α_τ and β_τ provide some extra information on the merger timescale evolution with galaxy mass and redshift. Note that those are parameters defining the *SMBHB* coalescence time which are unlikely to be measured by any other means. The normalization of the $M_{\rm bulge} - M_{\rm BH}$ relation is also significantly constrained, as shown by the tight M_* posterior distributions. Again we see both in the circular and eccentric cases the degeneracy between eccentricity e_0 and stellar density ζ_0, as in the *SKA20* eccentric case above. The posterior regions contain the injected values and exclude a large region from the prior: $e_0 < 0.45$, $\log_{10}\zeta_0 < 1.14$ for the circular case and $e_0 > 0.42$, $\log_{10}\zeta_0 > -0.22$ to the 95th percentile. Although, the *ideal*

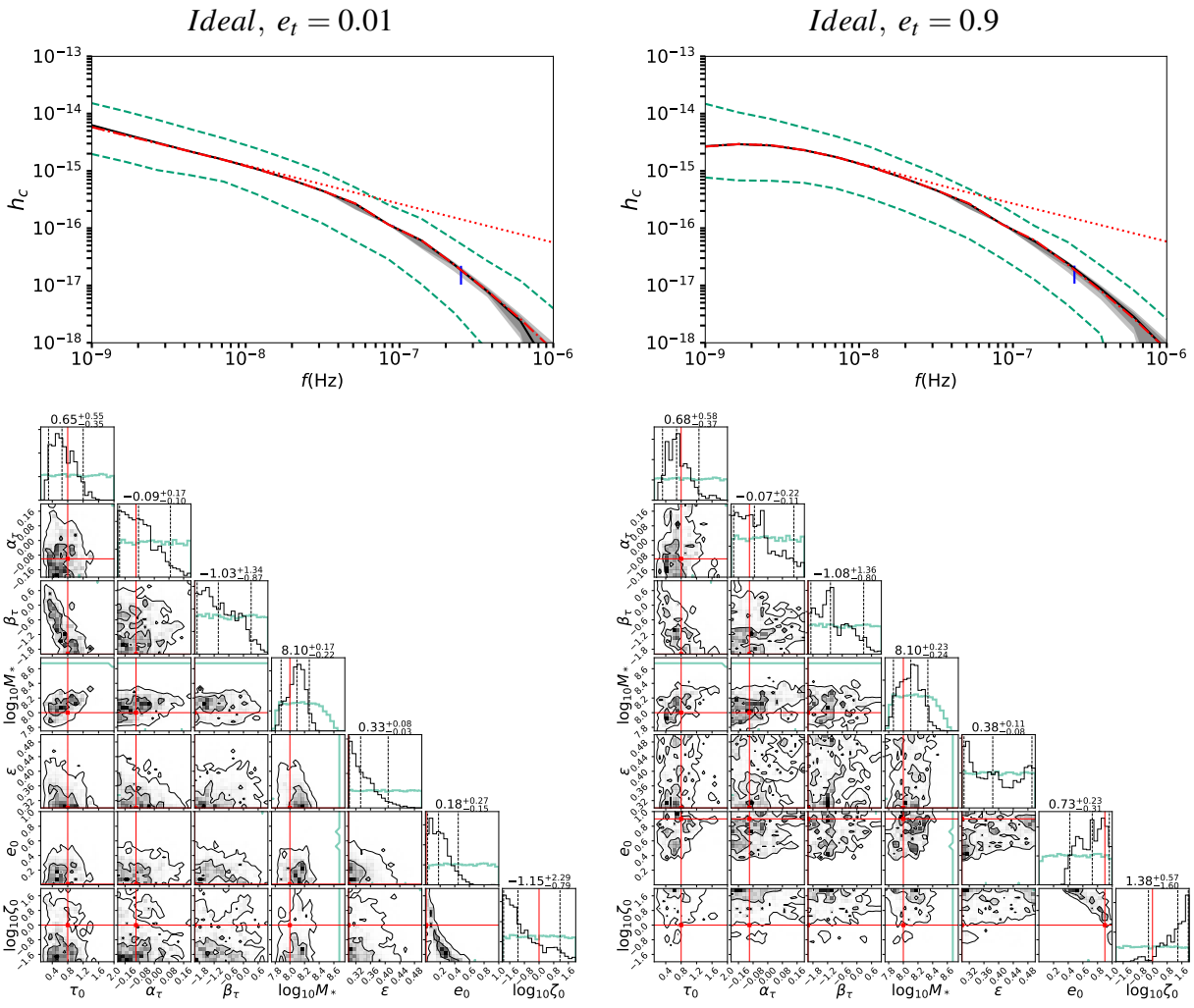

Figure 5.12: Implications of an ideal detection with 500 MSPs timed at sub-ns precision for 30 years. The injected model has default parameters with $e_t = 0.01$ (left column) and $e_t = 0.9$ (right column). Panel sequence and style as in figure 5.9.

parameter	$\log_{10} n_{\rm eff}$	τ_0	$\log_{10} M_*$	e_0	$\log_{10}\zeta_0$
prior	$-4.47^{+0.79}_{-0.61}$	$1.04^{+0.86}_{-0.85}$	$8.17^{+0.36}_{-0.32}$	$0.50^{+0.44}_{-0.44}$	$0.01^{+1.79}_{-1.80}$
IPTA30	$-4.46^{+0.70}_{-0.59}$	$0.94^{+0.89}_{-0.67}$	$8.20^{+0.29}_{-0.31}$	$0.55^{+0.40}_{-0.48}$	$0.08^{+1.73}_{-1.90}$
SKA20	$-4.35^{+0.63}_{-0.56}$	$0.76^{+0.94}_{-0.52}$	$8.18^{+0.26}_{-0.31}$	$0.75^{+0.22}_{-0.34}$	$1.20^{+0.74}_{-1.83}$
ideal	$-4.24^{+0.38}_{-0.38}$	$0.68^{+0.58}_{-0.37}$	$8.10^{+0.23}_{-0.24}$	$0.73^{+0.23}_{-0.31}$	$1.38^{+0.57}_{-1.60}$
injection	-4.0	0.8	8.0	0.9	0.0

Table 5.3: List of credible intervals for selected parameters of the model. Each column reports the median value together with the errors bracketing the 90% confidence regions for selected parameters. The five rows list the boundaries defined by the prior distributions, the posterior distributions as measured in the *IPTA30*, *SKA20* and *ideal* cases and the injected values from top to bottom.

eccentric detection has a vastly larger S/N than its *SKA20* analogue, the constraints on e_0 and $\log_{10}\zeta_0$ are comparable due to the degeneracy between the two parameters. Table 5.3 shows the increasing constraining power on selected key parameters as the detection S/N improves for the eccentric case.

CHAPTER 6

SUMMARY, CONCLUSIONS AND OUTLOOK

What we can learn from PTA observations has been the main question around which this thesis has developed. To solve this question I have introduced the theory and methodology of doing GW science with PTAs. These have been applied to PTA observations on the GWB to constrain the parameter space of models predicting the characteristic strains of such a GWB.

This thesis introduced a parametric model to quickly and accurately compute the characteristic strain of a GWB from a population of SMBHBs described by a phenomenological function. The semi-analytic model deviates from the $f^{-2/3}$ powerlaw with two prominent features: 1. a bend at low frequencies coming from including eccentric binaries in the population and 2. a drop at high frequencies due to the removal of individual resolvable sources from the population. We do not account for a full backwards evolution of the SMBHBs, but rather set an eccentricity when the evolution decouples from its stellar environment and becomes GW emission dominated. This generally happens at sub nHz frequencies, we have verified that the computed spectrum in the PTA sensitive band between nHz and mHz is only marginally affected. This low frequency drop is thus only dependent on the properties of the individual binaries. The high frequency drop is only dependent on the properties of the SMBHB population. Consequently, observing the spectrum at both ends should allow for a good recovery of the parameters of the merger rate and individual binaries.

Owing to the computational efficiency of the model, it was possible to do full Bayesian analyses on current PTA upper limits and simulated detections with this model to constrain its parameters. We showed that the current upper limit of $A_{yr} = 10^{-15}$ can only constrain the overall merger rate of SMBHBs to $\dot{n}_0 < 2.5 \times 10^{-3}\text{Gyr}^{-1}\text{Mpc}^3$. The three simulated detection cases for the *IPTA30*, *SKA20* and *Ideal* PTA setups all show improving constraints on the overall merger rate. A clear degeneracy between the mass of the SMBHB and its eccentricity at decoupling was also found. This degeneracy stems from the fact that lighter less eccentric binaries evolve similarly to heavier more eccentric binaries and can only be broken either with an *Ideal* detection up to very high frequencies or with independent constraints from other observations.

We revisited the astrophysical interpretation from the PPTA upper limit analysis (Shannon et al., 2015) with our Bayesian analysis framework. 4 representative models computing the SMBHB merger rate from electromagnetic observations were picked: a pessimistic, a fiducial, an optimistic and a general model including all of the previous models. These SMBHB merger rates were translated into different prior distributions. The Bayesian analyses yield little to no tension between the current SMBHBs assembly models and the non-detection of a GWB with PTAs. However, future upper limits at 3×10^{-16} and 1×10^{-16} do create tensions of $\sim 2\sigma$ and $\sim 4\sigma$ for optimistic models with larger SMBHB merger rates respectively.

To further complete our model and relate our SMBHB merger rates to other observables, we replaced the phenomenological SMBHB population function by one directly derived from observations of the galaxy stellar mass function, pair fraction, merger timescales and galaxy $M_{bulge} - M_{BH}$ relation. This allowed us to see how much PTA could help to improve current constraints or whether there was any tension. Additionally, we also expanded the dynamical properties of the binaries to also account for different stellar densitities around them. One current, one future and one theoretic upper limit and 3 simulated detection cases were analyzed. Preliminary results showed that current PTA upper limits can only add very little to our prior knowledge of the exisiting constraints on the astrophysical parameters. As the upper limit decreases to a realistic $A_{yr} = 10^{-16}$ and a theoretical $A_{yr} = 10^{-17}$, so do the overall $\sim 2.5\sigma$

and $> 5\sigma$ tensions between the upper limit and the current constraints on galaxy mergers and galaxy - black hole relations. Future upper limits may imply a lower than expected $M_{bulge} - M_{BH}$ scaling relation, stalling of binaries and extreme eccentricities and environments of the binaries. Simulated detections from *IPTA30* over *SKA20* to *Ideal* do progressively improve upon the constraints. Notable constrainable observables are the effective merger rate in the Universe, the time between pairing of the galaxies and the merger of the black holes, the scaling mass of the galaxy - black hole mass relation and the dynamical properties of the binaries, i.e. eccentricity and stellar density. Once again, these observables are dominant for the two main distinguishing features of the characteristic spectrum. The low bend corresponds to the dynamical properties of the SMBHB population. The high drop corresponds to the properties of the SMBHB population, which is mainly determined by the scaling mass in the $M_{bulge} - M_{BH}$ relation. Lastly, the general amplitude of the detection gives a measure of the effective merger rate as well as an idea on the merger time scale.

This thesis has used a parametric model to efficiently compute the characteristic strain of the GWB from a population of SMBHBs. The model has been expanded to include astrophysical observables for the galaxy mergers and $M_{bulge} - M_{BH}$ relation as well as parameters describing the properties of individual binaries, like eccentricity and density of the stellar environment. However, it still has simplifying assumptions: 1. each binary has the same eccentricity and stellar density at decoupling, 2. the evolution of the SMBHB up to GW emission is modelled as hardening in a stellar environment, this does not account for evolution due to gaseous accretion or subsequent galaxy merger and super massive black hole triplet interactions, 3. the population of SMBHBs is the average population and not a realization of the Universe.

All these assumptions have to be addressed to complete the model and give us an accurate overall picture on the constrainability of astrophysics with PTA GWB observations.

In addition, we have only focussed on the GWB, it is possible that there will be individual detectable sources, which have been removed in the high frequency regime. These individual GW sources have interesting individual properties of the SMBHB, but at the same time as they

come from realizations of the underlying population they also provide valuable information on the SMBHB merger rate. This information has been neglected in this thesis, but should be taken into account to combine all the knowledge we can gain into a coherent model.

As the complexity of the model increases, the effiency of the computation decreases. This limits the option to do sampling processes in a timely fashion to determine the posterior constraints. Ideally, one would also want to run the sampling together with the timing model and noise analysis for all the pulsars in the array simultaneously. Such a task is computationally not feasible yet. Machine learning and other intelligent algorithms to compute the spectrum quickly and accurately despite the increase in numbers of parameters in the model will become necessary. Although, the question of whether the model becomes so degenerate, that no meaningful physics can extracted, should also be posed.

Although, we can only learn very little from PTAs now with the current upper limits, in theory PTAs have the potential to put very strong constraints on several aspects of galaxy and SMBHB mergers. As the sensitivities of both electromagnetic and GW observations improve, we could learn more and more about the cosmic history of massive galaxies and super massive black hole binaries unveiling their astrophysical properties.

BIBLIOGRAPHY

Arzoumanian, Z., Baker, P. T., Brazier, A., Burke-Spolaor, S., Chamberlin, S. J., Chatterjee, S., Christy, B., Cordes, J. M., Cornish, N. J., Crawford, F., Thankful Cromartie, H., Crowter, K., DeCesar, M., Demorest, P. B., Dolch, T., Ellis, J. A., Ferdman, R. D., Ferrara, E., Folkner, W. M., Fonseca, E., Garver-Daniels, N., Gentile, P. A., Haas, R., Hazboun, J. S., Huerta, E. A., Islo, K., Jones, G., Jones, M. L., Kaplan, D. L., Kaspi, V. M., Lam, M. T., Lazio, T. J. W., Levin, L., Lommen, A. N., Lorimer, D. R., Luo, J., Lynch, R. S., Madison, D. R., McLaughlin, M. A., McWilliams, S. T., Mingarelli, C. M. F., Ng, C., Nice, D. J., Park, R. S., Pennucci, T. T., Pol, N. S., Ransom, S. M., Ray, P. S., Rasskazov, A., Siemens, X., Simon, J., Spiewak, R., Stairs, I. H., Stinebring, D. R., Stovall, K., Swiggum, J., Taylor, S. R., Vallisneri, M., van Haasteren, R., Vigeland, S., Zhu, W. W., and The NANOGrav Collaboration (2018a). The NANOGrav 11 Year Data Set: Pulsar-timing Constraints on the Stochastic Gravitational-wave Background. Astrophysical Journal, 859:47.

Arzoumanian, Z., Brazier, A., Burke-Spolaor, S., Chamberlin, S., Chatterjee, S., Christy, B., Cordes, J. M., Cornish, N., Crowter, K., Demorest, P. B., Dolch, T., Ellis, J. A., Ferdman, R. D., Fonseca, E., Garver-Daniels, N., Gonzalez, M. E., Jenet, F. A., Jones, G., Jones, M. L., Kaspi, V. M., Koop, M., Lam, M. T., Lazio, T. J. W., Levin, L., Lommen, A. N., Lorimer, D. R., Luo, J., Lynch, R. S., Madison, D., McLaughlin, M. A., McWilliams, S. T., Nice, D. J., Palliyaguru, N., Pennucci, T. T., Ransom, S. M., Siemens, X., Stairs, I. H., Stinebring, D. R., Stovall, K., Swiggum, J. K., Vallisneri, M., van Haasteren, R., Wang, Y., and Zhu, W. (2015). The NANOGrav Nine-year Data Set: Observations, Arrival Time Measurements, and Analysis

of 37 Millisecond Pulsars. Astrophysical Journal, 813:65.

Arzoumanian, Z., Brazier, A., Burke-Spolaor, S., Chamberlin, S., Chatterjee, S., Christy, B., Cordes, J. M., Cornish, N. J., Crawford, F., Thankful Cromartie, H., Crowter, K., DeCesar, M. E., Demorest, P. B., Dolch, T., Ellis, J. A., Ferdman, R. D., Ferrara, E. C., Fonseca, E., Garver-Daniels, N., Gentile, P. A., Halmrast, D., Huerta, E. A., Jenet, F. A., Jessup, C., Jones, G., Jones, M. L., Kaplan, D. L., Lam, M. T., Lazio, T. J. W., Levin, L., Lommen, A., Lorimer, D. R., Luo, J., Lynch, R. S., Madison, D., Matthews, A. M., McLaughlin, M. A., McWilliams, S. T., Mingarelli, C., Ng, C., Nice, D. J., Pennucci, T. T., Ransom, S. M., Ray, P. S., Siemens, X., Simon, J., Spiewak, R., Stairs, I. H., Stinebring, D. R., Stovall, K., Swiggum, J. K., Taylor, S. R., Vallisneri, M., van Haasteren, R., Vigeland, S. J., Zhu, W., and The NANOGrav Collaboration (2018b). The NANOGrav 11-year Data Set: High-precision Timing of 45 Millisecond Pulsars. ApJS, 235:37.

Arzoumanian, Z., Brazier, A., Burke-Spolaor, S., Chamberlin, S. J., Chatterjee, S., Christy, B., Cordes, J. M., Cornish, N. J., Crowter, K., Demorest, P. B., Deng, X., Dolch, T., Ellis, J. A., Ferdman, R. D., Fonseca, E., Garver-Daniels, N., Gonzalez, M. E., Jenet, F., Jones, G., Jones, M. L., Kaspi, V. M., Koop, M., Lam, M. T., Lazio, T. J. W., Levin, L., Lommen, A. N., Lorimer, D. R., Luo, J., Lynch, R. S., Madison, D. R., McLaughlin, M. A., McWilliams, S. T., Mingarelli, C. M. F., Nice, D. J., Palliyaguru, N., Pennucci, T. T., Ransom, S. M., Sampson, L., Sanidas, S. A., Sesana, A., Siemens, X., Simon, J., Stairs, I. H., Stinebring, D. R., Stovall, K., Swiggum, J., Taylor, S. R., Vallisneri, M., van Haasteren, R., Wang, Y., Zhu, W. W., and NANOGrav Collaboration (2016). The NANOGrav Nine-year Data Set: Limits on the Isotropic Stochastic Gravitational Wave Background. Astrophysical Journal, 821:13.

Backer, D. C., Kulkarni, S. R., Heiles, C., Davis, M. M., and Goss, W. M. (1982). A millisecond pulsar. Nature, 300:615–618.

Begelman, M. C., Blandford, R. D., and Rees, M. J. (1980). Massive black hole binaries in active galactic nuclei. Nature, 287:307–309.

Beifiori, A., Courteau, S., Corsini, E. M., and Zhu, Y. (2012). On the correlations between galaxy properties and supermassive black hole mass. Mon. Not. R. Astron. Soc., 419:2497–2528.

Bernardi, M., Meert, A., Sheth, R. K., Huertas-Company, M., Maraston, C., Shankar, F., and Vikram, V. (2016). The massive end of the luminosity and stellar mass functions and clustering from CMASS to SDSS: evidence for and against passive evolution. MNRAS, 455:4122–4135.

Bernardi, M., Meert, A., Vikram, V., Huertas-Company, M., Mei, S., Shankar, F., and Sheth, R. K. (2014). Systematic effects on the size-luminosity relations of early- and late-type galaxies: dependence on model fitting and morphology. MNRAS, 443:874–897.

Berry, C. P. L. and Gair, J. R. (2010). Gravitational wave energy spectrum of a parabolic encounter. Phys. Rev. D, 82(10):107501.

Bonetti, M., Haardt, F., Sesana, A., and Barausse, E. (2016). Post-Newtonian evolution of massive black hole triplets in galactic nuclei - I. Numerical implementation and tests. MNRAS, 461:4419–4434.

Bonetti, M., Sesana, A., Barausse, E., and Haardt, F. (2018). Post-Newtonian evolution of massive black hole triplets in galactic nuclei - III. A robust lower limit to the nHz stochastic background of gravitational waves. MNRAS, 477:2599–2612.

Booth, R. S., de Blok, W. J. G., Jonas, J. L., and Fanaroff, B. (2009). MeerKAT Key Project Science, Specifications, and Proposals. ArXiv e-prints.

Bundy, K., Fukugita, M., Ellis, R. S., Targett, T. A., Belli, S., and Kodama, T. (2009). The Greater Impact of Mergers on the Growth of Massive Galaxies: Implications for Mass Assembly and Evolution since z sime 1. Astrophys. J., 697:1369–1383.

Caballero, R. N., Lee, K. J., Lentati, L., Desvignes, G., Champion, D. J., Verbiest, J. P. W., Janssen, G. H., Stappers, B. W., Kramer, M., Lazarus, P., Possenti, A., Tiburzi, C., Perrodin, D., Osłowski, S., Babak, S., Bassa, C. G., Brem, P., Burgay, M., Cognard, I., Gair, J. R., Graikou, E., Guillemot, L., Hessels, J. W. T., Karuppusamy, R., Lassus, A., Liu, K., McKee,

J., Mingarelli, C. M. F., Petiteau, A., Purver, M. B., Rosado, P. A., Sanidas, S., Sesana, A., Shaifullah, G., Smits, R., Taylor, S. R., Theureau, G., van Haasteren, R., and Vecchio, A. (2016). The noise properties of 42 millisecond pulsars from the European Pulsar Timing Array and their impact on gravitational-wave searches. MNRAS, 457:4421–4440.

Chandrasekhar, S. (1943). Dynamical Friction. I. General Considerations: the Coefficient of Dynamical Friction. Astrophysical Journal, 97:255.

Chen, S., Middleton, H., Sesana, A., Del Pozzo, W., and Vecchio, A. (2017a). Probing the assembly history and dynamical evolution of massive black hole binaries with pulsar timing arrays. MNRAS, 468:404–417.

Chen, S., Sesana, A., and Conselice, C. J. (2018). Constraining astrophysical observables of Galaxy and Supermassive Black Hole Binary Mergers using Pulsar Timing Arrays. ArXiv e-prints.

Chen, S., Sesana, A., and Del Pozzo, W. (2017b). Efficient computation of the gravitational wave spectrum emitted by eccentric massive black hole binaries in stellar environments. MNRAS, 470:1738–1749.

Conselice, C. J., Bershady, M. A., Dickinson, M., and Papovich, C. (2003). A Direct Measurement of Major Galaxy Mergers at z $\lesssim$ 3. Astronomical Journal, 126:1183–1207.

Conselice, C. J., Wilkinson, A., Duncan, K., and Mortlock, A. (2016). The Evolution of Galaxy Number Density at z < 8 and Its Implications. Astrophysical Journal, 830:83.

Cordes, J. M. and Shannon, R. M. (2010). A Measurement Model for Precision Pulsar Timing. ArXiv e-prints.

Cordes, J. M., Shannon, R. M., and Stinebring, D. R. (2016). Frequency-dependent Dispersion Measures and Implications for Pulsar Timing. Astrophysical Journal, 817:16.

Cuadra, J., Armitage, P. J., Alexander, R. D., and Begelman, M. C. (2009). Massive black hole binary mergers within subparsec scale gas discs. MNRAS, 393:1423–1432.

Dabringhausen, J., Hilker, M., and Kroupa, P. (2008). From star clusters to dwarf galaxies: the properties of dynamically hot stellar systems. MNRAS, 386:864–886.

de Ravel, L., Le Fèvre, O., Tresse, L., Bottini, D., Garilli, B., Le Brun, V., Maccagni, D., Scaramella, R., Scodeggio, M., Vettolani, G., Zanichelli, A., Adami, C., Arnouts, S., Bardelli, S., Bolzonella, M., Cappi, A., Charlot, S., Ciliegi, P., Contini, T., Foucaud, S., Franzetti, P., Gavignaud, I., Guzzo, L., Ilbert, O., Iovino, A., Lamareille, F., McCracken, H. J., Marano, B., Marinoni, C., Mazure, A., Meneux, B., Merighi, R., Paltani, S., Pellò, R., Pollo, A., Pozzetti, L., Radovich, M., Vergani, D., Zamorani, G., Zucca, E., Bondi, M., Bongiorno, A., Brinchmann, J., Cucciati, O., de La Torre, S., Gregorini, L., Memeo, P., Perez-Montero, E., Mellier, Y., Merluzzi, P., and Temporin, S. (2009). The VIMOS VLT Deep Survey. Evolution of the major merger rate since z $\sim$ 1 from spectroscopically confirmed galaxy pairs. A&A, 498:379–397.

Dehnen, W. (1993). A Family of Potential-Density Pairs for Spherical Galaxies and Bulges. MNRAS, 265:250.

Del Pozzo, W. and Veitch, J. (2015). CPNest: Parallel nested sampling in python. https://github.com/johnveitch/cpnest.

Desvignes, G., Caballero, R. N., Lentati, L., Verbiest, J. P. W., Champion, D. J., Stappers, B. W., Janssen, G. H., Lazarus, P., Osłowski, S., Babak, S., Bassa, C. G., Brem, P., Burgay, M., Cognard, I., Gair, J. R., Graikou, E., Guillemot, L., Hessels, J. W. T., Jessner, A., Jordan, C., Karuppusamy, R., Kramer, M., Lassus, A., Lazaridis, K., Lee, K. J., Liu, K., Lyne, A. G., McKee, J., Mingarelli, C. M. F., Perrodin, D., Petiteau, A., Possenti, A., Purver, M. B., Rosado, P. A., Sanidas, S., Sesana, A., Shaifullah, G., Smits, R., Taylor, S. R., Theureau, G., Tiburzi, C., van Haasteren, R., and Vecchio, A. (2016). High-precision timing of 42 millisecond pulsars with the European Pulsar Timing Array. MNRAS, 458:3341–3380.

Detweiler, S. (1979). Pulsar timing measurements and the search for gravitational waves. Astrophysical Journal, 234:1100–1104.

Dewdney, P. E., Hall, P. J., Schilizzi, R. T., and Lazio, T. J. L. W. (2009). The Square Kilometre Array. IEEE Proceedings, 97:1482–1496.

Do, T., Wright, S. A., Barth, A. J., Barton, E. J., Simard, L., Larkin, J. E., Moore, A. M., Wang, L., and Ellerbroek, B. (2014). Prospects for Measuring Supermassive Black Hole Masses with Future Extremely Large Telescopes. Astronomical Journal, 147:93.

Dosopoulou, F. and Antonini, F. (2017). Dynamical Friction and the Evolution of Supermassive Black Hole Binaries: The Final Hundred-parsec Problem. Astrophysical Journal, 840:31.

Dotti, M., Sesana, A., and Decarli, R. (2012). Massive Black Hole Binaries: Dynamical Evolution and Observational Signatures. Advances in Astronomy, 2012:3.

Dvorkin, I. and Barausse, E. (2017). The nightmare scenario: measuring the stochastic gravitational wave background from stalling massive black hole binaries with pulsar timing arrays. MNRAS, 470:4547–4556.

Edwards, R. T., Hobbs, G. B., and Manchester, R. N. (2006). TEMPO2, a new pulsar timing package - II. The timing model and precision estimates. MNRAS, 372:1549–1574.

Enoki, M. and Nagashima, M. (2007). The Effect of Orbital Eccentricity on Gravitational Wave Background Radiation from Supermassive Black Hole Binaries. Progress of Theoretical Physics, 117:241–256.

Ferdman, R. D., van Haasteren, R., Bassa, C. G., Burgay, M., Cognard, I., Corongiu, A., D'Amico, N., Desvignes, G., Hessels, J. W. T., Janssen, G. H., Jessner, A., Jordan, C., Karuppusamy, R., Keane, E. F., Kramer, M., Lazaridis, K., Levin, Y., Lyne, A. G., Pilia, M., Possenti, A., Purver, M., Stappers, B., Sanidas, S., Smits, R., and Theureau, G. (2010). The European Pulsar Timing Array: current efforts and a LEAP toward the future. Classical and Quantum Gravity, 27(8):084014.

Foster, R. S. and Backer, D. C. (1990). Constructing a pulsar timing array. Astrophysical Journal, 361:300–308.

Genzel, R., Eisenhauer, F., and Gillessen, S. (2010). The Galactic Center massive black hole and nuclear star cluster. Reviews of Modern Physics, 82:3121–3195.

Gilmozzi, R. and Spyromilio, J. (2007). The European Extremely Large Telescope (E-ELT). The Messenger, 127.

Graham, A. W. (2012). Breaking the Law: The M $_{bh}$-M $_{spheroid}$ Relations for Core-Sérsic and Sérsic Galaxies. Astrophys. J., 746:113.

Graham, A. W., Onken, C. A., Athanassoula, E., and Combes, F. (2011). An expanded M_{bh}-σ diagram, and a new calibration of active galactic nuclei masses. Mon. Not. R. Astron. Soc., 412:2211–2228.

Graham, A. W. and Scott, N. (2013). The M $_{BH}$-L $_{spheroid}$ Relation at High and Low Masses, the Quadratic Growth of Black Holes, and Intermediate-mass Black Hole Candidates. Astrophysical Journal, 764:151.

Gültekin, K., Richstone, D. O., Gebhardt, K., Lauer, T. R., Tremaine, S., Aller, M. C., Bender, R., Dressler, A., Faber, S. M., Filippenko, A. V., Green, R., Ho, L. C., Kormendy, J., Magorrian, J., Pinkney, J., and Siopis, C. (2009). The M-σ and M-L Relations in Galactic Bulges, and Determinations of Their Intrinsic Scatter. Astrophysical Journal, 698:198–221.

Harding, A. K. (2017). Pulsar Emission Physics: The First Fifty Years. ArXiv e-prints.

Häring, N. and Rix, H.-W. (2004). On the Black Hole Mass-Bulge Mass Relation. Astrophys. J. Letters, 604:L89–L92.

Hellings, R. W. and Downs, G. S. (1983). Upper limits on the isotropic gravitational radiation background from pulsar timing analysis. Astrophysical Journal, 265:L39–L42.

Hernquist, L. (1990). An analytical model for spherical galaxies and bulges. Astrophysical Journal, 356:359–364.

Hewish, A., Bell, S. J., Pilkington, J. D. H., Scott, P. F., and Collins, R. A. (1968). Observation of a Rapidly Pulsating Radio Source. Nature, 217:709–713.

Hlavacek-Larrondo, J., Fabian, A. C., Edge, A. C., and Hogan, M. T. (2012). On the hunt for ultramassive black holes in brightest cluster galaxies. MNRAS, 424:224–231.

Hobbs, G., Archibald, A., Arzoumanian, Z., Backer, D., Bailes, M., Bhat, N. D. R., Burgay, M., Burke-Spolaor, S., Champion, D., Cognard, I., Coles, W., Cordes, J., Demorest, P., Desvignes, G., Ferdman, R. D., Finn, L., Freire, P., Gonzalez, M., Hessels, J., Hotan, A., Janssen, G., Jenet, F., Jessner, A., Jordan, C., Kaspi, V., Kramer, M., Kondratiev, V., Lazio, J., Lazaridis, K., Lee, K. J., Levin, Y., Lommen, A., Lorimer, D., Lynch, R., Lyne, A., Manchester, R., McLaughlin, M., Nice, D., Oslowski, S., Pilia, M., Possenti, A., Purver, M., Ransom, S., Reynolds, J., Sanidas, S., Sarkissian, J., Sesana, A., Shannon, R., Siemens, X., Stairs, I., Stappers, B., Stinebring, D., Theureau, G., van Haasteren, R., van Straten, W., Verbiest, J. P. W., Yardley, D. R. B., and You, X. P. (2010). The International Pulsar Timing Array project: using pulsars as a gravitational wave detector. Classical and Quantum Gravity, 27(8):084013.

Hobbs, G. and Dai, S. (2017). A review of pulsar timing array gravitational wave research. ArXiv e-prints.

Hobbs, G. B., Bailes, M., Bhat, N. D. R., Burke-Spolaor, S., Champion, D. J., Coles, W., Hotan, A., Jenet, F., Kedziora-Chudczer, L., Khoo, J., Lee, K. J., Lommen, A., Manchester, R. N., Reynolds, J., Sarkissian, J., van Straten, W., To, S., Verbiest, J. P. W., Yardley, D., and You, X. P. (2009). Gravitational-Wave Detection Using Pulsars: Status of the Parkes Pulsar Timing Array Project. , 26:103–109.

Hobbs, G. B., Edwards, R. T., and Manchester, R. N. (2006). TEMPO2, a new pulsar-timing package - I. An overview. MNRAS, 369:655–672.

Hoffman, L. and Loeb, A. (2007). Dynamics of triple black hole systems in hierarchically merging massive galaxies. MNRAS, 377:957–976.

Hogg, D. W. (1999). Distance measures in cosmology. ArXiv Astrophysics e-prints.

Hopkins, P. F., Richards, G. T., and Hernquist, L. (2007). An Observational Determination of the Bolometric Quasar Luminosity Function. Astrophysical Journal, 654:731–753.

Huerta, E. A., McWilliams, S. T., Gair, J. R., and Taylor, S. R. (2015). Detection of eccentric supermassive black hole binaries with pulsar timing arrays: Signal-to-noise ratio calculations. Phys. Rev. D, 92(6):063010.

Hulse, R. A. and Taylor, J. H. (1975). Discovery of a pulsar in a binary system. Astrophysical Journal, 195:L51–L53.

Ilbert, O., McCracken, H. J., Le Fèvre, O., Capak, P., Dunlop, J., Karim, A., Renzini, M. A., Caputi, K., Boissier, S., Arnouts, S., Aussel, H., Comparat, J., Guo, Q., Hudelot, P., Kartaltepe, J., Kneib, J. P., Krogager, J. K., Le Floc'h, E., Lilly, S., Mellier, Y., Milvang-Jensen, B., Moutard, T., Onodera, M., Richard, J., Salvato, M., Sanders, D. B., Scoville, N., Silverman, J. D., Taniguchi, Y., Tasca, L., Thomas, R., Toft, S., Tresse, L., Vergani, D., Wolk, M., and Zirm, A. (2013). Mass assembly in quiescent and star-forming galaxies since z $\simeq$ 4 from UltraVISTA. A&A, 556:A55.

Ivanov, P. B., Papaloizou, J. C. B., and Polnarev, A. G. (1999). The evolution of a supermassive binary caused by an accretion disc. MNRAS, 307:79–90.

Jaffe, A. H. and Backer, D. C. (2003). Gravitational Waves Probe the Coalescence Rate of Massive Black Hole Binaries. Astrophysical Journal, 583:616–631.

Janssen, G., Hobbs, G., McLaughlin, M., Bassa, C., Deller, A., Kramer, M., Lee, K., Mingarelli, C., Rosado, P., Sanidas, S., Sesana, A., Shao, L., Stairs, I., Stappers, B., and Verbiest, J. P. W. (2015). Gravitational Wave Astronomy with the SKA. Advancing Astrophysics with the Square Kilometre Array (AASKA14), page 37.

Jenet, F., Finn, L. S., Lazio, J., Lommen, A., McLaughlin, M., Stairs, I., Stinebring, D., Verbiest, J., Archibald, A., Arzoumanian, Z., Backer, D., Cordes, J., Demorest, P., Ferdman, R., Freire, P., Gonzalez, M., Kaspi, V., Kondratiev, V., Lorimer, D., Lynch, R., Nice, D., Ransom, S., Shannon, R., and Siemens, X. (2009). The North American Nanohertz Observatory for Gravitational Waves. ArXiv e-prints.

Jenet, F. A. and Romano, J. D. (2015). Understanding the gravitational-wave Hellings and Downs curve for pulsar timing arrays in terms of sound and electromagnetic waves. American Journal of Physics, 83:635–645.

Kass, R. E. and Raftery, A. E. (1995). Bayes factors. Journal of the American Statistical Association, 90:773–795.

Kauffmann, G., White, S. D. M., and Guiderdoni, B. (1993). The Formation and Evolution of Galaxies Within Merging Dark Matter Haloes. MNRAS, 264:201.

Keenan, R. C., Foucaud, S., De Propris, R., Hsieh, B. C., Lin, L., Chou, R. C. Y., Huang, S., Lin, J. H., and Chang, K. H. (2014). Evolution of the Major Merger Galaxy Pair Fraction at z < 1. Astrophysical Journal, 795:157.

Keith, M. J., Coles, W., Shannon, R. M., Hobbs, G. B., Manchester, R. N., Bailes, M., Bhat, N. D. R., Burke-Spolaor, S., Champion, D. J., Chaudhary, A., Hotan, A. W., Khoo, J., Kocz, J., Osłowski, S., Ravi, V., Reynolds, J. E., Sarkissian, J., van Straten, W., and Yardley, D. R. B. (2013). Measurement and correction of variations in interstellar dispersion in high-precision pulsar timing. MNRAS, 429:2161–2174.

Kelley, L. Z., Blecha, L., and Hernquist, L. (2017a). Massive black hole binary mergers in dynamical galactic environments. MNRAS, 464:3131–3157.

Kelley, L. Z., Blecha, L., Hernquist, L., Sesana, A., and Taylor, S. R. (2017b). The gravitational wave background from massive black hole binaries in Illustris: spectral features and time to detection with pulsar timing arrays. MNRAS, 471:4508–4526.

Kitzbichler, M. G. and White, S. D. M. (2008). A calibration of the relation between the abundance of close galaxy pairs and the rate of galaxy mergers. Mon. Not. R. Astron. Soc., 391:1489–1498.

Kormendy, J., Fisher, D. B., Cornell, M. E., and Bender, R. (2009). Structure and Formation of Elliptical and Spheroidal Galaxies. ApJS, 182:216–309.

Kormendy, J. and Ho, L. C. (2013). Coevolution (Or Not) of Supermassive Black Holes and Host Galaxies. ARA&A, 51:511–653.

Kormendy, J. and Richstone, D. (1995). Inward Bound—The Search For Supermassive Black Holes In Galactic Nuclei. ARA&A, 33:581.

Kramer, M., Stairs, I. H., Manchester, R. N., McLaughlin, M. A., Lyne, A. G., Ferdman, R. D., Burgay, M., Lorimer, D. R., Possenti, A., D'Amico, N., Sarkissian, J. M., Hobbs, G. B., Reynolds, J. E., Freire, P. C. C., and Camilo, F. (2006). Tests of General Relativity from Timing the Double Pulsar. Science, 314:97–102.

Kulier, A., Ostriker, J. P., Natarajan, P., Lackner, C. N., and Cen, R. (2015). Understanding Black Hole Mass Assembly via Accretion and Mergers at Late Times in Cosmological Simulations. Astrophysical Journal, 799:178.

Lam, M. T., Cordes, J. M., Chatterjee, S., and Dolch, T. (2015). Pulsar Timing Errors from Asynchronous Multi-frequency Sampling of Dispersion Measure Variations. Astrophysical Journal, 801:130.

Lee, K. J., Bassa, C. G., Janssen, G. H., Karuppusamy, R., Kramer, M., Liu, K., Perrodin, D., Smits, R., Stappers, B. W., van Haasteren, R., and Lentati, L. (2014). Model-based asymptotically optimal dispersion measure correction for pulsar timing. MNRAS, 441:2831–2844.

Lentati, L., Taylor, S. R., Mingarelli, C. M. F., Sesana, A., Sanidas, S. A., Vecchio, A., Caballero, R. N., Lee, K. J., van Haasteren, R., Babak, S., Bassa, C. G., Brem, P., Burgay, M., Champion, D. J., Cognard, I., Desvignes, G., Gair, J. R., Guillemot, L., Hessels, J. W. T., Janssen, G. H., Karuppusamy, R., Kramer, M., Lassus, A., Lazarus, P., Liu, K., Osłowski, S., Perrodin, D., Petiteau, A., Possenti, A., Purver, M. B., Rosado, P. A., Smits, R., Stappers, B., Theureau, G., Tiburzi, C., and Verbiest, J. P. W. (2015). European Pulsar Timing Array limits on an isotropic stochastic gravitational-wave background. MNRAS, 453:2576–2598.

Lin, L., Koo, D. C., Willmer, C. N. A., Patton, D. R., Conselice, C. J., Yan, R., Coil, A. L., Cooper, M. C., Davis, M., Faber, S. M., Gerke, B. F., Guhathakurta, P., and Newman, J. A. (2004). The DEEP2 Galaxy Redshift Survey: Evolution of Close Galaxy Pairs and Major-Merger Rates up to z ˜ 1.2. Astrophysical Journal, 617:L9–L12.

López-Sanjuan, C., Le Fèvre, O., Ilbert, O., Tasca, L. A. M., Bridge, C., Cucciati, O., Kampczyk, P., Pozzetti, L., Xu, C. K., Carollo, C. M., Contini, T., Kneib, J.-P., Lilly, S. J., Mainieri, V., Renzini, A., Sanders, D., Scodeggio, M., Scoville, N. Z., Taniguchi, Y., Zamorani, G., Aussel, H., Bardelli, S., Bolzonella, M., Bongiorno, A., Capak, P., Caputi, K., de la Torre, S., de Ravel, L., Franzetti, P., Garilli, B., Iovino, A., Knobel, C., Kovač, K., Lamareille, F., Le Borgne, J.-F., Le Brun, V., Le Floc'h, E., Maier, C., McCracken, H. J., Mignoli, M., Pelló, R., Peng, Y., Pérez-Montero, E., Presotto, V., Ricciardelli, E., Salvato, M., Silverman, J. D., Tanaka, M., Tresse, L., Vergani, D., Zucca, E., Barnes, L., Bordoloi, R., Cappi, A., Cimatti, A., Coppa, G., Koekemoer, A., Liu, C. T., Moresco, M., Nair, P., Oesch, P., Schawinski, K., and Welikala, N. (2012). The dominant role of mergers in the size evolution of massive early-type galaxies since z ˜ 1. A&A, 548:A7.

Lorimer, D. R. (2008). Binary and Millisecond Pulsars. Living Reviews in Relativity, 11.

Lorimer, D. R. and Kramer, M. (2012). Handbook of Pulsar Astronomy. Cambridge University Press, 2012.

Lotz, J. M., Jonsson, P., Cox, T. J., Croton, D., Primack, J. R., Somerville, R. S., and Stewart, K. (2011). The Major and Minor Galaxy Merger Rates at z < 1.5. Astrophysical Journal, 742:103.

Lotz, J. M., Jonsson, P., Cox, T. J., and Primack, J. R. (2010). The effect of mass ratio on the morphology and time-scales of disc galaxy mergers. Mon. Not. R. Astron. Soc., 404:575–589.

Luo, J., Ransom, S. M., Demorest, P., Ray, P. S., Stovall, K., Jenet, F., Ellis, J., van Haasteren, R., Bachetti, M., and NANOGrav PINT developer team (2018). PINT, A Modern Software

Package for Pulsar Timing. In American Astronomical Society Meeting Abstracts #231, volume 231 of American Astronomical Society Meeting Abstracts, page 453.09.

Manchester, R. N., Hobbs, G. B., Teoh, A., and Hobbs, M. (2005). The Australia Telescope National Facility Pulsar Catalogue. Astronomical Journal, 129:1993–2006.

Marconi, A. and Hunt, L. K. (2003). The Relation between Black Hole Mass, Bulge Mass, and Near-Infrared Luminosity. Astrophysical Journal, 589:L21–L24.

McConnell, N. J. and Ma, C.-P. (2013). Revisiting the Scaling Relations of Black Hole Masses and Host Galaxy Properties. Astrophysical Journal, 764:184.

McConnell, N. J., Ma, C.-P., Gebhardt, K., Wright, S. A., Murphy, J. D., Lauer, T. R., Graham, J. R., and Richstone, D. O. (2011). Two ten-billion-solar-mass black holes at the centres of giant elliptical galaxies. Nature, 480:215–218.

McWilliams, S. T., Ostriker, J. P., and Pretorius, F. (2014). Gravitational Waves and Stalled Satellites from Massive Galaxy Mergers at z <= 1. Astrophysical Journal, 789:156.

Melrose, D. B. and Rafat, M. Z. (2017). Pulsar radio emission mechanism: Why no consensus? Journal of Physics: Conference Series, 932(1):012011.

Middleton, H., Chen, S., Del Pozzo, W., Sesana, A., and Vecchio, A. (2018). No tension between assembly models of super massive black hole binaries and pulsar observations. Nature Communications, 9:573.

Middleton, H., Del Pozzo, W., Farr, W. M., Sesana, A., and Vecchio, A. (2016). Astrophysical constraints on massive black hole binary evolution from pulsar timing arrays. MNRAS, 455:L72–L76.

Milosavljević, M. and Merritt, D. (2003). The Final Parsec Problem. In Centrella, J. M., editor, The Astrophysics of Gravitational Wave Sources, volume 686 of American Institute of Physics Conference Series, pages 201–210.

Mingarelli, C. M. F., Lazio, T. J. W., Sesana, A., Greene, J. E., Ellis, J. A., Ma, C.-P., Croft, S., Burke-Spolaor, S., and Taylor, S. R. (2017). The local nanohertz gravitational-wave landscape from supermassive black hole binaries. Nature Astronomy, 1:886–892.

Mirza, M. A., Tahir, A., Khan, F. M., Holley-Bockelmann, H., Baig, A. M., Berczik, P., and Chishtie, F. (2017). Galaxy rotation and supermassive black hole binary evolution. MNRAS, 470:940–947.

Moore, C. J., Cole, R. H., and Berry, C. P. L. (2015a). Gravitational-wave sensitivity curves. Classical and Quantum Gravity, 32(1):015014.

Moore, C. J., Taylor, S. R., and Gair, J. R. (2015b). Estimating the sensitivity of pulsar timing arrays. Classical and Quantum Gravity, 32(5):055004.

Mortlock, A., Conselice, C. J., Hartley, W. G., Duncan, K., Lani, C., Ownsworth, J. R., Almaini, O., Wel, A. v. d., Huang, K.-H., Ashby, M. L. N., Willner, S. P., Fontana, A., Dekel, A., Koekemoer, A. M., Ferguson, H. C., Faber, S. M., Grogin, N. A., and Kocevski, D. D. (2015). Deconstructing the galaxy stellar mass function with UKIDSS and CANDELS: the impact of colour, structure and environment. MNRAS, 447:2–24.

Mundy, C. J., Conselice, C. J., Duncan, K. J., Almaini, O., Häußler, B., and Hartley, W. G. (2017). A consistent measure of the merger histories of massive galaxies using close-pair statistics - I. Major mergers at z < 3.5. MNRAS, 470:3507–3531.

Muzzin, A., Marchesini, D., Stefanon, M., Franx, M., McCracken, H. J., Milvang-Jensen, B., Dunlop, J. S., Fynbo, J. P. U., Brammer, G., Labbé, I., and van Dokkum, P. G. (2013). The Evolution of the Stellar Mass Functions of Star-forming and Quiescent Galaxies to z = 4 from the COSMOS/UltraVISTA Survey. Astrophysical Journal, 777:18.

Nan, R., Li, D., Jin, C., Wang, Q., Zhu, L., Zhu, W., Zhang, H., Yue, Y., and Qian, L. (2011). The Five-Hundred Aperture Spherical Radio Telescope (fast) Project. International Journal of Modern Physics D, 20:989–1024.

Perrodin, D. and Sesana, A. (2017). Radio pulsars: testing gravity and detecting gravitational waves. ArXiv e-prints.

Peters, P. C. and Mathews, J. (1963). Gravitational Radiation from Point Masses in a Keplerian Orbit. Physical Review, 131:435–440.

Phinney, E. S. (2001). A Practical Theorem on Gravitational Wave Backgrounds. ArXiv Astrophysics e-prints.

Quinlan, G. D. (1996). The dynamical evolution of massive black hole binaries I. Hardening in a fixed stellar background. , 1:35–56.

Rajagopal, M. and Romani, R. W. (1995). Ultra–Low-Frequency Gravitational Radiation from Massive Black Hole Binaries. Astrophysical Journal, 446:543.

Rasskazov, A. and Merritt, D. (2017). Evolution of massive black hole binaries in rotating stellar nuclei: Implications for gravitational wave detection. Phys. Rev. D, 95(8):084032.

Ravi, V., Wyithe, J. S. B., Hobbs, G., Shannon, R. M., Manchester, R. N., Yardley, D. R. B., and Keith, M. J. (2012). Does a "Stochastic" Background of Gravitational Waves Exist in the Pulsar Timing Band? Astrophysical Journal, 761:84.

Ravi, V., Wyithe, J. S. B., Shannon, R. M., and Hobbs, G. (2015). Prospects for gravitational-wave detection and supermassive black hole astrophysics with pulsar timing arrays. MNRAS, 447:2772–2783.

Reardon, D. J., Hobbs, G., Coles, W., Levin, Y., Keith, M. J., Bailes, M., Bhat, N. D. R., Burke-Spolaor, S., Dai, S., Kerr, M., Lasky, P. D., Manchester, R. N., Osłowski, S., Ravi, V., Shannon, R. M., van Straten, W., Toomey, L., Wang, J., Wen, L., You, X. P., and Zhu, X.-J. (2016). Timing analysis for 20 millisecond pulsars in the Parkes Pulsar Timing Array. MNRAS, 455:1751–1769.

Robotham, A. S. G., Driver, S. P., Davies, L. J. M., Hopkins, A. M., Baldry, I. K., Agius, N. K., Bauer, A. E., Bland-Hawthorn, J., Brough, S., Brown, M. J. I., Cluver, M., De Propris, R.,

Drinkwater, M. J., Holwerda, B. W., Kelvin, L. S., Lara-Lopez, M. A., Liske, J., López-Sánchez, Á. R., Loveday, J., Mahajan, S., McNaught-Roberts, T., Moffett, A., Norberg, P., Obreschkow, D., Owers, M. S., Penny, S. J., Pimbblet, K., Prescott, M., Taylor, E. N., van Kampen, E., and Wilkins, S. M. (2014). Galaxy And Mass Assembly (GAMA): galaxy close pairs, mergers and the future fate of stellar mass. MNRAS, 444:3986–4008.

Rosado, P. A., Sesana, A., and Gair, J. (2015). Expected properties of the first gravitational wave signal detected with pulsar timing arrays. MNRAS, 451:2417–2433.

Ryu, T., Perna, R., Haiman, Z., Ostriker, J. P., and Stone, N. C. (2018). Interactions between multiple supermassive black holes in galactic nuclei: a solution to the final parsec problem. MNRAS, 473:3410–3433.

Sanders, G. H. (2013). The Thirty Meter Telescope (TMT): An International Observatory. Journal of Astrophysics and Astronomy, 34:81–86.

Sani, E., Marconi, A., Hunt, L. K., and Risaliti, G. (2011). The Spitzer/IRAC view of black hole-bulge scaling relations. Mon. Not. R. Astron. Soc., 413:1479–1494.

Sazhin, M. V. (1978). Opportunities for detecting ultralong gravitational waves. Soviet Ast., 22:36–38.

Sesana, A. (2013a). Insights into the astrophysics of supermassive black hole binaries from pulsar timing observations. Classical and Quantum Gravity, 30(22):224014.

Sesana, A. (2013b). Systematic investigation of the expected gravitational wave signal from supermassive black hole binaries in the pulsar timing band. MNRAS, 433:L1–L5.

Sesana, A. and Khan, F. M. (2015). Scattering experiments meet N-body - I. A practical recipe for the evolution of massive black hole binaries in stellar environments. MNRAS, 454:L66–L70.

Sesana, A., Roedig, C., Reynolds, M. T., and Dotti, M. (2012). Multimessenger astronomy with pulsar timing and X-ray observations of massive black hole binaries. MNRAS, 420:860–877.

Sesana, A., Shankar, F., Bernardi, M., and Sheth, R. K. (2016). Selection bias in dynamically measured supermassive black hole samples: consequences for pulsar timing arrays. MNRAS, 463:L6–L11.

Sesana, A., Vecchio, A., and Colacino, C. N. (2008). The stochastic gravitational-wave background from massive black hole binary systems: implications for observations with Pulsar Timing Arrays. MNRAS, 390:192–209.

Sesana, A., Vecchio, A., and Volonteri, M. (2009). Gravitational waves from resolvable massive black hole binary systems and observations with Pulsar Timing Arrays. MNRAS, 394:2255–2265.

Shankar, F., Bernardi, M., Sheth, R. K., Ferrarese, L., Graham, A. W., Savorgnan, G., Allevato, V., Marconi, A., Läsker, R., and Lapi, A. (2016). Selection bias in dynamically measured supermassive black hole samples: its consequences and the quest for the most fundamental relation. MNRAS, 460:3119–3142.

Shankar, F., Salucci, P., Granato, G. L., De Zotti, G., and Danese, L. (2004). Supermassive black hole demography: the match between the local and accreted mass functions. MNRAS, 354:1020–1030.

Shannon, R. M., Ravi, V., Lentati, L. T., Lasky, P. D., Hobbs, G., Kerr, M., Manchester, R. N., Coles, W. A., Levin, Y., Bailes, M., Bhat, N. D. R., Burke-Spolaor, S., Dai, S., Keith, M. J., Osłowski, S., Reardon, D. J., van Straten, W., Toomey, L., Wang, J.-B., Wen, L., Wyithe, J. S. B., and Zhu, X.-J. (2015). Gravitational waves from binary supermassive black holes missing in pulsar observations. Science, 349:1522–1525.

Siemens, X., Ellis, J., Jenet, F., and Romano, J. D. (2013). The stochastic background: scaling laws and time to detection for pulsar timing arrays. Classical and Quantum Gravity, 30(22):224015.

Simon, J. and Burke-Spolaor, S. (2016). Constraints on Black Hole/Host Galaxy Co-evolution and Binary Stalling Using Pulsar Timing Arrays. Astrophysical Journal, 826:11.

Skilling, J. (2004). American institute of physics conference series. In American Institute of Physics Conference Series, volume 735, pages 395–405.

Smits, R., Kramer, M., Stappers, B., Lorimer, D. R., Cordes, J., and Faulkner, A. (2009). Pulsar searches and timing with the square kilometre array. A&A, 493:1161–1170.

Snyder, G. F., Lotz, J. M., Rodriguez-Gomez, V., Guimarães, R. d. S., Torrey, P., and Hernquist, L. (2017). Massive close pairs measure rapid galaxy assembly in mergers at high redshift. MNRAS, 468:207–216.

Springel, V., White, S. D. M., Jenkins, A., Frenk, C. S., Yoshida, N., Gao, L., Navarro, J., Thacker, R., Croton, D., Helly, J., Peacock, J. A., Cole, S., Thomas, P., Couchman, H., Evrard, A., Colberg, J., and Pearce, F. (2005). Simulations of the formation, evolution and clustering of galaxies and quasars. Nature, 435:629–636.

Swarup, G. (1991). Giant metrewave radio telescope (GMRT). In Cornwell, T. J. and Perley, R. A., editors, IAU Colloq. 131: Radio Interferometry. Theory, Techniques, and Applications, volume 19 of Astronomical Society of the Pacific Conference Series, pages 376–380.

Tang, Y., MacFadyen, A., and Haiman, Z. (2017). On the orbital evolution of supermassive black hole binaries with circumbinary accretion discs. MNRAS, 469:4258–4267.

Taylor, S. R., Huerta, E. A., Gair, J. R., and McWilliams, S. T. (2016a). Detecting Eccentric Supermassive Black Hole Binaries with Pulsar Timing Arrays: Resolvable Source Strategies. Astrophysical Journal, 817:70.

Taylor, S. R., Lentati, L., Babak, S., Brem, P., Gair, J. R., Sesana, A., and Vecchio, A. (2017a). All correlations must die: Assessing the significance of a stochastic gravitational-wave background in pulsar timing arrays. Phys. Rev. D, 95(4):042002.

Taylor, S. R., Simon, J., and Sampson, L. (2017b). Constraints on the Dynamical Environments of Supermassive Black-Hole Binaries Using Pulsar-Timing Arrays. Physical Review Letters, 118(18):181102.

Taylor, S. R., Vallisneri, M., Ellis, J. A., Mingarelli, C. M. F., Lazio, T. J. W., and van Haasteren, R. (2016b). Are We There Yet? Time to Detection of Nanohertz Gravitational Waves Based on Pulsar-timing Array Limits. Astrophysical Journal, 819:L6.

Tiburzi, C., Hobbs, G., Kerr, M., Coles, W. A., Dai, S., Manchester, R. N., Possenti, A., Shannon, R. M., and You, X. P. (2016). A study of spatial correlations in pulsar timing array data. MNRAS, 455:4339–4350.

Tomczak, A. R., Quadri, R. F., Tran, K.-V. H., Labbé, I., Straatman, C. M. S., Papovich, C., Glazebrook, K., Allen, R., Brammer, G. B., Kacprzak, G. G., Kawinwanichakij, L., Kelson, D. D., McCarthy, P. J., Mehrtens, N., Monson, A. J., Persson, S. E., Spitler, L. R., Tilvi, V., and van Dokkum, P. (2014). Galaxy Stellar Mass Functions from ZFOURGE/CANDELS: An Excess of Low-mass Galaxies since z = 2 and the Rapid Buildup of Quiescent Galaxies. Astrophysical Journal, 783:85.

Vasiliev, E., Antonini, F., and Merritt, D. (2014). The Final-parsec Problem in Nonspherical Galaxies Revisited. Astrophysical Journal, 785:163.

Vasiliev, E., Antonini, F., and Merritt, D. (2015). The Final-parsec Problem in the Collisionless Limit. Astrophysical Journal, 810:49.

Veitch, J., Raymond, V., Farr, B., Farr, W., Graff, P., Vitale, S., Aylott, B., Blackburn, K., Christensen, N., Coughlin, M., Del Pozzo, W., Feroz, F., Gair, J., Haster, C.-J., Kalogera, V., Littenberg, T., Mandel, I., O'Shaughnessy, R., Pitkin, M., Rodriguez, C., Röver, C., Sidery, T., Smith, R., Van Der Sluys, M., Vecchio, A., Vousden, W., and Wade, L. (2015). Parameter estimation for compact binaries with ground-based gravitational-wave observations using the LALInference software library. Phys. Rev. D, 91(4):042003.

Veitch, J. and Vecchio, A. (2010). Bayesian coherent analysis of in-spiral gravitational wave signals with a detector network. Phys. Rev. D, 81(6):062003.

Verbiest, J. P. W., Lentati, L., Hobbs, G., van Haasteren, R., Demorest, P. B., Janssen, G. H., Wang, J.-B., Desvignes, G., Caballero, R. N., Keith, M. J., Champion, D. J., Arzoumanian, Z.,

Babak, S., Bassa, C. G., Bhat, N. D. R., Brazier, A., Brem, P., Burgay, M., Burke-Spolaor, S., Chamberlin, S. J., Chatterjee, S., Christy, B., Cognard, I., Cordes, J. M., Dai, S., Dolch, T., Ellis, J. A., Ferdman, R. D., Fonseca, E., Gair, J. R., Garver-Daniels, N. E., Gentile, P., Gonzalez, M. E., Graikou, E., Guillemot, L., Hessels, J. W. T., Jones, G., Karuppusamy, R., Kerr, M., Kramer, M., Lam, M. T., Lasky, P. D., Lassus, A., Lazarus, P., Lazio, T. J. W., Lee, K. J., Levin, L., Liu, K., Lynch, R. S., Lyne, A. G., Mckee, J., McLaughlin, M. A., McWilliams, S. T., Madison, D. R., Manchester, R. N., Mingarelli, C. M. F., Nice, D. J., Osłowski, S., Palliyaguru, N. T., Pennucci, T. T., Perera, B. B. P., Perrodin, D., Possenti, A., Petiteau, A., Ransom, S. M., Reardon, D., Rosado, P. A., Sanidas, S. A., Sesana, A., Shaifullah, G., Shannon, R. M., Siemens, X., Simon, J., Smits, R., Spiewak, R., Stairs, I. H., Stappers, B. W., Stinebring, D. R., Stovall, K., Swiggum, J. K., Taylor, S. R., Theureau, G., Tiburzi, C., Toomey, L., Vallisneri, M., van Straten, W., Vecchio, A., Wang, Y., Wen, L., You, X. P., Zhu, W. W., and Zhu, X.-J. (2016). The International Pulsar Timing Array: First data release. MNRAS, 458:1267–1288.

Volonteri, M., Haardt, F., and Madau, P. (2003). The Assembly and Merging History of Supermassive Black Holes in Hierarchical Models of Galaxy Formation. Astrophysical Journal, 582:559–573.

Wang, N. (2014). Xinjiang qitai 110 m radio telescope. Scientia Sinica Physica, Mechanica & Astronomica, 44(8):783.

White, S. D. M. and Rees, M. J. (1978). Core condensation in heavy halos - A two-stage theory for galaxy formation and clustering. MNRAS, 183:341–358.

Xu, C. K., Zhao, Y., Scoville, N., Capak, P., Drory, N., and Gao, Y. (2012). Major-merger Galaxy Pairs in the COSMOS Field — Mass-dependent Merger Rate Evolution since z = 1. Astrophys. J., 747:85.

You, X. P., Hobbs, G., Coles, W. A., Manchester, R. N., Edwards, R., Bailes, M., Sarkissian, J., Verbiest, J. P. W., van Straten, W., Hotan, A., Ord, S., Jenet, F., Bhat, N. D. R., and Teoh, A.

(2007). Dispersion measure variations and their effect on precision pulsar timing. MNRAS, 378:493–506.

Yunes, N., Arun, K. G., Berti, E., and Will, C. M. (2009). Post-circular expansion of eccentric binary inspirals: Fourier-domain waveforms in the stationary phase approximation. Phys. Rev. D, 80(8):084001.

Appendices

A Supplementary material for chapter 4

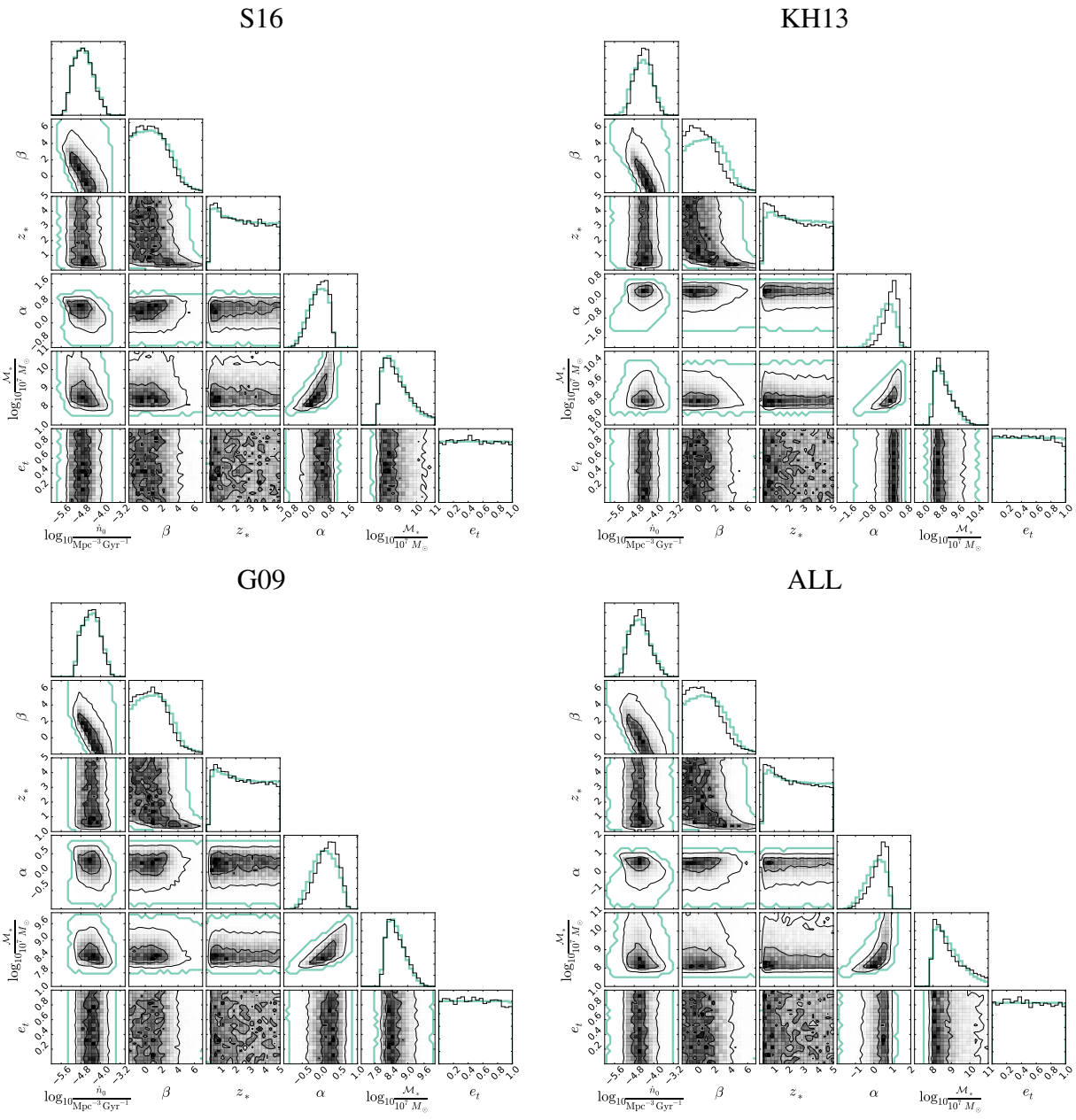

Figure A1

Figure A1: Posterior density functions on the model parameters given the PPTA upper limit. The nested sampling algorithm (see 4.4 in the main text) returns the full posteriors of the N-dimensional parameter space and the model evidences (see Supplementary Table A2). Here we show the posteriors for our main analysis of the PPTA upper limit using the default six parameter model ($\theta = \dot{n}_0, \beta, z_*, \alpha, \mathscr{M}_*, e_t$). The four panels show the result for each of the astrophysical model priors: top left S16; top right KH13, bottom left G09, bottom right ALL. Within each panel, the plots on the diagonal show the one-dimensional marginalised distributions for each parameter with the posterior (thin-black) and prior (thick-green). The central plots show the two-dimensional posterior distributions for each parameter pair (grey-shading) along with the extent of the prior (thick-green contour). It is clear by comparison of the prior and posterior that the current PTA observations impose little constraint on the shape of the SMBHB mass function. For S16, the most conservative model (top left), the prior and posterior are virtually identical. Even for the KH13 model (top right), the two distributions match closely, with only appreciable differences for β and α due to the PPTA limit excluding the highest values of h_c predicted by the model (cf main text Fig. 4.1) resulting in a preference for large α and negative β. In fact, for the mass function adopted in equation (4.2) of the main text, a large α results in a SMBHB population dominated by low mass systems, which tends to suppress the signal. Likewise, a small (or negative) β implies a sparser population of SMBHB at higher redshift, again reducing the GW background level. In any case, current PTA measurements provide little new information on the SMBHB cosmic population as also demonstrated by the small K-L divergences between prior and posterior of individual model parameters in Supplementary Table A1.

Model	K-L divergence					
	$\log_{10}\dot{n}_0$	β	z_*	α	$\log_{10}\mathscr{M}_*$	e_t
KH13	0.06	0.05	< 0.01	0.24	0.03	< 0.01
G09	< 0.01	0.01	< 0.01	0.04	0.01	< 0.01
S16	< 0.01	< 0.01	< 0.01	0.01	< 0.01	< 0.01
ALL	0.02	0.02	< 0.01	0.08	0.02	< 0.01

Table A1: Kullback-Leibler divergences for individual model parameters given the PPTA upper limit. The K-L divergences in the table compare the marginalised prior and posterior distributions for the individual parameters in the default 6-parameter model ($\theta = \dot{n}_0, \beta, z_*, \alpha, \mathscr{M}_*, e_t$) and given the PPTA upper limit. The K-L divergence is a measure of the degree of similarity between two probability distributions with zero being identical. The rows indicate the four astrophysical models used as priors in this study (KH13, G09, S16, ALL). As also seen qualitatively from Supplementary Fig. A1, there is little difference between the prior and posterior for all four models. KH13, the model predicting the highest characteristic strain as expected has the highest K-L divergences, however as also shown by Supplementary Fig. A1 the difference is still small.

Model	$h_{1\mathrm{yr},95\%} = 1\times10^{-15}$		$h_{1\mathrm{yr},95\%} = 3\times10^{-16}$		$h_{1\mathrm{yr},95\%} = 1\times10^{-16}$	
	e_t	$e_t+\eta$	e_t	$e_t+\eta$	e_t	$e_t+\eta$
KH13	$-2.36\,(0.85)$	$-2.23\,(0.84)$	$-5.68\,(2.25)$	$-5.47\,(2.25)$	$-13.17\,(5.18)$	$-9.03\,(7.11)$
G09	$-1.2\,(0.39)$	$-1.1\,(0.39)$	$-3.35\,(1.11)$	$-3.17\,(1.09)$	$-8.26\,(2.86)$	$-6.38\,(4.02)$
S16	$-0.6\,(0.37)$	$-0.57\,(0.38)$	$-1.62\,(0.69)$	$-1.6\,(0.71)$	$-3.82\,(1.42)$	$-3.56\,(1.48)$
ALL	$-1.23\,(0.62)$	$-1.14\,(0.62)$	$-2.68\,(1.33)$	$-2.63\,(1.31)$	$-5.74\,(2.50)$	$-5.09\,(2.53)$

Table A2: Progression of model constraints with improving upper limits. The table shows the natural logarithm of model evidences and associated h_c Kullback-Leibler (K-L) divergences (in parenthesis) for each of the astrophysical models: KH13, G09, S16 and ALL. We consider two different parametrisations of the SMBHB dynamics; one which has only e_t as a free parameter (column 'e_t', the 6 parameter model), and one where we add the normalization factor η to the density at the influence radius ρ_i as a free parameter (column '$e_t+\eta$', the 7 parameter model). Numbers are reported for three values of the 95% PTA upper limit; the current upper limit at 1×10^{-15} and two possible future upper limits at 3×10^{-16} and 1×10^{-16}. See also Supplementary Note A1.

A1 Supplementary Note 1
The progression of constraints given improvements on the upper limit

From Supplementary Table A2 we see that, given the current upper limit of $h_{1\mathrm{yr},95\%} = 1 \times 10^{-15}$, there are no significant differences between the 6 and 7 parameter results, with virtually identical evidences and K-L divergences. Together with the flat e_t posteriors shown in Supplementary Fig. A1, this leads us to an important conclusion: current PTA non detections do not favour (nor require) a strong coupling with the environment. Neither high stellar densities (i.e. efficient 3-body scattering) nor high eccentricities are preferred by the data. The conservative S16 model is always favoured, however even when compared to KH13, one obtains $\ln \mathscr{B} = 1.76$, which only mildly favours S16 (Kass and Raftery, 1995). In addition, all K-L divergences are smaller than unity, indicating only minor updates with respect to the h_c prior distributions. This is another measure of the fact that the data are not very informative.

Turning to the limit at $h_{1\mathrm{yr},95\%} = 3 \times 10^{-16}$, the K-L divergences of all models, with the exception of S16, are now larger than unity indicating that the upper limit is becoming more informative. In terms of model comparison, S16 is now mildly favoured with respect to G09 ($\ln \mathscr{B} = 1.73$) and strongly favoured compared to KH13 ($\ln \mathscr{B} = 4.06$). Again, we note that adding η does not make a significant difference to the model evidence. Even with such a low upper limit, neither high eccentricity nor strong coupling with the environment improve the agreement between model expectations and data. Although this seems counter-intuitive, we should keep in mind that the upper limit is set around $f \approx 5 \times 10^{-9}$Hz (cf main text Fig. 4.1). Any dynamical effect should therefore cause a turnover of the spectrum around 10^{-8}Hz to have an impact on model selection, which occurs only in a small corner of parameter space where both e_t and η are high. However, for all models $h_{1\mathrm{yr},95\%} = 3 \times 10^{-16}$ is still consistent with the tail of the h_c distribution when an $f^{-2/3}$ spectrum is assumed. Invoking high e_t and η is not necessary.

The limit becomes far more interesting if it reaches $h_{1\mathrm{yr},95\%} = 1 \times 10^{-16}$. Now all K-L divergences are substantial, indicating that the measurement is indeed informative. Model selection now strongly favours model S16 compared to any other model, whether η is included or not.

Even including all environmental effects, we find that S16 is decisively preferred over KH13 with $\ln \mathscr{B} = 5.47$. Note however, that S16 has a log evidence of -3.56 of its own, considerably lower than zero (the evidence of a model is unaffected by the measurement). Since delays and stalling can potentially decrease the GW background by preventing many SMBHB from merging, it is likely that a non detection at this level will provide strong support for those dynamical effects.

Paper	X	a	b	ε
(Häring and Rix, 2004)	M_*	8.2	1.12	0.30
(Sani et al., 2011)	M_*	8.2	0.79	0.37
(Beifiori et al., 2012)	M_*	7.84	0.91	0.46
(McConnell and Ma, 2013)	M_*	8.46	1.05	0.34
(Graham, 2012)	M_*	8.56	1.01	0.44
		(8.69)	(1.98)	(0.57)
(Kormendy and Ho, 2013)	M_*	8.69	1.17	0.29
(Sani et al., 2011)	L_i	8.19	0.93	0.38
(Gültekin et al., 2009)	σ	8.23	3.96	0.31
(Graham et al., 2011)	σ	8.13	5.13	0.32
(Beifiori et al., 2012)	σ	7.99	4.42	0.33
(McConnell and Ma, 2013)	σ	8.33	5.57	0.40
(Graham and Scott, 2013)	σ	8.28	6.01	0.41
(Kormendy and Ho, 2013)	σ	8.5	4.42	0.28
(Shankar et al., 2016)	σ	7.8	4.3	0.3

Table A3: SMBH-galaxy relations used to construct the astrophysical models. For each merging galaxy pair, we assign a black holes with masses drawn from 14 SMBH-galaxy relations found in the literature. In the table we list the relations used. The total black hole mass is described by the relation $\log_{10}M = a + b\log_{10}X$. Here $X = \{\sigma/200\mathrm{kms}^{-1}, L_i/10^{11}\mathrm{L}_\odot$ or $M_*/10^{11}\mathrm{M}_\odot\}$, with σ being the stellar velocity dispersion of the galaxy bulge, L_i its mid-infrared luminosity, and M_* its bulge stellar mass. Each relation is also characterized by an intrinsic scatter ε. In the table, we list the parameters a, b and ε for each of the relations taken from the literature. There are two entries for (Graham, 2012) who proposes a double power law with a break at $\bar{M}_* = 7 \times 10\mathrm{M}_\odot$, for which the values in parenthesis refer to $M_* < \bar{M}_*$.

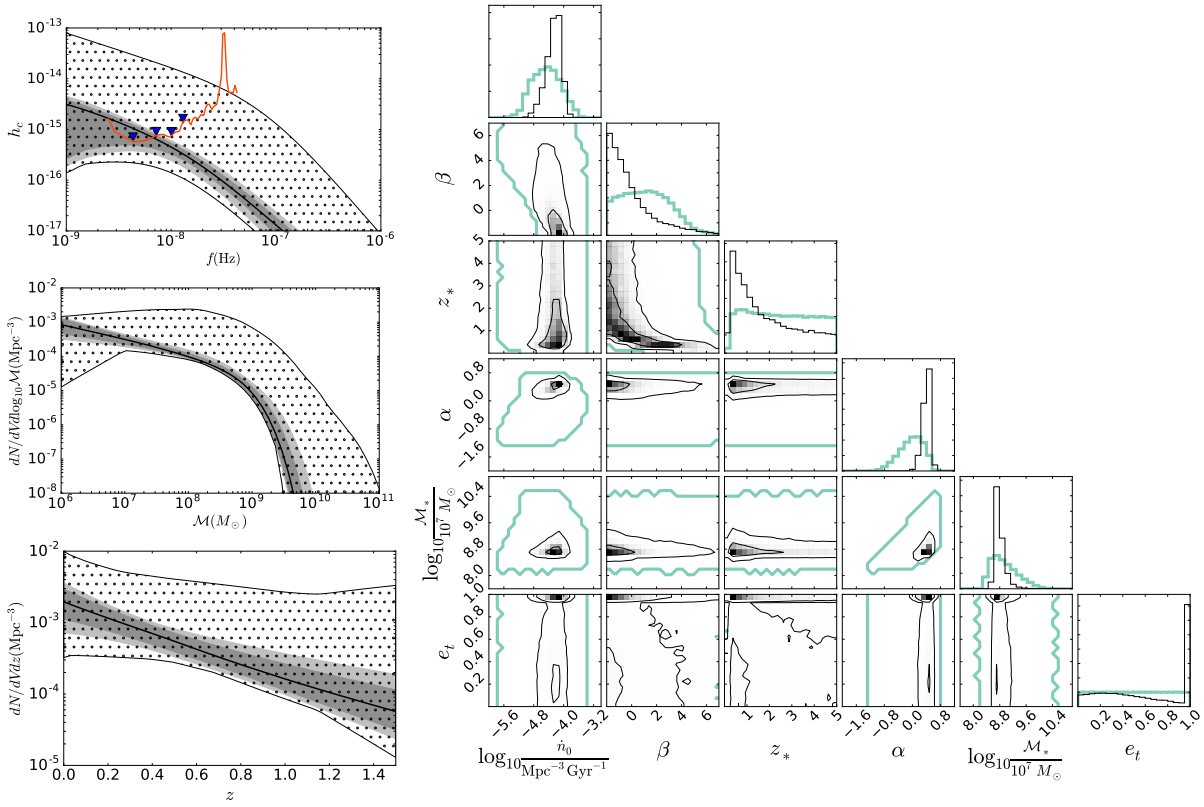

Figure A2: Posterior distrubtions for a putative upper limit at $h_{1\mathrm{yr}} = 1 \times 10^{-16}$. Here we show results of a upper limit of $h_{1\mathrm{yr},95\%} = 1 \times 10^{-16}$ for the six parameter model and astrophysical prior KH13. Left panel, from top to bottom: characteristic amplitude, density mass function and density redshift evolution of SMBHBs. In each panel, the dotted areas represent the astrophysical prior, the shaded bands are the 68% and 90% of the posterior distribution and the solid thick line is its median value. In the top panel only, the solid orange curve represents the bin-by-bin 95% upper limits at different frequency bins (with blue triangles indicating the frequency bins we use), resulting in an overall limit $h_{1\mathrm{yr},95\%} = 1 \times 10^{-16}$. Right panel: the individual posterior distributions. The diagonal plots show the one-dimensional posterior distribution (black) along with the prior (green-thick), whilst the central plots show the two-dimensional posterior for each of the parameter pairs again with the extent of the prior shown by the single green-thick contour. We see that now all the posteriors differ significantly from the respective prior. Low β and z_* are preferred, because this suppresses the total number of SMBHs at high redshifts. Note that higher values of $\dot{n}_0$ are preferred. Although this might be surprising, it is dictated by the shape of the prior of dn/dz (lower left panel); in order to minimize the signal, it is more convenient to allow a negative β at the expenses of a higher local normalization $\dot{n}_0$ of the merger rate. High α values are clearly preferred, since they imply a population dominated by low mass SMBHBs (middle left panel). The e_t posterior now shows a prominent peak close to the maximum $e_t = 0.999$, with a long tail extending to zero (right panel, final plot). Very high eccentricities are preferred, although low values are still possible. This is because 1×10^{-16} is only a 95% upper limit, therefore there is a small chance that a low eccentricity model producing a signal surpassing the 1×10^{-16} value is nonetheless accepted in the posterior.

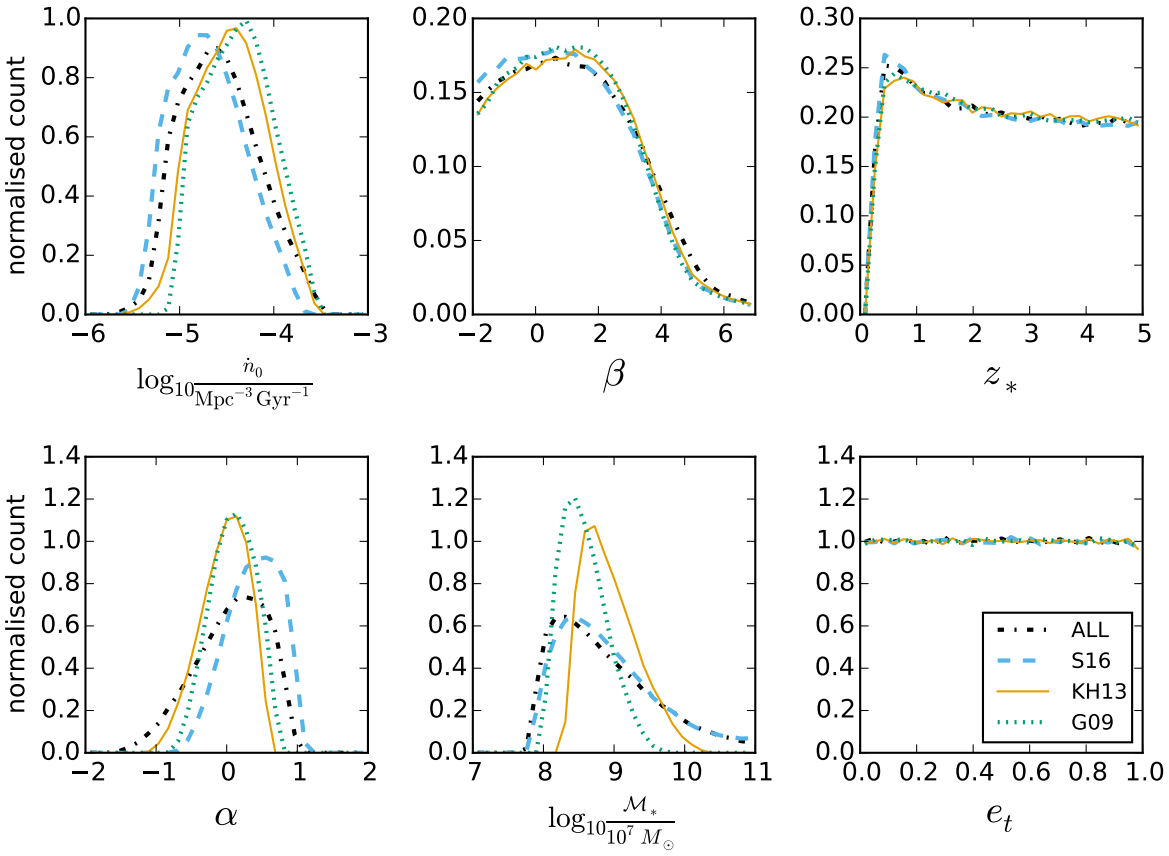

Figure A3: Prior density functions of the model parameters. The numerical SMBHB mass functions obtained from the prior bands in main text Fig. 4.3 need to be related analytically to the parameters of equation (4.2). Our strategy is therefore to make a large series of random draws of the five parameters defining equation (4.2), and to retain only those sets that produce dn/dz and $dn/d\mathscr{M}$ within the boundaries set by the empirical models shown in Fig. 4.3 of the main text. The prior distributions for the individual parameters obtained in this way are shown here. Top row from left to right $\dot{n}_0$, β, z_*; bottom row from left to right α, $\mathscr{M}_*$, e_t. The lines represent the priors for the four astrophysical models KH13 (orange, solid), S16 (blue, dashed), G09 (green dotted) and ALL (black dash-dot). We see that the redshift parameters (β and z_*) have a very similar prior for each of the models. The main differences are seen in the number rate density of mergers $\dot{n}_0$ and in the mass distribution parameters (α and $\mathscr{M}_*$). KH13 and ALL prefer higher values of $\dot{n}_0$. S16 allows for slightly higher values of α (in comparison to KH13 and G09), corresponding to a more negative slope on the mass distribution, with preference for a larger number of low mass binaries. The eccentricity parameter e_t is unaffected by the choice of model, therefore we place on it a flat prior in the range $10^{-6} < e_t < 0.999$.

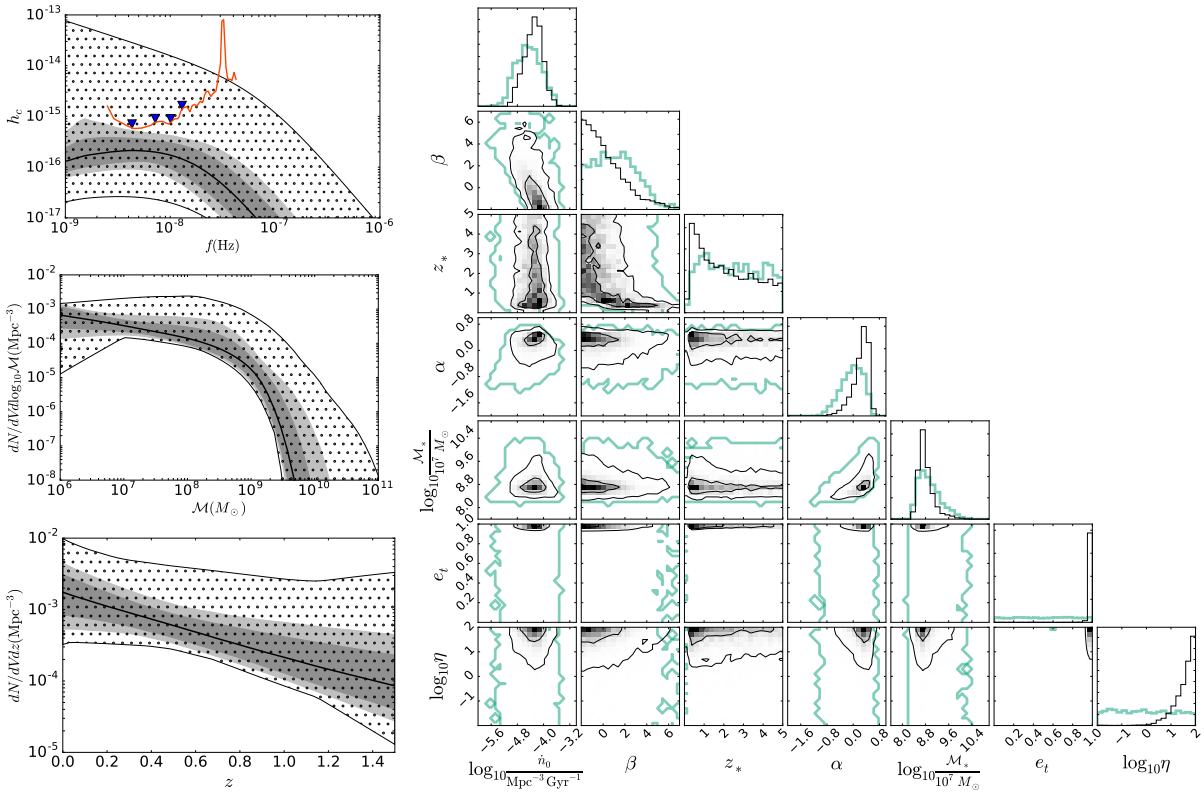

Figure A4: Posterior distributions for a putative upper limit at $h_{1\mathrm{yr}} = 1 \times 10^{-16}$ with the addition of a free stellar density parameter. Here we show results of a upper limit of $h_{1\mathrm{yr},95\%} = 1 \times 10^{-16}$ for the seven parameter model and astrophysical prior KH13. The plots show are identical to the description of Supplementary Fig. A2, the only difference being the addition of the stellar density parameter η. Most notably, we see now that extremely high eccentricities and high densities are strongly favoured. This is primarily because the addition of η extends the prior in h_c (shown in the upper left panel) downwards quite below the level imposed by the upper limit. It is therefore now easier to find points in the parameter space consistent with the measurement when e_t and η are large. Should other SMBH-host galaxy relations being ruled out by independent constraints, a PTA upper limit of 1×10^{-16} would provide strong evidence of surprisingly extreme dynamical conditions of SMBHBs.

B Supplementary material for chapter 5

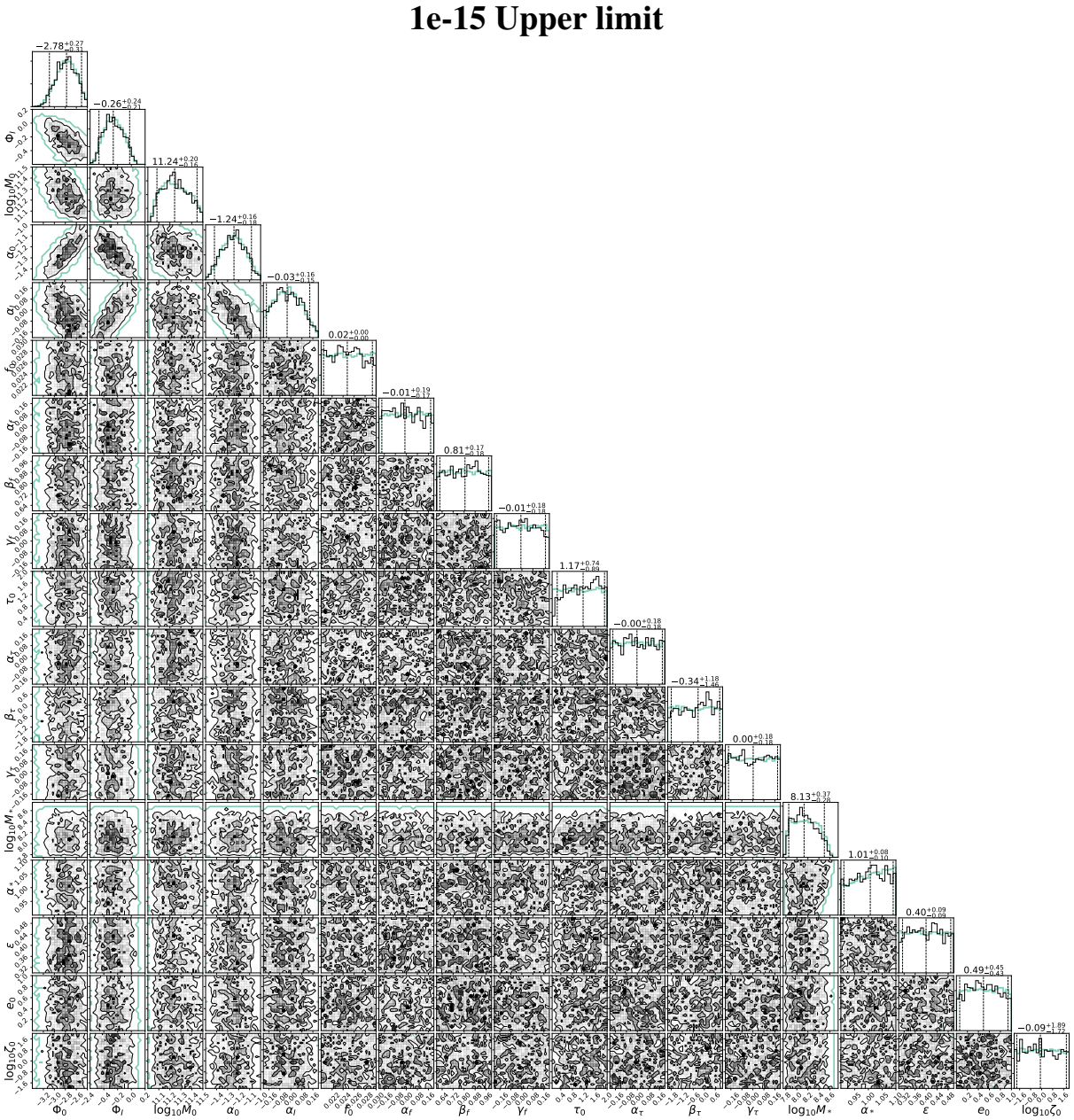

Figure B1: Full corner plot of the 18 parameters for the PPTA15 case

1e-16 Upper limit

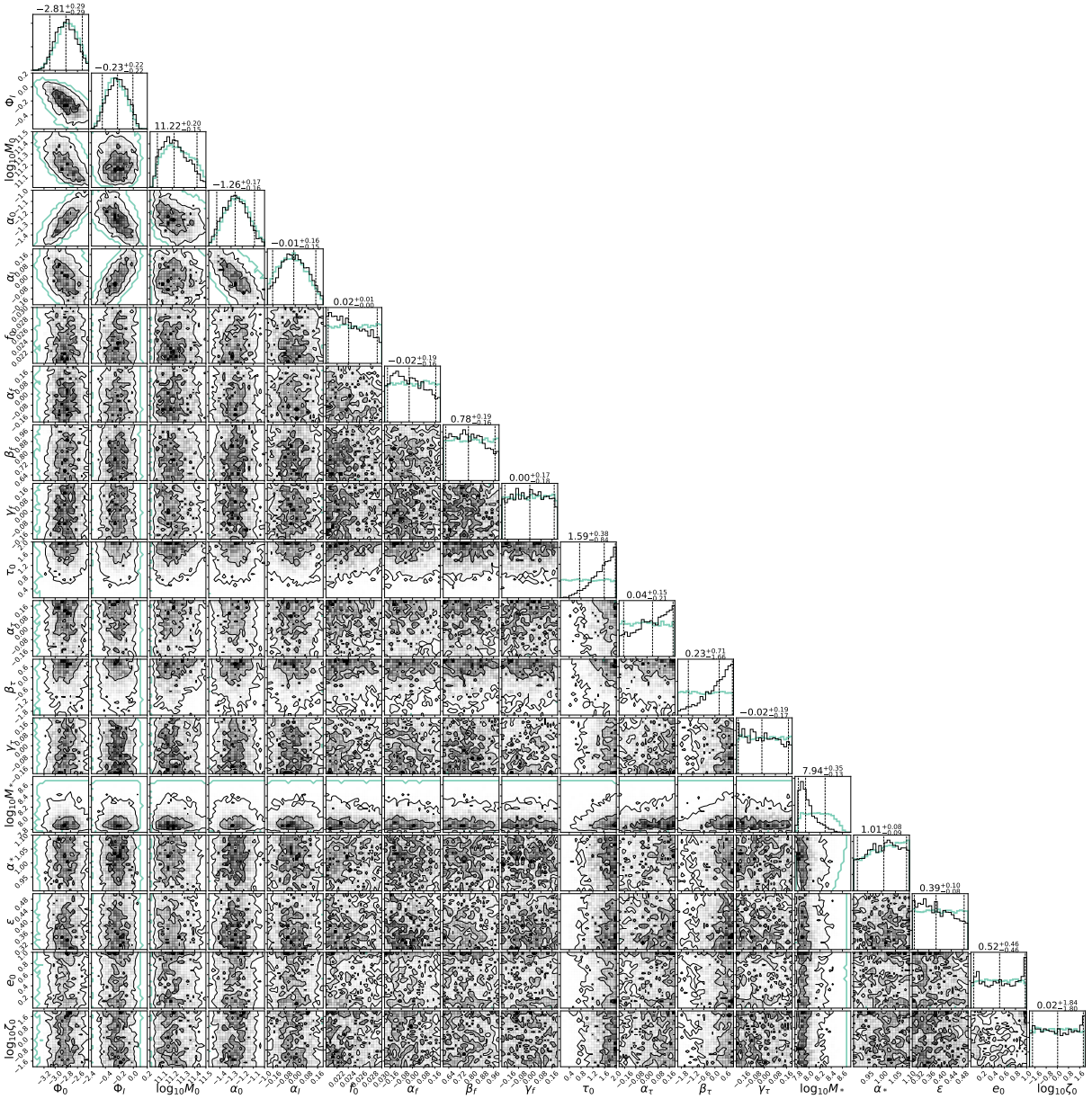

Figure B2: Full corner plot of the 18 parameters for the PPTA16 case

1e-17 Upper limit

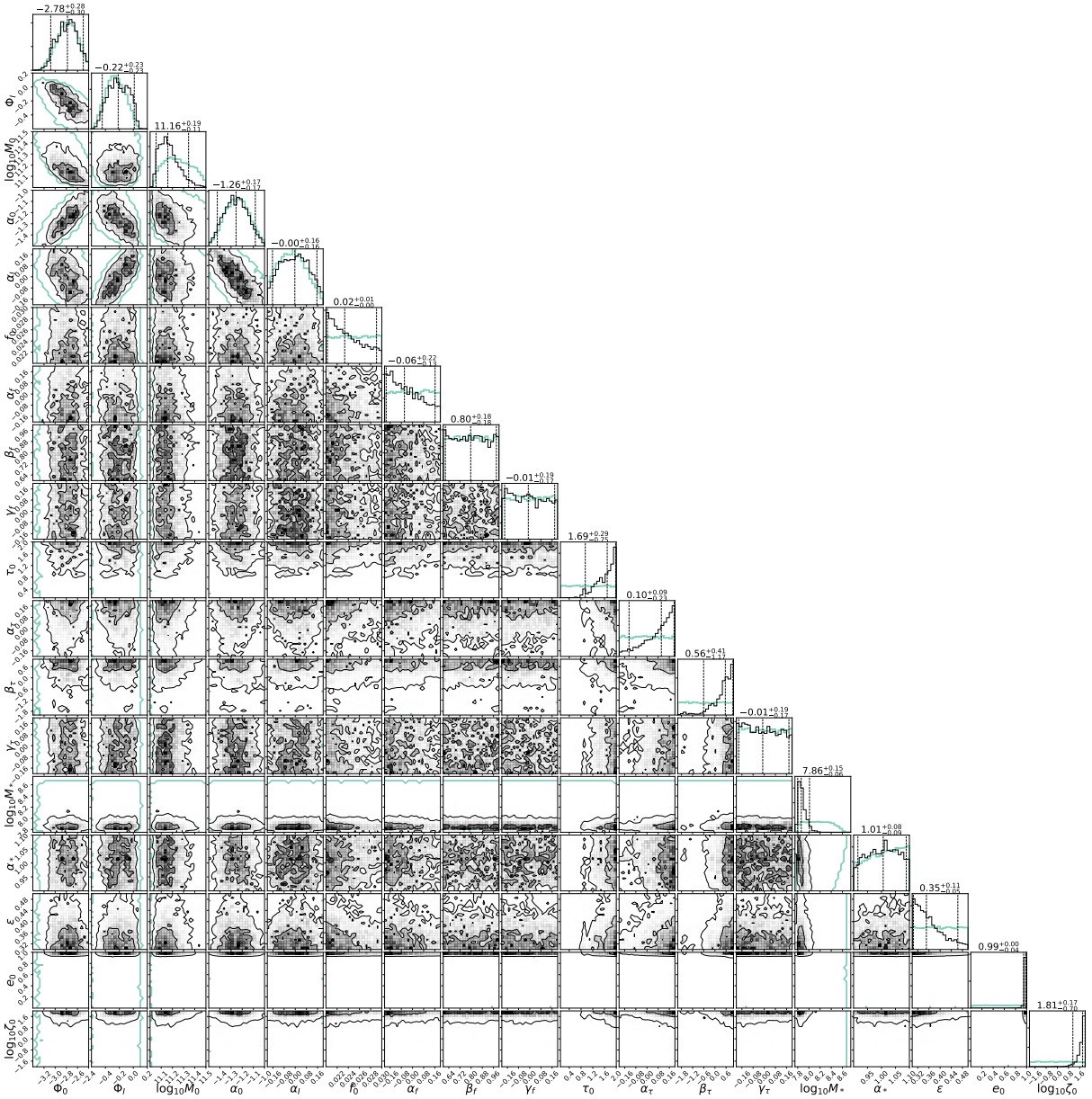

Figure B3: Full corner plot of the 18 parameters for the PPTA17 case

1e-17 Upper limit Extended Prior

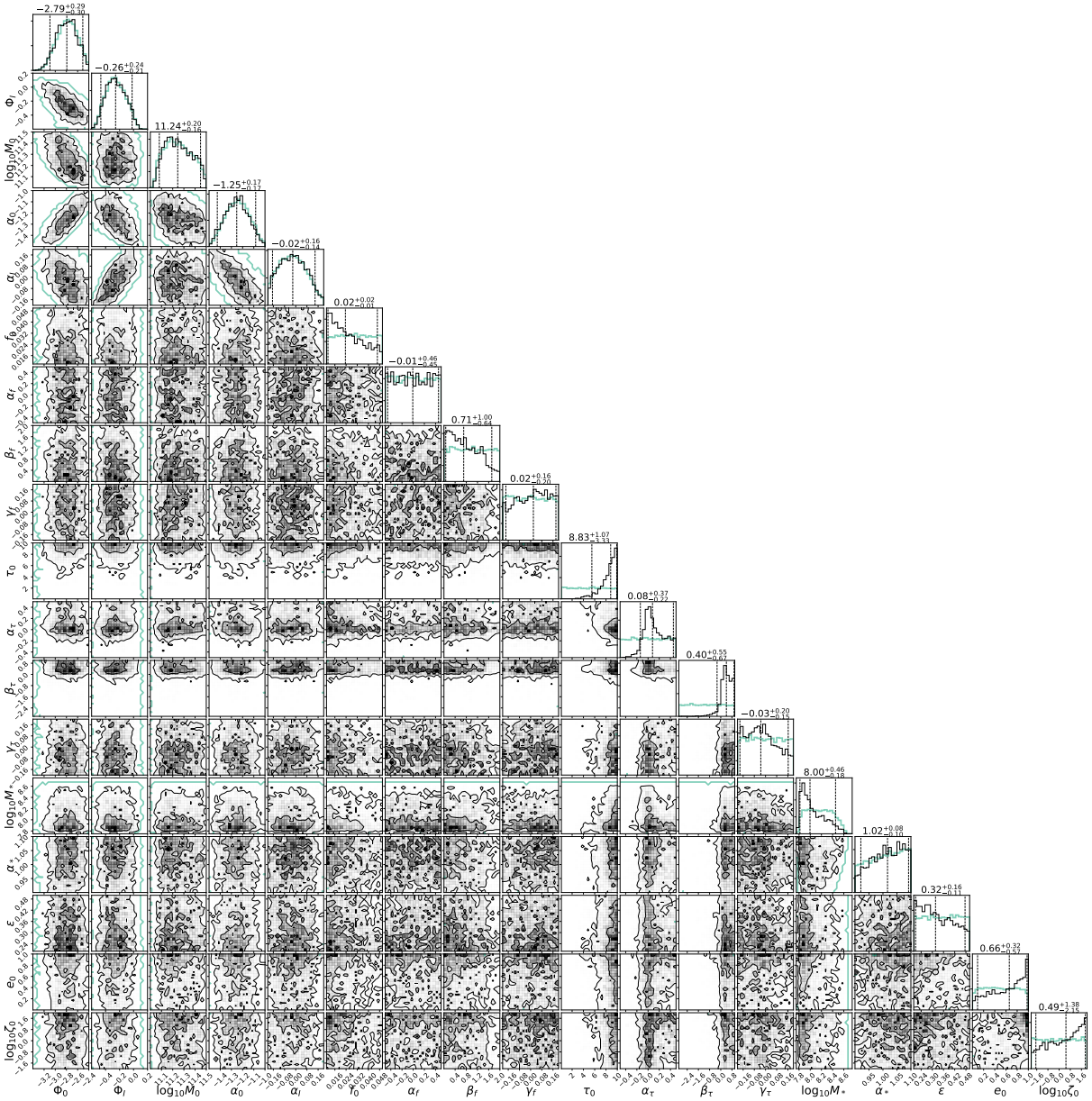

Figure B4: Full corner plot of the 18 parameters for the PPTA17 extended prior case

Circular case IPTA30

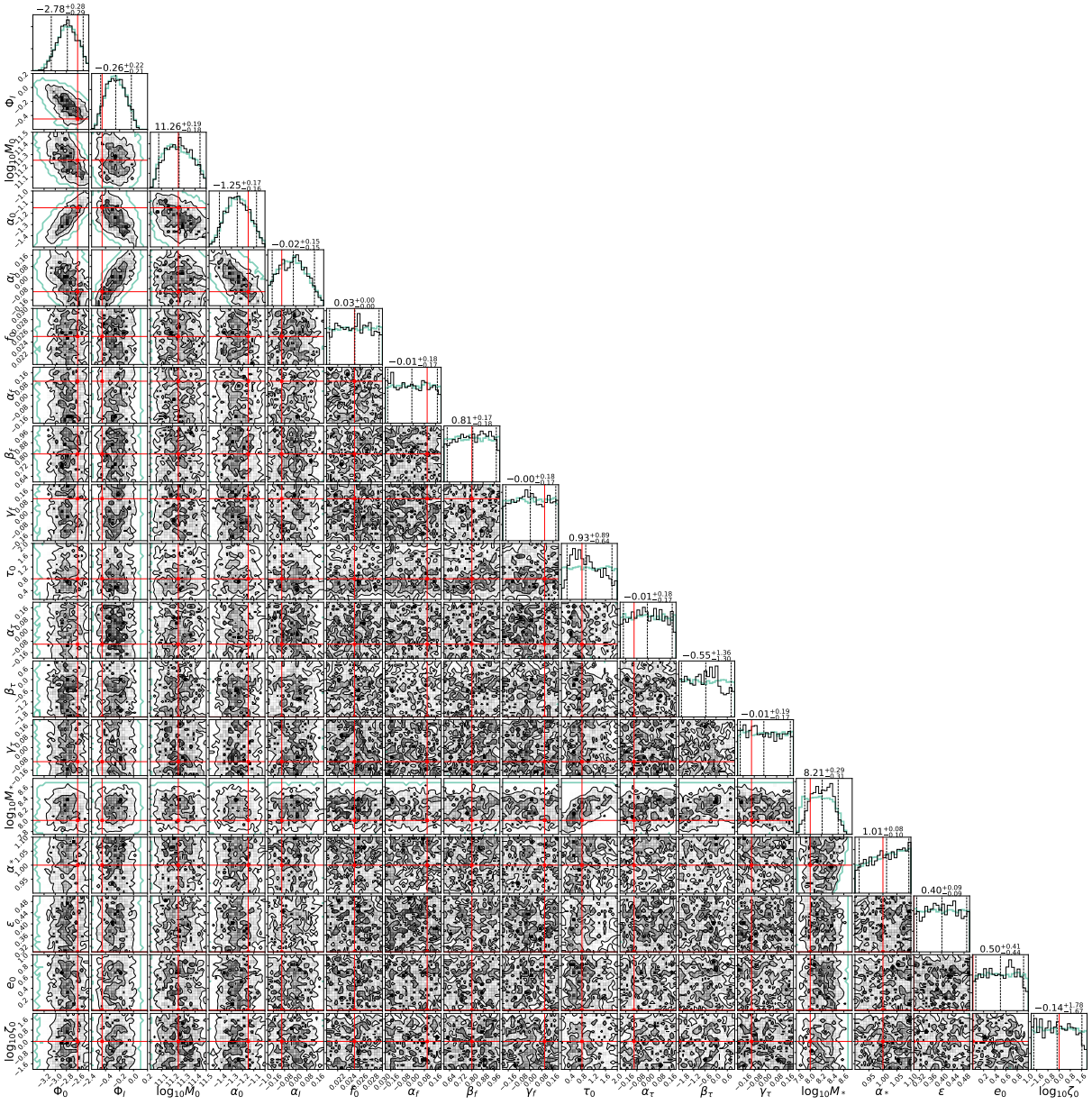

Figure B5: Full corner plot of the 18 parameters for the IPTA30 Circular case

Circular case SKA20

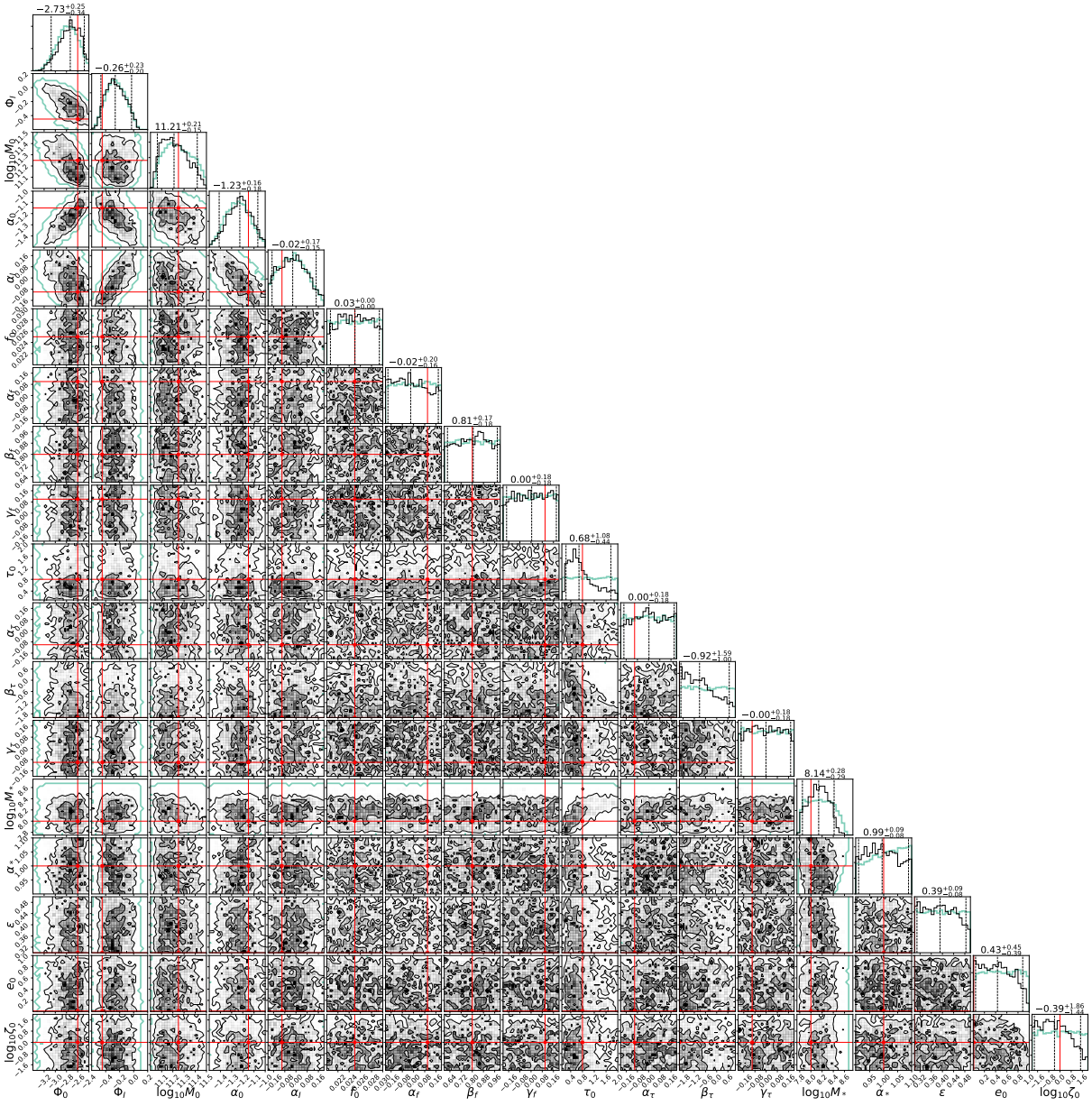

Figure B6: Full corner plot of the 18 parameters for the SKA20 Circular case

Eccentric case IPTA30

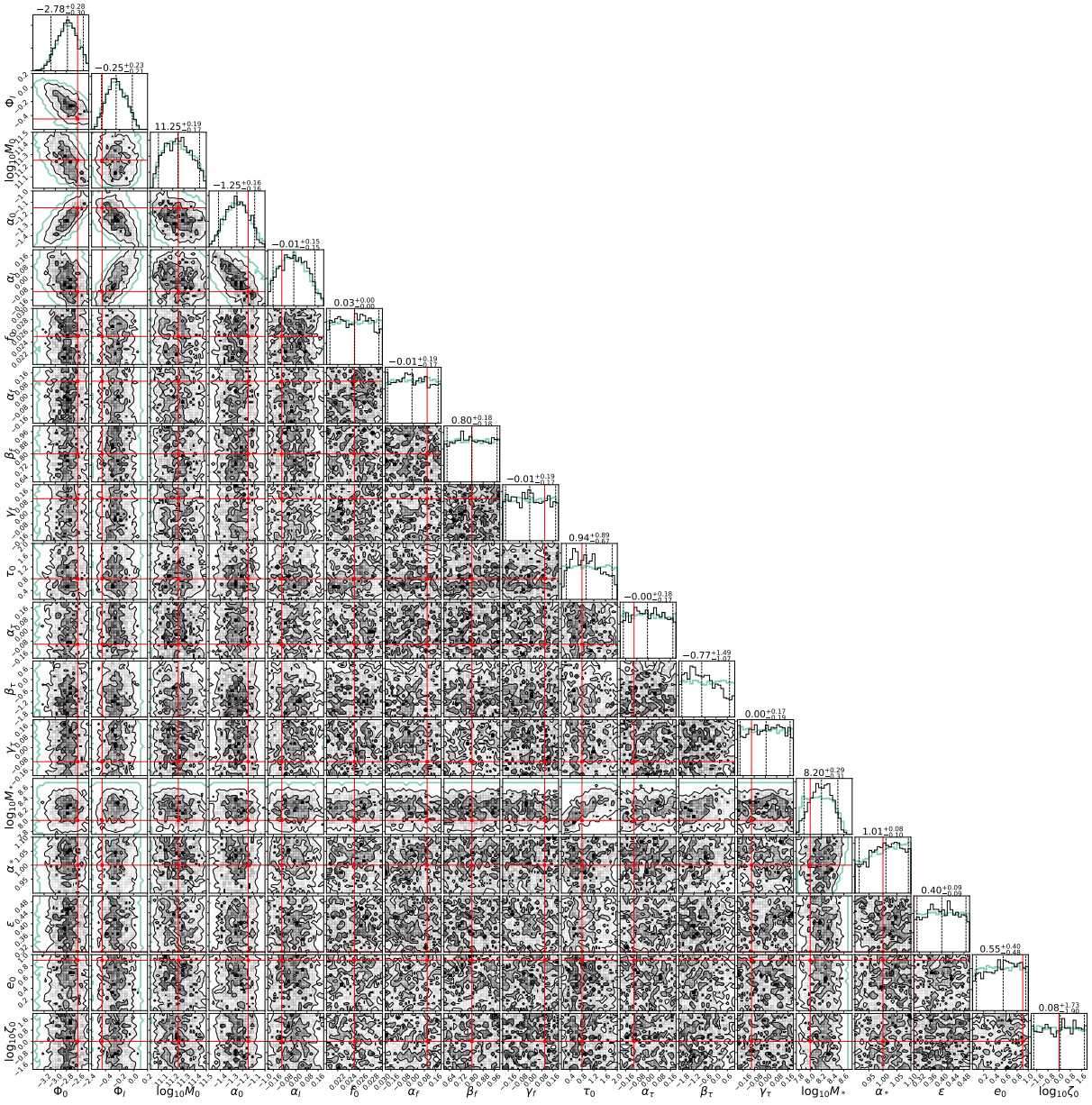

Figure B7: Full corner plot of the 18 parameters for the IPTA30 Eccentric case

Eccentric case SKA20

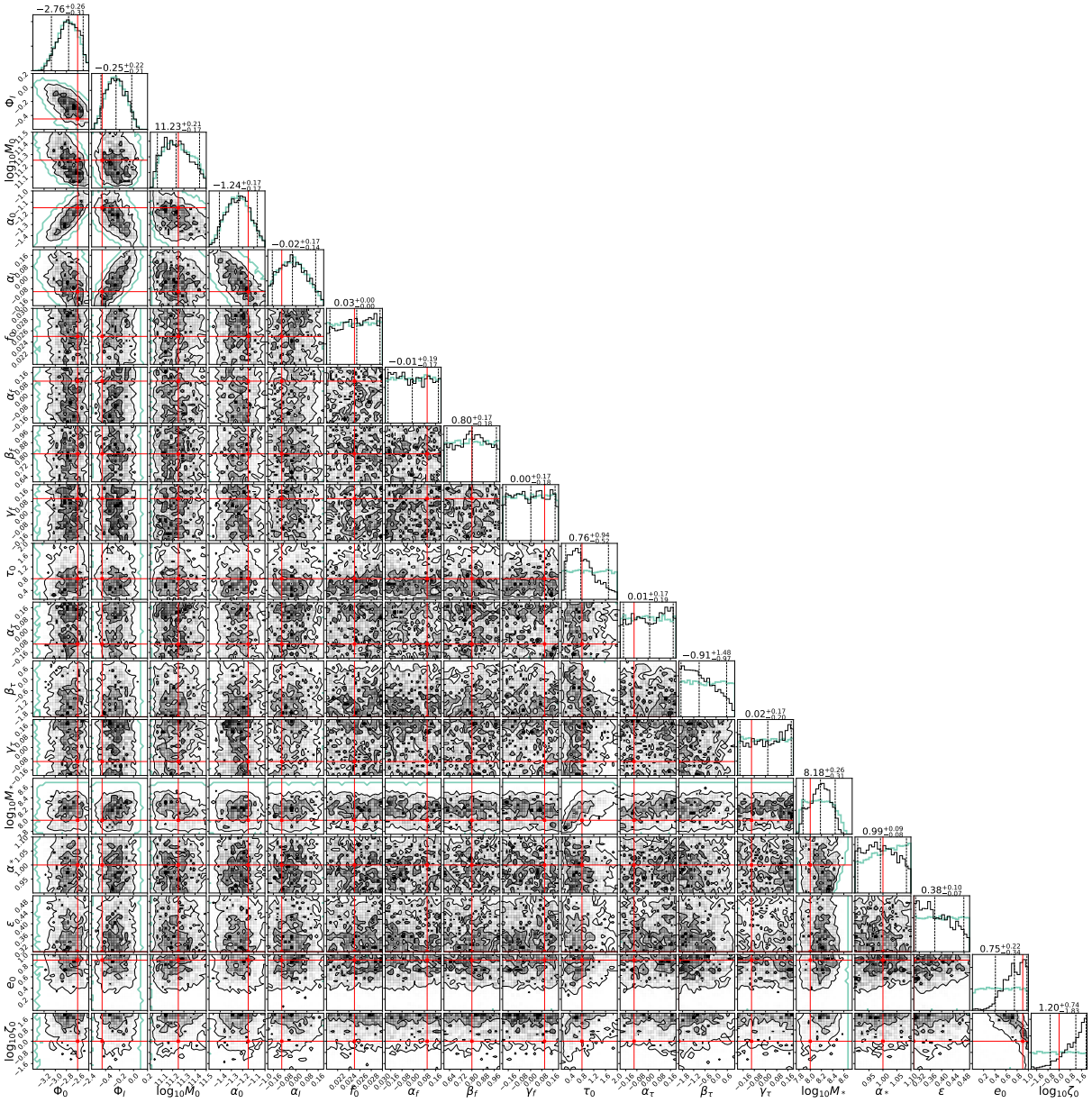

Figure B8: Full corner plot of the 18 parameters for the SKA20 Eccentric case

Circular case Ideal

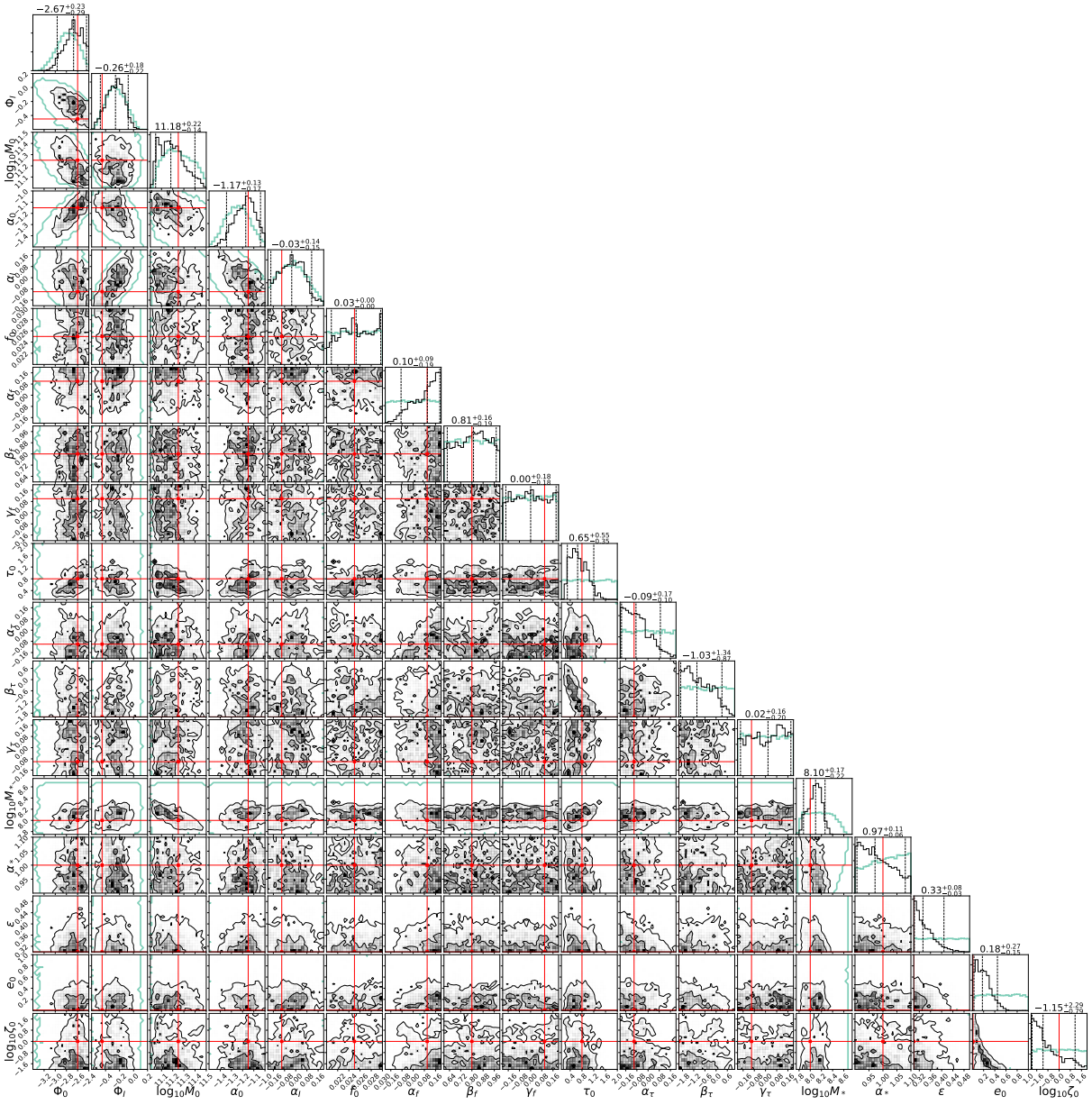

Figure B9: Full corner plot of the 18 parameters for the Ideal Circular case

Eccentric case Ideal

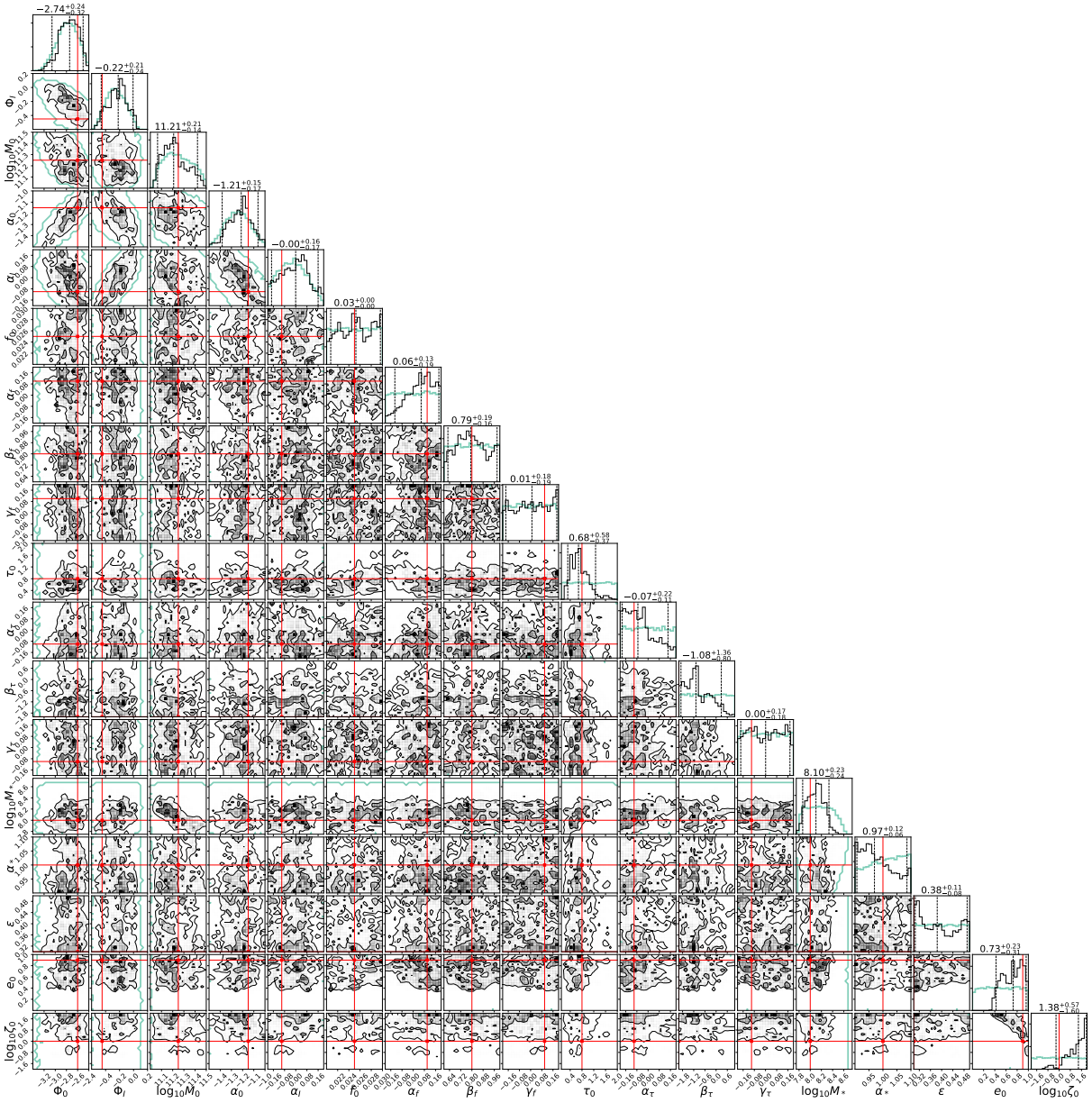

Figure B10: Full corner plot of the 18 parameters for the Ideal Eccentric case